On the corrosion and additive manufacturing of 316L stainless steel

Guilherme Sander Malab

B. Eng. (Metallurgical), Universidade Federal de Minas Gerais

A thesis (including published works) submitted for the degree of

Doctor of Philosophy

September 2020

Department of Materials Science and Engineering

Monash University

Victoria, Australia

Copyright notice

I certify that I have made all reasonable efforts to secure copyright permissions for third-party content included in this thesis and have not knowingly added copyright content to my work without the owner's permission.

Abstract

The corrosion resistance of additively manufactured stainless steels has only recently become a critical research topic. At the commencement of this project, the corrosion evaluation of such additively manufactured stainless steels in aggressive environments (i.e. chloride containing media) was not yet undertaken; however this is a field of study that is crucial to their application in service. The stainless steel AISI 316L is a popular choice for applications that require corrosion resistant alloys, weldability, biocompatibility, and, versatility (shapes, sizes, applications, etc.).

Selective laser melting (SLM) is an additive manufacturing technology that operates by incorporating a laser system with a powder-bed system and has now been extensively demonstrated to produce stainless steel 316L components. The parameters utilised for the SLM of metals and alloys have been discovered to have a direct influence on the resultant microstructure. Consequently, investigating and understanding the effect of SLM processing variables on alloy properties is of key relevance for the use of such materials in engineering applications.

For this project, 316L was additively manufactured by SLM and production parameters were varied, namely laser power, laser scan speed and build orientation. The variability of parameters and their respective effect on the microstructure (e.g. porosity) of 316L were investigated in the context of corrosion (with an emphasis on pitting). In addition, the effect of residual stresses generated in the SLM process was also assessed for its influence on electrochemical and immersion performance of 316L, relative to build orientation. The evaluation of the performance for SLM 316L specimens was assessed throughout by comparison with wrought 316L.

To understand pitting mechanisms in 316L, metastable pits and their transition to stability were investigated by in-situ surface imaging during potentiostatic polarisation. Visual assessment of the surface combined with electrochemical characterisation allowed the evaluation of pitting characteristics that were not well previously comprehended.

Finally, an exploratory study on the development of 316L/glass composite specimens by SLM was carried out in order to investigate the potential to develop new engineered materials utilising SLM technology. The resultant specimens were investigated for mechanical and electrochemical performance.

Publications during enrolment

1. **G. Sander**, S. Thomas, V. Cruz, M. Jurg, N. Birbilis, X. Gao, M. Brameld, C.R. Hutchinson, On The Corrosion and Metastable Pitting Characteristics of 316L Stainless Steel Produced by Selective Laser Melting, J. Electrochem. Soc. 164 (2017) C250–C257. https://doi.org/10.1149/2.0551706jes.
2. **G. Sander**, J. Tan, P. Balan, O. Gharbi, D.R. Feenstra, L. Singer, S. Thomas, R.G. Kelly, J.R. Scully, N. Birbilis, Corrosion of additively manufactured alloys: A review, Corrosion. 74 (2018) 1318–1350. https://doi.org/10.5006/2926.
3. **G. Sander**, A. Babu, X. Gao, D. Jiang, N. Birbilis, On the effect of build orientation and residual stress on the corrosion of 316L stainless steel prepared by selective laser melting, *manuscript under review at Corrosion Science* (2020).
4. **G. Sander**, V. Cruz, N. Bhat, Nick Birbilis, On the in-situ characterisation of metastable pitting using 316L stainless steel as a case study, *manuscript under review at Corrosion Science* (2020).
5. **G. Sander**, D. Jiang, Y. Wu, N. Birbilis, Exploring the possibility of a stainless steel and glass composite produced by additive manufacturing, *manuscript under review at Materials & Design* (2020).

Thesis including published works declaration

I hereby declare that this thesis contains no material which has been accepted for the award of any other degree or diploma at any university or equivalent institution and that, to the best of my knowledge and belief, this thesis contains no material previously published or written by another person, except where due reference is made in the text of the thesis.

This thesis includes 2 original papers published in peer reviewed journals and 3 submitted publications. The core theme of the thesis is on the corrosion and additive manufacturing of 316L stainless steel. The ideas, development and writing up of all the papers in the thesis were the principal responsibility of myself, the student, working within the Materials Science and Engineering Department (Faculty of Engineering) under the supervision of Professor Nick Birbilis.

The inclusion of co-authors reflects the fact that the work came from active collaboration between researchers and acknowledges input into team-based research

In the case of Chapter 2 and 3, my contribution to the work involved the following:

Thesis Chapter	Publication Title	Status	Nature and % of student contribution	Co-author name(s) Nature and % of Co-author's contribution*	Co-author(s), Monash student Y/N*
2	*Corrosion of additively manufactured alloys: A review.*	*Published*	*Concept, literature survey and writing (80%)*	*1) J. Tan; input into manuscript (1%).* *2) P. Balan; evaluation of manuscript and guiding comments (1%),* *3) O. Gharbi; input into manuscript (4%)* *4) D.R. Feenstra; input into manuscript (3%),* *5) S. Thomas; contribution to the manuscript (3%),* *6) L. Singer; evaluation of manuscript and guiding comments (1%),* *7) R.G. Kelly; evaluation of manuscript and guiding comments (1%),* *8) J.R. Scully; evaluation of manuscript and guiding comments (1%),* *9) N. Birbilis; input into manuscript (5%).*	*Yes* *No* *No* *Yes* *No* *No* *No* *No* *No*
3	*On the corrosion and metastable pitting characteristics of 316L stainless steel produced by selective laser melting.*	*Published*	*Concept, collection of experimental data, analysis of data and writing of manuscript (80%)*	*1) S. Thomas; input into manuscript (5%).* *2) V. Cruz; methodology (1.5%)* *3) M. Jurg; methodology (1.5%)* *4) N. Birbilis; evaluation of manuscript and supervision (5%).* *5) X. Gao; methodology and data analysis (2%)* *6) M. Brameld; evaluation of manuscript and guiding comments (1%),* *7) C.R. Hutchinson; evaluation of manuscript and guiding comments (4%)*	*No* *Yes* *No* *No* *No* *No* *No*

I have not renumbered sections of submitted or published papers in order to generate a consistent presentation within the thesis.

Student signature: [redacted] **Date:** **06/09/2020**

The undersigned certify that the above declaration correctly reflects the nature and extent of the student's and co-authors' contributions to this work. In instances where I am not the responsible author, I have consulted with the responsible author to agree on the respective contributions of the authors.

Main Supervisor signature: [redacted] **Date:** **06/09/2020**

Acknowledgements

I would like to firstly thank my supervisor Nick Birbilis, not only for teaching me immensurable positive lessons over the years but also for always believing in me and my work. Your guidance allowed me to become a better person and a better professional.

I would also like to specially thank Sebastian Thomas for all the support, advice, encouragement and friendship he gave me since the beginning of my doctorate program.

I acknowledge the incredible friendship, experiences, technical and emotional support I had the opportunity to receive from Darren Feenstra, Lee Djumas, Will Nash, Oumaïma Gharbi and Abirami Babu. You made this journey much more enjoyable, full of joy and laughter.

I am very thankful for have been able to work with Erin Brodie, Victor Cruz, Marten Jurg, Tim Murray, Derui Jiang and Qing Cao in the Woodside Innovation Centre. With you I was able to learn and share valuable experiences.

I am also very thankful to Edna Tan, Kris Wirthensohn, Michelle Lang, Ian Wheeler and the whole staff in the Department of Materials Science and Engineering at Monash University who work hard to support our research and make our lives easier.

I would like to thank all my friends in Australia, Brazil and Europe for always giving me the strength and the incentive to keep moving forward no matter which challenges were ahead of me. I am grateful to Giovanni Cuffaro for being by my side for final steps of this journey and for bringing so much joy to my life. Among these, I would like to specially thank Paula Magalhães for her unconditional support and friendship. My friend, I could never thank you enough for everything you have done for me.

Above all, I dedicate this accomplishment and express my utmost gratitude to my mother, my father and my brother for always being the base that supports who I am. You have inspired me every day to grow stronger and to become the better self I could possibly be.

Chapter 1: Introduction and research project aims

A manufacturing process is nowadays termed 'additive' when production follows a pre-determined set of commands based on a computer aided design (CAD) [1,2]. Historically, additive processes also include welding, or cumulative manufacturing that does not involve material subtraction. The general term 'additive manufacturing' (AM) is commonly referred to as simply '3D printing' when it employs a CAD design, and it has been performed for an increasing portfolio of materials such as polymers, metals, ceramics and composites over the last 30 years [3,4]. Stainless steels are a class of corrosion resistant iron (Fe) based alloys, that are commonly utilised in their wrought and cast type. More specifically, the AISI 316L is an austenitic stainless steel grade largely utilised in a wide range of applications from cutlery to offshore oil and gas refinery pipelines. The designation of '316' refers to a nominal composition of Fe – 16-18 % Cr – 10-14 % Ni – 0.03 % C – 2.0 % Mn – 1.0 %Si – 0.045 % P – 0.030 % S – 2.0-3.0 Mo (in wt. %); whilst the 'L' refers to a low-carbon concentration that is critical to improving alloy weldability. A relatively low cost (compared to corrosion resistant nickel alloys), high ductility, moderate yield strength (~ 350 MPa) and high corrosion resistance have ensured that 316L is an important alloy in industrial and general applications [5]. Technological advances in AM, have allowed the production of 316L by a variety of non-conventional methods [6–8]. The implementation of these AM 316L components into service requires characterisation and qualification. In order to be safely applied, the mechanical strength and durability of additively manufactured stainless steels must be equal or superior to their conventionally produced counterparts. The qualification of wrought and cast stainless steels (including the 316L grade) has been addressed and compiled for diverse applications over the last century [5,9]. Therefore, similar characterisation and qualification of the emerging AM stainless steels become essential for engineering applications.

Metal AM systems are usually classified based on the metal feeding system and energy supply [10,11]. The feedstock can be implemented to the AM system as powder either by a coater (or roller) that applies the material over a moving bed (i.e. substrate) [12] or by deposition through nozzles simultaneously to the energy application [13]. Metallic wires are also utilised as feedstock in AM systems [14]. The metal AM supply energy is usually applied either by laser or by focused electron beam. Three main systems have been extensively explored to produce AM alloys: selective laser melting (SLM), electron beam melting (EBM) and direct laser deposition (DLD) [10,15]. Each process uses specific parameters and methodologies to

produce consolidated structures from metallic powders. The production and characteristics of 316L stainless steel produced by SLM is the main focus of the present research thesis. The SLM process consists of a metallic powder bed, of which the upper-most layer is successively melted a high energy laser – in a manner following a layer by layer CAD arrangement until the final object is completed. There is an intrinsic design freedom in the SLM process, to produce components that were previously impossible, or rather difficult (e.g. not cost effective) to be fabricated by conventional manufacturing methods [1,10,16]. Thus, the design freedom and particular manufacturing technology associated to SLM and their effect on the performance in the context of stainless steels must be investigated.

Pitting corrosion is a common form of localised attack that occurs on stainless steels exposed to chloride (Cl^-) containing environments. The presence of Cl^- ions in a humid atmosphere catalyses the disruption of the protective passive chromium oxide layer upon stainless steels when the Cl^- ion concentration is above a threshold [17]. The corrosion of a nominally 'passive' alloy such as 316L, is typified by local dissolution – known as pitting – which is an autocatalytic process once initiated [18]. That means the corrosion products provide conditions favourable to a continuous pit growth. Such a corrosion process is well known as pitting and it has been hypothesised to occur in three consecutive stages: nucleation; metastable and stable pit growth [19,20]. The nucleation of a pit will occur if there is an electrochemical potential disparity between two features on the metal surface, or there is local disruption of the passive surface film (especially in the presence of Cl^- ions). A comparative assessment of pitting upon conventionally produced and SLM stainless steels can also reveal new paths to comprehending pitting mechanisms. In addition, understanding the correlation between SLM parameters and material properties (such as corrosion resistance) is fundamental for the performance optimisation of stainless steel components.

The broad aim of the present work was to understand the effect of SLM parameters on the microstructure and, consequently, the pitting of SLM 316L components. In addition, individual aspects of pitting, such as metastable pitting, were meticulously investigated. Furthermore, the manufacturing of 316L/glass composite was carried out by SLM in order to explore the production a potential new engineering material.

The specific aims of this research project included:

- The investigation of the effect of a variety of laser power and laser scan speed settings on the porosity of stainless steel 316L produced by SLM. Moreover, evaluate the influence porosity has the electrochemical response and metastable pitting of SLM 316L.
- The production of 316L specimens by SLM at different build orientations (namely 0º, 45º, 90º relative to the substrate) and the investigation of how each build orientation correlates to pitting.
- Measurements of residual stresses in 316L generated from the SLM process and the influence of residual stress on pitting.
- The study of metastable pit initiation, growth, repassivation and transition to stability - by in-situ imaging the surface of 316L specimens during potentiostatic polarisation.
- The development of a freeware tool to aid the analysis of metastable pitting related data.
- The production of 316L/glass composites by SLM, produced by adding glass waste powder to a 316L powder blend. Microstructural characterisation of the resultant 316L/glass specimens and evaluation of their respective mechanical and corrosion performance.

Chapter 2: Literature review

Costs associated with the repair and maintenance of damage caused by corrosion can be up to 4% of a nation's gross domestic product (GPD) yearly [21]. This significant expense creates the incentive and a constant desire to improve materials and systems to become more resistant to degradation phenomena. Recently, the advent and development of metal AM techniques has created an opportunity for the production of new alloys, or alloys with enhanced corrosion resistance. Researchers from both industry and academia have been extensively working on the development of AM for high-performance materials, to comply with their respective component and application requirements. Nevertheless, prior to applying these AM corrosion resistant alloys into service it is necessary to understand their corrosion performance and mechanisms, especially in environments where their conventional produced counterparts have been utilised over many years.

To inform and situate present research, a thorough literature review on the corrosion of AM alloys including stainless steel 316L was compiled. Although extensive investigation has been employed on the subject, there still remain several knowledge gaps, as identified in the review.

- A number of potential defects arising from the AM process have been identified, and their reproducibility (in production) and impact (on corrosion) are unclear in a holistic sense.
- The mechanical performance, and the durability (e.g. corrosion performance) of AM alloys has not been significantly investigated to date, and it is yet to be reported to any level of detail for non-laboratory-controlled environments or long-term exposures. Further performance evaluation is essential and must be carried out for AM components.
- The microstructure of AM corrosion resistant alloys commonly differs from their respective conventionally manufactured counterparts. Those microstructural changes consequently have an effect on their corrosion properties. Hence the cause-effect assessment of these 'altered' microstructures on durability must be well comprehended.

The present chapter was prepared as critical review published in the journal ***CORROSION***. The review article appears here as published.

Corrosion of Additively Manufactured Alloys: A Review

G. Sander,[‡,*,**] J. Tan,[***] P. Balan,[***] O. Gharbi,[*] D.R. Feenstra,[*,**] L. Singer,[****] S. Thomas,[*,**] R.G. Kelly,[****] J.R. Scully,[****] and N. Birbilis[*****]

ABSTRACT

Additive manufacturing (AM), often termed 3D printing, has recently emerged as a mainstream means of producing metallic components from a variety of metallic alloys. The numerous benefits of AM include net shape manufacturing, efficient use of material, suitability to low volume production runs, and the ability to explore alloy compositions not previously accessible to conventional casting. The process of AM, which is nominally performed using laser (or electron) based local melting, has a definitive role in the resultant alloy microstructure. Herein, the corrosion of alloys prepared by AM using laser and electron-based methods, relating the corrosion performance to the microstructural features influenced by AM processing, are reviewed. Such features include unique porosity, grain structures, dislocation networks, residual stress, solute segregation, and surface roughness. Correlations between reported results and deficiencies in present understanding are highlighted.

KEY WORDS: 3D printing, additive manufacturing, alloys, corrosion, laser sintering, selective laser melting

INTRODUCTION

With a growing demand for higher complexity in design and more efficient use of raw materials, additive manufacturing (AM), more commonly called 3D printing, has grown exponentially in both development and application.[1-2] The advantages of AM over traditional manufacturing methods are apparent; AM facilitates the fabrication of near-net-shaped structures with minimal waste generation and enables production of complex designs in less time. The influence of AM has challenged customary approaches to design and maintenance. In the aerospace industry alone, AM has become a large disruptor, being able to reduce the production lead time of a jet engine from months to weeks.[3-4] As an example, GE industries have announced their intention to put jet engines that are 35% produced by AM into service by 2020.[5] In the last decade, the capabilities of AM have expanded to a wide range of alloys, many incapable of production by other routes, often revealing enhanced mechanical properties.[6-8] However, there remain several obstacles before the impact of metal AM can be fully realized; both standardization of printing methods and the consistent production of qualified components require significant further development. Although there have been major strides in understanding the influence of AM on mechanical properties, the understanding

Submitted for publication: June 14, 2018. Revised and accepted: October 1, 2018. Preprint available online: October 1, 2018, https://doi.org/10.5006/2926.

‡ Corresponding author. E-mail: guilherme.sandermalab@monash.edu.
* Department of Materials Science and Engineering, Monash University, Clayton, VIC 3800, Australia.
** Woodside Innovation Centre, Monash University, Clayton, VIC 3800, Australia.
*** Chemical Engineering, School of Engineering, Monash University, Jalan Lagoon Selatan, 47500 Bandar Sunway, Selangor, Malaysia.
**** Department of Materials Science and Engineering, University of Virginia, Charlottesville, VA 22904.
***** College of Engineering and Computer Science, Australian National University, ACT 2601, Australia.

ISSN 0010-9312 (print), 1938-159X (online)

of the corrosion performance of AM-produced metals and alloys remains in its infancy. The review herein seeks to critically consolidate the relevant studies to date and identify key areas of future work.

Metal Additive Manufacturing

Metal AM processes are primarily divided into two main categories: powder bed fusion (PBF) processes, which include selective laser melting (SLM) and electron beam melting (EBM);[9] and direct laser deposition (DLD), in which both the material and energy are supplied simultaneously to the build surface. The latter is often also often interchangeably termed direct energy deposition (DED). Although various other AM processes for metal fabrication exist (for example, welding and cold spray), this review will focus only on SLM, EBM, and DLD, which are currently the most predominant metal AM methods, and those which involve the consolidation of metal or alloy powder.

SLM operates in a powder bed, building components layer-by-layer by rastering a high-powered laser as directed by a computer aided design (CAD) model. A typical schematic diagram for an SLM system is presented below in Figure 1(a),[10] along with its major features. After each layer is completed (i.e., consolidated via laser rastering), the build platform is lowered and an additional layer of powder is added via a recoater arm, capable of accurately producing layers of ~20 μm to 100 μm in thickness.[11] The build process occurs within an inert build chamber under a nitrogen or argon atmosphere to limit oxidation.[12] Furthermore, in order to reduce oxygen contamination, the chamber is kept under positive pressure.[13-14] SLM is suitable for producing highly complex parts with high dimensional tolerance. The build resolution is generally dictated by the powder size used, which is typically the range of 10 μm to 45 μm in diameter.[15] Components manufactured by SLM nominally achieve a surface roughness (R_a) of 9 μm to 16 μm as a result of SLM's high cooling rates, which are as high as ~6×10^6 °C/s.[16-19] High cooling rates can also result in isotropic, metastable, and refined microstructures in SLM fabricated samples.[19-21]

Similar to the SLM process, EBM is performed using a powder bed. However, EBM uses an electron beam as the energy source, which consequently requires that the process be operated in an evacuated build chamber so that a high-power electron beam can be generated to subsequently melt metal powder.[22] Vacuum pressure levels can vary, but levels near 10^{-6} torr are not uncommon. The chamber vacuum ensures that a high-quality electron beam is produced and contamination or oxidation is minimized in the case of reactive powders (i.e., titanium). To date, EBM has not been widely applied to many alloy systems, largely studied only in the case of titanium (Ti) alloys.[21]

In every AM process, the resulting microstructure (and hence the mechanical properties and, indeed,

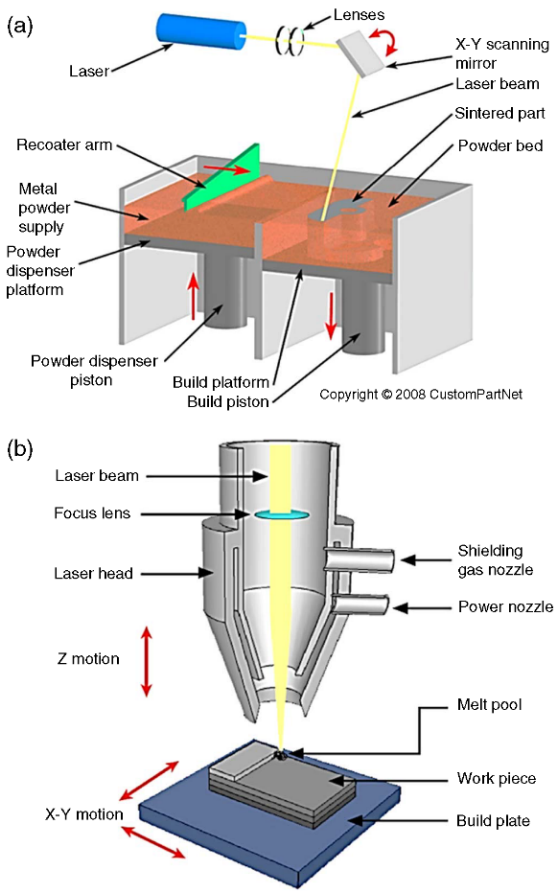

FIGURE 1. *Schematic representation of (a) SLM[10] and (b) the DLD process.[15,37]*

corrosion behavior) are highly dependent on the build parameters used. For each production method used, several key parameters have been identified that have a significant influence. Most critically, the input energy density (which is a parameter that is influenced by numerous input variables) will dictate the local temperature and local melt pool size (including shape and constancy), also influencing the cooling rate following solidification—all of which impact the resulting microstructure.[23-27] In PBF systems, the major parameters that affect the input energy density are the laser/electron beam energy power, laser spot size, and traverse speed.[28-29] The parameters that affect its thermal history are hatch spacing (the distance between two consecutive laser scans), scan pattern, layer thickness, and bed temperature.[30]

In contrast to PBF systems, DLD supplies its material to the build surface via blown powder simultaneously with its energy source.[31-32] Wire arc additive manufacturing (WAAM) is an AM method similar to

TABLE 1
Relative Advantages and Disadvantages of the AM Methods Reviewed Herein

	Advantages	Disadvantages
SLM	High dimensional tolerance. Relatively low residual stress of built components. Rapid cooling rates and microstructural refinement (which can translate to increased tensile strength). Permits the fabrication of complex shapes.	Restricted build volume. Slow deposition rate. Difficult to remove components from support substrate. Potential production of brittle parts due to rapid cooling (for select alloys). Inability to vary composition with the build.
EBM	Efficient energy heat source. Unique ability to control pore size of build materials. Allows the fabrication of complex shapes.	High surface roughness in nonhorizontal plane. Slow deposition rate. Not suitable for consolidation of many alloy systems. Restricted build volume. Inability to vary composition with the build.
DLD	Suitable for large build volumes. High build rate. Ability to fabricate gradient designs with different alloys. Capable of directly producing composite materials.	Poor surface finish for completed parts. Limitation in the creation of complex shapes. High residual stress. Lower dimensional tolerance than PBF methods.

DLD in which the energy input is supplied by electric arc and metallic wires are utilized as feedstock.[33] The DLD system operates on a 5 to 6 axis system, which makes it an ideal candidate for repair and cladding work, but also for the manufacture of large components. In the case of DLD, the powder size range utilized is between 50 μm and 150 μm and thus is comparatively larger than the powder size range used in the SLM process (10 μm to 50 μm).[34-35] The laser used for DLD is typically an Nd:YAG diode or CO_2 laser, while the metal powder is fed through a coaxial or multijet nozzle.[36] In order to maintain an inert atmosphere, an argon shielding gas may be introduced via the powder feed as shown in Figure 1(b).[15,37-38] Unmelted powder can be recycled depending on the operation. In the case of DLD systems, the energy density is affected by laser power, laser spot size, traverse speed, and powder input rate; and the thermal history by the scan pattern and hatch spacing.[39-42]

In view of growing understanding toward AM processes, extensive studies have been performed (noting that corrosion was not characterized in most cases) to determine the properties of the following alloys, which are traditionally weldable alloys:

SLM: stainless steels (Types 316L [UNS S31603[(1)]][43-44] and 304L [UNS S30403][45]), Ti-6Al-4V,[46] Inconel 625[†] (UNS N06625),[47] AlSi10Mg,[48] Al-Zn-Mg-Cu[49]

DLD: stainless steel Type 316L,[50-51] Ti-6Al-4V[52]

EBM: Ti-6Al-4V,[53-54] Inconel 718[†] (UNS N07718)[55]

Each AM process presents relative advantages and disadvantages, some of which are presented in Table 1.

[(1)] UNS numbers are listed in *Metals and Alloys in the Unified Numbering System*, published by the Society of Automotive Engineers (SAE International) and cosponsored by ASTM International.
[†] Trade name.

EFFECT OF PROCESS VARIABLES ON THE MICROSTRUCTURES PRODUCED

The microstructure of alloys produced by AM are significantly different from those produced using conventional production methods due to a variety of AM process variables.[21,56] For SLM, the most widely varied process variables include laser power, scanning speed, hatch distance, and layer thickness (all of which are typically varied by a trial-and-error process to optimize component density). The metal powder undergoes rapid heating (usually to temperatures >2,000°C) followed by rapid solidification during SLM to form the "build" as the laser beam rasters onto the metal powder.[56] The build is also subjected to several thermal cycles due to local heat transfer emanating during SLM. The rapid heating and fast cooling rates coupled with thermal cycling induces the formation of unique alloy microstructures that typically have refined grain structures,[21,56] dislocation cell substructures,[21,56] and residual stresses.[56] They also cause the formation of metallurgical defects, including hot tear cracks,[57-58] entrapped gas porosity,[56] lack of fusion porosity,[59] and dendritic growth within the build.[3,57] The AM process variables therefore govern the nature of the microstructures and defects formed in the build. The influence of such AM process parameters on the nature of the build are briefly reviewed below.

Surface Roughness

The surface roughness (R_a) of components manufactured by SLM is typically high. The R_a values for metal parts produced by SLM are normally in the range 10 μm to 30 μm, which is significantly higher than that produced by methods such as milling (~1 μm to 2 μm).[60] Wang, et al.,[60] studied the effect of laser energy density (ω) on the surface roughness of Type 316L manufactured by SLM. It was reported that when ω is <75 J/mm^3, the R_a value is ~15 μm and the surface

roughness is mainly attributed to sporadic lack of melting. However, when ω is between 100 J/mm^3 and 170 J/mm^3, the R_a was decreased below 10 μm. Furthermore, R_a was observed to increase with ω > 180 J/mm^3, possibly arising from excessive melting of the constituent powders. The phenomenon of "balling" was found to occur predominantly when ω was between 75 J/mm^3 and 120 J/mm^3;[60] balling is described as the formation of metallic droplets in opposition to a desired uniform spread of liquid metal on the molten surface.[59] Although there was some correlation between a number of SLM process variables and the surface roughness of the manufactured parts, the underlying mechanistic aspects are, to date, not clearly understood.

Porosity

Sander, et al.,[61] studied the effect of the laser power and laser scanning speed on the porosity of Type 316L specimens manufactured by SLM. A direct correlation between specimen porosity and the laser power/scanning speed was not derived in that study. Shang, et al.,[43] studied the influence of laser scanning speed on the porosity of Type 316L specimens (manufactured by SLM). In that work, the laser power was kept fixed at 195 W, hatch spacing at 0.09 mm, and layer thickness at 0.02 mm, while the scanning speed was varied between 800 mm/s and 1,083 mm/s. They observed that the porosities of the Type 316L specimens increased with the scanning speed, and proposed that at higher scanning speeds, the lack of melting might cause porosity. Similarly, Li, et al.,[44] investigated the influence of scanning speed on the porosities of Type 316L specimens. The laser power was kept fixed at 100 W, whereas the laser scanning speed was varied between 90 mm/s and 120 mm/s. They also observed that the porosity of the Type 316L specimen increased with increasing scanning speed. The effect of ω on the porosity of Type 316L was also studied by Cherry and co-workers,[59] who observed that at low ω such as ~40 J/mm^3, the porosity of the produced Type 316L specimens reached as high as 8.8% due to lack of melting of the metal powder and lack of sintering between the different layers. At higher ω, the porosity was found to remain comparatively high (~6.5%). It was suggested that the larger melt pools that were formed at higher ω may be susceptible to solidification microshrinkage porosity. Furthermore, the formation of gas voids could also result in the formation of spherical pores in the build. Undoubtedly, a mechanistic understanding of the effects of the laser parameters on the specimen porosity is still being clarified and is essential to understand on the basis (as elaborated further below) that porosity can influence corrosion, namely processes such as pit repassivation.[61]

Cellular Structures

The formation of dislocation cell sub-structures is considerably common in the alloy microstructures produced by AM. Shang, et al.,[43] reported that Type 316L manufactured by SLM was comprised of a dendritic and cellular microstructure. The primary dendritic spacing and the average diameter of the cellular structure were both found to decrease with increasing scanning speeds.[43] Such cellular growth was reported to result in solute segregation at the cell boundaries;[21,43,62-63] however, the extent of segregation upon Type 316L stainless steel was shown in one study, via careful atom probe tomography testing, to be near-negligible.[64] Of the studies to date, there is insufficient information available from nanoscale characterization to permit a more general understanding to emerge thus far. The mechanisms of dendritic/cellular growth, solute segregation, and their correlation with the laser parameters are yet to be elucidated in published works.

Residual Stress

The uneven heat distribution and the rapid cooling rates during AM commonly results in the generation of what may be large residual stresses in the build. Liu, et al.,[65] used x-ray methods to determine the residual stresses in Type 316L parts manufactured using SLM. Overall, it was observed that the residual stress is mainly compressive at the lower portions of the build and tensile in nature at the top of the build. This explanation is plausible, as during SLM, when the molten layers (at the top) solidify, they tend to shrink due to thermal contraction. This deformation is restricted by the layers below, resulting overall in a tensile stress at the top and compressive stresses in the lower/bottom layers.[66] Liu, et al.,[65] also observed that the residual stress is much larger in the direction parallel to the laser scanning direction, compared to the direction perpendicular to the laser scanning direction. In that study, the residual stress was determined to decrease with lower ω.

Nonequilibrium Microstructures

The rapid heating and rapid cooling rates in AM, particularly in SLM, tend to result in the formation of nonequilibrium microstructures; in particular, the high-temperature phases formed during melting are retained after rapid solidification. Chao, et al.,[64] observed that the manganese sulfide (MnS) typically present in Type 316L is annihilated during SLM, and instead manganese (Mn) or silicon (Si) oxide based inclusions are preferentially formed at the elevated temperatures. It is known that MnO and SiO have higher precipitation temperatures than MnS and they form in the liquid melt. These MnO/SiO inclusions are retained in the microstructure due to rapid solidification. Alam, et al.,[67] investigated the effects of varying the laser power/scanning speed on the resultant properties of Type 420 (UNS S42000), manufactured by DLD. They observed that higher laser power/scanning speed (2.5 kW, 10 mm/s) presented a higher percentage

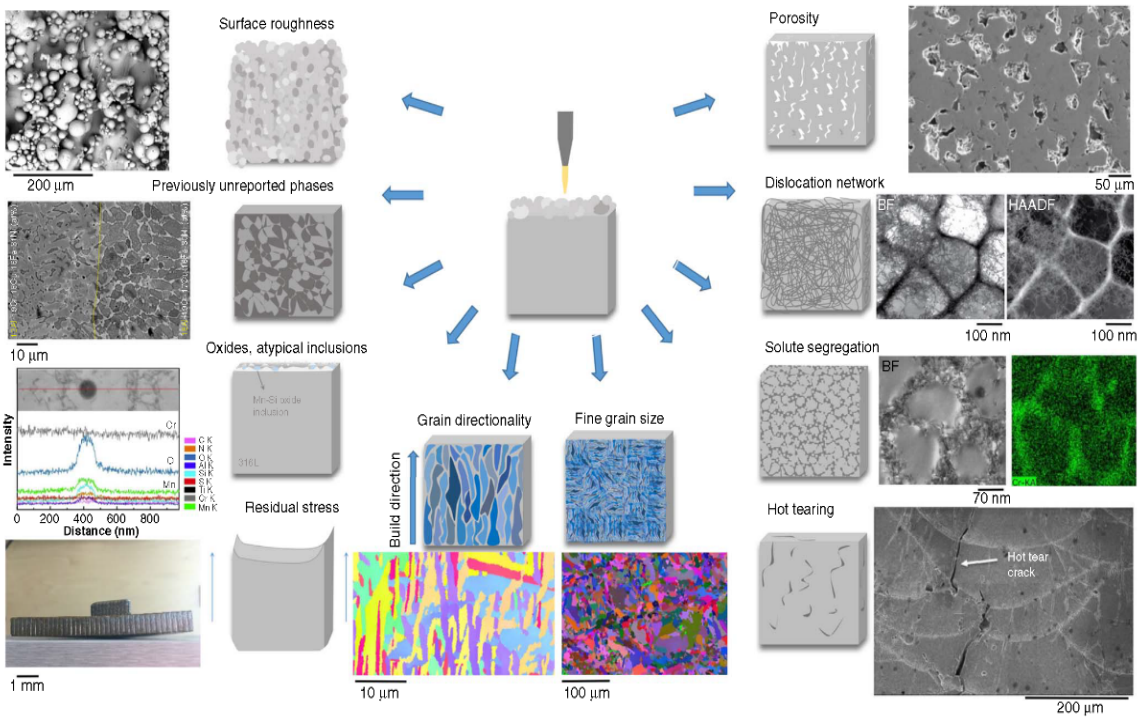

FIGURE 2. *Schematic diagram summarizing the potential impact of AM processing on the overall microstructure of the produced components. The potential influence of each processing variable is illustrated by data reported in the literature.*[21,58,61,64,68-69]

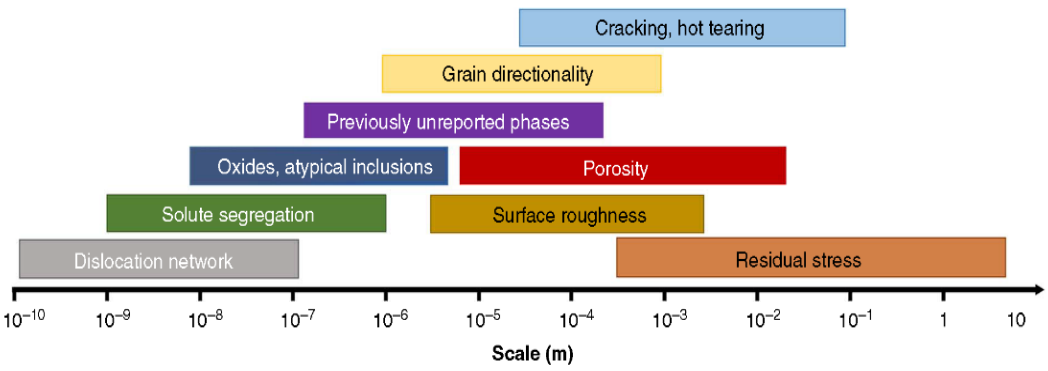

FIGURE 3. *The length scale of the common defects and features present in additively manufactured alloys.*

of nonequilibrium secondary phases (i.e., eutectic ferrite, retained austenite [γ-Fe], and metastable metallic carbide phases) formed compared to specimens produced with a lower laser power/scanning speed (2 kW, 7.5 mm/s). The Type 420 specimen manufactured with the higher laser power/scanning speed also exhibited higher hardness (743 Hv) and higher residual stress (486 MPa tensile stress and 1,002 MPa compressive stress), compared to the specimen manufactured with lower laser power/scanning speed. It is noted that such residual stresses are quite significant. It is routine in many production processes to perform a stress relief heat treatment immediately following AM component production.

A schematic depicting the effect of different process variables on the macro- and microstructural features of the build is shown in Figure 2.[21,58,61,64,68-69]

It is important to highlight that the aforementioned defects and microstructural features are not confined to a single length scale, but cover a scale of >10 orders of magnitude as seen in Figure 3.

EFFECT OF MICROSTRUCTURE ON CORROSION

As indicated in the preceding section, the AM process enables the production of unique and microstructurally complex systems.[19,36,70] In fact, it allows

(1) the formation of a significantly finer grain structure—i.e., 10 μm is the approximate average grain size for SLM 316L stainless steel, while 30 μm to 60 μm is common for the wrought counterpart;[21] (2) unique second phase precipitation—i.e., ultrafine (α+β) lamellar structures (200 nm to 300 nm) in SLM Ti6Al4V;[71] and (3) solute segregation—i.e., niobium (Nb) distribution in DLD 718.[72] Such changes not only significantly alter the composition, distribution, and size of second phase particles, but also have the potential to modify the electrochemical properties of AM-produced alloys. In order to consolidate a large number of studies and address the authors' assessments of their respective conclusions, this section will list the different processing variables encountered in AM and discuss their influence on corrosion susceptibility. Herein, only the key variables reported in the literature are covered (Table 2).[61,64,73-85]

Several researchers have, often with little to no experimental support, reported that porosity may significantly impact the pitting characteristics of alloys produced by AM.[61,73-77] However, a mechanistic description of how pores (particularly unconnected pores) may assist in pit initiation/propagation is yet to be clarified. Similarly, solute segregation driven by the formation of cellular structures has also been proposed to be detrimental toward pitting of alloys manufactured by AM.[86] However, advanced compositional characterization of the cellular structures formed in SLM 316L has shown that neither Cr nor Mo content are significantly depleted at the cell boundaries.[21] No post-mortem microstructural examination of corrosion upon SLM prepared Type 316L exists to date, which would reveal if corrosion preferentially occurs at sites of apparent solute segregation. The influence of the cellular structures and the associated solute segregation on the corrosion characteristics of alloys manufactured by AM is yet to be clarified for any alloy system. Similarly, the effects of residual stress, surface roughness, and ultra-refined grain structures on the corrosion characteristics of alloys manufactured by AM are topics that needs further investigation. Undoubtedly, the isolation of such microstructural variables may be a challenge; however, there exist a number of studies on model systems and nonAM systems that may be used as references.[87]

TABLE 2

Summary of the Effects of AM Process Variables and Their Influence on the Corrosion Susceptibility of Studied Alloy Systems

Process Variables	Effect on Corrosion Susceptibility	Systems Reported to be Affected
Surface roughness	Surface roughness was reported to cause an increase in the corrosion susceptibility of aluminum (Al) alloys and stainless steel by promoting electrolyte stagnation in the concaved zones, purported to influence localized corrosion.	SLM AlSi10Mg, SLM 17-4 PH
Porosity	The effect of porosity was investigated by several researchers in the context of corrosion.[61,73-77] Porosity has been reported to be a preferential pit initiation site if the porosity was >1%.[78] Porosity was suggested to possibly have a detrimental effect on the SCC susceptibility of SLM 316L.[76] Recent work from Sander, et al.,[61] suggested that porosity mainly affects the pit repassivation characteristics of SLM 316L, with no influence on pit initiation.	SLM 316L SLM 17-4 PH
Solute segregation	Microgalvanic coupling between the depleted matrix and the solute-rich area (i.e., Si for Al alloys or Mo and Cr for SLM 316L) causes localized corrosion at the border of melt pools.[79-80] It was also suggested that solute segregation can influence SCC in Type 316L in a hot pressurized environment.[77]	SLM 316L SLM AlSi10Mg SLM AlCoCrFeNi high entropy alloy
Previously unreported phase	The effect of unreported phases on the corrosion susceptibility has not been reported yet. Such unreported phases include quasicrystals in Al alloy 7075 (Al-Zn-Mg-Cu).[81]	SLM AA7075
Oxides, atypical inclusions	Typical MnS inclusions formed in wrought 316L were substituted by Mn-Si oxides in SLM 316L. The absence of MnS inclusions in SLM 316L could reduce pitting susceptibility.[64] An increase in the oxide thickness (Fe_2O_3 and Cr_2O_3) in the context of SLM 316L has been reported.[82]	SLM 316L
Grain directionality	Elongated grain structure along the build direction was shown to have a detrimental impact and increase the SCC growth rates in the case of SLM/DLD 316L.[77,83] While both SLM and DLD are reported to produce so-called "columnar" structures in the build direction, the attended influence on corrosion is yet to be studied.	SLM/DLD 316L
Refined grain size	Fine grain size and equiaxed microstructures were reported to have a beneficial effect on corrosion fatigue in the case of SLM 316L.[83] While the SLM process will generally result in finer microstructures than conventionally produced counterparts, the grain size effect has not been uniquely studied to date for AM-prepared specimens.	SLM 316L
Residual stress	Residual stress was not reported to be correlated with corrosion susceptibility in Ti6Al4V alloys;[84] however, corrosion susceptibility was increased when residual stress was found in SLM 316L.[85]	SLM Ti6Al4V SLM/DLD 316L

CORROSION OF ADDITIVELY MANUFACTURED ALLOYS

Al Alloys

Studies related to the corrosion of AM-prepared Al alloys have been essentially confined to the Al-Si alloy class, to date. The findings of such studies are summarized in Table 3.[79,88-94]

Some of the pertinent results summarized in Table 3 are discussed in more detail below, allowing for mechanistic aspects to be examined, but also illuminating that in many cases there are contradictory results from different studies. In cases where only a very small number of studies exist, contradictory conclusions between studies are the present hallmark of the status in the understanding of corrosion for many AM-prepared alloys.

The effect of the use of recycled powder, laser scan passes, and layer thickness on the corrosion of the AlSi10Mg produced by SLM was studied by Revilla, et al.[88] In the study, the corrosion potential (E_{corr}) values derived from potentiodynamic polarization of the cast and SLM AlSi10Mg specimens were similar, with values ranging between –0.7 $V_{Ag/AgCl}$ and –0.6 $V_{Ag/AgCl}$ (Figure 4). The corrosion characteristics observed for SLM and cast AlSi10Mg were correlated by Revilla, et al., who observed similar microstructure and composition. However, silicon-magnesium (Si-Mg) segregation was detected in the cast sample, whereas the same type of segregation was not observed in AM-prepared sample designated S2 (Figure 5). The presence of Si-Mg segregation increased the number of galvanic couples present on the sample surface, which was reported to directly enhance the localized corrosion of cast AlSi10Mg. The ability of SLM to refine such second phase regions was apparently beneficial in terms of corrosion.

The weight loss of AlSi10Mg produced by SLM immersed in a 3.5 wt% NaCl was investigated by Leon, et al.[89] This study showed that after 45 d of immersion, the SLM AlSi10Mg presented slightly lower weight loss than cast AlSi10Mg. Leon, et al., hypothesized that the corrosion is more accentuated in the cast alloy due to its extensive segregation of Fe- and Mn-containing phases, irregular porosity, and a dendritic microstructure. However, statistical analysis was not reported for the results, and empirical evidence was presented to support the suggested hypothesis. In a similar study, Leon, et al.,[90] investigated the effect of surface finish on the corrosion behavior of SLM AlSi10Mg. Corrosion tests (potentiodynamic polarization, immersion, electrochemical impedance spectroscopy [EIS], and fatigue) were conducted in 3.5 wt% NaCl for specimens denoted as a "polished" SLM AlSi10Mg sample (prepared by 1200 grit paper, unspecified abrasive, which should strictly be termed grinding as opposed to polishing) and for "unpolished" (i.e., as manufactured by SLM). The corrosion rate of the "polished" sample was lower than the "unpolished" in all tests performed. The presence of cavities and irregular surface morphology commonly observed for AM-prepared alloys was hypothesized by Leon, et al., to be the determining factor for the inferior corrosion resistance of the "unpolished" SLM AlSi10Mg. However, no mechanism nor detailed explanation was presented to support this hypothesis. Likewise, the corrosion of SLM AlSi10Mg was investigated by Fathi, et al.,[91] as a function of surface finish in 3.5 wt% NaCl solution. Ground and as-produced (AP) SLM AlSi10Mg were compared with cast counterparts under the same experimental conditions. The SLM AlSi10Mg specimens presented an apparently better corrosion resistance than their cast counterparts (albeit only through evaluation by corrosion potential values, which are not a measure of corrosion rate). If the results are to be considered reliable, then they may be in agreement with Leon, et al.,[89] though they contradict the results obtained by Revilla, et al.[88] In contrast, Fathi, et al.,[91] suggested that grinding the SLM AlSi10Mg specimens was detrimental to the continuous oxide layer formed on the AP specimen surface, inconsistent with the findings of Leon, et al.[90] Therefore, the role of surface finish (i.e., roughness) on the corrosion of SLM AlSi10Mg remains unclear. This lack of clarity is exacerbated by a lack of standardized testing by many authors, and also by the use of an arguably aggressive electrolyte for such an alloy, which might obscure surface finish effects.

The corrosion of SLM AlSi10Mg in aerated Harrison's solution (3.5 g/L $(NH_4)_2SO_4$ + 0.5 g/L NaCl) was investigated by Cabrini, et al.[79,92-93] The effect of heat treatment and surface finish on the corrosion of SLM AlSi10Mg[92] was investigated for three specimens: untreated (UT), stress relieved (SR) at 300°C for 2 h, and water quenched (WQ) after solution annealing (SA) at 550°C for 4 h. The UT, SR, and WQ specimens were subject to potentiodynamic polarization testing for AP and so-called polished (P) surface finishes (Figure 6). The AP samples showed active dissolution without passivity. The highest E_{corr} was measured for the UT condition, while the WQ specimen presented the highest dissolution rate over a range of potentials (Figure 6[a]). The surface polishing allowed the development of a passive window during the potentiodynamic polarization of the UT and SR samples, indicating an enhancement in corrosion resistance (Figure 6[b]). The WQ specimen did not exhibit improvement in decreasing electrochemical dissolution following polishing, and a passive range was not observed. Cabrini, et al., suggested that the AP designated samples had higher surface roughness, which increased the area susceptible to corrosion. In addition, it was suggested that thermally produced oxide layers formed during SLM and heat treatments were less effective than the oxide layers naturally formed in contact with the natural atmosphere. The active

TABLE 3

Summary of the Reported Studies on the Corrosion of AM Aluminum Alloys[(A)]

Alloy	AM Technique	Environment	Corrosion Characterization	Corrosion as a Function of	Comparison with Wrought/ Cast Counterpart	AM Alloy Corrosion Characteristics	Microstructure Characterization	References
AlSi10Mg	SLM	0.1 M NaCl	OCP, PDP	Scan strategy, powder layer thickness, exposed plane	Cast	Similar to cast.	SEM, EDS	88
	SLM	3.5 wt% NaCl	Mass loss, PDP, fatigue	—	Cast	Superior to cast.	OM, SEM, XRD	89
	SLM	3.5 wt% NaCl	Mass loss, PDP, EIS, fatigue	Surface finish	—	Superior for polished parts.	OM, SEM, XRD	90
	SLM	3.5 wt% NaCl	PDP, EIS	Surface finish	Cast	Superior to cast. Improved for unpolished parts.	OM, SEM, EDS	91
	SLM	Harrison's solution	EIS, PDP	Surface finish, heat treatment	—	Superior for polished parts.	SEM	92
	SLM	Harrison's solution	OCP, PDP, EIS	Surface finish, build direction, exposed plane	—	Superior for polished parts.	SEM	93
	SLM	Harrison's solution	OCP, PDP	Surface finish, conversion coating, exposed plane	—	Improved by conversion coating with Cerium(III). Reduced for the as-produced state and along the plane perpendicular to the substrate.	OM, SEM, EDS	79
Al12Si	SLM	0.01 to 0.1 M HNO_3	Mass loss	Heat treatment, electrolyte concentration	Cast	Similar for cast and SLM (as-produced). Reduced by heat treatment and in acidic environments.	OM, SEM	94

[(A)] OCP: open-circuit potential; PDP: potentiodynamic polarization; EIS: electrochemical impedance spectroscopy; OM: optical microscopy; SEM: scanning electron microscopy; XRD: x-ray diffraction; and EDS: energy dispersive spectroscopy.

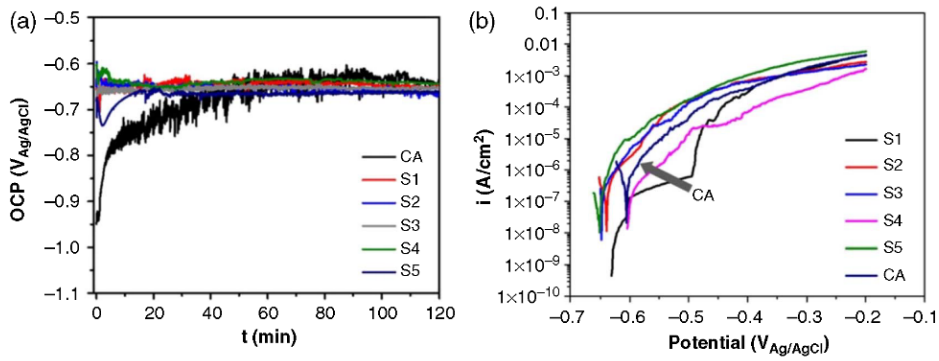

FIGURE 4. *The OCP and potentiodynamic polarization response of SLM (S1 to S5) and cast (CA) AlSi10Mg specimens in a 0.1 M NaCl: (a) open-circuit potential and (b) potentiodynamic polarization. Adapted from Revilla, et al.,[88] with permission from The Electrochemical Society, Copyright 2017.*

behavior in earlier stages of the polarized AP specimens was purported to be related to the surface morphology and oxide layer quality rather than their microstructures. The polished samples were suggested to have had their thermally produced oxide layers removed by mechanical grinding. It was also proposed that the oxide layer formed inside pores by the SLM process are sites for the initiation of localized attack, as observed in the case of UT and SR samples. The heat treatment of WQ samples was suggested to homogenize the α-Al phase, which was deemed to be susceptible to chemical dissolution when exposed to Harrison's solution. The scanning electron microscope (SEM) images of the UT and WQ cross sections after 164 h and 150 h of immersion, respectively, are shown in Figure 7. The pitting of WQ samples occurred as a large uniform cavity on the surface (Figure 7[a]), whereas for the UT samples it appears that pitting occurred with penetration along melting pool boundaries (Figure 7[b]).

The polished SLM AlSi10Mg specimens in general presented better corrosion resistance than the AP SLM AlSi10Mg. The heat treatment of SLM AlSi10Mg did not appear to alter corrosion performance when performed at low temperatures (at 300°C for stress relief of this alloy); however, heat treatment was detrimental when performed at higher temperatures (550°C) due to Si particle precipitation and coalescence. The results presented by Cabrini, et al., were analyzed statistically to validate their conclusions. However, in order to further understand the role of Si phases in the microstructure of SLM AlSi10Mg, characterization at the nanometer scales (e.g., transmission electron microscopy [TEM]) would aid the development of mechanistic models for the corrosion of SLM AlSi10Mg.

The effect of build orientation during SLM of the AlSi10Mg alloy was also investigated by Cabrini, et al.[93] The samples were built along the XY and XZ reference planes (Figure 8[a]) and compared electrochemically after being subjected to different surface treatments in an aerated Harrison's solution. The samples were analyzed as-received, after shot peening and 0.1 μm alumina polishing. The E_{corr} and E_{pit} of the specimens are shown in Figures 8(b) and (c). The E_{corr} was measured for different exposure times in Harrison's solution, where the values were similar for all of the specimens tested up to exposures of 2,000 s. However, the pitting potentials increased following a surface treatment of shot peening and polishing. The corrosion performance of AlSi10Mg in Harrison's solution was enhanced by abrasively treating the surface.

Furthermore, the effect of post-build surface treatment on the corrosion of the SLM AlSi10Mg was investigated[79] using hot bright dip (BD), Ce(III) conversion coatings and was compared to an untreated SLM specimen. Both polished and as-produced specimens were analyzed for two build directions, XZ and XY (Figure 8[a]), and polarized in an aerated Harrison's solution. The E_{pit} values determined from electrochemical tests are shown in Figure 9. It can be observed that a more noble E_{pit} was determined for the specimens tested in the XZ plane when compared with the specimens tested in the XY plane. The BD followed by the conversion coating using Ce(III) in the polished specimens presented improved resistance to pitting compared to the other tested specimens in all of the investigated planes. Furthermore, the surface polishing was beneficial to most of the specimens, except for the BD treated sample, as it removed the protective surface treatment applied on the surface. Therefore, the corrosion of the SLM AlSi10Mg could be improved by post-build surface treatments such as Ce(III) conversion coating. However, in this work, the mechanistic and microstructural scale phenomena that led to changes in corrosion with build direction were not thoroughly investigated.

The corrosion properties of SLM produced Al-12Si were investigated by Prashanth, et al.[94] In that study, the SLM Al-12Si specimens were heat treated in temperatures ranging from 200°C to 550°C, immersed in a 1 M HNO_3 (pH = 0) solution for 14 d, and

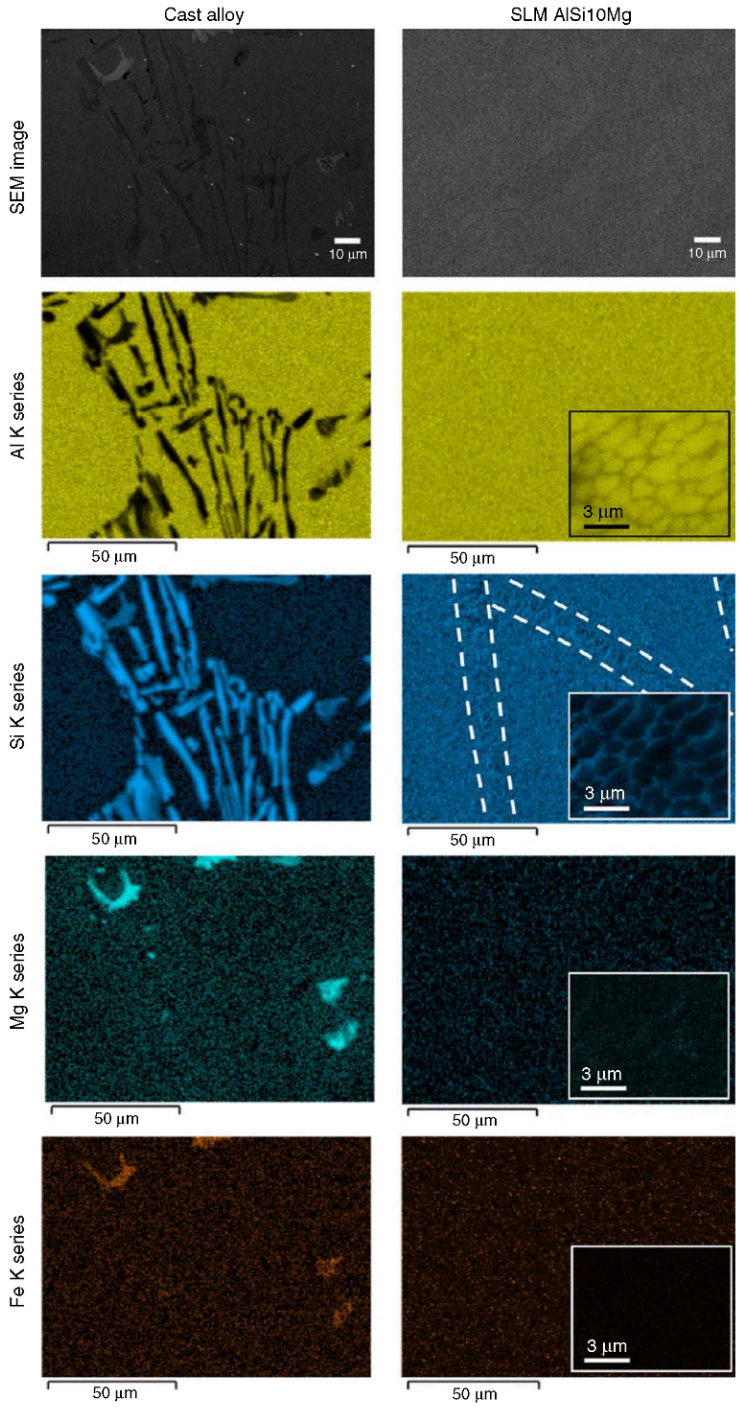

FIGURE 5. *The scanning electron microscopy and energy dispersive spectroscopy maps for Al, Si, Mg, and Fe of cast and SLM (S2) AlSi10Mg collected by Revilla, et al.*[88] *Reprinted with permission from The Electrochemical Society, Copyright 2017.*

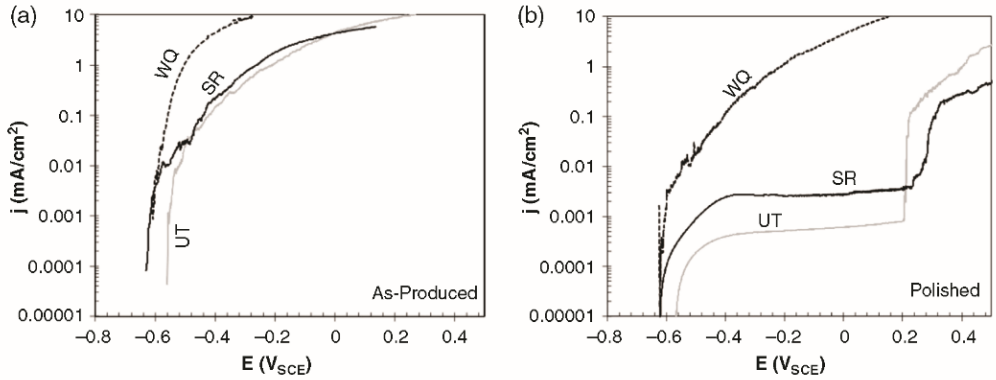

FIGURE 6. *The potentiodynamic polarization response for selective laser melted AlSi10Mg in Harrison's solution in the untreated (UT), stress relieved (SR), and water quenched (WQ) conditions for: (a) as-produced specimens, and (b) as-produced and polished. Adapted from Cabrini, et al.,[92] with permission from Elsevier, Copyright 2016.*

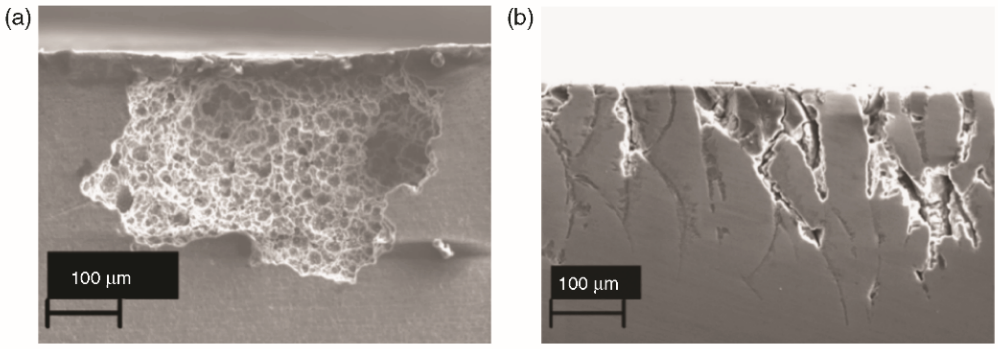

FIGURE 7. *SEM of cross sections of SLM AlSi10Mg immersed in Harrison's solution, revealing the corrosion morphology of: (a) a specimen that was heat treated and water quenched following 150 h immersion, revealing uniform corrosion penetration; and (b) a specimen that was untreated following 164 h immersion, showing localized attack on the melt pool boundaries. Adapted from Cabrini, et al.,[92] with permission from Elsevier, Copyright 2016.*

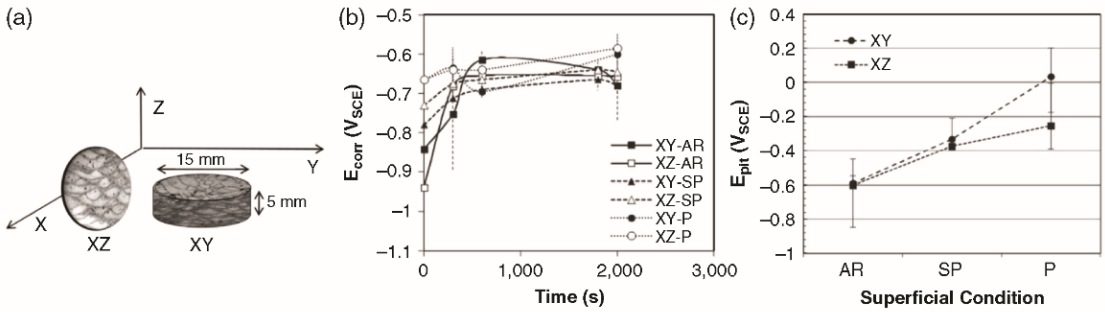

FIGURE 8. *The effect of build direction and surface finish on the electrochemical response of the SLM AlSi10Mg. (a) Specimen planes analyzed: XZ and XY. (b) E_{corr} and (c) pitting potential of the samples as received (AR), after shot peening (SP), and polished (P) for both building directions investigated in Harrison's solution by Cabrini, et al.[93] Adapted with permission from Elsevier, Copyright 2016.*

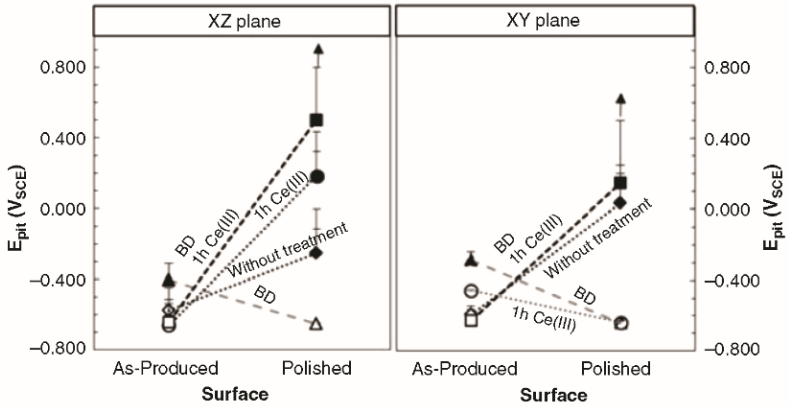

FIGURE 9. *The pitting potentials obtained for different surface treatments in two build directions without polishing (as-produced) and after polishing (polished). The untreated specimen was compared with the samples surface treated by: BD, 1 h conversion coating (1h Ce(III)), and BD followed by 1h Ce(III). Adapted from Cabrini, et al.,[79] with permission from John Wiley & Sons, Inc., Copyright 2016.*

tested using mass loss. Cast and SLM AP Al-12Si were subjected to the same immersion test conditions. The SLM and cast Al-12Si specimens presented a linear increase in weight loss with an increase of heat treatment temperature. The SLM (AP) and the cast Al-12Si had a similar weight loss, and both were inferior to the other heat-treated SLM Al-12Si. It was proposed that this behavior was correlated to the morphology of the Si phase within the alloy microstructure, with preferential dissolution of the Al phase occurring in the presence of HNO_3. The cast Al-12Si had Si plates, and the SLM AP Al-12Si had a Si network in their respective microstructures that prevented the detachment of Si phase from the surface. Spherical and disconnected Si particles created on the surface of the heat-treated SLM specimens were detached from the surface as Al was consumed. The so-called "vacancies" left by Si particles became exposed and the bulk Al became susceptible to further dissolution. However, the experiments were conducted in a highly corrosive, oxidizing acid environment, so investigations in milder solutions (e.g., dilute NaCl) may not fit in the proposed corrosion mechanism.

To date, the reported corrosion studies involving AM aluminum alloys remain essentially limited to Al-Si systems. The impact of the microstructures formed after AM on the corrosion of Al alloys are still not adequately understood or well reported. In order to understand corrosion mechanisms, further microstructural characterization, including methods that probe the nanoscale (e.g., TEM), should be combined with electrochemical characterization. Surface finish has been shown to influence the localized corrosion of SLM AlSi10Mg. The procedures adopted in the investigations reviewed herein (e.g., electrolyte, surface finish, heat treatments, etc.) did not follow common standards to produce comparable trends on the corrosion of SLM Al alloys.

Ferrous Alloys

The corrosion properties of AM-prepared Fe alloys have principally been reported for Type 316L stainless steel. However, a smaller number of accompanying studies regarding the corrosion of other steels have also been recently investigated. The tabulation of such studies are presented in Table 4.[61,64,73-77,80,82-83,86,95-104]

Environments containing chloride ions are well known to be detrimental to the durability of stainless steels, with a number of studies tabulated above appropriately focusing on such electrolytes.[105] In a study by Ganesh, et al.,[95] two batches of specimens (termed "A" and "B") were produced via DLD, by utilizing similar parameters to produce Type 316L specimens. The DLD 316L was analyzed by electrochemical polarization in 0.6 M NaCl, and the results were compared with the electrochemical polarization of both a solution annealed, wrought 316L, and a plasma-transferred arc weld (PTAW) 316L. The corrosion of the DLD 316L specimens was intended to be analyzed in three different sections: parallel to the top surface (S), transverse cross-section (T), and longitudinal cross-section (L).

The DLD 316L specimens were investigated AP and after SA, and were polished down to a 0.5 μm finish before electrochemical testing. The E_{pit} values measured by Ganesh, et al.,[95] after potentiodynamic polarization of the DLD 316L specimens are presented in Table 5. The results showed that the wrought 316L after SA is the most resistant to pit initiation, as judged by the pitting potential, E_{pit}. The PTAW 316L presented a large scatter of results, and comparison was deemed to not be reliable without further data acquisition and statistical validation. The overall resistance to pitting was inferior for the DLD 316L "set A," although the matrix presented was not completed.

TABLE 4

Summary of Reported Studies on the Corrosion of AM Ferrous Alloys[(A)]

Alloy	AM Technique	Environment	Corrosion Characterization	Corrosion as a Function of	Comparison with Wrought/ Cast Counterpart	AM Alloy Corrosion Characteristics	Microstructure Characterization	References
Type 316L	DLD	3.5 wt% NaCl, (0.5 M H_2SO_4 + 0.01 M KSCN)	PDP, PDP	Heat treatment, exposed plane	Wrought	Inferior to wrought. Slightly improved by annealing.	SEM, EDS, XRD	95
Type 316L	DLD	0.9 wt% NaCl	PDP	—	Wrought	Inferior to wrought.	OM, SEM, EDS, EBSD, XRD, TEM	80
Type 316L	SLM	0.6 M NaCl	OCP, LP	Heat treatment	Wrought	Superior to wrought. Not affected by annealing.	SEM, EBSD, TEM-EDS, APT	64
Type 316L	SLM	3.5 wt% NaCl	PDP	Laser scan speed, porosity	—	Improved for lower porosities. Not affected by laser scan speed.	OM	96
Type 316L	SLM	0.9 wt% NaCl	OCP, PDP, PSP	Laser scan speed, porosity	Wrought	Inferior to wrought. Better for higher scan speeds and worse for porosity >1%.	OM, SEM	74
Type 316L	SLM	0.1 M NaCl	OCP, PDP, PSP	Laser scan speed, laser power, porosity	Wrought	Superior to wrought. Lower repassivation potentials and no significant effect on pitting potentials with the increase of porosity.	OM, SEM, EBSD	61
Type 316L	SLM	0.1 M HCl	PDP	—	Wrought	Inferior to wrought.	OM, SEM, EDS, XRD, TEM	86
Type 316L	SLM	Water (288°C): Pure, 2 ppm DO, 63 ppb DH	Fatigue	Heat treatment, cold working, exposed plane, loading frequency, stress intensity (K)	Wrought	Inferior to wrought.	SEM, EBSD	83
Type 316L	SLM	Water (288°C): Pure, 2 ppm DO, 63 ppb DH	SCC	Heat treatment, porosity, cold working, exposed plane, stress intensity (K)	Wrought	Overall inferior to wrought; purported to be due to porosity.	OM, SEM, EBSD	76
Type 316L	SLM	Water (288°C): 2 ppm DO, 63 ppb DH	SCC	—	Wrought	Inferior to wrought in 2 ppm DO and superior to wrought in 63 ppb DH.	SEM, EDS	77
Type 316L	SLM	0.9 wt% NaCl, SBF	Tribocorrosion (OCP, PDP, PSP)	—	Wrought	Superior to wrought.	OM, SEM, EBSD	97
Type 316L	SLM	Ringer's solution	OCP, PDP	Oxidization	—	Enhanced for oxidation resistance up to 150 h at 700°C.	OM, SEM, EDS	82
Type 316L	SLM	0.5 M H_2SO_4	PDP	Porosity	Cast	Inferior to cast and corrosion rate increased with porosity.	OM, SEM, EDS	75
Type 316L	SLM	$MgCl_2$ – 155°C	SCC	Heat treatment	—	Results were unclear.	OM, SEM	98

(*continued*)

TABLE 4 (*Continued*)

Alloy	AM Technique	Environment	Corrosion Characterization	Corrosion as a Function of	Comparison with Wrought/ Cast Counterpart	AM Alloy Corrosion Characteristics	Microstructure Characterization	References
Type 316L	WAAM	3.5 wt% NaCl	PDP	Heat treatment	—	Significantly improved by heat treatment.	OM, SEM, EBSD	99
Novel SS + x wt% Ni	DLD	3.5 wt% NaCl	PDP	Nickel content	—	Corrosion rate decreased with the increase of Ni content.	OM, SEM	100
17-4 PH	SLM	0.6 M NaCl	OCP, PDP	Porosity	Wrought	Inferior to wrought, increased with porosity.	SEM, EDS	73
17-4 PH	SLM	0.5 M NaCl	PDP	Heat treatment, exposed plane	Wrought	Superior to wrought for all of the exposed planes and heat treatments performed.	OM, SEM, EDS	101
Type 4340	SLM	Artificial seawater—ASTM D1141-98	PDP, EIS, salt spray	SLM parameters	Wrought	Not significantly different to wrought.	OM	102
Gradient Low Cr Steel + Type 431 SS	DLD	0.48 M HNO_3 + 0.1 M KCl	PDP	Layer height	Wrought	No significant change or difference observed.	OM, SEM, EDS	103
FeMn-Ag	SLM	SBF	OCP, EIS	Exposure time	—	Impedance increased after longer exposure times.	SEM, EDS, Raman spectroscopy	104

(A) PH: precipitation hardened; DO: dissolved oxygen; DH: dissolved hydrogen; OCP: open-circuit potential; PDP: potentiodynamic polarization; PSP: potentiostatic polarization; EIS: electrochemical impedance spectroscopy; OM: optical microscopy; SEM: scanning electron microscopy; TEM: transmission electron microscopy; XRD: x-ray diffraction; EDS: energy dispersive spectroscopy; and APT: atom probe tomography.

TABLE 5

The Pitting Potentials (in V_{SCE}) Determined from Potentiodynamic Polarization of Type 316L in 0.6 M NaCl Solution for the Direct Laser Deposition (DLD) Similarly Prepared Sets A and B, Wrought, and the Plasma Transferred Arc Weld (PTAW) Specimens[(A)]

Pitting Potential, E_{pit} (V_{SCE})							
		DLD Set A			DLD Set B		
Wrought	PTAW	Section S	Section L	Section T	Section S	Section L	Section T
0.507	0.505	–0.173	–0.397	—	0.439	0.459	–0.005
		–0.237	–0.293	—	0.156	0.038	0.266
0.438			–0.272	—			
	0.140	DLD + SA (1,050°C)			DLD + SA (1,050°C)		
0.459		–0.025	–0.106		0.469	0.105	–0.082
		–0.114					0.565

[(A)] Adapted from Ganesh, et al.,[95] with permission from Elsevier, Copyright 2016.

A study performed by Zietala, et al.,[80] attempted to explain the corrosion DLD 316L in a 0.9 wt% NaCl solution. In their work, they concluded that AM samples present inferior corrosion performance; however, only limited electrochemical evidence to support their conclusions was provided.

The work performed by Chao, et al.,[64] investigated the pitting corrosion characteristics of SLM prepared Type 316L stainless steel. The experiments were conducted for three different Type 316L specimens: SLM "as-printed," SLM samples in the annealed condition, and a wrought (annealed) counterpart. The samples were potentiodynamically polarized in 0.6 M NaCl at 25°C (Figure 10). The polarization curves reveal that the E_{pit} values were notably higher in the as-printed (0.75 V_{SCE}) and the annealed (0.70 V_{SCE}) SLM 316L, when compared to the wrought alloy (0.30 V_{SCE}).

Chao, et al., suggest that there was more resistance to pit initiation in the SLM 316L specimen due to the nature of the inclusions formed in the

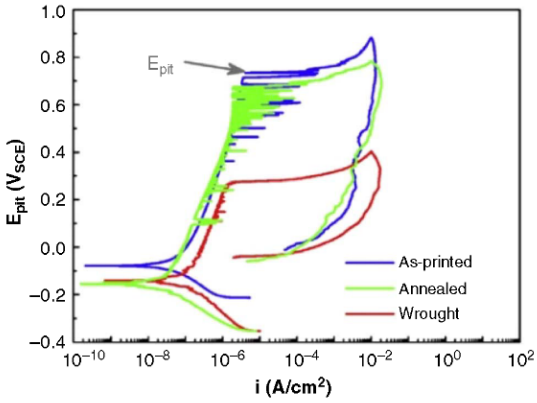

FIGURE 10. *The representative cyclic potentiodynamic polarization curves for SLM 316L in 0.6 M NaCl: (i) selective laser melted as-printed, (ii) selective laser melted after annealing at 1,100°C (annealed), and (iii) wrought. Adapted from Chao, et al.,[64] with permission from Elsevier, Copyright 2017.*

microstructure during the SLM process. The TEM-energy dispersive spectroscopy (EDS) maps (Figure 11) show the absence of MnS particles in the microstructure of SLM 316L, with Mn co-segregated or associated with what is principally oxygen and silicon. The presence of MnS particles in austenitic stainless steels (including Type 316L) has been reported to be associated with the initiation of pitting corrosion.[106-109] However, in the work of Chao, et al., it was revealed that MnS particles are annihilated during SLM, and do not reform upon rapid solidification. As a consequence, the authors have revealed a mechanistic rationalization for highly enhanced resistance to pit initiation.

The effect of porosity on pitting of the SLM 316L was investigated by Sun, et al.,[74] and Sander, et al.,[61] in NaCl solution with similar concentration. Prior to electrochemical testing, the Type 316L specimens (SLM and wrought) were ground to a 1200[74] and a 2000[61] grit finish using SiC paper. Herein, a composite figure has been prepared that reveals the parameters determined from electrochemical testing using potentiodynamic polarization performed by Sun, et al.,[74] and Sander, et al.,[61] as a function of porosity shown in Figure 12.

Generally, the reported E_{corr} and corrosion rate (i_{corr}) values of SLM 316L do not significantly vary with porosity (Figure 12), while the repassivation potential (E_{rep}) reveals a decrease with increasing porosity. Sander, et al., hypothesize that the lower E_{rep} could be related to pores being detrimental to repassivation (i.e., following the initiation of pitting, the presence of pores requires that a lower potential be reached before pits can be repassivated). Sun, et al., state that repassivation of pits formed on the SLM 316L is more difficult than in wrought 316L, although no rationale was presented to explain this finding. Given the relevance of the repassivation characteristics to the utilization and durability of stainless steel, a clear understanding of the origins of reduced repassivation potentials remains a research priority.

The trend in E_{pit} obtained for the two studies (Figure 12) reveals contradictory results in comparison

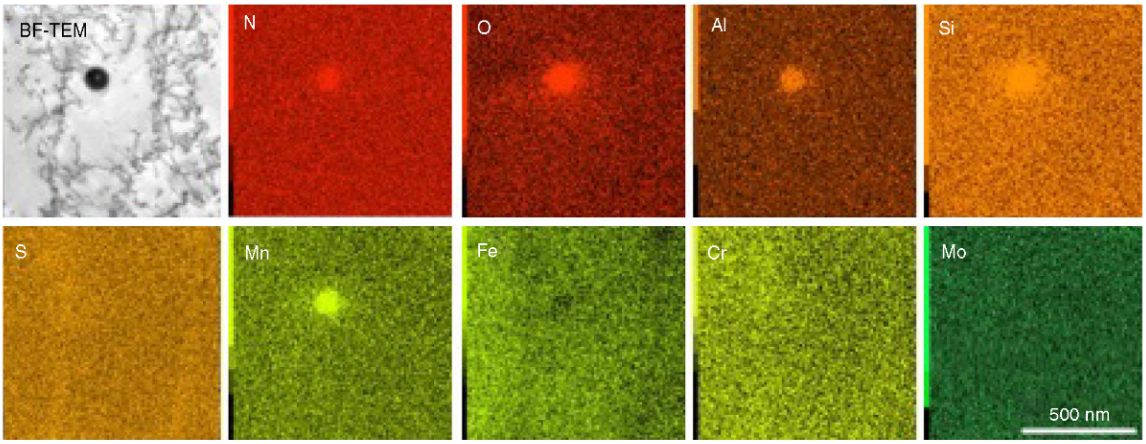

FIGURE 11. *STEM-EDS mapping of a Mn-bearing inclusion in an SLM 316L specimen, revealing that co-location of Mn and S is not evident, while co-location of Mn with Si and O is evident. Adapted from Chao, et al.,[64] with permission from Elsevier, Copyright 2017.*

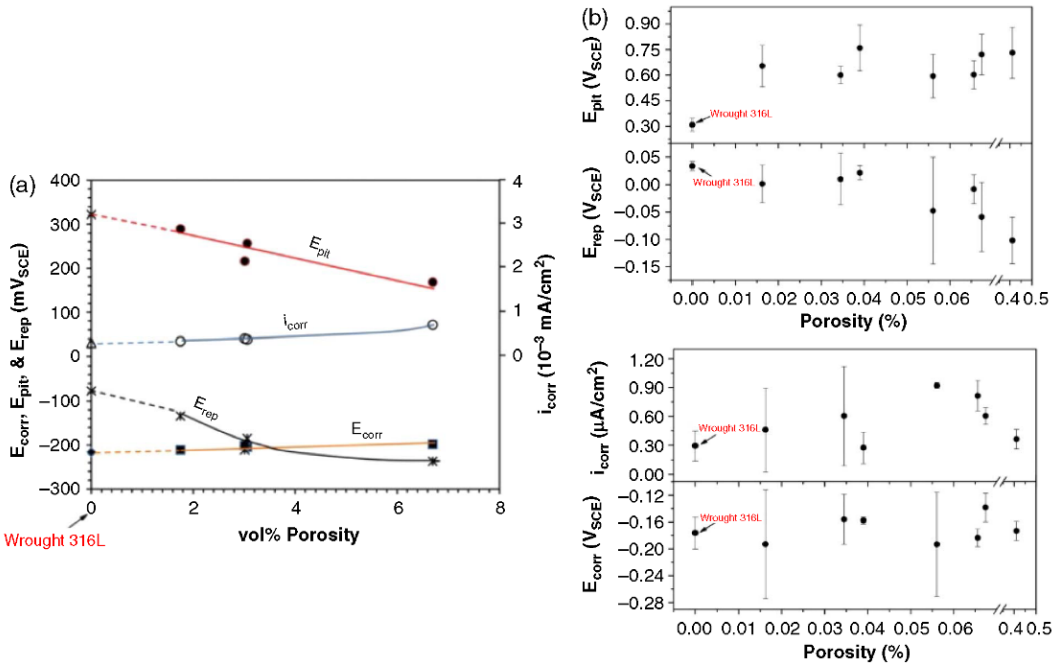

FIGURE 12. *The E_{pit}, E_{corr}, E_{rep}, and i_{corr} of the SLM prepared and wrought 316L stainless steel specimens as a function of porosity, analyzed by: (a) Sun, et al.,[74] and (b) Sander, et al.[61]*

with the wrought 316L. The increase of porosity was found to adversely influence the E_{pit} of the Type 316L in the work presented by Sun, et al.[74] In addition, the SLM 316L presented lower E_{pit} values than the analyzed wrought counterpart. Sun, et al., suggest that the SLM 316L specimens were more prone to pitting due to an ion diffusion barrier formed around on top of pores. Such a barrier is postulated to lead to the concentration of aggressive agents (e.g., chloride ions) inside the pores, hence increasing the probability of oxide layer breakdown, although evidence for neither hypothesis was presented and would be difficult to

experimentally validate. The SLM 316L analyzed by Sander, et al.,[61] shows E_{pit} values considerably more noble than 0.3 V_{SCE} (the E_{pit} of the wrought 316L), whereas no trend in E_{pit} was observed with the increase of porosity. The presence of a finer distribution of inclusions formed during the SLM of the 316L is hypothesized by Sander, et al.,[61] to reduce the number of pit nucleation sites on the metal surface and consequently decrease the susceptibility to pitting. The porosity values analyzed for the SLM 316L specimens are very distinct, varying between 1% and 7% in the work performed by Sun, et al.,[74] and between 0.01% and 0.4% in the work presented by Sander, et al. The antagonistic results create a performance window on the pitting of SLM 316L that requires further investigation to clarify how porosity could affect corrosion, or whether there is a true reversal of the porosity effect at some critical porosity between the two studies documented in Figure 12. The porosity of the SLM 316L specimens was determined to play a decisive role in the pitting of these alloys, evidenced by the reduction E_{pit} for porosities above 1%. However, for porosities lower than 0.4%, it was proven possible to produce SLM 316L specimens more resistant to pitting corrosion than the conventionally produced Type 316L (i.e., wrought). The specimens analyzed by Sun and Sander were produced by different machines using dissimilar powder batches, which could also affect the final product quality and properties. The corrosion of SLM 316L as a function of E_{corr} and i_{corr} was analyzed by Zhang, et al.[96] Despite showing decreased E_{corr} for more porous SLM 316L, the conclusions were made using a semiqualitative approach, and further characterization (i.e., quantitative porosity, microstructural imaging) should be performed to either support or refute the outcomes presented by Zhang, et al.[96] The effects of pore size and morphology on the corrosion of SLM 316L were not discussed in the studies performed by Sun, et al.,[74] Sander, et al.,[61] and Zhang, et al.[96]

Trelewicz, et al.,[86] investigated the corrosion of SLM 316L specimens in 0.1 M HCl. The SLM 316L was determined to be less resistant to corrosion than the wrought 316L in that environment, based on the passive current density measured during potentiodynamic polarization (135 $\mu A/cm^2$ and 22.5 $\mu A/cm^2$, respectively). This difference in the behavior is attributed to "inhomogeneous solute distribution and nonequilibrium microstructures" formed during the SLM of Type 316L. However, the explanations provided are insufficient in explaining the results, and further characterization would be required to better understand and validate the outcomes presented.

The environmentally assisted cracking (EAC) behavior of SLM 316L has been investigated by in the context of corrosion fatigue (CF),[83] different build directions,[76] and the role of inclusions on stress corrosion cracking (SCC).[77] In order to simulate the corrosive environment commonly present in nuclear reactors, hot pressurized water at 288°C with different contents of dissolved oxygen (DO) and dissolved hydrogen (DH) was utilized as an electrolyte. The CF was assessed for the SLM 316L and tested in two different directions: X-Z (load applied on the X plane and crack grow in the Z direction) and Z-X (load applied on the Z plane and crack growth in the X direction), as shown in Figure 13(a). The loading plane and direction were varied to observe the fatigue crack growth as a function load orientation. The SLM 316L specimens were also heat treated prior CF testing: (i) stress relieved at 650°C for 2 h and (ii) hot isostatically pressed (HIP'ed) at 1,150°C and 1,000 bar for 4 h in an inert argon atmosphere, followed by SA. The effect of mechanical deformation on CF was investigated after cold working (CW) the heat-treated SLM 316L specimens. The CF crack growth rate (da/dN) as a function of the loading frequency for the specimens after heat treatment and CW in high-temperature water with 2 ppm DO is shown in Figure 13. The SLM 316L specimens tested for the X-Z plane and cold-worked along the X direction presented higher crack growth rates for loading frequencies above 0.1 Hz (Figure 13[b]), and the cracks were associated with directional grain growth along during SLM.

The fatigue crack growth rate was reduced from 2 to 4×10^{-4} to $\sim 10^{-5}$ mm/cycle with the increase of loading frequency from 10^{-3} to 0.5 Hz for all of the analyzed Type 316L specimens. For loading frequency values close to 1 Hz, the crack growth rate was similar for the investigated specimens (~0.1 mm/cycle). The SLM 316L specimens after CW and HIP showed increased fatigue crack growth rate with the decrease of loading frequency (Figure 13[c]). The performance of the wrought 316L analyzed in the work presented by Lou, et al.,[83] was superior to the SLM 316L. However, the stress intensity range (ΔK) and load ratio (R) utilized to test wrought 316L ($\Delta K = 8.3$ MPa$\sqrt{m}$, R = 0.7) were not the same as SLM 316L specimens ($\Delta K = 11$ MPa$\sqrt{m}$, R = 0.6), as shown in Figure 13(c). The American Society of Mechanical Engineers, Section XI (ASME XI) fatigue crack growth rate in air of Type 316L stainless steel is included in Figures 13(b) and (c) for performance reference.

SCC of SLM 316L was analyzed in another study by Lou, et al.,[76] utilizing similar specimens as those shown in Figure 13(a). The SCC experiments were performed in pure water at 288°C with 2 ppm DO (normal oxidizing water chemistry), and in pure water at 288°C with 63 ppb DH (reducing hydrogen water chemistry). The main results arising from SCC testing of the SLM 316L are presented in Figure 14.

The 63 ppb DH solution successfully inhibited the growth of cracks for most of the analyzed SLM 316L samples. The crack growth rate was, however, found to be higher for the SLM 316L specimens in the 2 ppm DO electrolyte prior to CW (1.2×10^{-7} mm/s), as shown in Figure 14(a). Moreover, longer and branched

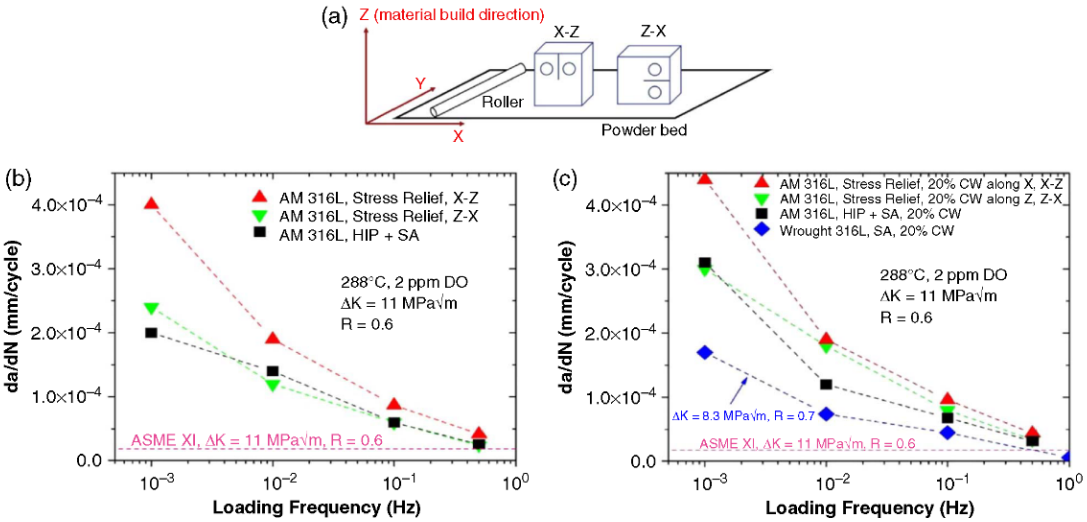

FIGURE 13. *The CF of SLM 316L evaluated by Lou, et al.,[83] for the crack growth rate as a function of loading frequency after different post-build treatments in different build directions and different (a) investigated planes, (b) after stress relief and hot isostatic pressing, and (c) after CW—as compared with wrought 316L. Adapted with permission from Elsevier, Copyright 2017.*

cracks grew over time for the X-Z sample, indicating that cracks propagate more easily along this direction of build.[76] After CW parallel to the Z direction, the SLM 316L specimens presented superior performance against SCC than the CW wrought 316L (Figure 14[b]). However, SCC rates were enhanced when 20%CW was performed on the X direction of the X-Z sample. CW further elongated the grains in the Z direction, which produced an elongated grain boundary path for cracks to propagate. In addition, the 63 ppb DH solution was not able to mitigate the crack growth of the X-Z sample 20%CW along the X direction as observed for the other specimens. The combination of HIP and CW was detrimental for the SCC of the SLM and wrought 316L, as shown in Figure 14(c). The HIP induces the formation of equiaxed grains which reduce the susceptibility toward cracks growth. The CW of the Type 316L specimens following HIP elongated the grains along the forging direction and facilitated crack growth. Low porosity was found to be beneficial toward reducing the crack growth rate in the SLM 316L, as revealed in Figure 14(d). The low porosity sample (0.08% mean porosity and 2.8 μm mean pore size) had a superior performance (i.e., 40% lower crack growth rate) when compared to the high porosity sample (0.3% mean porosity and 16 μm). The authors suggest that higher porosities on the SLM 316L enhanced the crack growth rate in hot pressurized water. They also note that more research on the effect of pores on the SCC of these alloys must be performed to provide more precise conclusions.

The influence of inclusions on the SCC of SLM 316L was also investigated by Lou, et al.,[77] in high-temperature water (288°C) and compared with their wrought counterpart. The authors found that Si-rich inclusions were detrimental to the SCC of SLM 316L due to preferential dissolution in hot water, thus increasing susceptibility to cracking. Therefore, controlling the formation of Si-rich phase could be essential to increasing the resistance of SLM 316L to SCC in hot water for suitable use of this alloy in nuclear applications.

Tribocorrosion of SLM 316L was investigated by Stendal, et al.,[97] in both 0.9 wt% NaCl and simulated body fluid (SBF) solution, and the performance compared to wrought 316L. The SLM 316L specimens showed a greater tendency to passivate and were less susceptible to metastable pitting than their wrought counterpart. After wear damage was imposed upon the samples, corrosion caused close to 50% lower volumetric material loss in SBF than in 0.9 wt% NaCl, for both SLM and wrought 316L. However, the effect of porosity and other microstructural features was not explored.

The so-called "oxidization" of SLM 316L was evaluated by Harun, et al.,[82] to examine the effect on the corrosion characteristics of SLM 316L in Ringer's solution (8.6 g/L NaCl + 0.48 g/L $CaCl_2$ + 0.30 g/L KCl). Thermal oxidation was applied to thicken the oxide layer on the SLM 316L specimen surfaces. Treatments at 700°C for 150 h were found to improve the corrosion of SLM 316L by presenting lower corrosion rates (3.34×10^{-6} mm/y) in comparison to the untreated SLM 316L (9.21×10^{-6} mm/y). Exposure for longer periods of 200 h and 250 h decreased the corrosion resistance of SLM 316L in Ringer's solution, with

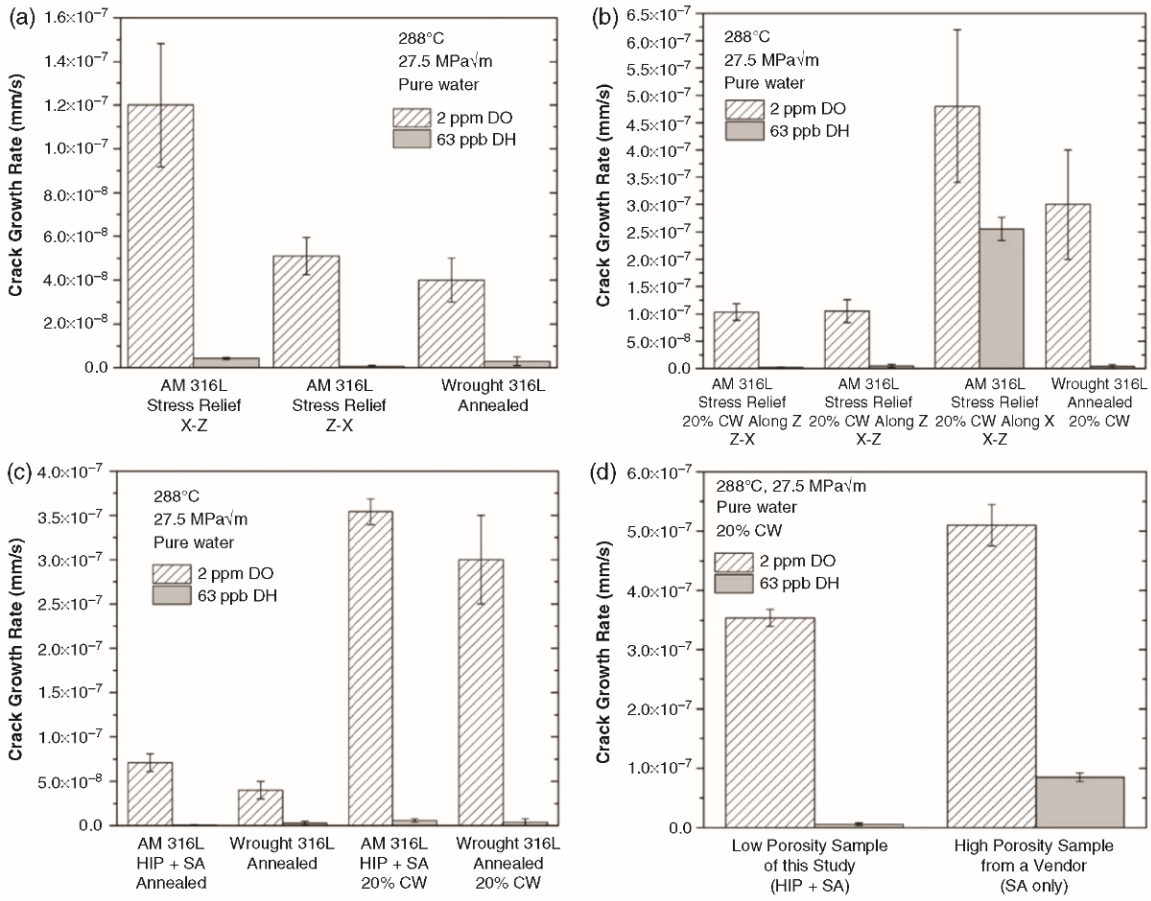

FIGURE 14. *The crack growth rate of SLM 316L compared to the wrought 316L in hot water (288°C) for contrasting concentrations of 2 ppm dissolved oxygen (DO) and 63 ppb dissolved hydrogen (DH) for different post-build treatments in different build directions and planes after: (a) stress relief, (b) CW, (c) hot isostatic pressing, and (d) low and high porosity SLM 316L specimens. Adapted from Lou, et al.,[76] with permission from Elsevier, Copyright 2017.*

corrosion rates higher than 1.53×10^{-5} mm/y. Porosity of SLM 316L was correlated to corrosion characteristics in 0.5 M H_2SO_4 by Geenen, et al.[75] The results were compared with SLM 316L after HIP and a cast counterpart. Corrosion susceptibility was increased by HIP of SLM 316L due to oxide shape transformation from lamellae into spheroid particles which led to passive current densities 10 times higher than the other analyzed specimens. Geenen, et al., also suggest that the oxides present inside pores or in residual cracks can coalesce during HIP[110] and apparently increasing the number of corrosion nucleation sites; however, the characterization of pores and residual cracks was not performed to confirm such a mechanism.

Heat treatments were performed in SLM 316L specimens to investigate SCC in boiling $MgCl_2$ (ASTM G36) in the work presented by Bruycker, et al.[98] The increase of heat-treatment temperature from 450°C to 950°C increased the resistance to SCC of SLM 316L based on visual inspection of cracks formed on the analyzed specimen. The SLM 316L heat treated at 950°C did not present visual cracks after SCC testing. However, the influence of other features, such as inclusions, surface finish, and grain size, on the SCC of SLM 316L were not investigated.

The corrosion characteristics of Type 316L produced by WAAM were investigated by Chen, et al.,[99] for AP and heat-treated specimens. Interestingly, in contrast with other AM methods capable of producing Type 316L specimens, WAAM of Type 316L promoted δ and σ phases in the AP microstructure. These phases played an adverse role in the corrosion of WAAM 316L, acting as nucleation sites for pitting. The heat treatment at 1,200°C for 4 h eliminated the residual delta and sigma phases and homogenized the

microstructure into the common austenitic monophasic Type 316L stainless steels. Thus, the heat treatment of WAAM 316L increased the resistance to pitting in 3.5 wt% NaCl solution by increasing E_{pit} from 0.4 V_{SCE} in the AP specimen to values above 1.0 V_{SCE} after heat treatments at temperatures >1,200°C for 1 h.

Zhang, et al.,[100] studied novel stainless steel + x wt% Ni produced by SLM with nickel contents varying as x = (0, 3, 6, and 9), in order to assess the effect of Ni on the corrosion of stainless steels. The increase of Ni wt% in iron alloys has been reported to enhance their corrosion performance.[110-112] As predicted, the SLM stainless steel specimen containing 9 wt% Ni presented better resistance to corrosion with higher E_{corr} and lower i_{corr} in 3.5 wt% NaCl than the lower Ni content alloys investigated by Zhang, et al.

The corrosion of precipitation hardened 17-4 PH (UNS S17400) stainless steels produced by SLM was investigated by Schaller, et al.,[73] and Stoudt, et al.,[101] in similar concentrations of NaCl solution (0.5 M and 0.6 M, respectively). Schaller, et al., analyzed the corrosion properties of SLM 17-4 PH as a function of porosity and compared the results with their wrought counterpart. The wrought 17-4 PH with average i_{corr} of 2.30×10^{-8} A/cm^2 showed better resistance to corrosion than the SLM 17-4 PH (i_{corr}: 2.41×10^{-7} A/cm^2), measured by potentiodynamic polarization after 1 h of open-circuit potential (OCP) exposure. The i_{corr} measured by linear polarization for both the wrought and SLM 17-4 PH decreased by one order of magnitude after 24 h OCP exposure values were determined to be 2.73×10^{-9} A/cm^2 and 7.28×10^{-8} A/cm^2, respectively. The effect of porosity was evaluated based on the average pore size of different specimens in comparison to their wrought counterpart (with no porosity). Specimens with pores larger than 50 μm were found to be more susceptible to pitting (E_{pit}: ~0.75 V_{SHE}) compared to specimens with pores smaller than ~10 μm (E_{pit}: ~0.5 V_{SHE}) and the wrought samples with no pores (E_{pit}: ~0.30 V_{SHE}). Therefore, the presence of pores in the SLM 17-4 PH was deemed detrimental to their resistance to corrosion. Although evidence reveals that pores were responsible for the inferior corrosion performance of SLM 17-4 PH, microstructure characterization by TEM and EDS techniques could unveil other factors (e.g., nano-inclusions, martensite vs. austenite or ferrite) affecting the corrosion characteristics of these alloys. The effect of post-build heat treatments and exposed plane on the pitting of SLM 17-4 PH specimens was analyzed by Stoudt, et al., in 0.5 M NaCl. The heat treatments increased the average E_{pit} of the SLM 17-4 PH (>−130 mV_{SCE}) when compared to the wrought counterpart (−135 mV_{SCE}). Three planes (XY, XZ, and YZ) of the analyzed SLM 17-4 PH specimen showed dissimilar average values for E_{pit} (−130 mV_{SCE}, −104 mV_{SCE}, and −93 mV_{SCE}, respectively) and evidence of anisotropic pitting behavior. Within the scatter of values recorded, the lowest E_{pit} of the SLM 17-4 PH is similar to the average E_{pit} detected for the wrought counterpart. The results presented by Schaller, et al., and by Stoudt, et al., are contradictory regarding the corrosion of SLM 17-4 PH. However, while Schaller, et al., did not heat treat the SLM 17-4 PH specimens, Stoudt, et al., did not investigate specimen porosities. Therefore, further investigations should more systematically consider analyzing both porosity and heat treatments of SLM 17-4 PH in order to clarify the results presented to date.

The corrosion in artificial seawater of Type 4340 (UNS G43400) stainless steel produced by SLM (ASTM D1141-98) was investigated by Schmidt, et al.[102] The work reveals that there is no significant difference in the corrosion rates of the SLM (4.1 mpy to 4.9 mpy) and wrought 4340 (3.6 mpy) calculated by polarization resistance testing. The work performed by Schmidt, et al., provides a preliminary insight regarding the corrosion of SLM 4340 stainless steel; however, the corrosion of such alloys requires further investigation.

In related work, Lefky, et al.,[103] worked on the development of low chromium steel support structures that were supposed to be electrochemically removed after the DLD of martensitic Type 431 (UNS S43100) stainless steels. DLD readily permits the deposition of various material/alloy types, making this possible. Such low chromium steel supports were sought to be removed utilizing nitric acid as the etchant. However, the etching process was not selective and the martensitic Type 431 was also dissolved. Although the initial purpose was not successfully achieved, Lefky, et al.,[103] suggest that the etching of low chromium steels can be controlled to improve the surface finish of steels produced by DLD. It is noted, however, that the correlation between surface finish of AM steels and corrosion characteristics is still unknown.

The corrosion of SLM FeMn-Ag was investigated by Wiesener, et al.,[104] in SBF. The interaction of Ag precipitates and FeMn matrix created a galvanic couple in the early stages of immersion in SBF. However, as corrosion progressed, both phases reacted with the SBF and deposition of oxides and phosphates on the surface reduced corrosion rates, elucidated by increased impedance from 600 Ω·cm^2 to 1,300 Ω·cm^2 at low frequency (0.1 Hz) and from 15 Ω·cm^2 to 25 Ω·cm^2 at high frequency (5 kHz) over 38 h. The work presented by Wiesener, et al., represents an example of utilizing AM to produce alloys under nonequilibrium conditions and with atypical corrosion behavior.

Steels produced by AM still require considerable characterization of corrosion performance and related mechanisms. There were no trends nor general conclusions on the corrosion of steels according to the results presented in the literature to date. However, it is evident that the microstructural changes arising from AM processing can differ from the microstructures of conventionally manufactured steels. These

microstructural changes directly affect the corrosion characteristics of AM steels. Thus, the variability of manufacturing strategies to produce steels via AM provides the tools necessary to manipulate potential microstructural features (e.g., porosity, inclusions, surface finish, etc.) in order to enhance corrosion.

Titanium Alloys

Titanium alloys find use in two key industries, namely aerospace and biomedical, owing to their good mechanical strength, corrosion resistance, and biocompatibility. The investigations related to the corrosion of AM-prepared Ti alloys reviewed in this work are summarized in Table 6.[68-69,84,113-132]

The work performed by Dai, et al.,[84,113] analyzes the corrosion characteristics of Ti6Al4V alloys produced by SLM in different chloride-containing media. The authors evaluated the corrosion of SLM Ti6Al4V by altering exposed planes to different electrolytes[84] and by post-build heat treatments.[113] The corrosion of SLM Ti6Al4V was not significantly affected by the specimen exposed plane in a 3.5 wt% NaCl. However, the same behavior was not observed in 1 M HCl whereby, according to Dai, et al., the plane parallel to the build substrate showed slightly better resistance to corrosion than the plane perpendicular to the substrate. Weight loss after 15 d immersion testing in 1 M HCl was measured to be 0.7 mg/cm^2 for the parallel plane to the substrate compared to 0.9 mg/cm^2 for the perpendicular plane. Potentiodynamic polarization revealed that the passive current densities of the parallel and perpendicular planes (to the substrate) were 2.8 μA/cm^2 and 2.5 μA/cm^2, respectively. This proposed corrosion rate difference between planes was attributed to the formation of "weaker" passive layer on the planes perpendicular to the substrate. In addition, the higher proportion of acicular martensitic phase (α′) along the perpendicular planes to the substrate was also correlated with lower corrosion rates.[84] Residual stresses were measured to be similar for both planes parallel and perpendicular to the substrate. Therefore, there was no evidence or suggestion in that work that the presence of residual stress in the SLM Ti6Al4V could influence corrosion in 3.5 wt% NaCl and 1 M HCl.[84] The corrosion of SLM Ti6Al4V and residual stresses from the build process still require further investigation in order to determine any causal or conclusive correlations. The SLM Ti6Al4V specimens investigated by Dai, et al.,[113] were heat treated for 2 h at 500°C, 850°C, and 1,000°C. The heat treatment of SLM Ti6Al4V was found to be detrimental to passivation in 3.5 wt% NaCl with passive current densities of 0.9 μA/cm^2 (no heat treatment), 1.3 μA/cm^2 (500°C), 1.5 μA/cm^2 (850°C), and no fixed value (although higher than 1.5 μA/cm^2) for heat treatments at 1,000°C.[113] The i_{corr} increased as a function of heat-treatment temperature, with magnitudes of 13.1 nA/cm^2, 14.6 nA/cm^2, 55.8 nA/cm^2, and 76.1 nA/cm^2 for no heat treatment, 500°C, 850°C, and 1,000°C, respectively. Although the heat treatments performed reduced the α′ phase volume fraction, there was an increase of the volume fraction of beta phase (β) which further reduced the corrosion resistance of SLM Ti6Al4V, which is usually unexpected for these alloys. The authors hypothesized that grain refinement during heat treatment could be responsible for the atypical correlation between corrosion resistance and β phase volume fraction, and further investigation should be performed to assess this hypothesis.

Chandramohan, et al.,[114] also investigated the effect of post-build heat treatments of SLM Ti6Al4V in 3.5 wt% NaCl. In accordance to the results obtained by Dai, et al.,[113] there was an increased corrosion rate of SLM Ti6Al4V in 3.5 wt% when post-build heat treatments at 1,100°C and 900°C were performed for 1 h. The corrosion rates were measured and found to be 1.97×10^{-4} (mm/y) for SLM Ti6Al4V with no heat treatment, 3.4×10^{-4} (mm/y) for SLM Ti6Al4V heat treated at 1,100°C, and 5.9×10^{-4} (mm/y) for SLM Ti6Al4V heat treated at 900°C. In that work, it was suggested that the increase of β phase against the reduction of α′ after heat treatment of SLM Ti6Al4V was responsible for the increase of corrosion susceptibility.[114] However, microstructural characterization was not presented to support such conclusions. The SLM Ti6Al4V specimens were also tested for corrosion in 1 M HCl and 1 M H_2SO_4 electrolytes for two different build directions: horizontal and vertical to the substrate. The authors concluded that build direction did not significantly affect the corrosion in all of the electrolytes studied[114] when compared to the effect of post-build heat treatment.[114] However, there was no trend on the susceptibility to corrosion of SLM Ti6Al4V immersed in 3.5 wt%, 1 M HCl, and 1 M H_2SO_4 built vertically and horizontally. In addition, the authors concluded that SLM Ti6Al4V is more resistant to corrosion in alkaline media, whereas the pH of the solutions analyzed was not presented and no comparison was made with wrought or cast counterparts.

SLM Ti6Al4V was exposed to Hank's solution on different planes for corrosion testing in the work performed by Chen, et al.[115] The corrosion resistance of the SLM Ti6Al4V on all of the exposed planes was found to be superior to wrought Ti6Al4V tested in the same electrolyte. Chen, et al., suggest that the defects generated during the rolling of wrought Ti6Al4V enhance the susceptibility to corrosion. However, the microstructural characterization provided by the authors was not sufficient to support this conclusion—not to mention that many Ti6Al4V products are actually never subjected to rolling. The SLM laser scan pattern was hypothesized to influence porosity and was associated to an anisotropic corrosion of SLM Ti6Al4V on differently exposed planes (X, Y, and Z). The X plane (perpendicular to the substrate and to the laser scan track) presented an E_{corr} of −0.48 $V_{Ag/AgCl}$, an i_{corr} of

TABLE 6

Summary of Reported Studies on the Corrosion of AM Titanium Alloys[(A)]

Alloy	AM Technique	Environment	Corrosion Characterization	Corrosion as a Function of	Comparison with Wrought/ Cast Counterpart	AM Alloy Corrosion Characteristics	Microstructure Characterization	References
Ti6Al4V	SLM	3.5 wt% NaCl, 1 M HCl	OCP, PDP, EIS	Exposed plane, electrolyte composition	—	Affected by exposed plane in 1 M HCl solution.	OM, SEM, XRD	84
		3.5 wt% NaCl	OCP, PDP, EIS	Heat treatment	—	Resistance to corrosion decreased with heat treatment.	OM, XRD	113
		3.5 wt% NaCl, 1 M H_2SO_4, 1 M HCl	OCP, PDP	Heat treatment, build direction, electrolyte composition	—	No trends were reported.	SEM, XRD	114
		Hank's solution	PDP, EIS	Exposed plane	Wrought	Superior to wrought for all of the exposed planes.	SEM, XRD	115
		PBS	PDP, PSP	—	Wrought	Similar to wrought.	SEM, XRD	116
		SBF	OCP, PDP	Heat treatment	Wrought	Superior to wrought. Improved by heat treatment.	OM, SEM, XRD, EBSD	117
		3.5 wt% NaCl	PDP, EIS	Heat treatment	Wrought	Superior to wrought. Improved by heat treatments below 100°C	OM, SEM, EDS, XRD	118
		SBF	PDP, tribocorrosion	Laser energy density	Wrought	Similar to wrought. Not significantly affected by laser energy density.	OM, SEM, XRD	119
	DLD	PBS	Tribocorrosion	—	Cast	Superior to cast.	SEM, EDS, XRD	120
	EBM	3.5 wt% NaCl	PDP, PSP	Temperature, pH	Wrought	Similar to wrought for all of the conditions tested.	—	121
		1 M HCl	PDP, EIS	Build direction	—	Affected by building direction.	SEM, EBSD, XRD	69
		Hank's solution	PDP	PDP scan rate	—	No significant conclusions.	OM, SEM	122
		PBS	OCP, PDP, EIS	—	Wrought	Superior to wrought.	SEM, XRD, TEM	123
		SBF	OCP, PDP	—	Wrought	Superior to wrought.	OM, XRD	124
	SLM/EBM	SBF	OCP, PDP, EIS, weight loss	AM technique	Wrought	Similar for wrought, SLM, and EBM specimens.	SEM, EBSD, XRD	125
Ti6Al4V – xCu	SLM	0.9 wt% NaCl	EIS	Copper content	—	Improved for higher Cu contents.	OM, SEM, XRD	126
Ti6Al4V/ TiC	DLD	3.5 wt% NaCl	OCP, PDP	Scan speed	Wrought	Superior to wrought. Improved by faster scan speeds.	OM, SEM	127
Ti-Mo	SLM	0.9 wt% NaCl	PDP, EIS	Molybdenum content, porosity	—	Similar for different Mo contents. Reduced by the increase of porosity.	SEM, XRD	68
		0.9 wt% NaCl	PDP, EIS	Molybdenum content	—	Reduced with the increase of Mo content.	SEM, XRD	128
Ti-TiB	SLM	Hank's solution	PDP, EIS	—	Pure Ti	Superior to pure Ti.	OM, SEM, EDS, XRD	129
Ti-Re		75 wt% Na_2SO_4 + 0.25 wt% NaCl salt at 600°C	Weight loss–hot corrosion	Rhenium content, exposure time	—	Maximized for Re 6 wt%.	OM, SEM, EDS, XRD	130

(*continued*)

TABLE 6 (*Continued*)

Alloy	AM Technique	Environment	Corrosion Characterization	Corrosion as a Function of	Comparison with Wrought/ Cast Counterpart	AM Alloy Corrosion Characteristics	Microstructure Characterization	References
γ-TiAl	EBM	Hank's solution and Hank's solution + 10% fetal bovine serum	PDP	Heat treatment	Pure Ti	Superior to pure Ti. Reduced by heat treatment.	OM, SEM, EBSD, XRD	131
Ti6Al4V + Custom Ti alloys	DLD/SLM	Minimum essential media (MEM) and MEM + H_2O_2 + albumin	PDP, PSP	Alloy composition, electrolyte composition	Wrought Ti6Al4V, pure Ti	Faster passivation for DLD and SLM alloys. Albumin + H_2O_2 enhanced Ti dissolution during anodic polarization.	OP	132

(A) PBS: phosphate buffered solution; SBF: simulated body fluid; OCP: open-circuit potential; PDP: potentiodynamic polarization; PSP: potentiostatic polarization; EIS: electrochemical impedance spectroscopy; OM: optical microscopy; SEM: scanning electron microscopy; TEM: transmission electron microscopy; XRD: x-ray diffraction; EDS: energy dispersive spectroscopy; EBSD: electron backscatter diffraction; and OP: optical profilometry.

0.03 μA/cm^2, and polarization resistance of 0.5 MΩ·cm^2. The Y (perpendicular to the substrate and parallel to the laser scan track) and Z (parallel to the substrate) planes showed similar (between each other) and superior E_{corr}, i_{corr}, and polarization resistance (–0.33 $V_{Ag/AgCl}$, 0.023 μA/cm^2, and 1.3 MΩ·cm^2, respectively) in comparison with the X plane. However, porosity was not quantitatively measured in their study to support the correlation that pores affect the corrosion of SLM Ti6Al4V.

Damborenea, et al.,[116] compared the corrosion of SLM Ti6Al4V with a wrought counterpart in phosphate buffered saline (PBS) at 37°C. The polarization curves reveal that at 2.4 $V_{Ag/AgCl}$, there was a sharp increase of current density for the SLM Ti6Al4V from ~5×10^{-6} A/cm^2 to ~5×10^{-2} A/cm^2, which was not observed for the wrought counterpart. The authors concluded that the SLM Ti6Al4V was more susceptible to the formation of hydrated titanium oxides on their surface at 2.4 $V_{Ag/AgCl}$, being associated with the current density increase during the polarization test. However, the validity of this assertion was not further tested in the work, and it was noted that the potential range being studied in such work was above the oxygen evolution potential and of no relevance to biomedical uses (for which PBS is often used as a test electrolyte).

SBF was utilized to investigate the corrosion of SLM Ti6Al4V as function of heat treatment and laser energy density by Xu, et al.[117] The SLM Ti6Al4V specimens were annealed by Xu, et al., at 700°C, 750°C, and 799°C for 4 h, and electrochemically corrosion tested following heat treatment. The results for the annealed SLM Ti6Al4V were compared to the AP SLM Ti6Al4V and their wrought counterpart. The heat-treated SLM Ti6Al4V (i_{corr} = 0.305, 0.295, and 0.202 [$\times10^{-2}$ A/m^2] for 700°C, 750°C, and 799°C, respectively) were less susceptible to corrosion in SBF than the AP specimen ($i_{corr} = 0.384\times10^{-2}$ A/cm^2). Although the wrought Ti6Al4V presented $i_{corr} = 0.270\times10^{-2}$ A/cm^2, their anodic current density increased two orders of magnitude from i_{corr} during potentiodynamic polarization after breakdown at 2.4 $V_{Ag/AgCl}$. Passivity breakdown was not observed for the SLM Ti6Al4V specimens before and after heat treatment. The annealing process in the SLM Ti6Al4V produced acicular microstructures purported to generate more stable oxides, while the equiaxed wrought Ti6Al4V allowed alloying element segregation. The fast cooling inherent of the SLM process enabled metastable α′ phase to form, which increased corrosion susceptibility, as observed for the AP Ti6Al4V. Therefore, according to Xu, et al., the annealing of SLM Ti6Al4V at higher temperatures allowed for the reduction of the α′ volume fraction, decrease of α/β interface area, and agglomeration of the β phase. These microstructural changes deriving from the annealing of SLM Ti6Al4V were attributed in the improvement of their performance against corrosion through reduction of their i_{corr}.

The effect of heat treatment on the corrosion of SLM Ti6Al4V in 3.5 wt% NaCl was investigated by Yang, et al.[118] Electrochemical characteristics of SLM Ti6Al4V before and after heat treatments were compared to their wrought counterpart. Heat treatment at 750°C was shown to decrease the corrosion rate of SLM Ti6Al4V to ~2×10^{-3} mm/y in comparison to wrought (4×10^{-3} mm/y) by controlling microstructural transformations (i.e., altering grain size, type, and morphology of the constituent phases). Volume fractions of metastable α′ phase were hypothesized by Yang, et al.,[118] to be reduced with the heat treatment of SLM Ti6Al4V, hence improving their corrosion resistance. This hypothesis is in accordance with the findings presented by Xu, et al.[117]

The tribocorrosion of SLM Ti6Al4V was investigated by Chiu, et al.,[119] in SBF by altering SLM parameters. The laser scan speed, laser power, and hatch distance were altered to change the surface energy density (i.e., laser energy input per area) to produce the SLM Ti6Al4V specimens. Because none of the SLM parameters were fixed, any comparison of trends regarding the effect of energy density on corrosion was rather difficult, although significant change in corrosion resistance between the analyzed SLM Ti6Al4V and wrought counterpart was not observed. Wear loads of 1 N, 2 N, and 5 N were applied on both the SLM and wrought Ti6Al4V. The tribocorrosion was evaluated by the corrosion/wear ratio (C/W) and was found to be lower for wrought Ti6Al4V (< ~10%) than for SLM Ti6Al4V (> ~10%) for all of the loads applied.

Tribocorrosion of DLD Ti6Al4V in PBS solution in comparison with their hot pressed (HP) and cast counterparts was reported by Buciumeanu, et al.[120] Corrosion was assessed by the electrochemical potential before and simultaneous to wearing the surface. The OCP values measured for the undamaged samples were –0.03 V_{SCE} for the DLD, –0.25 V_{SCE} for the HP Ti6Al4V, and –0.36 V_{SCE} for the cast Ti6Al4V. The damage on the surface of the analyzed samples caused the OCP to drop to values around –0.61 V_{SCE}, –0.72 V_{SCE}, and –0.91 V_{SCE}, respectively. After wear, the OCP returned to the initial values of the undamaged surfaces for all specimens. The DLD Ti6Al4V was deemed less susceptible to corrosion than the HP Ti6Al4V and cast Ti6Al4V before, during, and after surface wear. The correlations between the phases present in the microstructure of DLD Ti6Al4V and tribocorrosion characteristics were not provided to enable a better explanation for enhanced wear corrosion.

The corrosion of EBM Ti6Al4V in 3.5 wt% NaCl with pH ranging from acid to alkaline was evaluated by Abdeen and Palmer.[121] The critical pitting temperature (CPT) of EBM Ti6Al4V in neutral 3.5 wt% NaCl was also investigated and compared to its wrought counterpart. The CPT was found to be around 30°C for both EBM and wrought Ti6Al4V specimens in

3.5 wt% NaCl. The pH levels did not seem to significantly affect the corrosion of the EBM Ti6Al4V. The current densities during potentiostatic polarization of the specimens were similar and did not exceed 30 $\mu A/cm^2$. However, electrochemical characterization was not performed multiple times to ensure reproducibility of results, and the microstructure of the EBM Ti6Al4V was not investigated to provide explanatory conclusions for the observed corrosion behavior. Gong, et al.,[69] investigated the corrosion of EBM Ti6Al4V in chloride-containing electrolyte (1 M HCl) as a function of different build directions (i.e., angles relative to the substrate). The grain boundary length and proportion of α and β phases in the grain boundary of each specimen, built in different directions, were found to directly influence corrosion. The corrosion performance of the EBM Ti6Al4V specimens is not compared to the wrought or cast counterpart in the work presented by Gong, et al.[69] Almanza, et al.,[122] compares the corrosion performance of EBM Ti6Al4V with the ASTM F75 (Co-Cr) alloy in Hank's solution. Aside from comparing two distinct alloys, the work reported by Almanza, et al., does not evaluate the corrosion of the studied alloys in comparison with their respective (conventional) counterparts. Bai, et al.,[123] reported that the resistance to corrosion of Ti6Al4V specimens in PBS solution is enhanced when produced by EBM in comparison to the wrought counterpart. The presence of higher volume fraction of β phase and refined lamellar α/β phase are suggested to be the factors leading to the observed superior corrosion resistance of EBM Ti6Al4V.

Devika, et al.,[124] conclude that the EBM Ti6Al4V corrosion is superior to their wrought counterpart in SBF. However, the data presented are insufficient to assess the corrosion performance of the studied alloys. The corrosion performance of SLM and EBM Ti6Al4V are compared to their wrought counterpart by Zhao, et al.,[125] in SBF. The SLM Ti6Al4V presents superior overall resistance to corrosion when compared to the EBM and wrought counterparts. However, the EBM Ti6Al4V is less prone to crevice corrosion than the SLM and wrought counterparts, which is suggested to be related to grain boundary density. Based on the above works, however, the corrosion performance of EBM Ti6Al4V, particularly relative to the body of knowledge on wrought Ti6Al4V, is inconclusive.

The effect of Cu content on the corrosion performance of SLM Ti6Al4V was investigated by Liu, et al.,[126] in 0.9 wt% NaCl. The increase of Cu content up to 6 wt% was found to be beneficial for the oxide layer formed on the surface of the alloys, which decreased the corrosion rate of the SLM Ti6Al4V by 67% to 82%. The authors[126] assume that the presence of Cu influenced the oxide layer formation, although the oxide layer characteristics were not investigated. Mahamood, et al.,[127] investigated the corrosion of DLD Ti6Al4V/TiC composite in 3.5 wt% NaCl. The laser scan speed utilized to manufacture the DLD Ti6Al4V/TiC specimens was varied from 0.005 m/s to 0.05 m/s. The increase of laser scan speed caused the reduction of corrosion rates from 0.323 mm/y to 0.008 mm/y. This reduction in corrosion rate was associated to the morphology and melting efficiency of the carbides present in the alloy microstructure.

The effect of porosity[68] and Mo content[128] on the corrosion of SLM Ti-Mo alloys in 0.9 wt% NaCl was investigated by Xie, et al. The results are similar for both studies, whereby the increase of Mo content led to higher porosity (as opposed to a chemically dictated influence) which was associated with reduced corrosion resistance. The SLM Ti-TiB composite was compared to commercially pure Ti for corrosion performance in Hank's solution by Chen, et al.[129] The presence of TiB phase facilitated the oxide layer deposition on the SLM Ti-TiB surface, which reduced the average i_{corr} from 0.75 $\mu A/cm^2$ to 0.22 $\mu A/cm^2$ and increased the E_{pit} from 0.70 V_{SCE} to 1.23 V_{SCE}. Hot corrosion of SLM Ti-Re was investigated by Majchrowicz, et al.,[130] as function of rhenium (Re) content in a 75% Na_2SO_4/25% NaCl salt mix. Corrosion of SLM Ti-Re did not follow any trends with the increase of Re content. However, the greatest corrosion resistance was observed for the SLM Ti-Re specimen with the highest Re content analyzed (6%). Mohammad, et al.,[131] investigated the corrosion of EBM γ-TiAl in a mixture of Hank's solution with 10% of fetal bovine serum. The results obtained by Mohammad, et al., were compared to HIP γ-TiAl and commercially pure Ti. The AP EBM γ-TiAl (i_{corr} = 0.002 μA) presents what is apparently better corrosion performance than the HIP γ-TiAl (i_{corr} = 0.103 μA) and the commercially pure Ti (i_{corr} = 0.330 μA). However, the corrosion current values reported are not area corrected current densities, so it is difficult to know if this ranking is valid or meaningful.

Corrosion of a varied group of alloys—SLM Ti6Al4V, DLD 50Ti-35Nb-15Zr, DLD 67Ti-25Nb-8Zr, and DLD pure Ti—was investigated by Wang, et al.,[132] in MEM. The AM Ti alloys analyzed by Wang, et al., were compared to wrought Ti6Al4V, commercially produced pure Ti, and a custom cast Ti-29Nb-13Ta-4.5Zr alloy. The passivation of all of the Ti alloys studied by Wang, et al., was tested by scratching the specimens in situ during potentiostatic polarization in MEM. The wrought/cast Ti alloys showed slower repassivation (132 s to 167 s) after scratching during potentiostatic polarization than the tested AM Ti alloys (22 s to 50 s).

Titanium alloys clearly present anisotropic corrosion for dissimilar planes on the AM specimens. Surfaces near planes parallel to the AM build direction tend to show comparatively poorer corrosion resistance. This behavior is often associated with the commonly observed columnar shaped grains on the mentioned planes.[9,19,21,70] Therefore, the AM build direction could play a decisive role to control grain growth and consequently reduce the anisotropic corrosion behavior. Also, the distribution, shape, and

morphology of constituent phases in the AM Ti alloys, especially α′ martensite, was found to influence corrosion characteristics. The corrosion of AM-prepared Ti alloys reported to date are either comparable or superior to their wrought/cast counterparts for most studies, although some exceptions were reported; in particular, the corrosion performance of EBM prepared Ti alloys would benefit from more research.

Other Alloy Systems (CoCr, Ni, Mg, Cu, and High Entropy Alloys)

Limited investigations have been performed on the corrosion behavior of AM-produced alloys other than aluminum, iron, and titanium, including cobalt-chromium (CoCr), Ni, Mg, Cu, and high entropy alloys (HEAs). The findings from such studies are summarized in Table 7.[133-148]

In the case of CoCr, Xin, et al.,[133] investigated the corrosion characteristics of SLM CoCr in artificial saliva solution—due to the applicability of CoCr-based alloys in odontology—and compared the results with a cast counterpart. The SLM CoCr (i_{corr} = 0.02 μA/cm^2) exhibited similar corrosion characteristics to cast (i_{corr} = 0.07 μA/cm^2) from potentiodynamic polarization in the analyzed environment. In a similar study, Xin, et al.,[134] analyzed the effect of the artificial saliva solution pH on the corrosion of SLM CoCr. The corrosion resistance of SLM CoCr was similar to the cast counterpart in artificial saliva solution with pH = 5, with charge transfer resistance measured by EIS of 4.25 MΩ·cm^2 and 3.82 MΩ·cm^2, respectively. However, the SLM CoCr was less susceptible to corrosion in artificial saliva solutions at pH = 2.5 (charge transfer resistance = 5.83 MΩ·cm^2). The surface of SLM CoCr was treated via porcelain firing by Xin, et al.,[135] and tested for corrosion at different pH levels in artificial saliva solution. Porcelain firing is a common practice in dental prostheses for aesthetic reasons.[135] Xin, et al., reported that this surface treatment reduced the SLM and cast CoCr charge transfer resistance by approximately 50%, in comparison with the untreated specimens in both 2.5 pH and 5 pH artificial saliva. The porcelain-fired SLM CoCr showed higher charge transfer resistance (2.88 MΩ·cm^2) than the porcelain fired cast counterpart (0.78 MΩ·cm^2) in pH 2.5. In pH 5 artificial saliva, cast and SLM CoCr presented similar charge transfer resistance of 2.90 MΩ·cm^2 and 2.88 MΩ·cm^2, respectively. The total ion release (Co, Cr, and Mo) was measured to evaluate the corrosion susceptibility of the heat treated and non-heat treated SLM CoCr in artificial saliva by Alifui-Segbaya, et al.[136] The SLM CoCr was heat treated in two steps: 450°C for 30 min, followed by 45 min exposure at 750°C. The heat-treated sample had a total ion release of 16.47 μg/L over 42 d exposure, while the nonheat-treated sample presented a total ion release of 0.63 μg/L over the same period. The release of those ions from potential SLM CoCr dental prostheses could be a hazard for biological applications.[136] Guoqing, et al.,[139] investigated the biocompatibility of SLM CoCrMo in artificial saliva and 0.9 wt% NaCl solution in comparison to their cast counterpart. The ion concentration of the electrolyte after 4 weeks was measured to be ~175 μg/L (Co) and ~80 μg/L (Cr) for the cast CoCrMo and ~125 μg/L (Co) and ~5 μg/L (Cr) for the SLM CoCrMo in artificial saliva. The Co ion concentration was similar for both cast and SLM CoCrMo samples in 0.9 wt% NaCl after 4 week immersion. However, the Cr ion concentration measured over the same period was significantly inferior in 0.9 wt% NaCl, being ~1 μg/L and 3 μg/L for the SLM and cast CoCrMo, respectively.

Preliminary investigation on the corrosion characteristics of SLM CoCrW and DLD CoCrMo alloys were reported by Lu, et al.,[137] and Mantrala, et al.,[138] respectively. Both studies intended to correlate the laser parameters utilized in each manufacturing process with corrosion performance. Lu, et al.,[137] found that SLM CoCrW resistance to corrosion was enhanced in 0.9 wt% NaCl when the alloy was produced with laser scan speeds between 700 mm/s and 900 mm/s. The laser scan speed of 700 mm/s showed lowest i_{corr} (7.9 nA/cm^2), with a small increase at 900 mm/s (9.8 nA/cm^2). The SLM CoCrW sample produced with laser scan speed of 300 mm/s showed an i_{corr} of 17.4 nA/cm^2, and a significant increase of i_{corr} was measured for the sample produced with laser scan speed of 1,500 mm/s (70.8 nA/cm^2). Mantrala, et al.,[138] reported that 200 W laser power with a 10 mm/s laser scan speed at 5 g/min powder feed rate was optimal to produce DLD CoCrMo resistant to corrosion in 3.5 wt% NaCl with i_{corr} of 0.013 μA/cm^2.

In vitro corrosion of SLM CoCrMo was investigated by Hedberg, et al.,[140] in PBS and PBS + bovine serum albumin, and compared to their cast counterpart. The SLM parameters were altered in order to optimize the corrosion resistance of the SLM CoCrMo. The metal release during exposure over 2 h and 168 h was utilized to evaluate corrosion susceptibility. The total amount of metal released by the SLM CoCrMo (~0.2 μg/cm^2) was lower than the cast counterpart (~0.5 μg/cm^2) when immersed in PBS for 2 h. After 168 h, the total metal release in PBS increased to approximately 0.5 μg/cm^2 and 1.2 μg/cm^2 for the SLM and cast CoCrMo, respectively. The SLM CoCrMo specimens immersed in PBS + bovine serum albumin showed metal release around 0.6 μg/cm^2 after 2 h and 168 h, whereas the cast counterpart presented metal release of ~1.2 μg/cm^2 after 2 h and approximately 0.8 μg/cm^2 after 168 h. Hedberg, et al., suggested that the improved corrosion resistance of the SLM CoCrMo could be attributed to the segregation of Mo to the boundaries of cellular structures, which suppresses the formation of phases that preferentially dissolve in this alloy system (Cr-depleted regions and carbide-rich boundaries).

Corrosion of SLM and DLD NiTi was investigated by Marattukalam, et al.,[141] and Ibrahim, et al.,[142]

TABLE 7

Summary of the Reported Studies on the Corrosion of AM-Prepared CoCr, Ni, Mg, Cu, and HEA[(A)]

Alloy	AM Technique	Environment	Corrosion Characterization	Corrosion as a Function of	Comparison with Wrought/Cast Counterpart	AM Alloy Corrosion Characteristics	Microstructure Characterization	References
CoCr	SLM	Artificial saliva solution	PDP, EIS	—	Cast	Similar to cast.	SEM, EDS, XPS	133
		Artificial saliva solution	PDP, EIS	pH	Cast	Similar to cast for artificial saliva at pH = 5 and inferior at pH = 2.5.	SEM, XPS	134
		Artificial saliva solution	PDP, EIS	Porcelain firing treatment	Cast	Superior to cast in pH = 2.5 artificial saliva solution after porcelain firing.	OM, XPS	135
		Artificial saliva solution	Ion release	Heat treatment	—	Increased ion release with heat treatment.	—	136
CoCrW	SLM	0.9 wt% NaCl	PDP	Laser scan speed	—	Corrosion was inferior for higher laser scan speeds.	OM, SEM, XRD	137
CoCrMo	DLD	3.5 wt% NaCl	PDP	Laser scan speed, laser power, and powder feed rate	—	Optimized for 10 mm/s laser scan speed, 200 W laser power, and 5 g/min powder feed rate.	OM, SEM, XRD	138
	SLM	Artificial saliva, 0.9 wt% NaCl	Immersion	Electrolyte, exposure time	Cast	Co and Cr release reduced in both solutions.	OM, SEM, EDS	139
		1 M NaCl, PBS, and PBS + bovine serum albumin	PDP, immersion	Exposure time, solution composition, scan strategy	Cast	Smaller amount of metal released in PBS and PBS + bovine serum albumin.	OM, SEM	140
NiTi	DLD	Ringer's solution	PDP	Laser power	—	Corrosion rate decreased with the increase of laser power up to 400 W.	SEM, XRD	141
NiTi	SLM	SBF	PDP, immersion	Porosity	Conventionally produced—not specified if cast or wrought	Similar to the conventionally produced counterpart. Improved for lower porosities.	SEM, EDS, XRD	142
Inconel 718	SLM	13 wt% NaCl—80°C	OCP, PDP	Build direction	Conventionally produced—not specified if cast or wrought. Age hardened	Inferior to conventionally produced counterpart. Not affected by build orientation.	—	143
Mg-Zn-Zr	SLM	Hank's solution	Immersion test—hydrogen volume evolution rate	Laser input energy density	—	Corrosion apparently optimized for laser energy density of 600 J/mm^2.	OM, SEM, EDS, XRD	144
Mg WE43	SLM	SBF + 5% fetal bovine serum	Immersion, OCP, PDP	Exposure time	—	Corrosion rates slightly decreased after 14 d.	OM, SEM, EDS, XRD	145
Cu-30Ni	DLD	ASTM G31	Weight loss	Composition gradient—from C71500 substrate to DLD Cu-30 Ni	—	Inferior to C71500 substrate. Superior on the C71500/DLD Cu-30Ni interface than on the DLD Cu-30Ni.	OM, SEM, XRD, TEM	146

(*continued*)

TABLE 7 (*Continued*)

Alloy	AM Technique	Environment	Corrosion Characterization	Corrosion as a Function of	Comparison with Wrought/Cast Counterpart	AM Alloy Corrosion Characteristics	Microstructure Characterization	References
CoCrFeNiTi—HEA	EBM	3.5 wt% NaCl—80°C	PDP	Heat treatment	—	Superior for water quenched than for air cooled.	SEM, EDS, XRD, TEM	147
AlCoCrFeNi—HEA	DLD	0.6 M NaCl	PDP	Heat treatment	Comparison with 304L stainless steel	Corrosion rate decreased with heat treatment at 1,200°C for 168 h. Corrosion resistance inferior to Type 304L stainless steel.	SEM, EDS, XRD, EBSD, TEM, APT	148

(A) HEA: high entropy alloy; SBF: simulated body fluid; OCP: open-circuit potential; PDP: potentiodynamic polarization; OM: optical microscopy; SEM: scanning electron microscopy; TEM: transmission electron microscopy; XRD: x-ray diffractometry; EDS: energy dispersive spectroscopy; EBSD: electron backscatter diffraction; APT: atom probe tomography, and XPS: x-ray photoelectron spectroscopy.

respectively. Marattukalam, et al.,[141] aimed to further improve the corrosion resistance of SLM NiTi by altering the laser power and scan speed utilized during the manufacturing process. The increase of laser power from 200 W to 400 W did not affect the i_{corr} of SLM NiTi in Ringer's physiological solution for scan speeds of 10 mm/s and 20 mm/s. The E_{corr} values moved toward nobler values by approximately 100 mV_{SCE} for the SLM NiTi produced with scan speed of 20 mm/s, in comparison with the specimens produced with scan speed of 10 mm/s. The increase of laser power also increased the E_{corr} of the SLM NiTi specimens by ~30% for both laser scan speeds. Although the corrosion resistance could be improved by the laser scan strategy, no comparison was performed with conventionally produced NiTi alloys. Ibrahim, et al.,[142] analyzed the effect of porosity on the corrosion of DLD NiTi by measuring the Ni ion release after immersion in SBF for 3 d. The conventionally fabricated NiTi and dense DLD NiTi (porosity not provided) presented similar Ni ion release of 59.45 ppb and 64 ppb, respectively. The porous DLD NiTi was produced with porosities of 15, 25, 35, and 50% and presented Ni ion release of 127.94, 176.35, 194.3, and 196.8 ppb, respectively. Therefore, the increase of porosity enhanced the susceptibility of DLD NiTi to corrode in SBF.

Sarmiento Klapper, et al.,[143] reported the corrosion performance of SLM 718 in a highly corrosive environment containing 13 wt% NaCl solution at 80°C. The SLM 718 was also produced with different build orientations to analyze their effect on corrosion. The resistance to pitting of SLM 718 was found to be inferior to the conventionally produced counterpart (not specified if wrought or cast). The E_{pit} of the conventionally produced Alloy 718 presented an average value of 416 mV_{SHE}, whereas a large amount of scatter was detected for the E_{pit} of the SLM 718 with potentials varying approximately from 250 mV_{SHE} to 450 mV_{SHE}. The build direction did not appear to affect the overall corrosion characteristics of the SLM 718 in the studied environment.

Shuai, et al.,[144] reported successful production of a SLM Mg-Zn-Zr (ZK60 [UNS M16600]) alloy, and the corrosion performance was subsequently investigated in Hank's solution. The laser input energy density was varied in order to optimize the corrosion performance of the SLM ZK60. The hydrogen evolution rate reflecting on the alloy dissolution was optimal for the SLM Mg-Zn-Zr specimens produced with energy densities of 600 J/mm^3 (0.006 $mL \cdot cm^{-2} \cdot h^{-1}$). The cast ZK60 presented significant higher hydrogen evolution rate of 0.154 $mL \cdot cm^{-2} \cdot h^{-1}$, hence lower resistance to corrosion than the SLM ZK60. The corrosion of Mg WE43 (UNS M18430) produced by SLM was investigated by Li, et al.,[145] in SBF + 5% fetal bovine serum. The specimens were assessed by measuring the hydrogen (H_2) release over 28 d immersion and by potentiodynamic polarization at different exposure intervals over 14 d. The temporal evolution of hydrogen release presents a linear slope over the analysis period, suggesting a constant corrosion rate during the exposure test. The potentiodynamic polarization of the SLM Mg WE43 showed a maximum i_{corr} of ~0.6 $\mu A/cm^2$ after 1 d of exposure, which was reduced to approximately 0.2 $\mu A/cm^2$ after 14 d. Li, et al., suggest that the formation of calcium (Ca), Mg, and phosphorus (P) products were responsible for the reduction of corrosion current density over time during the electrochemical testing, which is not atypical in such an SBF electrolyte.

The corrosion of DLD Cu-30Ni was investigated by Bhattacharya, et al.,[146] following ASTM Standard G31. The blown powder composition was gradually altered from the substrate composition of C71500 to Cu-30Ni. Bhattacharya, et al.,[146] report that the C71500 presented the lowest corrosion rate (0.08 mpy), whereas the DLD Cu-30Ni (i.e., 100% Cu-30Ni) presented the highest corrosion rate (0.36 mpy). The lower corrosion resistance was associated to the high porosity levels on the DLD Cu-30Ni.

There are limited studies on the corrosion of AM-prepared HEAs; however, the corrosion of HEAs produced by EBM and DLD were reported by Fujieda, et al.,[147] and Wang, et al.,[148] respectively. The EBM CoCrFeNiTi was analyzed for the effect of heat treatment on corrosion performance in 3.5 wt% NaCl at 80°C.[147] Water quenching post air exposure at 1,120°C for 3 h was observed to improve the resistance to pitting of the EBM CoCrFeNiTi from the as-built condition. However, a corrosion comparison between the EBM CoCrFeNiTi with their cast or wrought counterparts was not performed. Wang, et al.,[148] investigated the corrosion of DLD AlCoCrFeNi in 0.6 M NaCl solution for different heat treatments and also compared the results with the corrosion performance of Type 304L stainless steel for reference. The DLD AlCoCrFeNi resistance to pitting was enhanced for aging at 1,200°C; however, the overall corrosion performance was inferior to Type 304L stainless steels.

Given the great interest in AM at present, the variety of alloys produced by AM is, almost daily, extending beyond the number of investigations reviewed herein. Such emerging studies have been identified as necessary, as the review herein has identified that there exist numerous knowledge gaps in the context of all of the alloy systems and variables reviewed.

KNOWLEDGE GAPS AND FUTURE WORK

The review herein has indicated that corrosion has been considered in a number of studies that are concerned with AM metallic alloys. In many cases, the studies have been quite specific and not systematic, or of insufficient depth (in terms of the subject of

corrosion) to provide general findings. As a consequence, the following points may be made.

- Corrosion studies of AM-prepared alloys to date have investigated corrosion in a vast range of electrolytes, with different compositions and different pH, making cross-study comparisons (even for the same alloys) difficult.
- Similarly, studies to date have investigated corrosion using a range of different corrosion test methods (such as polarization testing, impedance spectroscopy, exposure followed by electron microscopy, etc.), making cross-study comparisons (even for the same alloys) difficult.
- Of the studies reviewed herein, there is a vast range of AM process parameters utilized. Various laser powers, scan speeds, etc., were used even for the same alloy on the same AM instrument, and indeed the variations were even more vast factoring in the variety of AM instruments utilized in the works reported in this review
- Following on the preceding point, there is an obvious lack of standards for which baseline or standardized tests are executed. This situation is not only the case for the corrosion testing itself, but for the AM process.
- A number of studies present results for alloys that have a wrought (or cast) counterpart, while others do not compare the AM sample with the fully dense wrought (or cast) counterpart. The latter means that the rationalization of conclusions is weakened. Furthermore, there are instances where comparison of alloys has been performed when the AM-prepared alloy is not from the same alloy or powder.
- There are, in some cases, studies where feedstock powders have been either argon- or nitrogen-atomized, and build chambers either argon- or nitrogen-purged, making the matrix of variables that may influence the final consolidated component rather vast (even for the same alloy produced).
- There exist very limited data on the EAC of AM-prepared alloys. Similarly, there are very limited data relating to the exposure of AM-prepared alloys to nuclear conditions.
- Similarly, there is a distinct lack of information on hydrogen effects for AM-prepared metals and alloys.
- To date, there are essentially no reports of "very long-term" exposure, such as the data that are available from exposure site testing, or from extended test periods (i.e., beyond many weeks and into the relevant exposure timescale of months and years).
- In essentially all studies, the results (and conclusions) are "pigeon-holed," in the sense that there is little or no attempt to generalize findings from critical appraisal of accompanying literature, or by including supplementary testing to compare with the conditions in like studies.
- The study of corrosion of AM-prepared Al alloys has been limited to the Al-Si alloy system to date.
- There have been no studies that have studied corrosion on the range of length scales that correspond to the length scale of AM microstructures, or defects as outlined in Figure 4. Not all studies have presented results with "control materials" or relationships to model materials, meaning a fundamental understanding of key factors in AM alloy corrosion are yet to be determined.
- The literature has a lack of separation of variables; i.e., it is complex to generate trends from changes in porosity and chemistry simultaneously.
- The understanding and control of surface finish is essential for a wide range of applications. However, the surface finish of AM-produced alloys has yet to be optimized during production, while post processing also remains a nascent field with little progress to date.

Based on the above points, it is clear that there exists significant future work to be executed in the broader understanding related to the corrosion of AM-prepared metals and alloys. One means by which this could be accelerated is by standardized testing procedures (which may be aided by professional bodies, such as ASTM in the United States or any equivalent), and by relating the corrosion observed to key microstructural (i.e., deterministic) features where possible. Separation of variables and systematic studies are also recommended. A coherent understanding of the corrosion of AM-prepared metals and alloys will be essential in the assessment of novel or emerging "AM-only" alloys, for which there is no benefit of a cast or wrought counterpart to compare.

SUMMARY

It is clear from the numerous works reviewed herein, in the context of corrosion but also more generally in the context of AM, that a range of unique microstructural defects can form in metals/alloys. Such microstructural defects are distinct in comparison with those of cast or wrought alloys, and span many orders of magnitude in length scale. Defects such as solute segregation or dislocation networks are on the order of atoms/nanometers, while porosity or cracking can be micrometer to millimeter scale, and residual stress can be on the scale of meters.

It was revealed that many alloys are capable of being successfully produced by AM processes. It is also possible to make the very general—and in the context of this review, extremely important—statement that the vast majority of studies revealed that corrosion

performance was affected for AM-prepared alloys and is not identical to performance in wrought counterparts. As a consequence, AM plays a significant role in corrosion performance. There are in some cases beneficial outcomes, such as increased pitting resistance in austenitic stainless steels, while in the case of Ti alloys, the influence of AM was overall minimal. Conversely, there are numerous examples of detrimental influences arising from AM, and high variability in findings (such as in the case of Al-Si alloys reviewed herein).

Overall, there are significant prospects for AM to contribute to the development of durable alloys, and the prospect of new and superior alloys. In general, the metallurgy of AM-prepared alloys is also in need of deeper fundamental understanding, with evidence of metastable phases in AM alloys, and rapid solidification microstructures (and associated phases) revealed.

The number of unique variables in the AM process that may influence corrosion is high with many degrees of freedom, ranging from laser power to build orientation to name but a few, that challenge straightforward identification of structure property relationships—and at this stage a unified (or holistically meaningful) understanding is difficult to obtain. In order to approach a unified understanding, the need for standards—not only standardized testing, but also standards in specimen preparation—is critical.

ACKNOWLEDGMENTS

ST and NB gratefully acknowledge financial support from the Office of Naval Research (ONR) and Office of Naval Research Global (with Dr. Airan Perez and Dr. Pae Wu as Scientific Officers). JRS and RGK also acknowledge support from the ONR (with Dr. Airan Perez and contract monitor). The work was also supported by Woodside Energy and the Pump Priming Scheme (Advanced Engineering Platform, Monash University Malaysia).

REFERENCES

1. P. Kocovic, "History of Additive Manufacturing," in *3D Printing and Its Impact on the Production of Fully Functional Components: Emerging Research and Opportunities* (Hershey, PA: IGI Global, 2017), p. 1-24.
2. D.R. Eyers, A.T. Potter, *Comput. Ind.* 92-93 (2017): p. 208-218.
3. T. Kellner, "An Epiphany of Disruption: GE Additive Chief Explains How 3D Printing Will Upend Manufacturing," *GE Reports*, November 13, 2017, https://www.ge.com/reports/epiphany-disruption-ge-additive-chief-explains-3d-printing-will-upend-manufacturing/ (June 4, 2018).
4. P. Han, *Engineering* 3 (2017): p. 648-652.
5. M. Van Dusen, "GE's 3D-Printed Airplane Engine Will Run This Year," *GE Reports*, June 19, 2017, https://www.ge.com/reports/mad-props-3d-printed-airplane-engine-will-run-year/ (Aug. 8, 2018).
6. L.E. Murr, S.M. Gaytan, D.A. Ramirez, E. Martinez, J. Hernandez, K.N. Amato, P.W. Shindo, F.R. Medina, R.B. Wicker, *J. Mater. Sci. Technol.* 28 (2012): p. 1-14.
7. L.E. Murr, E. Martinez, K.N. Amato, S.M. Gaytan, J. Hernandez, D.A. Ramirez, P.W. Shindo, F. Medina, R.B. Wicker, *J. Mater. Res. Technol.* 1 (2012): p. 42-54.
8. H. Gong, K. Rafi, H. Gu, T. Starr, B. Stucker, *Addit. Manuf.* 1-4 (2014): p. 87-98.
9. J.J. Lewandowski, M. Seifi, *Annu. Rev. Mater. Res.* 46 (2016): p. 151-186.
10. "Additive Fabrication: Direct Metal Laser Sintering," *CustomPart.Net*, 2018, https://www.custompartnet.com/wu/direct-metal-laser-sintering (Oct. 21, 2018).
11. H. Shipley, D. McDonnell, M. Culleton, R. Coull, R. Lupoi, G. O'Donnell, D. Trimble, *Int. J. Machine Tools. Manuf.* 128 (2018): p. 1-20.
12. P.K. Gokuldoss, S. Kolla, J. Eckert, *Materials (Basel)* 10 (2017): p. 672.
13. V. Bhavar, P. Kattire, V. Patil, S. Khot, K. Gujar, R. Singh, "A Review on Powder Bed Fusion Technology of Metal Additive Manufacturing," 4th Int. Conf. Exhib. On Additive Manufacturing Technologies, held September 1-2, 2014 (Banglore, India: AMSI, 2014).
14. M. Mani, B.M. Lane, M.A. Donmez, S.C. Feng, S.P. Moylan, *Int. J. Prod. Res.* 55 (2017): p. 1400-1418.
15. W.J. Sames, F.A. List, S. Pannala, R.R. Dehoff, S.S. Babu, *Int. Mater. Rev.* 61 (2016): p. 315-360.
16. D. Herzog, V. Seyda, E. Wycisk, C. Emmelmann, *Acta Mater.* 117 (2016): p. 371-392.
17. J. Suryawanshi, K.G. Prashanth, S. Scudino, J. Eckert, O. Prakash, U. Ramamurty, *Acta Mater.* 115 (2016): p. 285-294.
18. K.G. Prashanth, J. Eckert, *J. Alloy. Compd.* 707 (2017): p. 27-34.
19. T. DebRoy, H.L. Wei, J.S. Zuback, T. Mukherjee, J.W. Elmer, J.O. Milewski, A.M. Beese, A. Wilson-Heid, A. De, W. Zhang, *Prog. Mater. Sci.* 92 (2018): p. 112-224.
20. W.M. Tucho, V.H. Lysne, H. Austbø, A. Sjolyst-Kverneland, V. Hansen, *J. Alloy. Compd.* 740 (2018): p. 910-925.
21. S. Gorsse, C. Hutchinson, M. Gouné, R. Banerjee, *Sci. Technol. Adv. Mater.* 18 (2017): p. 584-610.
22. B. Vayre, F. Vignat, F. Villeneuve, *Mech. Ind.* 13 (2012): p. 89-96.
23. M.F. Zaeh, M. Ott, *CIRP Ann.—Manuf. Technol.* 60 (2011): p. 259-262.
24. D.D. Gu, W. Meiners, K. Wissenbach, R. Poprawe, *Int. Mater. Rev.* 57 (2012): p. 133-164.
25. H. Gu, H. Gong, D. Pal, K. Rafi, T. Starr, B. Stucker, "Influences of Energy Density on Porosity and Microstructure of Selective Laser Melted 17- 4PH Stainless Steel," Solid Freeform Fabrication Proc. (Austin, TX: University of Texas, 2013), p. 474-489.
26. Q. Jia, D. Gu, *J. Alloy. Compd.* 585 (2014): p. 713-721.
27. S.M. Yusuf, N. Gao, *Mater. Sci. Technol.* 33 (2017): p. 1269-1289.
28. X. Gong, T. Anderson, K. Chou, "Review on Powder-Based Electron Beam Additive Manufacturing Technology," ASME/ISCIE 2012 Int. Symp. on Flexible Automation (New York, NY: ASME, 2012), p. 507.
29. S.A. Khairallah, A.T. Anderson, A. Rubenchik, W.E. King, *Acta Mater.* 108 (2016): p. 36-45.
30. K.G. Prashanth, S. Scudino, J. Eckert, *Acta Mater.* 126 (2017): p. 25-35.
31. N. Shamsaei, A. Yadollahi, L. Bian, S.M. Thompson, *Addit. Manuf.* 8 (2015): p. 12-35.
32. G.K. Lewis, E. Schlienger, *Mater. Des.* 21 (2000): p. 417-423.
33. S.W. Williams, F. Martina, A.C. Addison, J. Ding, G. Pardal, P. Colegrove, *Mater. Sci. Technol.* 32 (2016): p. 641-647.
34. R. Koike, I. Unotoro, Y. Kakinuma, T. Aoyama, Y. Oda, T. Kuriya, M. Fujishima, *Procedia Manuf.* 14 (2017): p. 105-110.
35. Q. Chao, T. Guo, T. Jarvis, X. Wu, P. Hodgson, D. Fabijanic, *Surf. Coatings Technol.* 332 (2017): p. 440-451.
36. W.E. Frazier, *J. Mater. Eng. Perform.* 23 (2014): p. 1917-1928.
37. T. Majumdar, N. Eisenstein, J.E. Frith, S.C. Cox, N. Birbilis, *Adv. Eng. Mater.* 20 (2018): p. 1800172.
38. D. Kotoban, A. Nazarov, I. Shishkovsky, *Procedia IUTAM* 23 (2017): p. 138-146.
39. M. Labudovic, D. Hu, R. Kovacevic, *J. Mater. Sci.* 38 (2003): p. 35-49.
40. Y. Zhang, G. Yu, X. He, *Sci. China Physics Mech. Astron.* 55 (2012): p. 1431-1438.
41. L. Song, V. Bagavath-Singh, B. Dutta, J. Mazumder, *Int. J. Adv. Manuf. Technol.* 58 (2012): p. 247-256.
42. N. Shamsaei, A. Yadollahi, L. Bian, S.M. Thompson, *Addit. Manuf.* 8 (2015): p. 12-35.
43. Y. Shang, Y. Yuan, D. Li, Y. Li, J. Chen, *Int. J. Adv. Manuf. Technol.* 92 (2017): p. 4379-4385.
44. R. Li, J. Liu, Y. Shi, M. Du, Z. Xie, *J. Mater. Eng. Perform.* 19 (2010): p. 666-671.

45. K. Guan, Z. Wang, M. Gao, X. Li, X. Zeng, *Mater. Des.* 50 (2013): p. 581-586.
46. W. Xu, E.W. Lui, A. Pateras, M. Qian, M. Brandt, *Acta Mater.* 125 (2017): p. 390-400.
47. P. Wang, B. Zhang, C.C. Tan, S. Raghavan, Y.-F. Lim, C.-N. Sun, J. Wei, D. Chi, *Mater. Des.* 112 (2016): p. 290-299.
48. M. Tang, P.C. Pistorius, *Int. J. Fatigue* 94 (2017): p. 192-201.
49. P. Wang, H.C. Li, K.G. Prashanth, J. Eckert, S. Scudino, *J. Alloy. Compd.* 707 (2017): p. 287-290.
50. P. Guo, B. Zou, C. Huang, H. Gao, *J. Mater. Process. Technol.* 240 (2017): p. 12-22.
51. Z. Wang, T.A. Palmer, A.M. Beese, *Acta Mater.* 110 (2016): p. 226-235.
52. Y. Zhai, H. Galarraga, D.A. Lados, *Procedia Eng.* 114 (2015): p. 658-666.
53. P. Wang, W. Sin, M. Nai, J. Wei, *Materials* 10 (2017): p. 1121.
54. P. Wang, X. Tan, M. Ling, S. Nai, S. Tor, J. Wei, *Mater. Des.* 95 (2016): p. 287-295.
55. R.R. Dehoff, M.M. Kirka, W.J. Sames, H. Bilheux, A.S. Tremsin, L.E. Lowe, S.S. Babu, *Mater. Sci. Technol.* 31 (2015): p. 931-938.
56. E. Liverani, S. Toschi, L. Ceschini, A. Fortunato, *J. Mater. Process. Technol.* 249 (2017): p. 255-263.
57. I. Todd, *Nature* 549 (2017): p. 342-343.
58. J.H. Martin, B.D. Yahata, J.M. Hundley, J.A. Mayer, T.A. Schaedler, T.M. Pollock, *Nature* 549 (2017): p. 365-369.
59. J.A. Cherry, H.M. Davies, S. Mehmood, N.P. Lavery, S.G.R. Brown, J. Sienz, *Int. J. Adv. Manuf. Technol.* 76 (2014): p. 869-879.
60. D. Wang, Y. Liu, Y. Yang, D. Xiao, *Rapid Prototyp. J.* 22 (2016): p. 706-716.
61. G. Sander, S. Thomas, V. Cruz, M. Jurg, N. Birbilis, X. Gao, M. Brameld, C.R. Hutchinson, *J. Electrochem. Soc.* 164 (2017): p. C250-C257.
62. A. TakaichiSuyalatu, T. Nakamoto, N. Joko, N. Nomura, Y. Tsutsumi, S. Migita, H. Doi, S. Kurosu, A. Chiba, N. Wakabayashi, Y. Igarashi, T. Hanawa, *J. Mech. Behav. Biomed. Mater.* 21 (2013): p. 67-76.
63. M. Zhang, Y. Yang, C. Song, Y. Bai, Z. Xiao, *J. Alloy. Compd.* 750 (2018): p. 878-886.
64. Q. Chao, V. Cruz, S. Thomas, N. Birbilis, P. Collins, A. Taylor, P.D. Hodgson, D. Fabijanic, *Scrip. Mater.* 141 (2017): p. 94-98.
65. Y. Liu, Y. Yang, D. Wang, *Int. J. Adv. Manuf. Technol.* 87 (2016): p. 647-656.
66. P. Mercelis, J. Kruth, *Rapid Prototyp. J.* 12 (2006): p. 254-265.
67. M.K. Alam, A. Edrisy, J. Urbanic, J. Pineault, *J. Mater. Eng. Perform.* 26 (2017): p. 1076-1084.
68. F. Xie, X. He, S. Cao, M. Mei, X. Qu, *Electrochim. Acta* 105 (2013): p. 121-129.
69. X. Gong, Y. Cui, D. Wei, B. Liu, R. Liu, Y. Nie, Y. Li, *Corros. Sci.* 127 (2017): p. 101-109.
70. L.E. Murr, *Metallogr. Microstruct. Anal.* 7 (2018): p. 103-132.
71. W. Xu, M. Brandt, S. Sun, J. Elambasseril, Q. Liu, K. Latham, K. Xia, M. Qian, *Acta Mater.* 85 (2015): p. 74-84.
72. Y. Tian, D. McAllister, H. Colijn, M. Mills, D. Farson, M. Nordin, S. Babu, *Metall. Mater. Trans. A* 45 (2014): p. 4470-4483.
73. R.F. Schaller, J.M. Taylor, J. Rodelas, E.J. Schindelholz, *Corrosion* 73 (2017): p. 796-807.
74. Y. Sun, A. Moroz, K. Alrbaey, *J. Mater. Eng. Perform.* 23 (2014): p. 518-526.
75. K. Geenen, A. Röttger, W. Theisen, *Mater. Corros.* 68 (2017): p. 764-775.
76. X. Lou, M. Song, P.W. Emigh, M.A. Othon, P.L. Andresen, *Corros. Sci.* 128 (2017): p. 140-153.
77. X. Lou, P.L. Andresen, R.B. Rebak, *J. Nucl. Mater.* 499 (2018): p. 182-190.
78. Z. Sun, X. Tan, S.B. Tor, W.Y. Yeong, *Mater. Des.* 104 (2016): p. 197-204.
79. M. Cabrini, S. Lorenzi, T. Pastore, S. Pellegrini, M. Pavese, P. Fino, E.P. Ambrosio, F. Calignano, D. Manfredi, *Surf. Interface Anal.* 48 (2016): p. 818-826.
80. M. Ziętala, T. Durejko, M. Polański, I. Kunce, T. Płociński, W. Zieliński, M. Łazińska, W. Stępniowski, T. Czujko, K.J. Kurzydłowski, Z. Bojar, *Mater. Sci. Eng. A* 677 (2016): p. 1-10.
81. S.K. Kairy, O. Gharbi, J. Nicklaus, D. Jiang, C.R. Hutchinson, N. Birbilis, "On the Characterisation of a Hitherto Unreported Icosahedral Quasicrystal Phase in Additively Manufactured Aluminium Alloy AA7075," preprint (2018): arXiv:1808.05033v1.
82. W.S.W. Harun, R.I.M. Asri, F.R.M. Romlay, S. Sharif, N.H.M. Jan, F. Tsumori, *J. Alloy. Compd.* 748 (2018): p. 1044-1052.
83. X. Lou, M.A. Othon, R.B. Rebak, *Corros. Sci.* 127 (2017): p. 120-130.
84. N. Dai, L.C. Zhang, J. Zhang, X. Zhang, Q. Ni, Y. Chen, M. Wu, C. Yang, *Corros. Sci.* 111 (2016): p. 703-710.
85. A. Hemmasian Ettefagh, S. Guo, *Addit. Manuf.* 22 (2018): p. 153-156.
86. J.R. Trelewicz, G.P. Halada, O.K. Donaldson, G. Manogharan, *JOM* 68 (2016): p. 850-859.
87. K.D. Ralston, N. Birbilis, *Corrosion* 66 (2010): p. 0750051-01 to 075005-13.
88. R.I. Revilla, J. Liang, S. Godet, I. De Graeve, *J. Electrochem. Soc.* 164 (2017): p. C27-C35.
89. A. Leon, A. Shirizly, E. Aghion, *Metals (Basel)* 6 (2016): p. 148.
90. A. Leon, E. Aghion, *Mater. Charact.* 131 (2017): p. 188-194.
91. P. Fathi, M. Mohammadi, X. Duan, A.M. Nasiri, *J. Mater. Process. Technol.* 259 (2018): p. 1-14.
92. M. Cabrini, S. Lorenzi, T. Pastore, S. Pellegrini, E.P. Ambrosio, F. Calignano, D. Manfredi, M. Pavese, P. Fino, *Electrochim. Acta* 206 (2016): p. 346-355.
93. M. Cabrini, S. Lorenzi, T. Pastore, S. Pellegrini, D. Manfredi, P. Fino, S. Biamino, C. Badini, *J. Mater. Process. Technol.* 231 (2016): p. 326-335.
94. K.G. Prashanth, B. Debalina, Z. Wang, P.F. Gostin, A. Gebert, M. Calin, U. Kühn, M. Kamaraj, S. Scudino, J. Eckert, *J. Mater. Res.* 29 (2014): p. 2044-2054.
95. P. Ganesh, R. Giri, R. Kaul, P. Ram Sankar, P. Tiwari, A. Atulkar, R.K. Porwal, R.K. Dayal, L.M. Kukreja, *Mater. Des.* 39 (2012): p. 509-521.
96. Y. Zhang, F. Liu, J. Chen, Y. Yuan, *J. Laser Appl.* 29 (2017): p. 022306.
97. J. Stendal, O. Fergani, H. Yamaguchi, N. Espallargas, *J. Bio-Tribo-Corros.* 4 (2018): p. 9.
98. E. De Bruycker, M.L.M. Sistiaga, F. Thielemans, K. Vanmeenseel, *Mater. Sci. Appl.* 8 (2017): p. 223-233.
99. X. Chen, J. Li, X. Cheng, H. Wang, Z. Huang, *Mater. Sci. Eng. A* 715 (2018): p. 307-314.
100. H. Zhang, C.H. Zhang, Q. Wang, C.L. Wu, S. Zhang, J. Chen, A.O. Abdullah, *Opt. Laser Technol.* 101 (2018): p. 363-371.
101. M.R. Stoudt, R.E. Ricker, E.A. Lass, L.E. Levine, *JOM* 69 (2017): p. 506-515.
102. D.P. Schmidt, E. Jelis, M.P. Clemente, N.M. Ravindra, "Corrosion of 3D Printed Steel," Materials Science & Technology Conf. 2015 (Columbus, OH: MS and T, 2015), p. 93-100.
103. C.S. Lefky, B. Zucker, A.R. Nassar, T.W. Simpson, J. Owen, *Acta Mater.* 153 (2018): p. 1-7.
104. M. Wiesener, K. Peters, A. Taube, A. Keller, K.P. Hoyer, T. Niendorf, G. Grundmeier, *Mater. Corros.* 68 (2017): p. 1028-1036.
105. G.T. Burstein, C. Liu, R.M. Souto, S.P. Vines, *Corros. Eng. Sci. Technol.* 39 (2004): p. 25-30.
106. J. Stewart, D.E. Williams, *Corros. Sci.* 33 (1992): p. 457-474.
107. M.P. Ryan, D.E. Williams, R.J. Chater, B.M. Hutton, D.S. McPhail, *Nature* 415 (2002): p. 770-774.
108. I. Muto, D. Ito, N. Hara, *J. Electrochem. Soc.* 156 (2009): p. C55.
109. D.E. Williams, M.R. Kilburn, J. Cliff, G.I.N. Waterhouse, *Corros. Sci.* 52 (2010): p. 3702-3716.
110. A.J. Sedriks, *Corrosion of Stainless Steels*, 2nd ed. (Hoboken, NJ: John Wiley & Sons, 1996).
111. N. Alharthi, E.S.M. Sherif, H.S. Abdo, S.Z. El Abedin, *Adv. Mater. Sci. Eng.* 2017 (2017): p. 1893672.
112. S. Szklarska-Smialowska, "Effect of Internal Factors on Pitting," in *Pitting Corrosion of Metals* (Houston, TX: NACE International, 1986), p. 143-144.
113. N. Dai, J. Zhang, Y. Chen, L.-C. Zhang, *J. Electrochem. Soc.* 164 (2017): p. C428-C434.
114. P. Chandramohan, S. Bhero, B.A. Obadele, P.A. Olubambi, *Int. J. Adv. Manuf. Technol.* 92 (2017): p. 3051-3061.
115. L.Y. Chen, J.C. Huang, C.H. Lin, C.T. Pan, S.Y. Chen, T.L. Yang, D.Y. Lin, H.K. Lin, J.S.C. Jang, *Mater. Sci. Eng. A* 682 (2017): p. 389-395.
116. J.J. de Damborenea, M.A. Arenas, M.A. Larosa, A.L. Jardini, C.A. de Carvalho Zavaglia, A. Conde, *Appl. Surf. Sci.* 393 (2017): p. 340-347.
117. Y. Xu, Y. Lu, K.L. Sundberg, J. Liang, R.D. Sisson, *J. Mater. Eng. Perform.* 26 (2017): p. 2572-2582.
118. J. Yang, H. Yang, H. Yu, Z. Wang, X. Zeng, *Metall. Mater. Trans. A* 48 (2017): p. 3583-3593.
119. T. Chiu, M. Mahmoudi, W. Dai, A. Elwany, H. Liang, H. Castaneda, *Electrochim. Acta* 279 (2018): p. 143-151.
120. M. Buciumeanu, A. Bagheri, N. Shamsaei, S.M. Thompson, F.S. Silva, B. Henriques, *Tribol. Int.* 119 (2018): p. 381-388.
121. D.H. Abdeen, B.R. Palmer, *Rapid Prototyp. J.* 22 (2016): p. 322-329.

122. E. Almanza, M.J. Pérez, N.A. Rodríguez, L.E. Murr, *J. Mater. Res. Technol.* 6 (2017): p. 251-257.
123. Y. Bai, X. Gai, S. Li, L.C. Zhang, Y. Liu, Y. Hao, X. Zhang, R. Yang, Y. Gao, *Corros. Sci.* 123 (2017): p. 289-296.
124. D. Devika, S.S. Dass, S. Kumar Chaudhary, *J. Biomimetics Biomater. Biomed. Eng.* 22 (2015): p. 63-75.
125. B. Zhao, H. Wang, N. Qiao, C. Wang, M. Hu, *Mater. Sci. Eng. C* 70 (2017): p. 832-841.
126. L. Liu, M. He, X. Xu, C. Zhao, Y. Gan, J. Lin, J. Luo, J. Lin, *Mater. Sci. Eng. C* 72 (2017): p. 631-640.
127. R.M. Mahamood, E.T. Akinlabi, *Mater. Sci.* 53 (2017): p. 76-85.
128. F. Xie, X. He, Y. Lv, M. Wu, X. He, X. Qu, *Corros. Sci.* 95 (2015): p. 117-124.
129. Y. Chen, J. Zhang, N. Dai, P. Qin, H. Attar, L.C. Zhang, *Electrochim. Acta* 232 (2017): p. 89-97.
130. K. Majchrowicz, Z. Pakieła, D. Moszczyńska, T. Kurzynowski, E. Chlebus, *Oxid. Met.* 90 (2017): p. 83-96.
131. A. Mohammad, A.M. Al-Ahmari, V.K. Balla, M. Das, S. Datta, D. Yadav, G.D. Janaki Ram, *Mater. Des.* 133 (2017): p. 186-194.
132. J.L. Wang, R.L. Liu, T. Majumdar, S.A. Mantri, V.A. Ravi, R. Banerjee, N. Birbilis, *Acta Biomater.* 54 (2017): p. 469-478.
133. X.Z. Xin, J. Chen, N. Xiang, B. Wei, *Cell Biochem. Biophys.* 67 (2013): p. 983-990.
134. X.Z. Xin, N. Xiang, J. Chen, D. Xu, B. Wei, *J. Mater. Sci.* 47 (2012): p. 4813-4820.
135. X.Z. Xin, J. Chen, N. Xiang, Y. Gong, B. Wei, *Dent. Mater.* 30 (2014): p. 263-270.
136. F. Alifui-Segbaya, J. Lewis, D. Eggbeer, R.J. Williams, *Rapid Prototyp. J.* 21 (2015): p. 111-116.
137. Y. Lu, Y. Gan, J. Lin, S. Guo, S. Wu, J. Lin, *Rapid Prototyp. J.* 23 (2017): p. 28-33.
138. K.M. Mantrala, M. Das, V.K. Balla, C. Srinivasa Rao, V.V.S. Kesava Rao, *J. Mater. Res.* 29 (2014): p. 2021-2027.
139. Z. Guoqing, Y. Yongqiang, S. Changhui, F. Fan, Z. Zimian, *J. Med. Biol. Eng.* 38 (2018): p. 76-86.
140. Y.S. Hedberg, B. Qian, Z. Shen, S. Virtanen, I. Odnevall Wallinder, *Dent. Mater.* 30 (2014): p. 525-534.
141. J.J. Marattukalam, A.K. Singh, S. Datta, M. Das, V.K. Balla, S. Bontha, S.K. Kalpathy, *Mater. Sci. Eng. C* 57 (2015): p. 309-313.
142. H. Ibrahim, A. Jahadakbar, A. Dehghan, N.S. Moghaddam, A. Amerinatanzi, M. Elahinia, *Metals (Basel)* 8 (2018): p. 164.
143. H. Sarmiento Klapper, N. Molodtsov, M. Burns, C. Wangenheim, "Critical Factors Affecting the Pitting Corrosion Resistance of Additively Manufactured Nickel Alloy in Chloride Containing Environments," CORROSION 2017, paper no. 9345 (Houston, TX: NACE, 2017).
144. C. Shuai, Y. Yang, P. Wu, X. Lin, Y. Liu, Y. Zhou, P. Feng, X. Liu, S. Peng, *J. Alloy. Compd.* 691 (2017): p. 961-969.
145. Y. Li, J. Zhou, P. Pavanram, M.A. Leeflang, L.I. Fockaert, B. Pouran, N. Tümer, K.U. Schröder, J.M.C. Mol, H. Weinans, H. Jahr, A.A. Zadpoor, *Acta Biomater.* 67 (2017): p. 378-392.
146. S. Bhattacharya, G.P. Dinda, A.K. Dasgupta, H. Natu, B. Dutta, J. Mazumder, *J. Alloy. Compd.* 509 (2011): p. 6364-6373.
147. T. Fujieda, H. Shiratori, K. Kuwabara, M. Hirota, T. Kato, K. Yamanaka, Y. Koizumi, A. Chiba, S. Watanabe, *Mater. Lett.* 189 (2017): p. 148-151.
148. R. Wang, K. Zhang, C. Davies, X. Wu, *J. Alloy. Compd.* 694 (2017): p. 971-981.

Chapter 3: On the corrosion and metastable pitting characteristics of 316L stainless steel produced by selective laser melting

Due to their established (and notionally satisfactory) resistance to corrosion in marine environments, wrought 316L is a popular choice for components in service near in marine applications, in coastal cities, etc. Although 316L is generally resistant to corrosion in marine environments (where the temperature remains below ~ 22 ºC, which is the critical pitting temperature of stainless steel 316L [22]), 316L remains vulnerable to localised corrosion. One of the main localised corrosion mechanisms that takes place in 316L components employed in the vicinity of Cl^- containing media (e.g. seawater) is chloride induced pitting. Pitting is a form of localised corrosion typical of alloys that do not undergo uniform corrosion when exposed to a humid atmosphere or aqueous environments. The susceptibility of an alloy to pitting is directly associated with their surface chemical composition and microstructure. In the context of conventionally manufactured 316L, the presence of MnS inclusions in the alloy is known to degrade the protective oxide layer on the alloy surface. These inclusions have been found to increase pitting susceptibility to the extent that low temperature pitting and even pitting in low chloride concertation are possible.

The SLM of 316L becomes an alternative manufacturing process that, by altering the microstructure and consequently the formation of MnS inclusions, could enhance the resistance of this alloy to pitting. However, porosity derived from the manufacturing process is consistently present in SLM alloys, including in 316L. The presence of pores in the bulk of 316L alloys could potentially alter their surface protective oxide layer and consequently also affect pitting.

In this chapter, the effect of SLM laser parameters on porosity was correlated to the pitting resistance of the 316L in 0.1 M sodium chloride. Initial analysis on the metastable pitting behaviour of this alloy was also investigated. The results obtained from the SLM 316L were compared to a wrought counterpart tested under the same experimental conditions.

This chapter was prepared as a paper and published in the ***Journal of The Electrochemical Society***. The paper is presented here as published.

On The Corrosion and Metastable Pitting Characteristics of 316L Stainless Steel Produced by Selective Laser Melting

G. Sander,[a,b] S. Thomas,[a,b,*,z] V. Cruz,[a,b] M. Jurg,[a,b] N. Birbilis,[a,b,**] X. Gao,[a,b] M. Brameld,[b,c] and C. R. Hutchinson[a,b]

[a]Department of Materials Science and Engineering, Monash University, Clayton, Victoria 3800, Australia
[b]Woodside Innovation Centre, Monash University, Clayton, Victoria 3800, Australia
[c]Woodside Energy, Perth WA 6000, Australia

The austenitic stainless steel 316L was additively manufactured using Selective Laser Melting (SLM). The corrosion characteristics of the additively manufactured (3D printed) specimens were investigated by both potentiodynamic and potentiostatic techniques. The production parameters were deliberately varied during SLM, to produce 316L specimens fabricated by different laser scan speed (in the range of 860–1160 mm/s) and laser power (in the range of 165–285 W). The fabrication parameters were found to influence the porosity of the resulting specimens. The pitting potentials, metastable pitting rates and repassivation potentials of the 3D printed specimens are presented herein as a function of the laser scan speed and laser power, and also discussed in the context of specimen porosity. The corrosion characteristics of the 3D printed 316L were also compared with wrought 316L, revealing higher pitting potentials and lower rates of metastable pitting for most SLM 316L specimens, the related concepts of which are discussed herein.

Manuscript submitted December 28, 2016; revised manuscript received March 13, 2017. Published March 25, 2017.

Stainless steels are a critically important class of alloy in several industries.[1] The corrosion resistance of stainless steel (SS) is attributed to the presence of alloyed chromium (> ∼11 wt%), enabling the formation of a chromium oxide (Cr_2O_3) based passive film upon the metal surface.[1–3] The addition of elements such as nickel, nitrogen, molybdenum, carbon, aluminum, copper, sulfur and selenium can modify the corrosion resistance, strength, ductility, machinability, and the phases present (and their stability) in stainless steels.[1–3] The types of stainless steel are most conveniently categorized according to their microstructure, classified as: austenitic, martensitic, ferritic and austenoferritic (duplex). Such structures are realized by specific alloying additions and metallurgical processing.[1–4] Additive manufacturing has recently been explored as a means to produce SS components in net shape,[5–7] circumventing the requirement of traditional manufacturing methods such as casting, rolling, welding, machining, forging, etc. Selective Laser Melting (SLM) is one such additive manufacturing method, which can produce dense products by laser processing of metal powders. In SLM, metal powder layers are successively fused in a layer-by-layer manner into the requisite 3D structure, employing a fiber laser.[8–11] The metallic component in essence is therefore 3D printed into the requisite shape, by additive manufacturing processes like SLM. The process takes place in chamber of well-controlled inert atmosphere (either nitrogen or argon). The primary parameters that govern the microstructure of a 3D printed specimen are the laser power and the laser scan speed, as they influence the thermal gradients and growth rate of the metal at the solid-liquid interface (in the melt pool).[12] The porosity that may develop in 3D printed specimens depends upon the heating and cooling rates of the melt pool.[13] The laser scan speed relates to the duration for which the laser beam is in contact with the metal powder, thus influencing melting and solidification. It has been observed that when the laser power is too low, the melting of metal powder may not be uniform and pores may develop in the printed structure.[14,15] Wolf et al.[16] observed that if the laser power is too high, gases may become entrapped in the printed structure, resulting in higher porosity. The mechanical properties of the 3D printed porous 316L (austenitic SS) specimens were investigated by Verlee et al.,[17] whilst there are also some initial reports of the general corrosion behavior of additively manufactured 316 (austenitic SS).[18–21]

Whilst 3D printing of metals is not new *per se*, the 3D printing of stainless steels is comparatively new, owing to the fact that the value proposition (i.e. the relative cost saving or cost benefits arising) has traditionally been greatest for the additive manufacture of Ni or Ti alloys.[22,23] As a result, there is a paucity of work related to the corrosion performance of the important alloy 316L, when produced by 3D printing. Of the very few works to date that report corrosion of 3D printed austenitic stainless steels, the outcomes are inconclusive. For example, Sun et al.[19] studied SLM 316L in 0.9% NaCl for specimens with porosities of >1.7% (in some cases as high as 6.7%), representing very high porosity levels for an engineering material. This work indicating that for the specimens tested, a slightly higher passive current density was observed in the case of 3D printed specimens. However in the same electrolyte of 0.9% NaCl, Zietala et al.[20] reported a lower passive current density in the case of 316L prepared by the LENS method, which is a blown powder laser manufacturing process. In the only other relevant report, Trelewicz[21] reported a single set of polarization scans for SLM 316L relative to wrought 316L, suggesting that SLM 316L presented 'reduced passivity' in 0.1 M HCl. However the data reported in that study does not resemble the typical polarization response of 316L in 0.1 M HCl,[24,25] the polarization response being possibly influenced by crevice corrosion. Furthermore, more extensive corrosion data or its reproducibility (either by duplicate data or testing, or by the presentation of data with error analysis or error bars) has not been presented in any works to date. There appears to be a clear knowledge gap in the literature regarding the corrosion performance of 3D printed stainless steels.

The objective of the present study was to analyze and relate the impact of the different SLM parameters - namely laser power and laser scan speed - on the porosity and the electrochemical characteristics of the 316L specimens. Such a test matrix allows the collection of a large number of data sets, on a large number of unique samples, providing a suitable overview of the corrosion performance of 3D printed 316L. The corrosion characteristics of the 3D printed specimens were also compared with commercial wrought 316L. In order to gain a deeper insight into the electrochemical response of SLM 316L, the pitting characteristics were also explored using potentiostatic testing to assess metastable pitting characteristics.

The corrosion characteristics of 3D printed SS has not previously been systematically explored as a function of laser power and laser scan speed, nor has the effect of porosity on the pitting characteristics of SS been reported. The work herein aims to both elucidate and clarify the effect of the printing parameters on the porosity and

*Electrochemical Society Member.
**Electrochemical Society Fellow.
zE-mail: sebastian.thomas@monash.edu

Table I. The SLM parameters used for manufacturing the different specimens investigated in this study.

Sample	Laser Scan Speed (mm/s)	Laser Power (W)
1	960	285
2	960	245
3	960	205
4	960	165
5	1060	285
6	1160	285
7	860	285

pitting characteristics of 316L SS, providing a reference for researchers exploring 3D printing to manufacture 316L components.

Experimental

Materials.—AISI 316L stainless steel powder with a spherical particle size distribution from 10 to 53 μm was supplied by TLS Technik GmbH (Germany). Cubic samples were manufactured using selective laser melting (SLM) using an EOS M280 (EOS GmbH, Krailling, Germany) with an Yb-fiber laser (1070 nm) having a fixed laser diameter of 100 μm and an inert nitrogen-purged atmosphere. The main laser exposure parameters of laser power and scan speed were varied for the building/printing of each unique specimen, with all other parameters held constant. In the first instance, the laser scan speed was kept fixed at 960 mm/s and the laser power was varied between 165 to 285 W. Then, the laser power was kept fixed at 285 W and the laser scan speed was varied from 860 mm/s to 1160 mm/s. All samples were produced in the same build with the distance between laser passes (hatch distance) for the core exposure was 110 μm, and the layer thickness was 40 μm. The laser power and laser scan speeds used in this study for the fabrication of different samples is shown in Table I. The specimens were taken from near the edges of each cubic sample, with the electrochemical tests and porosity measurements performed on the surface perpendicular to the build direction. Wrought 316L was sourced from Interalloy (Victoria, Australia). The chemical compositions of both the wrought 316L and powder 316L are presented in Table II.

Porosity determination.—Specimens were metallographically prepared by surface grinding to a P2500 grit surface finish, using silicon carbide paper. They were then polished to a 1 μm surface finish using diamond particle suspension and subject to ultrasonic cleaning. The polished surfaces were then observed using an optical microscope. Images were collected at different magnifications between 5–20 x and the resultant images were analyzed using the ImageJ software. The porosity of specimens were then quantified using a statistical approach from numerous images at various magnifications from each sample.

Table II. Chemical compositions of both 316L wrought and powder utilized in this study.

Element (%)	Wrought	Powder
Fe	Bulk	Bulk
Cr	16.0–18.0	17.7
Ni	10–14	10.5
Mn	0–2.0	1.7
Cu	NP	NP
Si	0–1.0	0.8
S	0–0.03	NP
Mo	2.0–3.0	2.2
Co	NP	NP
C	0–0.03	0.02
P	0–0.045	NP
N	0–0.10	NP

Np - Not provided by the manufacturer.

Cyclic potentiodynamic polarization (CPP).—Mounted specimens were successively ground to a P2000 grit finish and then thoroughly cleaned in an ultrasonic bath. Each specimen (the working electrode) was then introduced into an electrochemical flat cell, which contained a saturated calomel reference electrode (RE) and a platinum mesh counter electrode (CE). The electrolyte used was NaCl solution (0.58% w/V, 0.1 M). A dilute solution was used to minimize the localized corrosion of the SS, so that metastable pitting events may be readily recognized during analysis of the current transients from the potentiostatic tests. The CPP test was performed using a scan rate of 1 mV/s, commencing from −0.25 V (vs. OCP) to +1.0 V_{SCE}. The direction of the scan was reversed at 100 $\mu A/cm^2$. Prior to polarization, specimens were allowed to stabilize in the test electrolyte, during which the open circuit potentials (OCP) of the specimens were measured. The CPP was repeated at least 5 times for each specimen to ensure reproducibility and consistency of the collected data.

Potentiostatic testing.—The characterization of metastable pitting requires a small area of the exposed metal to the test electrolyte in order to avoid overlapping of the metastable pitting events during potentiostatic experiments.[26] Therefore, the 3D printed cubes were machined to prepare specimens with a mean area of 3 mm^2. The specimens were flush mounted in epoxy, with an electrical connection at one end. The epoxy mount/sample interface was insulated using lacquer, to prevent crevice corrosion during electrochemical tests. A conventional three-electrode set-up was used for potentiostatic experiments as per CPP, including the same electrolyte (0.1 M NaCl). The potential applied during potentiostatic was 0.1 V_{SCE} below the average pitting potential (E_{pit}) of the respective specimen, as measured by CPP. As such, samples were all tested with a fixed underpotential relative to E_{pit}, which was noted as being the most suitable manner for comparison of metastable pitting characteristics of different specimens.[27] The current transients generated by the potentiostatic experiments were monitored for 30 minutes and assessed by utilising the automated peak counting approach as presented by Cavanaugh.[28]

Scanning electron microscopy and electron backscatter diffraction.—The polished 316L specimens were characterized using a scanning electron microscope (SEM) in the secondary electron (SE) mode. EBSD images were also collected using an electron backscatter diffraction (EBSD) system. The grain size was analyzed by TSL orientation image mapping software.

Results

Effect of laser power and scan speed on porosity of 316L.—The porosities of the 3D printed specimens were determined using optical microscopy and are presented here as a function of the build parameters (Figure 1). The porosities of the specimens decreased with increasing laser power (Figure 1a), when the laser scan speed was kept fixed at 960 mm/s and the laser power varied in the range 165–285 W. In contrast, there was no specific correlation observed between the specimen porosities and the laser scan speeds, when the laser power was kept fixed at 285 W and the laser scan speed varied from 860 mm/s-1160 mm/s (Figure 1b). The effect of the laser parameters (given by the ratio, Laser Power/Laser scanning speed) on the porosities of the manufactured specimens is presented in Figure 1c. It is noted that the laser beam energy density (L_E) can be calculated as function of laser power and laser scan speed as shown in Equation 1.[5]

$$L_E\left(J/mm^2\right) = L_P/\left(L_s.L_D\right) \quad [1]$$

Where L_p is the laser power (W), L_s is the laser scan speed (mm/s) and L_D is the laser diameter (mm). Sample 4 which was prepared with the lowest laser power (165 W) was found to have the highest porosity (at 0.4%). Sample 7, prepared with the highest laser power (285 W)

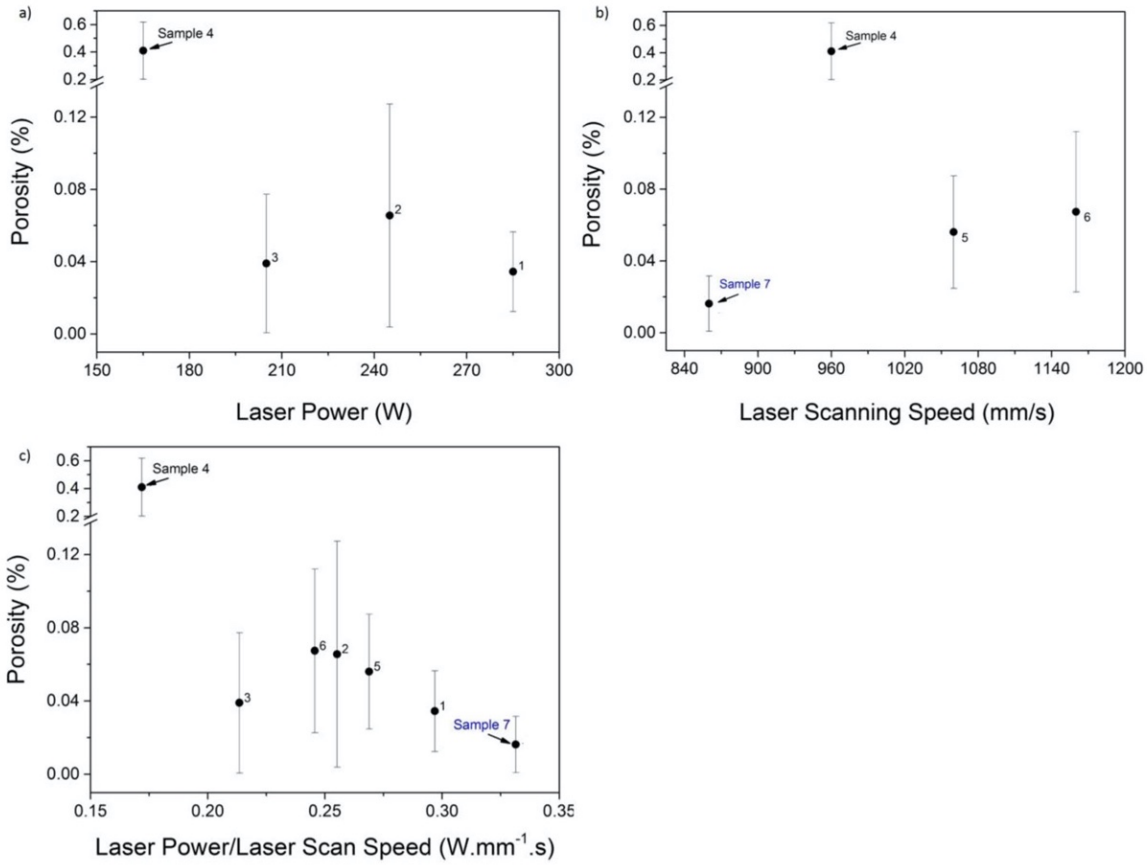

Figure 1. The porosities of SLM 316L specimens as determined using optical microscopy, for specimens manufactured using different fabrication parameters. a) Porosity variation for specimens prepared using different laser power (165–285 W) and a ***fixed*** laser scanning speed (960 mm/s). b) Porosity variation for specimens prepared using different laser scanning speeds (860–1160 mm/s) and a ***fixed*** laser power (285 W). c) The variation of specimen porosity as a function of the ratio of laser power to laser scan speed. The porosities of Sample 4 and Sample 7 are specifically indicated in the figure. The sample numbers are presented beside the porosity values of the respective specimen.

and the lowest scan speed exhibited the lowest porosity (<0.03%) (Figure 1).

The optical images of both Sample 4 and Sample 7 are shown in Figure 2. The SEM images and EBSD orientation maps corresponding to both these specimens are also presented in Figures 3–4. The SEM images reveal that both specimens are replete with sub-micron sized pores, with diameters < 1 μm (Figures 3a and Figure 4a). The optical images reveal the presence of much larger pores, with diameters > 10 μm (Figure 2). The impact of sub-micron sized pores on the determination of porosity is numerically less significant than the contribution from larger pores, and so the specimen porosities reported are dominated by the large pores (viz. > 10 μm) as detected from optical imaging alone. Quantitatively, Sample 4 presented a higher distribution of large pores with diameters > 10 μm, when compared with Sample 7 (Figure 2). The EBSD images reveal the relative grain sizes in both the specimens (Figures 3–4). For each specimen, the grain size is relatively uniform, indicating successful building. Furthermore, whilst not evident from the IPF maps, the phase identification revealed that samples were fully austenitic (single phase).

Cyclic polarization characteristics of 3D printed 316L.—The CPP curves of Sample 4, Sample 7 and wrought 316 are presented in Figure 5, visually revealing that the 3D printed specimens have much higher E_{pit} values when compared to wrought 316L. The E_{pit} values of all the 3D printed specimens were found to be within the range 0.60–0.75 V_{SCE} (Figure 6), which is about 300 mV higher than the E_{pit} of the wrought 316 specimen, and similarly is about 300 mV higher than the reported values of E_{pit} for 316 SS in the wider literature. The effects of the laser energy and the ratio of laser power/laser scan speed, on the E_{pit} values of the different specimens are shown in Figure 6. This plot indicates that there is no significant correlation between the laser parameters and the E_{pit} values, for the set of conditions used in this work to manufacture 316L using SLM.

The corrosion potential (E_{corr}), corrosion current density (i_{corr}), E_{pit} and repassivation potential (E_{rep}) of all the 316L specimens tested are plotted against the respective specimen porosity in Figure 7. The porosity of the wrought 316 specimen was assumed to be zero. The determined E_{corr} and i_{corr} values of the 3D printed specimens were found to be independent of the specimen porosity. Furthermore, the E_{pit} values did not show any statistically significant correlation with sample porosity. However, interestingly the E_{rep} values of the 3D printed specimens were found to decrease with increasing porosity of the specimen. The E_{rep} of Sample 4 (−0.1 V_{SCE}) which has the highest porosity was significantly lower than the E_{rep} of Sample 7 (0.035 V_{SCE}) thus, revealing the detrimental impact of specimen porosity on E_{rep}. The data also suggests that porosity is one material factor that can

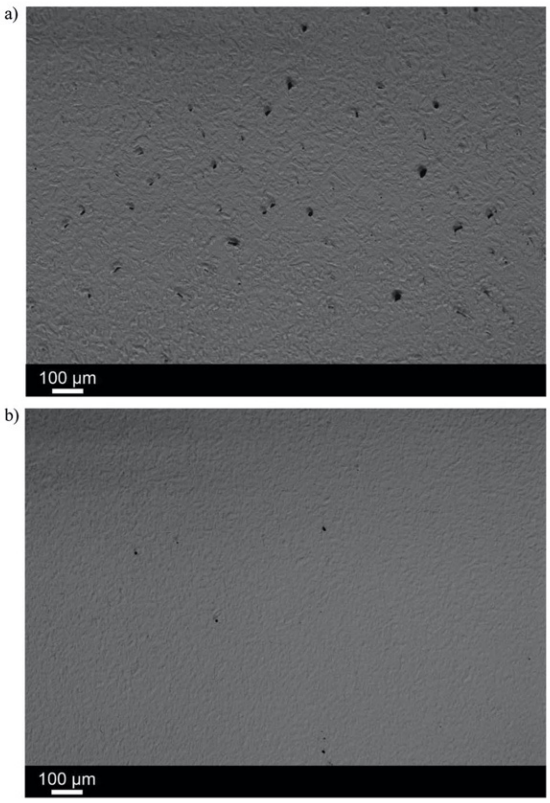

Figure 2. Optical micrographs of; a) Sample 4 (with the highest porosity) and b) Sample 7 (with the lowest porosity).

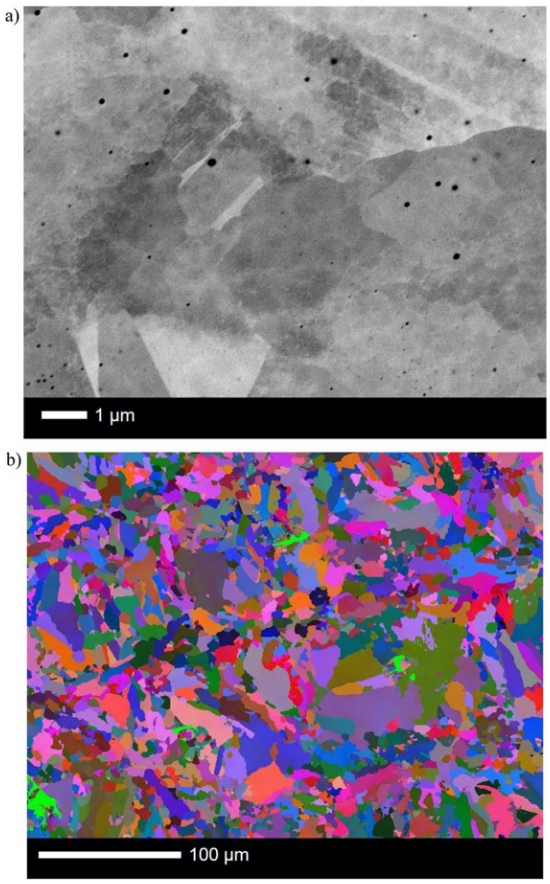

Figure 3. a) The SEM image and b) the EBSD orientation map revealing the microstructure of Sample 4.

influence repassivation, but not necessarily E_{pit}, which is an important revelation.

Metastable pitting characteristics of 3D printed 316L.—The metastable pitting characteristics of specimens were determined via potentiostatic testing and the sensitive recording of fluctuations in current (i.e. chronoamperometry transients) as shown in Figure 8.

For the period of testing, it is interesting note some generalities. Typically, the 3D printed specimens showed a higher frequency of current fluctuations in the first 15 minutes of the potentiostatic testing, whereas the wrought 316L specimens showed current fluctuations throughout the test period and typically more current 'spikes' in the final 15 minutes of potentiostatic experiments (Figure 8). The number of metastable pitting events were counted and normalised to the surface area and exposure time of each specimen, to obtain a metastable pit frequency, λ (in $cm^{-2}.s^{-1}$) which is presented in Figure 9.

The wrought 316L specimen (with zero porosity) was found to have a metastable pit frequency of 4.52 $cm^{-2}.s^{-1}$. Sample 4 showed the highest metastable pit frequency (5.04 $cm^{-2}.s^{-1}$), whereas Sample 7 had one of the lowest metastable pit frequencies (2.18 $cm^{-2}.s^{-1}$). This indicates that the porosity of a 3D printed specimen influences its metastable pitting characteristics (but interestingly, not influencing E_{pit}). The area under the potentiostatic curve (I vs t curve) for each sample was integrated to obtain the cumulative charge passed through each sample during the potentiostatic experiment. Similarly, the area under the I vs t curve after subtracting all the current peaks was also obtained by integration. The difference between the cumulative charges passed in both these cases, corresponds to the cumulative charge passed through the metastable pits of each sample (in mC/cm^2). The cumulative charge passed via the metastable pits of each sample is plotted against the respective sample's metastable pit frequency (Figure 10) and also the porosity (Figure 11). Sample 4 showed the highest cumulative charge (3.67 mC/cm^2) and highest metastable pit frequency, whereas sample 7 showed the lowest cumulative charge (0.10 mC/cm^2) and lowest metastable pit frequency. This indicates that the sample with the highest porosity (Sample 4) tends to suffer more damage during metastable pitting events when compared to the sample with the lowest porosity (Sample 7). The wrought 316L specimen showed some interesting characteristics. The metastable pit frequency of the wrought specimen was one of the highest (Figure 9), however the cumulative charge passed through the metastable pits of the wrought specimen was among the lowest, around 0.2 mC/cm^2 (Figures 10–11). This reveals that although the E_{pit} of the wrought specimen is less noble and its metastable pit frequency much higher than that of most 3D printed specimens, it seems to suffer far less damage during the metastable pitting events compared to the 3D printed specimens.

Discussion

The porosities of the 3D printed specimens were found to decrease with an increase in the laser power used for SLM (in the range of 165–285 W). However, the variations in the laser scan speed (in the

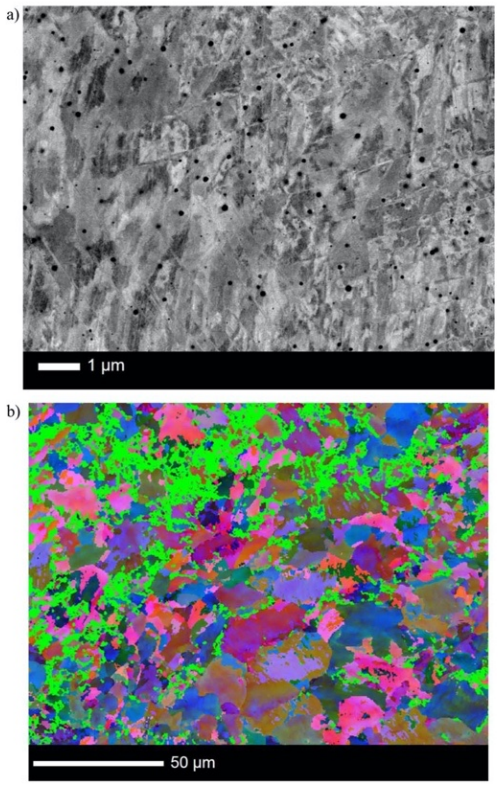

Figure 4. a) The SEM image and b) the EBSD orientation map revealing the microstructure of Sample 7.

range of 860–1160 mm/s) did not have a significant impact on the porosities of the specimens. The E_{corr}, i_{corr} and E_{pit} values of the 3D printed specimens did not show significant variation with specimen porosity. This is suggestive that specimen porosity is not a principal controlling factor in stable pit initiation. However, E_{rep} was found to decrease with increasing specimen porosity. This reveals that once stable pitting has occurred, its cessation is more difficult in the presence of increasing porosity. The metastable pit frequency was also found to increase with increasing specimen porosity for the 3D printed specimens. This indicates that porosity can contribute to metastable pitting events, but not necessarily to a lowering of E_{pit}. This means that metastable pits that are activated and repassivated at potentials below E_{pit}, are not principally responsible for lowering E_{pit} and potentially not the cause of subsequent stable pitting.

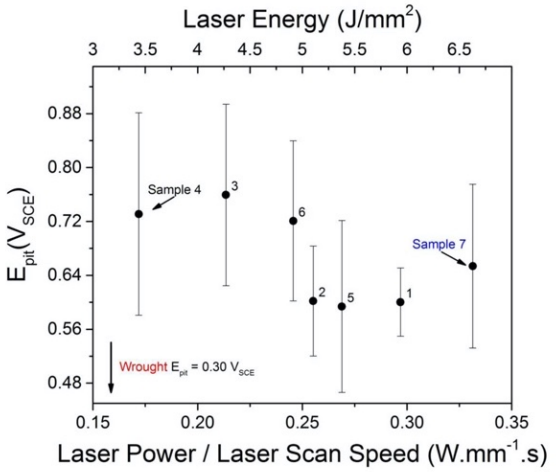

Figure 6. Pitting potentials (E_{pit}) of SLM 316L presented as a function of the Laser Power/Laser Scan Speed ratio and laser energy. The wrought 316L specimen possessed a lower E_{pit} value when compared to SLM specimens. The sample numbers are presented beside the E_{pit} values of the respective specimen.

The 3D printed specimens had significantly higher E_{pit} values than the benchmark wrought 316L specimen (by about 300 mV), revealing that 3D printed specimens are more resistant to stable pit initiation. However, the wrought specimen had a higher E_{rep} than most of the 3D printed specimens, indicating that the cessation of stable pitting (by repassivation) in 3D printed specimens is less favored when compared to the wrought specimen. The metastable pit frequency of the wrought specimen was found to be relatively higher when compared to frequencies of most 3D printed specimens. However, the

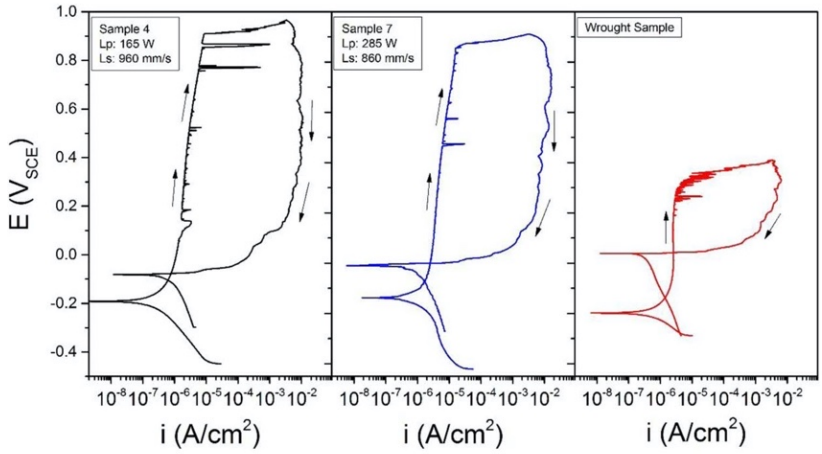

Figure 5. CPP curves for SLM 316L specimens (Sample 4 and Sample 7) and wrought 316L.

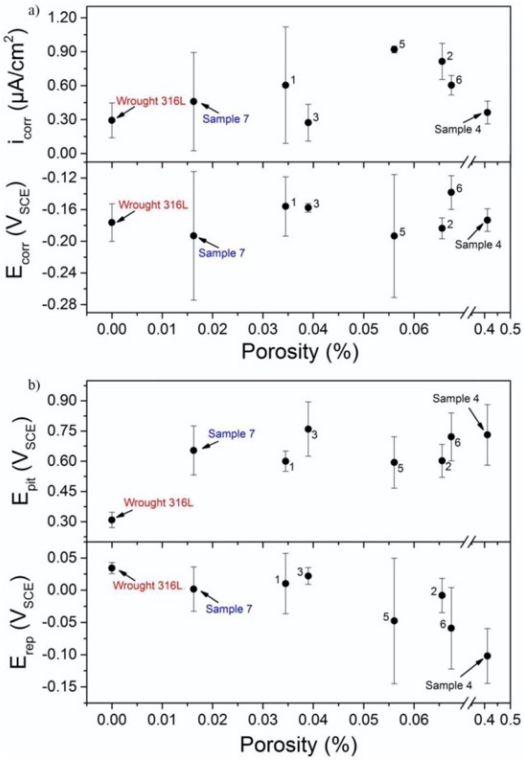

Figure 7. (a-b): The E_{corr}, i_{corr}, E_{pit} and E_{rep} values of the SLM 316L specimens plotted against the respective sample porosity. The data corresponding to Sample 4 (with the highest porosity), Sample 7 (with the lowest porosity) and wrought 316L (no porosity) has been labelled. The sample numbers are presented beside the respective data points for the remaining samples.

cumulative damage (or charge passed through metastable pits) was observed to be much lower for the wrought specimen when compared to the 3D printed specimens. These results indicate that the repassivation of metastable pits too is less favored upon 3D printed specimens compared to the wrought specimen.

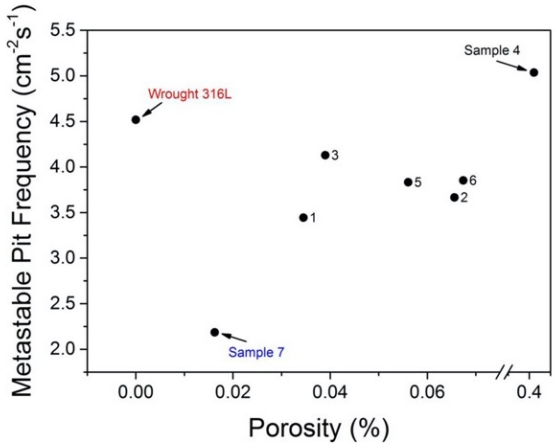

Figure 9. The metastable pit frequencies, λ, of wrought and SLM 316L, plotted against the respective sample porosities. The metastable pit frequencies of Sample 4, Sample 7 and wrought 316L are specifically indicated. The sample numbers are presented beside the respective data points for the remaining samples.

The effect of SLM parameters on porosity.—The porosities of the 3D printed specimens were found to decrease with an increase in laser power/laser energy. A similar effect has been observed recently for additively manufactured duplex SS.[7] At low laser energy densities and high laser scan speeds, the metal particles may not uniformly melt, resulting in ineffective powder deposition, which may contribute to porosity. Similarly, at high laser energy densities and low laser scan speeds, gases may be entrapped in the melt pool thus contributing to porosity. An optimal laser power/laser scan speed to minimise the specimen porosity can be inferred from the current work, for the range of parameters explored herein (noting that this may not be universal depending on the power or specifications of the various metal 3D printers presently on the market). A laser power of 285 W and laser scan speed of 860 mm/s were found to be the most optimum here, to minimise the porosity of SLM manufactured 316L SS specimens. The lowest porosity achieved herein, is also noted as being very low for AM builds, and much lower than the porosity reported in other works.[19]

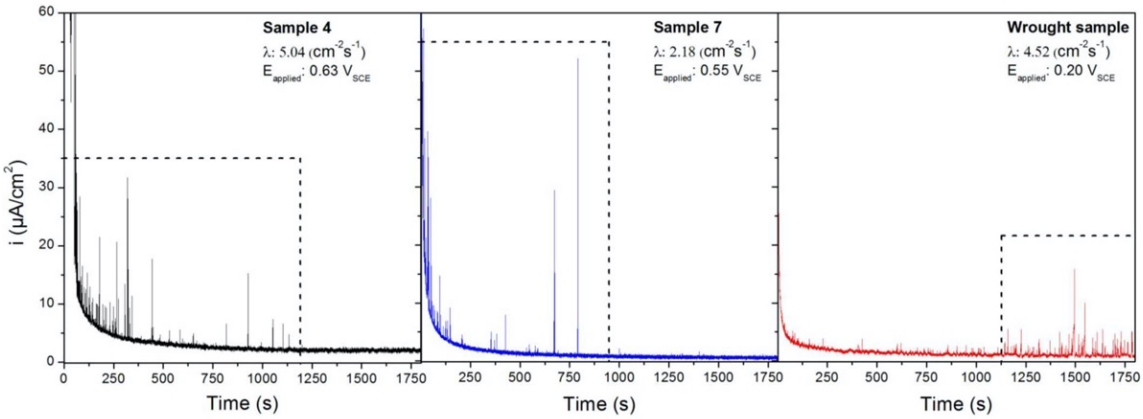

Figure 8. The current transients measured during the potentiostatic testing of Sample 4, Sample 7 and wrought 316L. The potentiostatic potential applied to each sample is shown, representative of a fixed potential below the average E_{pit} for the sample. The regions within the plots with a high metastable pit frequency, λ, are enclosed within the dashed squares.

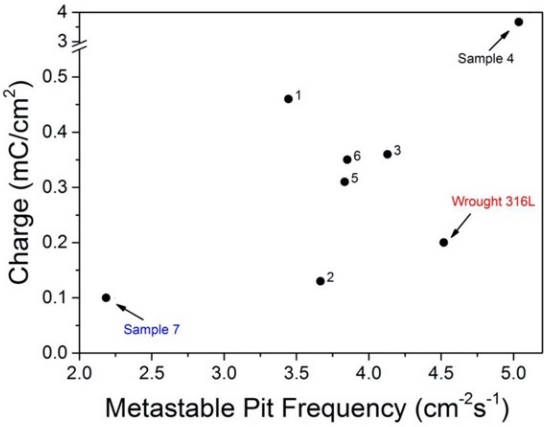

Figure 10. The cumulative charge passed (in mC/cm^2) through metastable pits for each sample, plotted against the respective sample's metastable pit frequency. The cumulative charge passed through Sample 4, Sample 7 and wrought 316L (during metastable pitting) are specifically indicated in the figure. The sample numbers are presented beside the respective data points for the remaining samples.

The corrosion characteristics of 3D printed 316L specimens.— The microstructures of 316L specimens produced by SLM are different as compared to those of wrought 316L. They are homogeneous in the sense that they do not inherit grain shapes or crystallographic texture from wrought operations. In addition, it has been noted (but not explored herein) that SLM prepared 316L specimens contain nanoscale dislocation cell structures[29,30] corresponding to very high as-built dislocation densities. The presence of such dislocation cell structures will impact the mechanical properties of the SS, and may also be a contributor to electrochemical properties – the extent to which is unknown. Referring to the limited prior work in this field, Trelewicz et al.[21] observed that SLM produced 316L had a lower resistance to pitting, when compared to wrought 316L in 0.1 M HCl solution. They postulated that molybdenum (Mo) segregation occurs at the walls of the cell structures, causing a heterogeneous distribution of Mo in the matrix of the SLM produced 316L. The segregation of Mo was postulated to detrimentally influence the pitting resistance of SLM produced 316L.[21] The present work however has revealed that the E_{pit} of the 3D printed 316L is much higher than that of wrought 316L, indicating that the 3D printed specimens are more resistant to pit initiation.

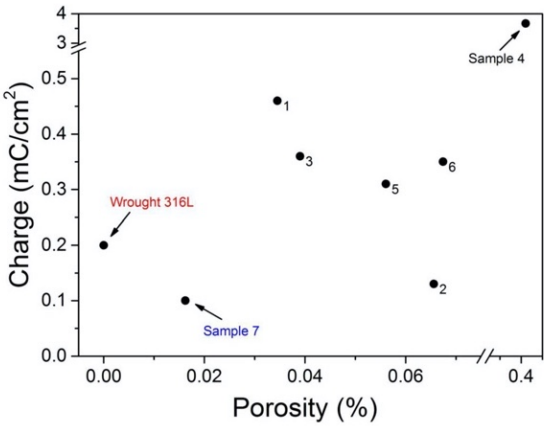

Figure 11. The cumulative charge passed (in mC/cm^2) through metastable pits for each sample, plotted against the respective sample's porosity. The cumulative charge passed through Sample 4, Sample 7 and wrought 316L (during metastable pitting) are specifically indicated in the figure. The sample numbers are presented beside the respective data points for the remaining samples.

Pit initiation in 3D printed specimens appears to be inhibited by some feature or characteristic that is not directly or principally related to the porosity of the specimen. Manganese sulfide (MnS) inclusions are common impurities dispersed in the matrix of austenitic SS and are considered to be the preferred sites for pit nucleation in austenitic SS.[31–34] They also promote stable pit growth in austenitic SS.[33–35] In fact, it was recently revealed by using high-resolution secondary ion mass spectroscopy (SIMS) that an iron-sulfide (FeS) rich "halo" up to 100 nm thick surrounds such MnS inclusions, which plays a critical role in the initiation of pitting corrosion at such inclusions.[35] It was proposed that the dissolution of this "halo" results in the formation of a polysulphide skin between the MnS inclusion and the steel, within which a pit can be triggered.[35] The pitting susceptibility of SS such as 304L was related to the size/distribution of the sulfide inclusions and when the sulfide particles are below a certain size (between 0.008 and 0.5 μm^3 for spheroidal particles), they are considered to be too small to nucleate a pit.[31] Stewart et al. observed that laser surface melting (LSM) of 304L significantly reduced the sizes of the dispersed sulfide inclusions and correspondingly improved the pitting resistance of the SS.[31] Recently, Stoudt et al.[36] observed that the E_{pit} values of additively manufactured 17–4 PH SS was about 10 mV higher than that of wrought 17–4 PH SS. They observed that additively manufactured SS had a finer martensite lath structure and a more homogenous dispersion of niobium carbide (NbC) precipitates compared to the wrought specimen. Interestingly, the sizes of the NbC precipitates were found to be an order of magnitude smaller in the additively manufactured specimens compared to the wrought specimens.[36] It is therefore hypothesized that SLM may similarly impact the presence of, or size distribution of MnS inclusions, such that the inclusions are either annihilated and cannot reform from rapid solidification of the melt pool, or are too fine to trigger pit initiation in 3D printed 316L.

Overall, the E_{corr}, i_{corr} and E_{pit} values of the 3D printed SS specimens did not significantly vary with specimen porosities. The metastable pit frequency and also the cumulative charge passed through the metastable pits were found to increase with the specimen porosity. The E_{rep} was also found to decrease with specimen porosity. These results indicate that the Cr-based passive film protects the metal surface even at the pores. The passive film may however be more susceptible to "break-down" at such pores, causing the onset of several metastable pits during potentiostatic experiments. The film spontaneously re-generates at such sites and apparently prevents the transition from metastable to stable pitting. The wrought 316L (no porosity) has shown the highest E_{rep} within the analyzed samples, whereas Sample 4 (highest porosity) has shown the lowest E_{rep}. This indicates that in the case of 3D printed specimens the system is initially controlled by pit stabilization. However, once pitting has commenced the system transitions to one being controlled by pit initiation.[37]

The influence of porosity on the kinetics of repassivation of the SS specimens will need to be investigated in future work. This may be due to several different factors; firstly the impurities or inclusions on the surface of 3D printed 316L (or the pores) may be different to that of wrought 316L and could be detrimentally influencing repassivation. Similarly, in 3D printed 316L shallow pits may be opening into a large cavities (or pores) within the metal which could restrict repassivation. The presence of sub-surface pores could restrict repassivation after stable pit growth as they may merge with pits growing into the metal. Finally, the relatively rougher surface of the pores could also impede repassivation of pits within pores. Such aspects point to diverse and significant needs for important future work.

Conclusions

A total of seven 316L austenitic specimens were manufactured by SLM. The specimens were all unique as they were prepared by varying the two SLM parameters, namely laser power (in the range 165–285 W) and laser scanning speed (in the range 860–1160 mm/s). The porosity of each specimen was measured and related to the respective cyclic polarization and metastable pitting characteristics. The porosity of specimens produced was confined to $< \sim 0.4\%$. The following are the main conclusions from the present work;

(i) 3D printed 316L specimens fabricated by SLM were found to be more resistant to pit initiation than wrought 316L specimens. This was determined on the basis of E_{pit} values of the 3D printed 316L specimens which were found to be about 300 mV more noble than that of a wrought 316L specimen. Furthermore, the typical metastable pit frequency of 3D printed 316L specimens was lower (in many cases, considerably lower) than wrought 316L in all cases but for the highest porosity specimen. It is hypothesized that SLM may impact the surface concentration and size distribution of inclusions, such that the inclusions are either annihilated or are too miniscule to trigger pit initiation in 3D printed 316L.

(ii) The E_{corr}, i_{corr} and E_{pit} values of the 3D printed specimens did not vary significantly with the specimen porosities. In all cases, E_{pit} of 3D printed 316L was considerably higher than wrought 316L. However, two important parameters were determined to vary with specimen porosity, namely: (a) metastable pit frequency was to found to increase with specimen porosity and (b) E_{rep} was found to decrease with specimen porosity. In other words, repassivation after stable pitting as triggered by anodic polarization was less favored in specimens with higher porosity. Inferior repassivation of SLM 316L is at odds with the notion that a higher E_{pit} and lower metastable pit frequency represent higher corrosion resistance; suggestive that the mechanism responsible for higher E_{pit} and lower metastable pit frequency is not capable of influencing repassivation. Hypotheses for such mechanisms were discussed herein.

Acknowledgments

We are grateful for support of the Woodside Futurelab. We also thank M.K. Cavanaugh for supplying the original code for which the transient analysis herein was based. We thank Yuxiang Wu for supplementary XRD analysis. Microscopy and microanalysis was performed at the Monash Centre for Electron Microscopy. We also thank the Monash Centre for Additive Manufacturing.

References

1. A. J. Sedriks, *Corrosion of stainless steels*, 2nd edition, Wiley-Interscience, New York (1996).
2. J. R. Davis, *ASM Specialty Handbook - Stainless Steels*, ASM International (1994).
3. A. Al-Amr, *Mechanical behaviour and structure of passive films on austenitic stainless steels, Doctoral dissertation*, Washington State University, Washington, U. S. A (2005).
4. C. O. Olsson and D. Landolt, Passive films on stainless steels—chemistry, structure and growth, *Electrochimica Acta*, **48**, 1093 (2003).
5. G. Scotti, V. Matilainen, P. Kanninen, H. Piili, A. Salminen, T. Kallio, and S. Franssila, *Laser additive manufacturing for stainless steel micro fuel cells*, **272**, 356 (2014).
6. C. Kamath, B. El-dasher, G. F. Gallegos, W. E. King, and A. Sisto, Density of additively-manufactured, 316 SS parts using laser powder-bed fusion at powers up to 400 W, *International Journal of Advanced Manufacturing Technology*, **74**, 65 (2014).
7. K. Davidson and S. Singamneni, Selective laser melting of duplex stainless steel powders: An investigation, *Materials and Manufacturing Processes*, **31**, 1543 (2016).
8. D. Herzog, V. Seyda, E. Wycisk, and C. Emmelmann, Additive manufacturing of metals, *Acta Materialia*, **117**, 371 (2016).
9. K. Zhang, W. Liu, and X. Shang, Research on the processing experiments of laser metal deposition shaping. *Optics & Laser Technology*, **39**, 549 (2007).
10. R. M. Mahamood and E. T. Akinlabi, *Laser additive manufacturing. Advanced manufacturing techniques using laser material processing, IGI Global book series Advances in Civil and Industrial Engineering (ACIE)*, Pennsylvania, U.S.A. (2016).
11. D. Pham and S. S. Dimov, *Rapid manufacturing: the technologies and applications of rapid prototyping and rapid tooling.* Springer Science & Business Media, pp. 33 (2012).
12. M. Francois, *Towards modelling and simulations of additive manufacturing of metals at Los Alamos National Laboratory. Predictive Theoretical and Computational Approaches for Additive Manufacturing: Proceedings of a Workshop* (2016).
13. V. Shapovalov, *Porous Metals. Mrs Bulletin*, **19**, 24 (1994).
14. C. Zhong, T. Biermann, A. Gasser, and R. Poprawe, "Experimental study of effects of main process parameters on porosity, track geometry, deposition rate, and powder efficiency for high deposition rate laser metal deposition." *Journal of Laser Applications* **27**(4), (2015).
15. M. K. Imran, S. H. Masood, and M. Brandt, *Influence of Process Parameters in the Direct Metal Deposition of H13 Tool Steel on Copper Alloy Substrate, Proceedings of the World Congress on Engineering* (2010).
16. S. Wolff, T. Lee, E. Faierson, K. Ehmann, and J. Cao, *Anisotropic Properties of Directed Energy Deposition (DED)-Processed Ti-6Al-4V, SME North American Manufacturing Research Conference (NAMRC)*, June 27-July 1, Blacksburg, V.A (2016).
17. B. Verlee, T. Dormal, and J. Lecomte-Beckers, Density and porosity control of sintered 316L stainless steel parts produced by additive manufacturing. *Powder Metallurgy*, **55**, 260 (2012).
18. C. Carboni, P. Peyre, G. Beranger, and C. Lemaitre, Influence of high power diode laser surface melting on the pitting corrosion resistance of type 316L stainless steel. *Journal of materials science*, **37**, 3715 (2002).
19. Y. Sun, A. Moroz, and K. Alrbaey, Sliding wear Characteristics and Corrosion behaviour of Selective Laser Melted 316L Stainless Steel, *Journal of Materials Engineering and Performance*, **23**, 518 (2014).
20. M. Zietala, T. Durejko, M. Polanski, I. Kunce, T. Plocinski, W. Zielinski, M. Lazinska, W. Stepniowski, T. Czujko, K. Kurzydlowski, and Z. Bojar, The microstructure, mechanical properties and corrosion resistance of 316L stainless steel fabricated using laser engineered net shaping, *Materials Science and Engineering A*, **677**, 1 (2016).
21. J. R. Trelewicz, G. P. Halada, O. K. Davidson, and G. Manogharan, Microstructure and corrosion resistance of laser additively manufactured 316L stainless steel, *Journal of Materials*, **68**, 850 (2016).
22. M. S. Domack and J. M. Baughman, Development of nickel-titanium graded composition components, *Rapid Prototyping Journal*, **11**, 41 (2005).
23. X. Lin, T. M. Yue, H. O. Yang, and W. D. Huang, Phase Evolution in Laser Rapid Forming of Compositionally Graded Ti-Ni Alloys, *Journal of Engineering Materials And Technology*, **131**, 041002 (2009).
24. Y. A. Albrimi, A. Eddib, J. Douch, Y. Berghoute, M. Hamdani, and R. M. Souto, Electrochemical behaviour of AISI 316 austenitic stainless steel in acidic media containing chloride ions, *International Journal of Electrochemical Science*, **6**, 4614 (2011).
25. A. Robin, G. Silva, and J. L. Rosa, Corrosion behaviour of HA-316L SS biocomposites in aqueous solutions. *Materials Research*, **16**, 1254 (2013).
26. P. C. Pistorius and G. T. Burstein, Metastable pitting corrosion of stainless steel and the transition to stability. Philosophical Transactions of the Royal Society of London A: Mathematical, *Physical and Engineering Sciences*, **341**, 531 (1992).
27. R. K. Gupta, N. L. Sukiman, M. K. Cavanaugh, B. R. W. Hinton, C. R. Hutchinson, and N. Birbilis, Metastable pitting characteristics of aluminum alloys measured using current transients during potentiostatic polarisation, *Electrochimica Acta*, **66**, 245 (2012).
28. M. K. Cavanaugh, N. Birbilis, and R. Buchheit, A quantitative study on the effects of environment and microstructure on pit initiation in Al-alloys, *ECS Transactions*, **52**, 1 (2009).
29. Y. Zhong, L. Liu, S. Wikman, D. Cui, and Z. Shen, Intergranular cellular segregation network structure strengthening 316L stainless steel prepared by selective laser melting, *Journal of Nuclear Materials*, **470**, 170 (2016).
30. K. Saeidi, X. Gao, Y. Zhong, and Z. J. Shen, Hardened austenite steel with columnar sub-grain structure formed by laser melting, *Materials Science and Engineering A*, **625**, 221 (2015).
31. J. Stewart and D. E. Williams, The initiation of pitting corrosion on austenitic stainless steel: on the role and importance of sulfide inclusions, *Corrosion Science*, **33**, 457465 (1992).
32. M. P. Ryan, D. E. Williams, R. J. Chater, B. M. Hutton, and D. S. McPhail, Why stainless steel corrodes. *Nature*, **415**(6873), 770 (2002).
33. R. Ke and R. Alkire, Surface analysis of corrosion pits initiated at MnS inclusions in 304 stainless steel, *Journal of the Electrochemical Society*, **139**, 1573 (1992).
34. R. Ke and R. Alkire, Initiation of corrosion pits at inclusions on 304 stainless steel. *Journal of the Electrochemical Society*, **142**, 4056 (1995).
35. D. E. Williams, M. R. Kilburn, C. John, and G. I. N. Waterhouse, Composition changes around sulfide inclusions in stainless steels, and implications for the initiation of pitting corrosion, *Corrosion Science*, **52**, 3702 (2010).
36. M. R. Stoudt, R. E. Ricker, E. A. Lass, and L. E. Levine, Influence of postbuild microstructure on the electrochemical behavior of additively manufactured 17-4 PH stainless steel, *Journal of Materials*, **69**, 506 (2017).
37. G. S. Frankel, T. Li, and J. R. Scully, Localized corrosion: Passive film breakdown vs pit growth stability, *Journal of the Electrochemical Society*, **164**, C180 (2017).

Chapter 4: On the effect of build orientation and residual stress on the corrosion of 316L stainless steel produced by selective laser melting

One of the most attractive characteristics of AM is the innovative design freedom to manufacture unique components. Since AM is carried out in an additive manner, objects are produced as they are manufactured to a near-net shape requiring little to no post manufacturing treatment. On the other hand, traditional manufacturing methods (e.g. casting, forging, rolling, extruding, cutting, etc.) are classified as subtractive manufacturing technologies. The production of components by these subtractive technologies usually require a series of post treatments before being put into service. In general, this increase overall production complexity and require accompanying infrastructure. The rapid-manufacturing and design freedom within AM allow high component-design variability at low costs which can boost the development of innovative and high-end technologies.

Prior to safely implement AM components into service, characterisation and qualification of their performance must be carried out. In the context of metal AM, the main alterations observed for components in comparison to their conventionally manufactured counterparts include microstructural variations, surface roughness, porosity and residual stresses. These alterations are sensible to AM process configuration such as laser parameters, substrate temperature, inert gas flow, material distribution pattern, support structure and build orientation. In this chapter, the corrosion characteristics SLM 316L specimens were investigated by both electrochemical and immersion techniques. Build direction was varied during SLM, to produce 316L specimens fabricated with different angles relative to their respective substrate (namely 0º, 45º and 90º) to evaluate their effect on pitting. In addition, build orientation and pitting were also discussed in the context of residual stresses generated from SLM.

The present chapter was prepared as a journal article and is under submission in ***Corrosion Science.*** The journal article appears here 'as submitted'.

On the effect of build orientation and residual stress on the corrosion of 316L stainless steel prepared by selective laser melting

G. Sander[a,1], A. Babu[a, b], X. Gao[a], D. Jiang[a,b], N. Birbilis[c, ‡]

[a]Department of Materials Science and Engineering, Monash University, Clayton, VIC 3800, Australia.

[b]Monash Centre for Additive Manufacturing, Monash University, Notting Hill, Victoria, 3168, Australia.

[c]College of Engineering and Computer Science, Australian National University, ACT 2601, Australia.

[1]Corresponding authors e-mail: guilherme.sandermalab@monash.edu

Key words: 316L; corrosion; build orientation; selective laser melting; residual stress

Abstract

During additive manufacturing of AISI 316L stainless steel, heating and cooling cycles during selective laser melting (SLM) are responsible for grain anisotropy in the 'as-built' condition. Columnar grains form on the plane parallel to the build direction, whilst equiaxed grains are observed on planes perpendicular to the build direction. Anisotropy may affect corrosion and pitting of this alloy. In addition, residual stresses originating from the rapid heating and cooling inherent to SLM, may also influence corrosion and pitting of 316L stainless steel. Electrochemical and immersion testing was carried out for 316L as a function of build direction and residual stresses.

Introduction

The development of additive manufacturing (AM) techniques in recent decades has resulted in a broader context of the way in which components are now manufactured in their net-shape [1,2]. In general, the AM process is defined by the addition of a certain material (or a combination of different materials) in a layer-by-layer fashion, guided by computer aided design (CAD) [3]. Selective laser melting (SLM) is one of such AM techniques that is classified as a laser powder bed fusion (LPBF) process. For SLM the energy source (i.e. the laser) is scanned onto a powder bed which selectively melts the feedstock material. Once one layer is finished, a subsequent powder layer is applied onto the melted layer, and the process is repeated until a solid unit is produced [4]. Advantages of utilising SLM to produce components include rapid manufacturing, high design freedom and the capability to produce near net-shape complex components [5]. Furthermore, the design freedom associated with SLM can potentially lead to components possessing a diverse range of shapes and angles. Consequently, as the complexity of elements produced by SLM increase so does the complexity of phase transformations and solidification phenomena. Local heating (inclusive of melting) and cooling occur almost instantaneously (up to 10^8 K/s) [6,7] on localised micrometric melting pools during metal SLM. The heat remnant from the melt pool solidification dissipates across the metallic structure towards its adjacent powder and more intensively towards the substrate [8]. This particular heat gradient can generate non-uniform heat distribution across the SLM component and consequently lead to microstructural anisotropy. In addition, build orientation usually varies when complex structures are produced by SLM which increases the intricacy of heat transfer and solidification even further. Hence the investigation of such anisotropic microstructures on the performance of SLM metals and alloys is of critical importance.

Stainless steels produced by SLM, more specifically the AISI 316L (with the nominal composition of Fe – 16-18 % Cr – 10-14 % Ni – 0.03 % C – 2.0 % Mn – 1.0 %Si – 0.045 % P – 0.030 % S – 2.0-3.0 Mo (in wt. %)), have been extensively investigated [9–14]. It has been reported that SLM 316L stainless steel components have aspects of their microstructures altered during SLM when compared to their wrought counterpart [15]. Consequently, mechanical properties and durability of such alloys are prone to be altered when specimens are produced SLM. For instance, several studies demonstrated that SLM 316L stainless steel possess higher yield strength than their conventionally produced counterparts [8,16–18]. This has often been attributed to small grain size distribution, grain anisotropy and intergranular microcellular dislocation structures that hinder plastic deformation [8,19]. Those changes in grain morphology have been correlated to the previously mentioned heat transfer history observed during SLM [8]. More specifically, once each layer is melted, the underlying layers are submitted to cyclic re-heating due to the temperature gradient from the upper layers (subjected to the laser melting) towards the substrate (i.e. base). The heat transfer history and rapid cooling rates reported in SLM have also been associated with the generation of residual stresses in components produced by this manufacturing process [20,21].

Corrosion of 316L stainless steels produced by SLM have been reported in the literature, rather extensively in recent years [22–29]. The altered microstructure generated from the SLM of 316L has been reported to affect pitting [24] and stress corrosion cracking [30] in chloride (Cl^-) containing media. Chao et al. [26] reported that SLM significantly reduced the segregation of manganese sulphide (MnS) in 316L stainless steel. This MnS segregation has been associated with one of the most critical nucleation sites for the pitting of stainless steels [31] including the 316L type. Thus, by reducing or eliminating MnS by SLM the resistance to pit nucleation in Cl^- containing media for 316L stainless steel was superior to their wrought counterpart [24,26]. Moreover, the effect of SLM parameters such as laser power, laser scanning speed, hatch distance, layer height on pitting of 316L stainless steel has also been reported elsewhere [23,24,32,33]. In the sole study in the context, the effect residual stress on the pitting of SLM 316L stainless steel was recently studied by Cruz et al. [30] for as-built and heat treated specimens. In their work, compressive residual stresses did not significantly affect the pitting of SLM 316L stainless steels. However, additional studies, or, a study regarding the synergetic effect of build orientation and the effect of residual stresses generated during the production of SLM 316L stainless steels to pitting, remain unclear. This work aims to investigate the influence of microstructure anisotropy and residual stresses generated from the SLM of 316L stainless steels to pitting in chloride (Cl^-) containing media. Besides, a series of electrochemical and immersion tests – the latter showing the longer-term material performance as opposed to electrochemical testing alone – were performed and correlated to the microstructure of 316L stainless steel specimens produced by SLM in different build orientations. Residual stresses in the context of pitting resistance was also discussed herein.

Experimental procedures

Materials production

Stainless steel (AISI 316L grade) was additively manufactured by SLM using gas atomised spherical powder, sourced from TLS Technik GmbH & Co. Spezialpulver KG (Germany). The 316L powder possessed a particle size distribution between 10 – 53 µm.

Specimens preparation was carried out utilising an EOS M280 (EOS GmbH, Krailling, Germany) instrument, equipped with an Yb-fiber laser (1070 nm). Specimens of 50 x 50 x 12 mm were prepared, to be suitable for tensile testing. For the SLM process, laser diameter was fixed at 100 µm and the oxygen level inside the build chamber was maintained < 0.30 % by inert nitrogen-purging. Laser power was maintained at 205 W, laser scan speed at 960 mm/s, and the distance between the core of two consecutive passes (hatch distance) was maintained at 110 µm with a layer height of 40 µm. The specimens were manufactured at varied build orientations, namely, vertical (90°), horizontal (0°) and 45° as shown in **Figure 1a**. The build orientation angles were relative to a wrought 316L substrate (sourced from Interalloy (Victoria, Australia)).

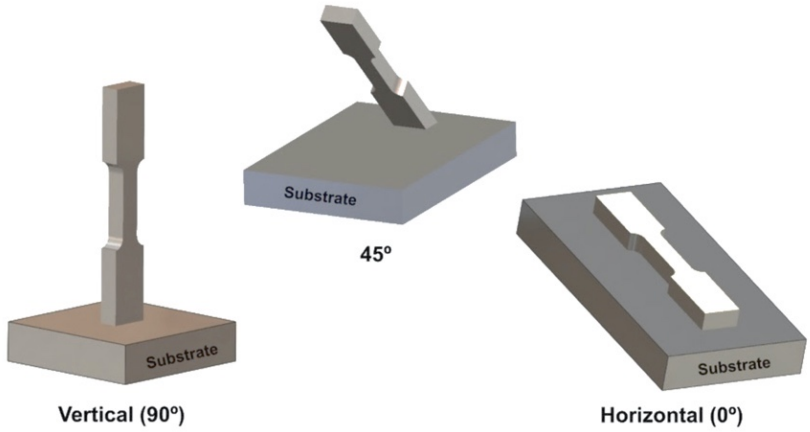

Figure 1: Build directions studied for selective laser melted 316L tensile specimen produced: vertical (90°), horizontal (0°) and 45° relative to build substrate.

Microstructural characterisation

Samples were prepared from the respective wrought, vertical, 45º and horizontal 316L stainless steel specimens. The SLM 316L samples were investigated on surfaces perpendicular their respective production build orientation (i.e. vertical, horizontal and 45º) whilst the wrought 316L sample was analysed for the surface perpendicular to their rolling direction. All samples were metallographically prepared by sequentially grinding the surface to a P2500 grit finish (utilising silicon carbide paper) and polishing them to 1 µm surface finish (utilising diamond particle suspension). Posteriorly to surface preparation, each sample was individually subjected to ultrasonic bath cleaning in order to remove any residual contaminants from the surface. Porosity was measured by optical microscopy for the polished vertical, horizontal and 45º SLM 316L stainless steel specimens.

Further microstructural observation was carried out by scanning electron microscopy (SEM) via a JOEL JSM-7001F FEG-SEM. In addition, all 316L stainless steel specimens were measured by electron backscattered diffraction (EBSD) utilising an Oxford Instruments Nordlys Max2 EBSD detector integrated to the SEM system. Horizontal and vertical SLM 316L stainless steel samples were also examined by transmission electron microscopy (TEM) and energy dispersive x-ray spectrometry (EDXS) with a FEI Tecnai G2F20 SuperTwin FEG-STEM instrument operated at 200kV, equipped with a Bruker XFlash windowless silicon drift detector and Bruker Esprit 1.9 software. STEM images were recorded simultaneously using Gatan bright field (BF) and Fischione high angle annular dark-field (HAADF) detectors.

Mechanical testing and residual stress measurement

Tensile stress measurements were performed for the wrought and SLM 316L specimens utilising an INSTRON 100 KN model 4505 instrument with a displacement rate of 0.02 mm/s using a 100 KN load cell and a 10 mm extensometer.

Residual stress measurements were performed on the electropolished surface of SLM 316L specimens fabricated at horizontal, vertical and 45º directions. The electropolishing was carried out by exposing the investigated specimen surface to a solution of choline chloride and ethylene glycol (2:1 molar ratio) under 6 V (DC power supply) for 45 minutes. After that, five different points along the build direction were chosen and residual stress measurements were carried out on the surface of those points in all the samples. A Bruker® D8 Discover X-ray diffractometer equipped with a centric Eulerian cradle and Vantec-500 2D detector operating with a characteristic Cu K_α radiation source with a wavelength (λ) of 1.5405 Å was utilised. An accelerating X-ray voltage of 40 kV and beam current of 40 mA were used. To investigate the SLM 316L specimens, the α-Fe (220) diffraction peak was chosen with the 2θ range between 73º – 76º at a step size of 0.1º. The irradiated X-ray beam was 2 mm in diameter and the sample was rotated about the Φ axes and tilted about ψ axes to evaluate all the components of the stress tensor. The magnitude of residual stress was determined using the $\sin^2\psi$ method at six Φ angles (0º, 45º, 90º, 180º, 225º, 270º) and seven ψ directions (0º - 60º). A Bruker® Diffrac.Leptos software (version 7.10) was used to calculate the residual stresses where the utilised X-ray elastic constants are $s_1 = -1.35 \times 10^{-6}$ 1/MPa, $\frac{1}{2} s_2 = 6.18 \times 10^{-6}$ 1/MPa, Young's modulus (E) = 207.04 GPa, Poisson ratio (ν) = 0.280 and an anisotropy factor of 1.

Electrochemical and immersion testing

Cyclic-potentiodynamic polarisation (CPP) was carried out for metallographically prepared (to a P1200 grit finish) SLM (vertical, 45º, horizontal) and wrought 316L stainless steel samples. Electrochemical measurements were carried out in a three-electrode system utilising a flat cell containing saturated calomel electrode (SCE) as reference and platinum mesh as the counter electrode (CE). The 316L specimens behaved as the working electrode (WE) with 1 cm^2 exposed area. All CPP testing was carried out in 0.6 M sodium chloride (NaCl) solution at room temperature. Prior to each polarisation the samples were left at open circuit potential (OCP) for 30 minutes. The specimens were polarised from - 0.250 V against OCP up to 1.0 V_{SCE} having the scan direction reversed when current density values reached 10^{-3} A/cm^2 threshold. The reversed scan continued until the specimens were polarised down to - 0.20 V below their respective OCP.

Immersion testing following the ASTM G48 – A standard [34] was carried out for SLM (vertical, horizontal, 45°) and wrought 316L samples. Metallographic surface preparation was carried out for each sample by grinding all their respective surfaces to a P1200 grit finish, followed by ultrasonically cleaning the ground samples in ethanol. After surface preparation, the samples were dried utilising compressed air. The weight of each dried sample was measured and calculated as a function of their respective exposed area. In sequence,

all samples were individually immersed in iron chloride (III) – ($FeCl_3$) 6 wt. % solution at room temperature for 72 hours. Following exposure, each sample was ultrasonically cleaned in ethanol and dried thoroughly. Then their final weight was measured over and conflicted with the pre-immersion measurements in order to calculate their respective weight loss after immersion in the condition above. The described immersion method was independently performed in triplicate for each specimen type.

Results

Mechanical testing and residual stress

The response of SLM and wrought 316L stainless steel specimens to tensile testing was summarised in **Table 1**. Similar yield strength was measured for the SLM specimens in all build directions and ranging from 520 MPa (45º) to 577 MPa (horizontal).

Table 1 : Summary of mechanical properties determined for specimens herein.

Specimen	Yield strength (MPa)	Ultimate tensile strength (MPa)	Elongation (%)
Vertical	**520**	**620**	**75**
Horizontal	**577**	**688**	**65**
45^0	**536**	**660**	**62**
Wrought	**331**	**641**	**70**

For the wrought 316L, the measured yield strength (320 MPa) was considerably below their respective SLM counterparts. However, the ultimate tensile strength (UTS) for the wrought 316L was similar to the horizontal, 45 and vertical SLM 316L specimens (with average values between 620 – 688 MPa). Significant work hardening was not observed for the SLM specimens as their yield strength and UTS values differed by a maximum of 124 MPa. On the other hand, the difference between yield strength and UTS for the wrought 316L was 310 MPa which indicated that this alloy can undergo significant work hardening. All 316L stainless steel specimens investigated in the present work showed good ductility with elongation registered above 62 % with small variations across the build direction of the SLM. Residual stress was detected for each SLM 316L stainless steel specimen as shown in **Figure 2**. Compressive stresses were measured for the horizontal (-160.6 ± 47.8 MPa) and vertical (-112.5 ± 32.5 MPa) specimens. Interestingly in contrast to the other two SLM specimens, tensile residual stresses were measured for the 45º specimen (183.7 ± 59 MPa).

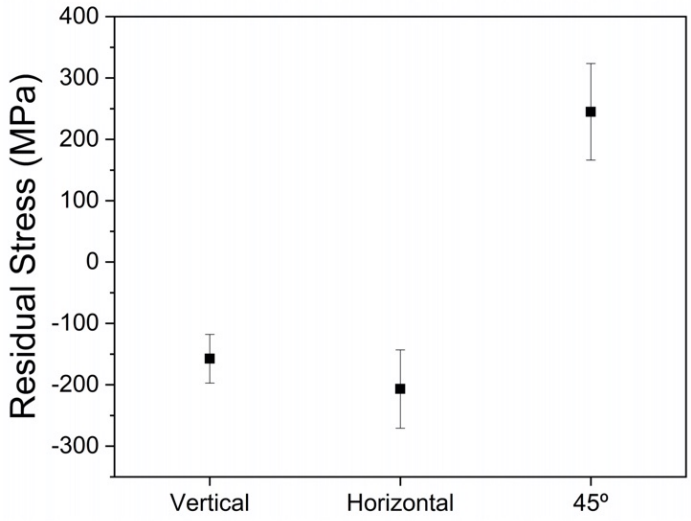

Figure 2: Residual stress measured for the selective laser melted 316L specimens in their as-built state as a function of build orientation.

Microstructure characterisation

Images collected from SEM analysis revealed that grain shape and size varied with build direction for the 316L stainless steel specimens as observed in **Figure 3**.This grain anisotropy as a consequence of manufacturing the specimens in different build directions has been reported in the literature [8] and correlated to heat transfer history during SLM . Columnar and longer grains were observed for the horizontal specimen (**Figure 3a**) whilst the vertical (**Figure 3b**) and 45º (**Figure 3c**) specimens presented smaller and near-equiaxed grains. Porosity, which is a common defect in AM alloys [35] was observed for all the SLM specimens as highlighted in **Figure 3**. Usually this porosity is not present in wrought 316L stainless steel components. The features detected in the wrought 316L SEM imaging (**Figure 3d**) were correlated to manganese sulphide (MnS) inclusions commonly observed in this alloy [31,36–38] . Similar MnS inclusions have not been detected for 316L stainless steels manufactured by SLM as reported elsewhere [22,24,26]. Therefore, it is logical to assume that the features observed in **Figure 3 a, b** and **c** are in fact pores remnant from the SLM process and not MnS inclusions.

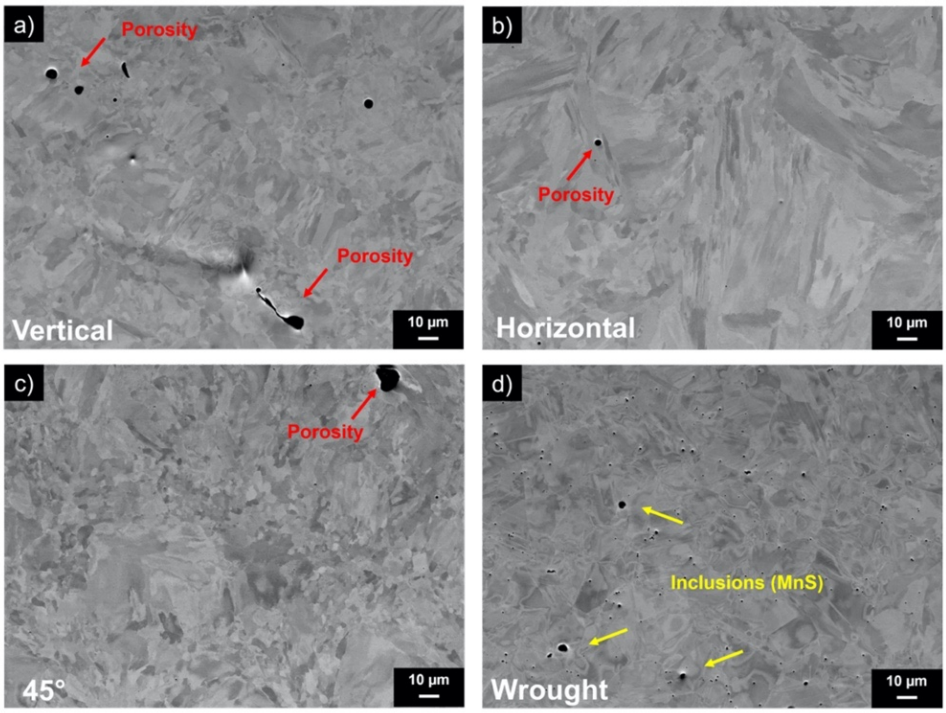

Figure 3: Secondary electron micrographs for the 316L stainless steel samples. Selective laser melted and a) vertical orientation, b) horizontal orientation, c) 45º orientation (with red arrows highlighting the presence of pores on the surface); and d) wrought 316L highlighting inclusions (manganese sulphides (MnS)) on the surface.

Microstructure images were also collected by EBSD (**Figure 4**) for the SLM 316L stainless steel specimens and their wrought counterpart. Once again, significant different grain morphology was observed amongst the SLM 316L stainless steel specimens as a function of build orientation. Chessboard pattern from the laser scan tracking strategy with small columnar grains and slightly larger equiaxed grains was detected for the vertical SLM 316L stainless steel specimen as shown in **Figure 4a**. Large columnar grains near-parallel (or low angled) to the build orientation were observed for the horizontal SLM 316L stainless steel specimen as shown in **Figure 4b**. Such coordinated microstructure (i.e. grain morphology) has been previously reported for SLM 316L stainless steels on surfaces perpendicular to the substrate due to the particular thermal history distribution during metal SLM. For the 45º SLM 316L stainless steel specimen, smaller grains were detected in comparison with their vertical and horizontal orientation counterparts. In addition, a grain distribution pattern could not be correlated to the 45º SLM build orientation (**Figure 4c**) as it was for the vertical (**Figure 4a**) and horizontal (**Figure 4b**) SLM 316L stainless steel specimens. The wrought 316L stainless steel specimen EBSD imaging (**Figure 4d**) revealed microstructure composed of high-angle equiaxed grains and 'moderate' twining typically observed for this alloy [39].

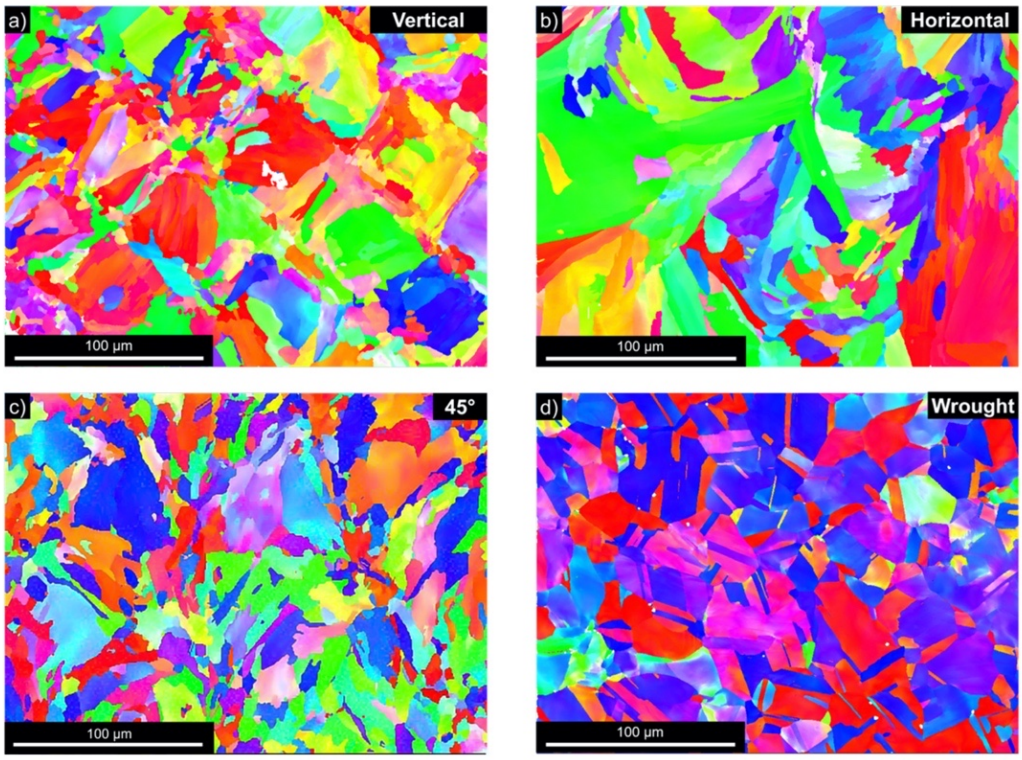

Figure 4: Electron backscatter diffraction with unique grain colour images for the 316L stainless steel samples. Selective laser melted at a) vertical orientation, b) horizontal orientation, c) 45º orientation, and, d) wrought316L.

Corrosion

Immersion testing revealed that the majority of the investigated samples presented similar pitting behaviour when exposed to 6 wt. % $FeCl_3$ at 21º C (**Figure 5**). According to the ASTM G 48 standard [34], steels that have weight losses (normalised to their respective sample area) higher than 0.0001 g/cm^2 after immersion in 6 wt. % $FeCl_3$ for 72 hours are considered to be damaged by pitting. Based on that, pitting was detected for all the SLM and wrought 316L stainless steel specimens in at least two of the three samples tested for each specimen. However, the measured average weight loss was lower for the SLM 316L specimens in comparison to their wrought counterpart.

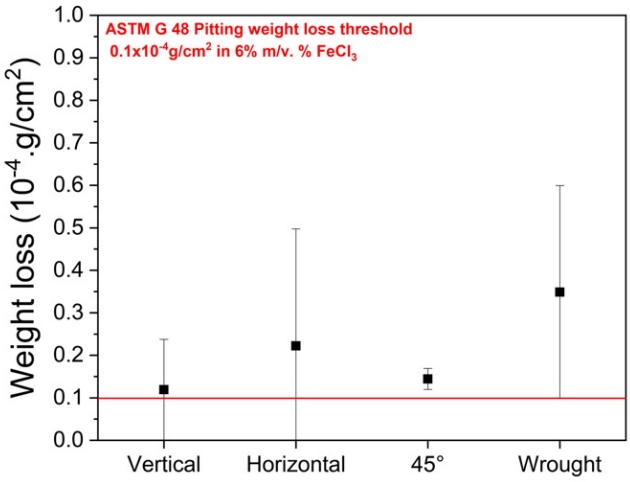

Figure 5: Weight loss measured the selective laser melted and wrought 316L stainless steel specimens after 72-hour exposure to $FeCl_3$ 6 wt. % at room temperature (21º C).

The average weight loss measured for the vertical, 45º and horizontal SLM 316L stainless steel specimens were 1.19 x 10^{-4} g/cm^2, 1.44 x 10^{-4} g/cm^2, and 2.22 x 10^{-4} g/cm^2 respectively. For the wrought 316L, the average weight loss was calculated as 3.48 x 10^{-4} g/cm^2. Therefore, considering the average weight losses measured for the 316L stainless steel, the resistance to pitting was superior for the vertical SLM followed by the 45, horizontal and wrought specimens as summarized in **Table 2**.

Table 2: Summary of weight loss for the SLM (Horizontal, Vertical and 45º) and wrought 316L specimens after immersion in 6% $FeCl_3$ solution for 48 hours at room temperature.

Sample	Weight Loss (10^{-4}. g/cm^2)
Vertical	**1.19 ± 1.18**
Horizontal	**2.22 ± 2.75**
45º	**1.44 ± 0.25**
Wrought	**3.48 ± 2.5**

Polarisation curves for the 316L specimens in 0.6 M NaCl revealed that the pitting potential (E_{pit}) values detected for the vertical, horizontal and 45º SLM stainless steel specimens were considerably higher than the one detected for their wrought counterpart (**Figure 6**). The average E_{pit} varied between 0.87 and 1.01 V_{SCE} for the SLM 316L specimens which was at least 0.45 V_{SCE} above the average E_{pit} recorded for the wrought 316L (0.25 V_{SCE}). Amidst the SLM specimens, the horizontal specimen presented the highest average E_{pit} (1.01 V_{SCE}) followed by the 45º (0.90 V_{SCE}) and vertical (0.87 V_{SCE}). Also, the corrosion current density (i_{corr}) and corrosion potential (E_{corr}) also varied between the 316L specimens as highlighted in **Figure 6**.

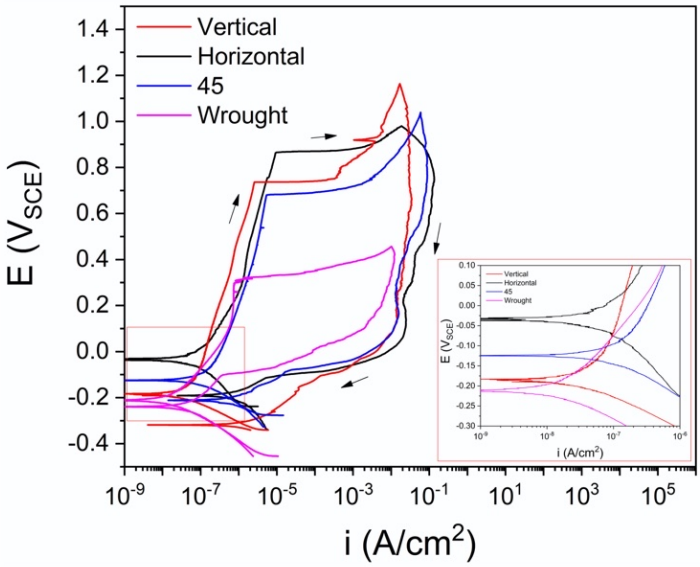

Figure 6: Representative cyclic-potentiodynamic polarisation curves for the selective laser melted and wrought 316L stainless steel samples in 0.6 M NaCl. The region showing the transition from the cathodic to the anodic overpotentials is highlighted in the red square inset.

The measured i_{corr} for the SLM 316Lstainless steel specimens were 0.019 A/cm^2, 0.027 A/cm^2 and 0.056 A/cm^2 for the horizontal, vertical and 45° build orientations respectively. Interestingly, the wrought 316L specimen showed i_{corr} value (0.59 A/cm^2) similar to the i_{corr} measured for the SLM 316L stainless steel specimen built at 45°. The E_{corr} values varied from - 0.198 V_{SCE} (for wrought specimen) to - 0.064 V_{SCE} (for the horizontal SLM specimen). The horizontal SLM 316L stainless steel specimen showed superior performance (i.e. resistance to corrosion) in 0.6 M NaCl than the SLM (vertical and 45°) and wrought counterparts. The findings obtained from the CPP testing in addition to each specimen porosity is summarised in **Table 3**.

Table 3: Summary of electrochemical response for the SLM (Horizontal, Vertical and 45°) and wrought 316L specimens in 0.6 M NaCl solution and their respective porosity.

Sample	i_{corr} (µA/cm^2)	E_{corr} (V_{SCE})	E_{pit} (V_{SCE})	E_{rep} (V_{SCE})	Porosity (%)
Vertical	**0.027 ± 0.018**	**-0.131 ± 0.019**	**0.87 ± 0.17**	**-0.19 ± 0.02**	**0.15 ± 0.09**
Horizontal	**0.019 ± 0.009**	**-0.064 ± 0.051**	**1.01 ± 0.16**	**-0.20 ± 0.06**	**0.14 ± 0.11**
45°	**0.056 ± 0.015**	**-0.098 ± 0.019**	**0.90 ± 0.21**	**-0.18 ± 0.03**	**0.43 ± 0.13**
Wrought	**0.059 ± 0.046**	**-0.198 ± 0.029**	**0.25 ± 0.04**	**-0.26 ± 0.03**	**-**

Discussion

Mechanical properties and residual stresses

The mechanical resistance to tensile stresses for the SLM 316L stainless steel (in the as-built state) was coherent with other studies previously reported in the literature [8]. Slightly higher yield strength was measured for the horizontal 316L stainless steel specimen as shown in **Table 1**. The build-oriented granular anisotropy observed on SLM 316L stainless steels specimens (**Figure 4**) have the potential to affect their mechanical response to tensile stresses. Depending on the orientation in which the tensile stress is applied, the deformation by yield stress can vary due to their characteristic grain anisotropy. Columnar and larger grains were parallel to the build orientation and to the applied stress for the vertical specimens. On the other hand, the force applied to the horizontal specimen was parallel to smaller and equiaxed grains. The 45º specimen showed a variation of smaller and larger grains and consequently presenting intermediary yield strength in comparison to the other two build orientations. Therefore, in accordance with the Hall-petch relationship, the horizontal specimen would have a higher yield strength point than their vertical and 45º counterparts as shown in **Table 1**.

Compressive residual stresses were measured for both horizontal and vertical SLM 316L stainless steel specimens. The nature of the residual stresses measured for these specimens would be expected to be similar. The reason is that both vertical and horizontal specimens differ solely by the length extension over the substrate. However, the 45º specimens were built at a unique orientation relative to the substrate. Consequently, the nature of residual stresses measured for the 45º specimen would potentially differ from their horizontal and vertical counterparts as it was observed in **Figure 2**. The heat transfer distribution during SLM may have been altered at 45º thus altering the stresses generated during the heating and cooling cycles. The solidification steps that lead to the generation of tensile stresses in SLM 316L stainless steel components will not be discussed in the scope of this manuscript, although further investigation on the subject should be thoroughly investigated.

Immersion and potentiodynamic tests

Based on the average weight loss values measured for the 316L stainless steel specimens after immersion testing in 6 wt. % $FeCl_3$ (**Figure 5**), the vertical SLM was more resistant to pitting than their SLM and wrought counterparts. However, according to the CPP testing carried out on the same specimens in 0.6 M NaCl showed that the horizontal SLM was more resistant to pitting (**Figure 6**). Fundamentally, both testing methods (immersion and electrochemical) do not represent the real interaction between metal and environment (in service) since corrosion processes or damage (especially for corrosion resistant alloys) usually take years. Instead, these testing techniques aim to simulate and predict the behaviour of metals and alloys in such corrosive environments in an accelerated fashion (from a couple of hours to a few days). In any case, valuable information can be drawn out from these predictions. For instance, it was observed that SLM 316L stainless

steel was less susceptible to damage from pitting than their wrought counterpart (**Figure 5**). Similarly, the same SLM 316L stainless steel specimens were less susceptible to pit initiation in comparison to the wrought 316L stainless steel as shown in **Figure 7**. The repassivation potential, or potential threshold to cease pit initiation and growth, was also higher for the SLM 316L specimens than for their wrought counterpart as shown in **Figure 7**. Between the SLM 316L stainless steel specimens investigated in the present work, the horizontal specimen was less susceptible to pit initiation (on average) then the 45º and vertical specimens, respectively. However, the E_{pit} values measured for all the SLM 316L stainless steel specimens ranged from approximately 0.7 V_{SCE} to ~ 1.15 V_{SCE}. The tendency to pit repassivation occurred in a similar fashion where E_{rep} values ranged from - 0.26 V_{SCE} to - 0.15 V_{SCE} for the SLM 316L stainless steel specimens (**Table 3**).

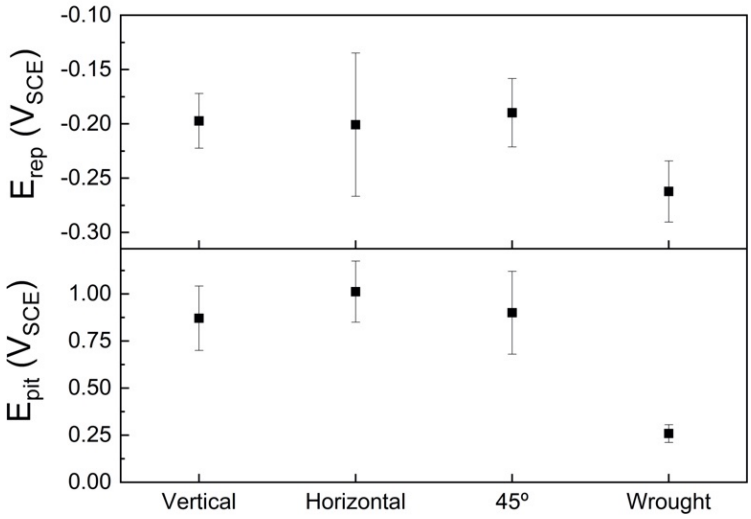

Figure 7: Repassivation potential and pitting potential for the wrought 316L and selective laser melted 316L specimens in 0.6 M NaCl as a function of build orientation.

The i_{corr} and E_{corr} values calculated from potentiodynamic polarisations are not usually critical to evaluate the corrosion resistance of corrosion resistant alloys such as stainless steels in 0.6 M NaCl whereas E_{pit} is more investigated for that matter. Nonetheless both i_{corr} and E_{corr} provide information on the interaction between the protective alloy surface and environment. Lower i_{corr} and higher E_{corr} values indicate that a more stable protective oxide layer (in the context of 316L in aerated NaCl solution) is formed on the surface. Once again, the SLM 316L stainless steel specimens investigated herein presented more stable protective oxide layers in 0.6 M NaCl than their wrought counterpart as shown in **Figure 8**. Porosity has been reported by Sander et al. [24] to have no significant negative effect on the resistance to pitting in SLM 316L stainless steel specimens when porosity values are below 0.4% in 0.1 M NaCl. Similar correlation was drawn out for 316L SLM polarised in 0.6 M NaCl as presented in **Table 3**.

Table 3. Porosity did not increase the susceptibility to pitting when the chloride concentration increases from 0.1 M to 0.6 M. Further evidence was given herein that indicated that low levels of porosity (< 0.4 %) do not

influence pit initiation in 316L stainless steels. It is important to note that other researchers have reported SLM 316L stainless steel components with reduced corrosion resistance relative to their respective wrought counterparts [22]. The conditions that influence such corrosion variability were not within the scope of the present work and should be addressed in future research.

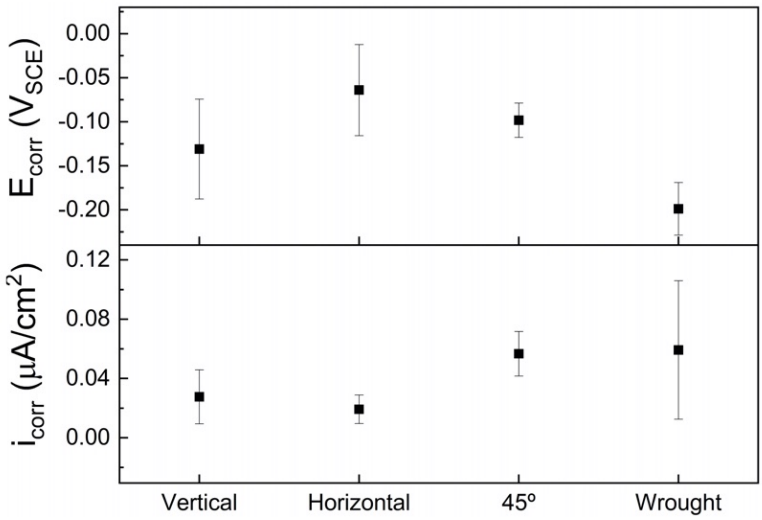

Figure 8: Corrosion potential and corrosion current density for the wrought 316L and selective laser melted 316L specimens in 0.6 M NaCl as a function of build orientation.

Influence of residual stress upon pitting

Residual stresses from the SLM of 316L stainless steel did not significantly influence the pitting characteristics of this alloy as observed in **Figure 9**. This was evidenced by similar E_{pit} values measured for the vertical and 45º SLM 316L stainless steel specimens despite the fact that compressive and tensile residual stresses were measured for these specimens in their as-built state, respectively. The horizontal SLM 316L stainless steel specimen presented slightly higher E_{pit} and lower average compressive residual stress than their vertical counterpart. Among other reasons larger grain size, lower compressive residual stresses and elemental segregation could have caused the higher pitting resistance observed for the horizontal SLM 316L stainless steel specimen.

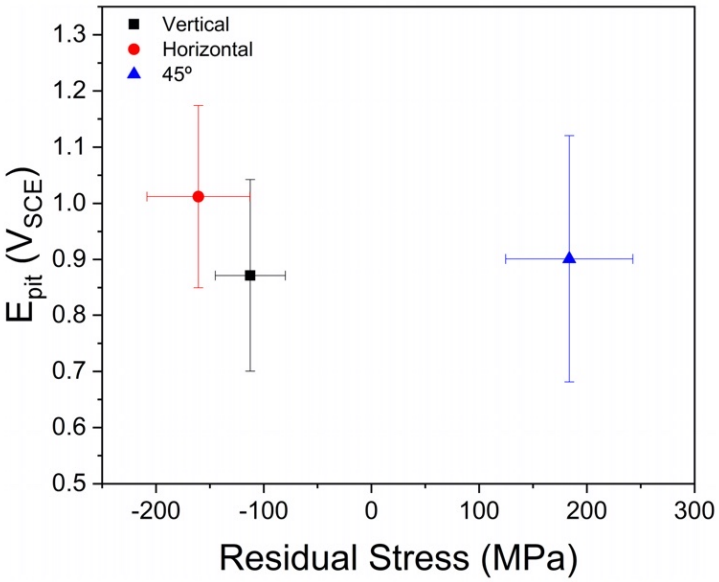

Figure 9: Pitting potential measured in 0.6 M NaCl solution as a function of residual stress from the selective laser melting of 316L stainless steel specimens.

Elemental segregation was investigated by TEM-EDXS in order to assess if chemical composition influenced pitting of the horizontal and vertical SLM 316L stainless steel specimens since both specimens had compressive residual stresses in their microstructure. Segregation of chromium (Cr), nickel (Ni) and molybdenum (Mo) upon the cell boundaries was detected by TEM-EDXS line scans for the vertical SLM 316L stainless steel specimen as observed in **Figure 10**.

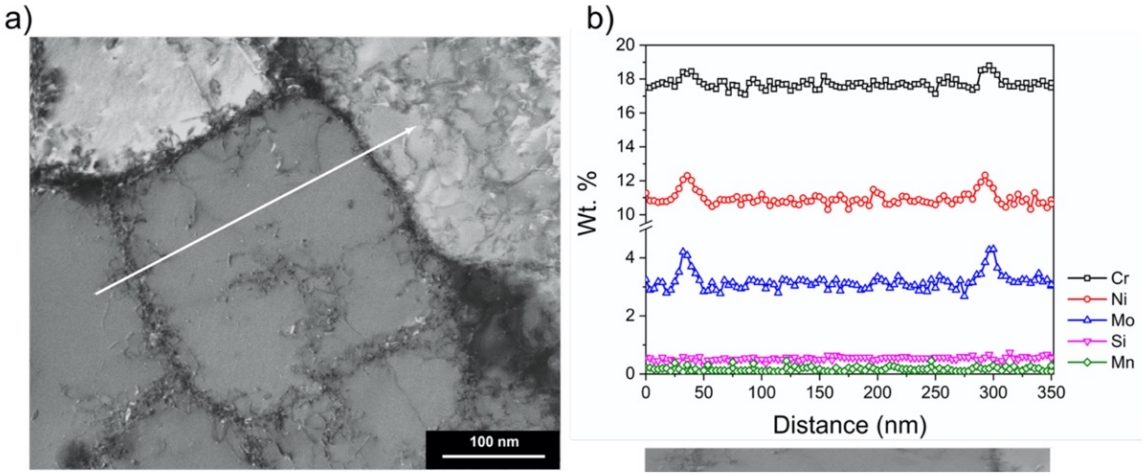

Figure 10: a) Bright-field transmission electron microscopy image highlighting the line scanned by energy diffraction x-ray spectrometry and b) chemical composition variation across the scanned line for the vertical selective laser melted 316L stainless steel specimen

Such sub-cells structure has been previously reported for SLM stainless steels [8]. Similar segregation was observed for the horizontal SLM 316L stainless steel specimen as shown in **Figure 11**, but in lower intensity. The higher nano-segregation (measured in wt. %) observed for the vertical specimen could explain their lower E_{pit} in comparison to the horizontal SLM 316L stainless steel specimen.

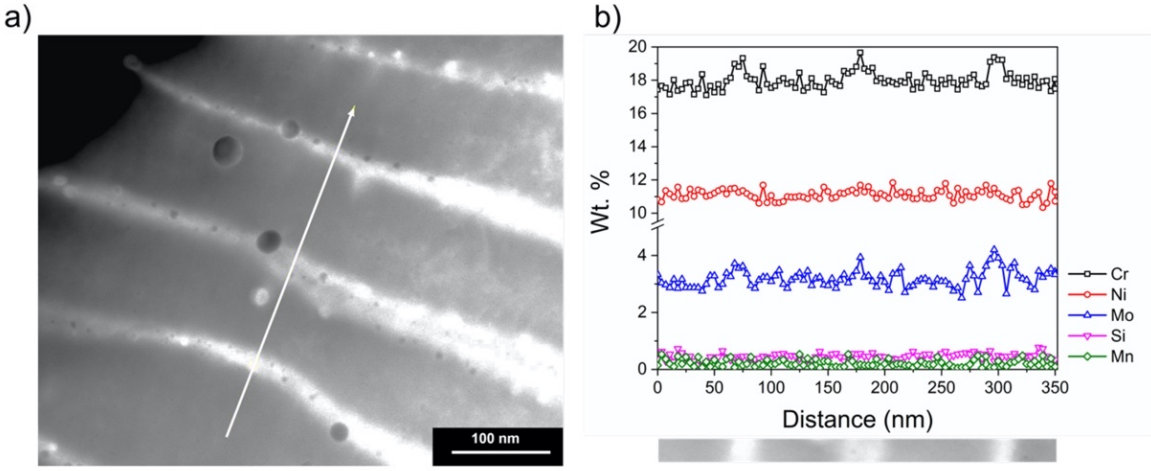

Figure 11: a) Bright-field transmission electron microscopy image highlighting the line scanned by energy diffraction x-ray spectrometry and b) chemical composition variation across the scanned line for the horizontal selective laser melted 316L stainless steel specimen.

Residual stresses measured for the SLM 316L stainless steel specimens (**Figure 2**) were seen to be considerably lower than their respective measured yield strength (**Table 1**), which is as-anticipated, and also commensurate with why component warpage is not seen in the SLM method. The measured residual stresses were of an elastic nature and are there defined as minor disturbances (i.e. strain) in the metallic unit cell. The cumulation of these minor lattice disturbances – on the order of fractions of an Angstrom – macroscopically affect the bulk of components [20]. Since residual stresses are distributed in static equilibrium over the lattice structure [40], their free surface must also be influenced by such stresses (however noting that the surface atoms are only several monolayers compared to the myriad of atomic layers in the bulk) the influence of residual stress is essentially influencing the bulk material. The lattice disturbances in the atomic structure of the free surface were not sufficient to disrupt the passivity hence increase the susceptibility of 316L stainless steel specimens to pitting as observed in **Figure 9**. Additionally, those disturbances were not overwhelming with respect to SLM build orientation based on the empirical testing herein. In other works, the residual stresses (thermal or mechanical) have been reported to be relevant for the performance of austenitic stainless steel components in the context of fatigue and stress corrosion cracking [41,42] – where the magnitude of the residual stress is additive in a stress related failure scenario. Therefore, residual stresses should not be universally assumed to be insignificant in the performance of SLM 316L stainless steel components - even though the free corrosion and pitting as studied herein were not impacted. However, based on extensive

investigation reported in the literature and the results presented herein, alloy chemistry appears to be a more critical factor to the pitting of SLM 316L stainless steel components than lattice configuration.

Conclusions

The findings from microstructural, residual stress, electrochemical and immersion investigations as carried out herein, may be summarised as follows:

1. Build orientation is a critical factor on the performance of metals and alloys produced by AM as it can directly affect their microstructure. Larger grains oriented parallel to the build direction were obtained for the horizontal orientation specimen while smaller and more equiaxed grains were observed for both vertical and 45º orientation specimens. This microstructural anisotropy was associated to extremely fast heating/cooling cycles and oriented thermal distribution during SLM.
2. The SLM 316L stainless steel specimens presented superior resistance to pitting and greater passive window than their respective wrought counterpart in 0.6 M NaCl. This finding was consistent, regardless of the SLM build orientation.
3. Compressive and tensile residual stresses were measured for the SLM 316L stainless steel specimens. However, the nature of the residual stress remnant from the SLM process did not seem to affect pitting resistance of 316L stainless steel in their as-built state. The small lattice disturbances caused by those residual stresses on the specimen free surface of SLM 316L stainless steel did not influence the disruption of their passivity and consequently their pitting susceptibility.
4. Nano segregation on the sub-cellular boundaries of the vertical SLM 316L stainless steel specimen was hypothesised to be responsible for a slightly lower pitting resistance in this build direction.
5. The horizontal build direction produced samples with the highest resistance against pitting among the investigated SLM 316L stainless steel specimens. However, the vertical and 45º SLM specimens performance against pitting did not differ significantly from the horizontal one.

CRediT authorship contribution statement

Guilherme Sander: Conceptualisation, Writing – Original Draft, Methodology, Investigation. **Abirami Babu**: Methodology. **Xiang Gao**: Methodology. **Derui Jiang**: Methodology. **Nick Birbilis**: Conceptualisation, Writing – Review & Editing

Declaration of Competing Interest

The authors declare that they have no known competing financial interests or personal relationships that could have appeared to influence the work reported in this paper.

Acknowledgements

We gratefully acknowledge the support of Woodside Energy, and also acknowledge the Monash Centre for Electron Microscopy (MCEM) where microscopy and microanalysis were performed. The technical assistance of Dr. Wenwen Sun is also acknowledged.

Data availability

The raw/processed data required to reproduce these findings can be shared upon request.

References

[1] M. Attaran, The rise of 3-D printing: The advantages of additive manufacturing over traditional manufacturing, Bus. Horiz. 60 (2017) 677–688. https://doi.org/10.1016/j.bushor.2017.05.011.

[2] T.T. Wohlers, Wohlers report 2019 : 3D printing and additive manufacturing state of the industry, 2019.

[3] T.D. Ngo, A. Kashani, G. Imbalzano, K.T.Q. Nguyen, D. Hui, Additive manufacturing (3D printing): A review of materials, methods, applications and challenges, Compos. Part B Eng. 143 (2018) 172–196. https://doi.org/10.1016/j.compositesb.2018.02.012.

[4] S. Bremen, W. Meiners, A. Diatlov, Selective Laser Melting, Laser Tech. J. 9 (2012) 33–38. https://doi.org/10.1002/latj.201290018.

[5] M. Schmidt, M. Merklein, D. Bourell, D. Dimitrov, T. Hausotte, K. Wegener, L. Overmeyer, F. Vollertsen, G.N. Levy, Laser based additive manufacturing in industry and academia, CIRP Ann. 66 (2017) 561–583. https://doi.org/10.1016/j.cirp.2017.05.011.

[6] D. Gu, Laser Additive Manufacturing of High-Performance Materials, 1st ed., Springer Berlin Heidelberg, Berlin, Heidelberg, 2015. https://doi.org/10.1007/978-3-662-46089-4.

[7] U. Scipioni Bertoli, G. Guss, S. Wu, M.J. Matthews, J.M. Schoenung, In-situ characterization of laser-powder interaction and cooling rates through high-speed imaging of powder bed fusion additive manufacturing, Mater. Des. 135 (2017) 385–396. https://doi.org/10.1016/j.matdes.2017.09.044.

[8] S. Gorsse, C. Hutchinson, M. Gouné, R. Banerjee, Additive manufacturing of metals: a brief review of the characteristic microstructures and properties of steels, Ti-6Al-4V and high-entropy alloys, Sci. Technol. Adv. Mater. 18 (2017) 584–610. https://doi.org/10.1080/14686996.2017.1361305.

[9] A. Yadollahi, N. Shamsaei, Y. Hammi, M.F. Horstemeyer, Quantification of tensile damage evolution in additive manufactured austenitic stainless steels, Mater. Sci. Eng. A. 657 (2016) 399–405. https://doi.org/10.1016/j.msea.2016.01.067.

[10] J. Suryawanshi, K.G. Prashanth, U. Ramamurty, Mechanical behavior of selective laser melted 316L stainless steel, Mater. Sci. Eng. A. 696 (2017) 113–121. https://doi.org/10.1016/j.msea.2017.04.058.

[11] J. Li, D. Deng, X. Hou, X. Wang, G. Ma, D. Wu, G. Zhang, Microstructure and performance optimisation of stainless steel formed by laser additive manufacturing, Mater. Sci. Technol. (United Kingdom). 32 (2016) 1223–1230. https://doi.org/10.1080/02670836.2015.1114774.

[12] S. Yusuf, Y. Chen, R. Boardman, S. Yang, N. Gao, Investigation on Porosity and Microhardness of 316L Stainless Steel Fabricated by Selective Laser Melting, Metals (Basel). 7 (2017) 64. https://doi.org/10.3390/met7020064.

[13] M.M. DEWIDAR, K.A. KHALIL, J.K. LIM, Processing and mechanical properties of porous 316L stainless steel for biomedical applications, Trans. Nonferrous Met. Soc. China (English Ed. 17 (2007) 468–473. https://doi.org/10.1016/S1003-6326(07)60117-4.

[14] K. Saeidi, Stainless steels fabricated by laser melting: Scaled-down structural hierarchies and microstructural heterogeneities, 2016.

[15] E. Yasa, J.P. Kruth, Microstructural investigation of selective laser melting 316L stainless steel parts exposed to laser re-melting, Procedia Eng. 19 (2011) 389–395. https://doi.org/10.1016/j.proeng.2011.11.130.

[16] T.M. Mower, M.J. Long, Mechanical behavior of additive manufactured, powder-bed laser-fused materials, Mater. Sci. Eng. A. 651 (2016) 198–213. https://doi.org/10.1016/j.msea.2015.10.068.

[17] D. Herzog, V. Seyda, E. Wycisk, C. Emmelmann, Additive manufacturing of metals, Acta Mater. 117 (2016) 371–392. https://doi.org/10.1016/j.actamat.2016.07.019.

[18] F. Bartolomeu, M. Buciumeanu, E. Pinto, N. Alves, O. Carvalho, F.S. Silva, G. Miranda, 316L stainless steel mechanical and tribological behavior—A comparison between selective laser melting, hot pressing and conventional casting, Addit. Manuf. 16 (2017) 81–89. https://doi.org/10.1016/j.addma.2017.05.007.

[19] L.E. Murr, A Metallographic Review of 3D Printing/Additive Manufacturing of Metal and Alloy Products and Components, Metallogr. Microstruct. Anal. 7 (2018) 103–132. https://doi.org/10.1007/s13632-018-0433-6.

[20] J.L. Bartlett, X. Li, An overview of residual stresses in metal powder bed fusion, Addit. Manuf. 27 (2019) 131–149. https://doi.org/10.1016/j.addma.2019.02.020.

[21] A.S. Wu, D.W. Brown, M. Kumar, G.F. Gallegos, W.E. King, An Experimental Investigation into Additive Manufacturing-Induced Residual Stresses in 316L Stainless Steel, Metall. Mater. Trans. A Phys. Metall. Mater. Sci. 45 (2014) 6260–6270. https://doi.org/10.1007/s11661-014-2549-x.

[22] G. Sander, J. Tan, P. Balan, O. Gharbi, D.R. Feenstra, L. Singer, S. Thomas, R.G. Kelly, J.R. Scully, N. Birbilis, Corrosion of additively manufactured alloys: A review, Corrosion. 74 (2018) 1318–1350. https://doi.org/10.5006/2926.

[23] X. Ni, D. Kong, W. Wu, L. Zhang, C. Dong, B. He, L. Lu, K. Wu, D. Zhu, Corrosion Behavior of 316L Stainless Steel Fabricated by Selective Laser Melting Under Different Scanning Speeds, J. Mater. Eng. Perform. 27 (2018). https://doi.org/10.1007/s11665-018-3446-z.

[24] G. Sander, S. Thomas, V. Cruz, M. Jurg, N. Birbilis, X. Gao, M. Brameld, C.R. Hutchinson, On The Corrosion and Metastable Pitting Characteristics of 316L Stainless Steel Produced by Selective Laser Melting, J. Electrochem. Soc. 164 (2017) C250–C257. https://doi.org/10.1149/2.0551706jes.

[25] C. Prieto, M. Singer, T. Cyders, D. Young, Investigation of Pitting Corrosion Initiation and Propagation of a Type 316L Stainless Steel Manufactured by the Direct Metal Laser Sintering Process, Corrosion. 75 (2018) 140–143. https://doi.org/10.5006/3075.

[26] Q. Chao, V. Cruz, S. Thomas, N. Birbilis, P. Collins, A. Taylor, P.D. Hodgson, D. Fabijanic, On the enhanced corrosion resistance of a selective laser melted austenitic stainless steel, Scr. Mater. 141 (2017) 94–98. https://doi.org/10.1016/j.scriptamat.2017.07.037.

[27] X. Lou, M.A. Othon, R.B. Rebak, Corrosion fatigue crack growth of laser additively-manufactured 316L stainless steel in high temperature water, Corros. Sci. 127 (2017) 120–130. https://doi.org/10.1016/j.corsci.2017.08.023.

[28] C. Man, Z. Duan, Z. Cui, C. Dong, D. Kong, T. Liu, S. Chen, X. Wang, The effect of sub-grain structure on intergranular corrosion of 316L stainless steel fabricated via selective laser melting, Mater. Lett. 243 (2019) 157–160. https://doi.org/10.1016/j.matlet.2019.02.047.

[29] J.R. Trelewicz, G.P. Halada, O.K. Donaldson, G. Manogharan, Microstructure and Corrosion Resistance of Laser Additively Manufactured 316L Stainless Steel, Jom. 68 (2016) 850–859. https://doi.org/10.1007/s11837-016-1822-4.

[30] V. Cruz, Q. Chao, N. Birbilis, D. Fabijanic, P.D. Hodgson, S. Thomas, Electrochemical studies on the effect of residual stress on the corrosion of 316L manufactured by selective laser melting, Corros. Sci. 164 (2020) 108314. https://doi.org/10.1016/j.corsci.2019.108314.

[31] M.P. Ryan, D.E. Williams, R.J. Chater, B.M. Hutton, D.S. McPhail, Why stainless steel corrodes, Nature. 415 (2002) 770–774. https://doi.org/10.1038/415770a.

[32] Y. Sun, A. Moroz, K. Alrbaey, Sliding wear characteristics and corrosion behaviour of selective laser melted 316L stainless steel, J. Mater. Eng. Perform. 23 (2014) 518–526. https://doi.org/10.1007/s11665-013-0784-8.

[33] A.B. Kale, J. Singh, B.-K. Kim, D.-I. Kim, S.-H. Choi, Effect of initial microstructure on the deformation

heterogeneities of 316L stainless steels fabricated by selective laser melting processing, J. Mater. Res. Technol. 9 (2020) 8867–8883. https://doi.org/10.1016/j.jmrt.2020.06.015.

[34] ASTM G48-11, Standard Test Methods for Pitting and Crevice Corrosion Resistance of Stainless, ASTM Internaltional. 11 (2011) 1–11. https://doi.org/10.1520/G0048-11R15.Copyright.

[35] I. Gibson, D. Rosen, B. Stucker, Additive Manufacturing Technologies, Springer New York, New York, NY, 2015. https://doi.org/10.1007/978-1-4939-2113-3.

[36] N.J. Laycock, R.C. Newman, Localised dissolution kinetics, salt films and pitting potentials, Corros. Sci. 39 (1997) 1771–1790. https://doi.org/10.1016/S0010-938X(97)00049-8.

[37] D.E. Williams, Y.Y. Zhu, Explanation for Initiation of Pitting Corrosion of Stainless Steels at Sulfide Inclusions, J. Electrochem. Soc. 147 (2000) 1763. https://doi.org/10.1149/1.1393431.

[38] D.E. Williams, M.R. Kilburn, J. Cliff, G.I.N. Waterhouse, Composition changes around sulphide inclusions in stainless steels, and implications for the initiation of pitting corrosion, Corros. Sci. 52 (2010) 3702–3716. https://doi.org/10.1016/j.corsci.2010.07.021.

[39] S. Mishra, K. Narasimhan, I. Samajdar, Deformation twinning in AISI 316L austenitic stainless steel: Role of strain and strain path, Mater. Sci. Technol. 23 (2007) 1118–1126. https://doi.org/10.1179/174328407X213242.

[40] G. Totten, M. Howes, T. Inoue, Handbook of Residual Stress and Deformation of Steel, ASM International, 2002.

[41] G. Van Boven, W. Chen, R. Rogge, The role of residual stress in neutral pH stress corrosion cracking of pipeline steels. Part I: Pitting and cracking occurrence, Acta Mater. 55 (2007) 29–42. https://doi.org/10.1016/j.actamat.2006.08.037.

[42] O. Takakuwa, H. Soyama, Effect of Residual Stress on the Corrosion Behavior of Austenitic Stainless Steel, Adv. Chem. Eng. Sci. 05 (2015) 62–71. https://doi.org/10.4236/aces.2015.51007.

Chapter 5: On the in-situ characterisation of metastable pitting using 316L stainless steel as a case study

Due to its critical importance on the performance of metals and alloys, a comprehension of the mechanisms typical to pitting has been the aim of several industrial and academic studies over the years. By definition, the development of pits in corrosion resistant alloys follow three sequential steps, that are: nucleation, metastable pitting and stable pitting.

The nucleation of a pit arises from the disruption of the protective surface layer of corrosion resistant alloys (i.e. a local deviation from the passive state). This protective layer breakdown can be triggered by components in the solution in contact with the surface, by defects on the surface, by weak points in the protective layer or by the existence of microgalvanic coupling from microstructural variations. Once a pit has nucleated, it enters a metastable state and it will either repassivate or develop into a stable growth state. The pit is called stable once the healing of the protective layer is hindered inside that pit. This inability to heal or repassivate the pit surface is usually caused by secondary products from electrochemical reactions in the pitting site. These sub-products sustain further metal dissolution hence creating an autocatalytic reaction site.

For this chapter, the metastable pitting of 316L was investigated by in-situ surface imaging simultaneously to potentiostatic polarisation techniques. In Chapter 3, this method was used to great success for the determination of pitting (quantitatively) for specimens with very small variations in processing parameters (and the same bulk composition). That study – whilst successful, made it clear that the method employed can serve to answer fundamental questions in the pitting of metals and alloys, that are yet to be determined. As a consequence, a 'deep dive' into the method was carried out to further advance the findings in this thesis. Herein, a custom electrochemical cell was produced to sustain in-situ imaging during the electrochemical testing. The development of an analytical code was also carried out, and shared in an open access platform to facilitate the analysis of the data obtained by potentiostatic polarisation testing by others.

The current chapter was prepared as a journal article and is under submission in ***Corrosion Science***. The review article appears here as re-submitted following peer review.

On the in-situ characterisation of metastable pitting using 316L stainless steel as a case study

Guilherme Sander[a, b, 1], Victor Cruz[a, b], Ninad Bhat[c,d], Nick Birbilis[d]

[a]Department of Materials Science and Engineering, Monash University, Clayton, Victoria, 3800, Australia

[b]Woodside Innovation Centre, Monash University, Clayton, Victoria, 3800, Australia

[c]Indian Institute of Technology Bombay, Powai, Maharashtra, 400076, India

[d]College of Engineering and Computer Science, The Australian National University, Acton, A.C.T., 2601, Australia.

[1]Corresponding author: guilherme.sandermalab@monash.edu

Keywords: pitting corrosion; stainless steel; potentiostatic; polarisation; electrochemical calculation

Abstract

Metastable pitting upon 316L stainless steel was studied herein. The combination of electrochemical testing, in-situ imaging and ex-situ characterisation was carried out to address the following questions: Does each metastable pit site correspond to a single current transient or do multiple metastable pits occur at the same site? Is each recorded current transient a unique individual metastable pitting event? Does the calculated metal loss from electrochemical testing reconcile to physical damage? The results herein respond to these questions, and additionally, a user tool for analysis of metastable pitting is also presented herein.

Introduction

Localised corrosion that commences in the form of pitting is a typical corrosion initiation process in the case of stainless steels, particularly in marine environments [1]. Failure of stainless steel components is not typically a result of pitting initiation alone, but from corrosion propagation from pit sites. The stages in which pits develop are commonly described by pit nucleation, metastable pitting, and ultimately, stable pitting [2–5]. Pit nucleation can occur when the passive layer formed on the surface of stainless steels is 'broken', exposing the underlying metal to the electrolyte [6,7]. Chromium oxide (Cr_2O_3) can serve as a passive layer upon on stainless steels [8], with chromium oxide being formed spontaneously on the surface of stainless steels in contact with oxygen - when the chromium (Cr) concentration is higher than ~11 wt. % [1]. The so-called 'breakdown' of the passive layer is aided by a number of factors, that may include: aggressive anions such as chloride ions (Cl^-), which can locally disturb the chromium oxide structure [7]; the presence of microstructural and surface defects such as impurities or embedded particles [7,9,10]; the segregation of alloying elements (including alloy sensitisation from thermal exposure) [1,11], and the presence of deleterious phases that disrupt local oxide uniformity, such as sulphide inclusions [12,13]. Immediately following passive layer breakdown, the exposed active metal surface may react with the electrolyte, and so-called metastable pitting occurs [3]. Metastable pitting is the intermediate step prior to either repassivation of the newly nucleated pit (by restoration of the Cr_2O_3 layer), or the further and sustained dissolution of the metastable pit resulting in the transition to stable pit growth [14]. A quantification of this phenomenology has been given by the following expression that defines the local current necessary to sustain pitting and prevent repassivation as $i_x > (i_x)_{crit}$ [15,16]. Frankel et al. [10,14,17] demonstrated that once the passive layer is broken, a cover is formed over the metastable pit mouth from the remnant protective oxide (or from the concomitant formation of corrosion products). The presence of this pit cover may sustain dissolution of the underlying metal until the cover is ruptured [18]. Ernst and Newman [19] also demonstrated that the pit cover shape and perforation density are sensitive to the concentration of Cl^- anions in the bulk electrolyte. The mix of entrapped pit anolyte and bulk electrolyte after the perforation of the pit cover allows the repassivation of the metastable pit - provided that the metal dissolution occurs below a critical pit stability product [20]. Stable pits grow due to their autocatalytic nature in which the cations released from the anodic reactions can be hydrolysed, increasing the acidity inside the pit [3,10], and this process may also be aided by the recycling of Cl^- ions that are soluble following their reaction with metal species.

The presence of a locally acidic environment within pits is detrimental to repassivation of the pit. Other factors such as the capacity of ions to diffuse to the reaction sites and the charge balance between corrosion products and bulk electrolyte also influence stable pit growth [2,7,18].

Susceptibility to pitting is commonly evaluated by exposure testing or electrochemical tests [21,22]. Both techniques provide information regarding aspects of corrosion and allow the comparison of the pitting resistance for different specimens. In the context of 316L stainless steel, exposure tests usually consist of the immersion of 316L into a 6 wt. % iron chloride (III) ($FeCl_3$) solution over a minimum of 72 hours (ASTM G48[23]). Exposed specimens are measured for weight loss, whilst the number of pits on the surface may be quantified by optical microscopy. Conversely, electrochemical characterisation of pitting is performed by potentiodynamic and potentiostatic polarisation techniques. Potentiodynamic tests reveal a range of information including corrosion current density, corrosion potential, passive current density, passive range, pitting (breakdown) potential and repassivation potential – also providing information regarding the kinetics of anodic and cathodic processes. For potentiostatic polarisation testing however, the applied potential is fixed, with tests providing information regarding the alloy interaction with the test electrolyte at specified potential. The benefit of potentiostatic testing, is that when a constant applied potential is proximate to (but *not* more anodic than) the pitting potential, the measured current signal is able to (electrochemically) reveal the propensity to metastable pitting. Consequently, potentiostatic testing and the analysis of the resultant current transient signals may be used as a quantitative assessment tool in the context of quantification of metastable pitting rates – which have been demonstrated to be proportional to an alloys susceptibility to stable pitting via a quantifiable 'death rate' as shown by Williams et. al [24]. Examples in the literature have shown that the application of potentiostatic testing to compare the pitting susceptibility of different alloys [25–29] or the same alloy in different environments [30–32] has been successful. By quantifying metastable pitting events, potentiostatic testing could permit the quantification of pit susceptibility of an alloy in a different manner, i.e. by how much pitting would occur (as opposed to the assessment of pitting by the pitting potential, which is a singular value that doesn't relate to pit propensity), and thus also provide a quantitative index to the pitting resistance in a given environment and for a given alloy.

None the less, in the utilisation of potentiostatic testing as a means for studying pitting of engineering alloys, there still remains important research in the context of physical validation and in probing some yet to be resolved questions, that can be addressed by the assessment of

current transients in-situ. Understanding these aspects will permit a more nuanced understanding of the results arising from potentiostatic testing. The in-situ optical imaging characterisation of pitting has been previously reported in literature for aluminium and iron (Fe) alloys [33–42]. However, high magnification and high-resolution video recording of micrometric metastable pitting events for 316L stainless steel has not been carried out to date; nor has such high magnification analysis such as that herein been attempted in any prior study (for any material type).

In the present work, a combination of electrochemical testing and in-situ optical imaging was applied to characterise metastable pitting of 316L stainless steel with the aim answering the following questions:

1) Is each metastable pitting site that corresponds to a current transient a unique site, or can multiple metastable pits occur on the same site?
2) Current transients are associated to the metastable pitting events on the metal surface. Is the metal loss calculated by Faraday's law and damage from the metastable pitting (dissolution) process the same?
3) Is each current transient measured from potentiostatic testing representative of one unique individual metastable pitting event?

Furthermore, the development of a software tool to aid researchers in the analysis of metastable pitting data was also developed and utilised, and the open source details of which are provided herein.

Experimental

Sample preparation

Wrought AISI 316L stainless steel, supplied by Interalloy (Victoria, Australia), was employed to perform the in-situ image characterisation of metastable pitting. Electrochemical test specimens were prepared by mounting small cubes (10 x 5 x 10 mm^3) in epoxy resin with one surface exposed on one side and wires attached on the opposite surface for electrical connection. The exposed face was metallographically prepared being successively ground using silicon carbide (SiC) paper to a 2500 grit finish followed by polishing using diamond paste suspensions to a 0.1 μm mirror finish. After surface preparation, the 316L specimens were cleaned ultra-sonically and dried using compressed air prior to electrochemical testing.

Electrical insulation was implemented by applying enamel lacquer on the metal/epoxy interfaces to prevent crevice corrosion.

Potentiodynamic polarisation

Cyclic-potentiodynamic polarisation (CPP) was performed on the mounted specimens working electrode (with 0.5 cm^2 exposed area) introduced into an electrochemical flat cell (Model K0235) with saturated calomel electrode (SCE) as the reference electrode and platinum mesh as the counter electrode forming a standard three-electrode setup. Sodium chloride (NaCl) solution was used as the electrolyte with a concentration of 0.1 M at 21 ºC as in previous work [28] to avoid the overlap of metastable pitting electrochemical response which allowed those pits to be correlated the current transients obtained from potentiostatic polarisation. The CPP tests were performed using a scan rate of 1mV/s, commencing from -0.25 V (vs. OCP) to +1.0 V_{SCE} having the scan direction reversed when current density values reached 100 µA/cm^2. Prior to polarisation, specimens were allowed to stabilise in the test electrolyte for 10 minutes, during which the open circuit potentials (OCP) of the specimens were measured. To ensure reproducibility and consistency of the data collected, the CPP was repeated 3 times for the 316L stainless steel specimen.

In-situ imaging of potentiostatic polarisation tests

In-situ imaging of the specimens' surface simultaneously to their potentiostatic polarisation was carried out using a custom electrochemical cell fashioned by a computer aided design (CAD) software (**Figure 1a**) and additively manufactured by fused deposition modelling having a nylon-carbon fibre composite as build material. The custom electrochemical cell was designed to: arrest the 316L specimen in a chamber immersed with electrolyte; support the placement of the required electrical connections and electrodes; and provide an aperture for the optical microscope insertion as shown in **Figure 1b**. Images of the exposed surface were recorded utilising a high definition camera linked to the inserted optical microscope as shown in **Figure 1c**.

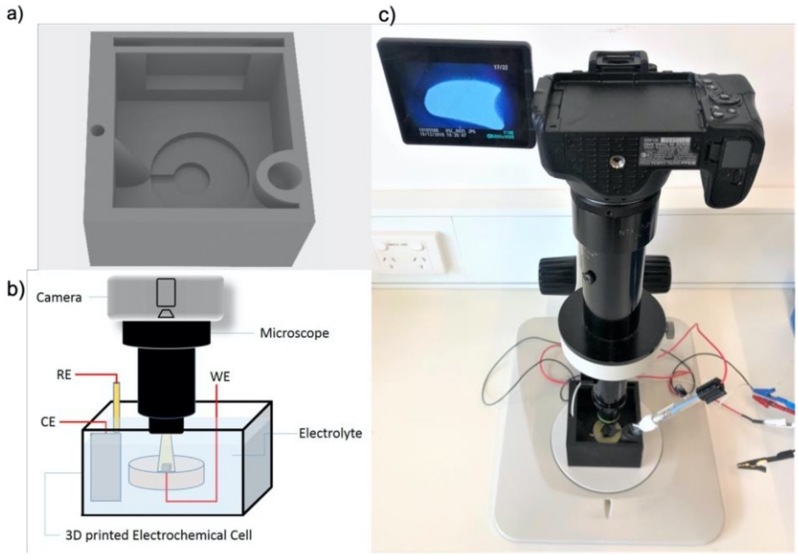

Figure 1: Electrochemical cell utilised for the in-situ imaging of the chronoamperometry tests: a) computer aided design (CAD) rendering of the custom electrochemical cell; b) schematics showing the placement of the camera, microscope and working (WE), reference (RE) and counter (CE) electrodes in relation to the 3D printed electrochemical cell; c) Experimental set up utilised for the in-situ imaging showing the camera, microscope and custom electrochemical cell. The camera screen displayed the surface of the working electrode while reference and counter electrodes were also placed in the cell.

Enamel lacquer was utilised to tailor the working electrode exposed surface area as shown in **Table 1** so the whole exposed area was imaged preventing the occurrence of metastable pitting events outside the scope of the microscope and limit the number of pitting events detected.

Table 1: Working electrode area under potentiostatic polarisation in 0.1 M NaCl for Samples I, II and III.

	Sample I	**Sample II**	**Sample III**
Working electrode area (10^{-4} x cm^2)	4.38	7.14	11.96

The imaged potentiostatic polarisation tests were performed on the mounted 316L stainless steel to promote metastable pitting. Samples were tested in the custom set-up presented in **Figure 1b** at fixed potentials of 0.025 V below (Sample I), equal to (Sample III) and 0.05 V above (Sample II), the wrought SLM 316L average pitting potential value obtained by CPP (0.30 V_{SCE}). Prior to the potentiostatic polarisation testing, each specimen was held at the open

circuit potential (OCP) for 10 minutes. The fixed potentials were applied to samples I, II and III in 0.1 M NaCl solution at 21 ºC for 30, 16 and 4 minutes respectively. The testing time periods were chosen based on the electrochemical response and the pits formed on the exposed surface of the samples and their values will be further discussed in the following sections of this work.

Metastable pit profilometry

Profilometry was performed upon the exposed surface of sample III after potentiostatic polarisation. A Veeco WYKO NT1100 optical profilometer was used to measure the volume and depth of pits that were formed during potentiostatic polarisation. Prior to volume measurements, sample III surface was ultrasonically cleaned with deionised water and thoroughly dried by a compressed air gun to remove any reminiscent corrosion products from the pit surface. The metastable pit volumes and profilometry profiles were plotted utilising the Veeco Vision software attached to the measuring apparatus. The measurements were carried out on an area of 159.8 µm x 112.8 µm surrounding the metastable pits and the optical profilometry depth resolution was 0.1 nm.

Automated metastable pitting analysis

In this study, a metastable pitting analyser (MPA) was also developed as a user-friendly tool to analyse the output electrochemical data from potentiostatic polarisation tests. This tool was developed into a piece of custom software (freeware) that automates the calculation of common metastable pitting related outputs [25,30] such as: the number of current transients over time (metastable pit frequency); the density of electrons detected by the potentiostat during the potentiostatic polarisation (charge passed); and the total number of current density transients. It noted that these parameters were normalised by the *total* exposed area for each specimen to create baseline values that allow the comparison of the results presented herein, to other systems [3,14,43–48]. The MPA software was created utilising a Python® scripted code and freely available at www.metastablepitting.com. The functionality of the MPA relies on data input from the user, requiring them to provide data files with current density in A/cm^2 and the polarisation time in seconds. Once a data file is uploaded to the MPA, a plot is produced, of current density as a function of time – along with the abovementioned outputs displayed. This software was created in order to work as user friendly tool for analysis of metastable pitting events – since this analytical process is not included in commercial software for

electrochemical analysis. The calculation parameters utilised are explained in the following paragraphs (however it is noted that users of the MPA have the freedom to change those calculation settings to adapt their data analysis to their respective studies).

In order to identify the current transients (i.e. peaks), the MPA software code evaluated each *i* vs. *t* data point, taking into consideration sequential data points before and after each data point in order to detect transient events. Following the work performed by Cavanaugh et al.[30], a pit was considered metastable if four conditions were met: (i) the current density was increased by at least 1.5% from the baseline current density; (ii) the current density increase was sustained for more than 1.5 seconds; (iii) the current density also decreased by 1.5% after a peak (or maximum value); and (iv) the current density eventually returned to the baseline indicating that no stable pitting was initiated. The baseline was considered to be the passive current density (usually in nA/cm^2) where no current transients were detected, and no appreciable corrosion of the metal occurred under the passive layer. The MPA software allows the user to analyse current transients (i.e. peaks) in a "Relative" mode as described above and in an "Absolute" mode. The former requires an input from the user to define the baseline based on a specific current density value (Threshold Value). In "Absolute" mode, the code considers a peak to be transients that surpass the inputted baseline value. The "Relative" mode also allowed the MPA user to change the percentage (condition '(i)' described above) in which the current density values should increase to be considered a peak (Peak Height). Once data is uploaded to the MPA software, a curve is plotted as a function $i\,(t)$ for the appropriate calculations where i is the current density and t is the experiment time. The charge passed (in C/cm^2) on the metal surface will be calculated by integrating the $i\,(t)$ function as shown in **Equation 1**, where t_1 is the initial and t_2 is the final analysed period.

$$\text{charge} = \int_{t1}^{t2} i\,(t)\,dt$$

(**Equation 2**)

The charge calculations are automated to be performed for the whole data set (i.e. the whole of the *i* vs *t* curve) once the "Calculate" option is selected in the "Results" section. Additionally, the MPA software allows the use to analyse individual (or many) pits by manually selecting an area of the curve either from two specific time values or from a specific tailored region of the plotted data.

The metastable pit frequency, mpf (in $s^{-1}.cm^{-2}$), was calculated by dividing the number of current density transients by the total experiment time and exposed area as shown in **Equation**

2.

$$\text{mpf} = \frac{\text{number of peaks}}{\text{time} \times \text{area}}$$

(**Equation 2**)

Figure 2 shows a demonstrative graph plotted utilising the website highlighting the main features described above.

Figure 2: Metastable pitting analyser website highlighting the raw data representation plotted (demonstrative), the input options available for the user and the outputs obtained by the data analysis.

In the development of the MPA software, peaks were also counted manually for each specimen and the resulting mpf was compared to MPA results. The charge passed on the surface during the transient events was also calculated utilising the integration tool available in Origin®, which allows the user to select an arbitrary range of data on a graph, using the region of interest (ROI) object. The ROI was selected from the initial recording time (t= 0) to the respective final time for samples I, II and III.

Results

Potentiodynamic polarisation of 316L stainless steel

Cyclic potentiodynamic polarisation (CPP) was utilised to determine the average pitting potential and average repassivation potential for 316L stainless steel in 0.1 M NaCl as shown in **Table 2**.

Table 2: Average pitting potential and repassivation potential of the wrought 316L stainless steel obtained by cyclic-potentiodynamic polarisation in 0.1 M NaCl.

Pitting potential (V_{SCE})	Repassivation potential (V_{SCE})
+ 0.30 ± 0.03	+ 0.03 ± 0.01

A representative CPP curve for 316L specimens is presented in **Figure 3**. The average pitting potential obtained was utilised as reference for the applied potential during potentiostatic polarisation tests.

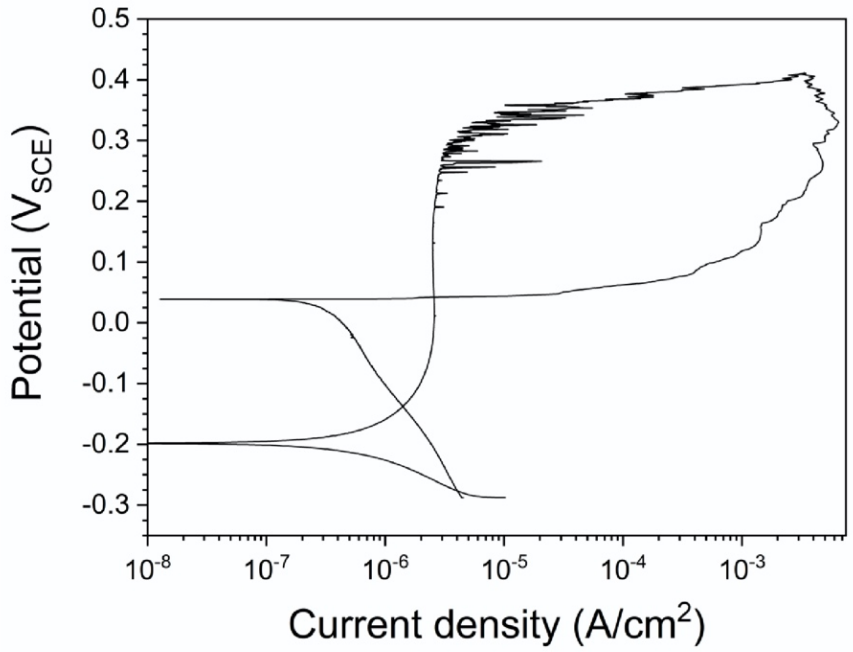

Figure 3: Representative cyclic potentiodynamic polarisation of wrought 316L in 0.1 M NaCl.

In-situ imaging of potentiostatic polarisation of 316L stainless steel

The 316L stainless steel samples were tested to observe their metastable pitting behaviour when potentiostatically polarised at fixed potentials in 0.1 M NaCl, namely for three different conditions termed I, II and III. Test condition I (referred to as Sample I) correlates to polarisation at + 0.275 V_{SCE} (which is 0.025 V below the average pitting potential of 316L) for 30 minutes, and the current density versus time was plotted as presented in **Figure 4**.

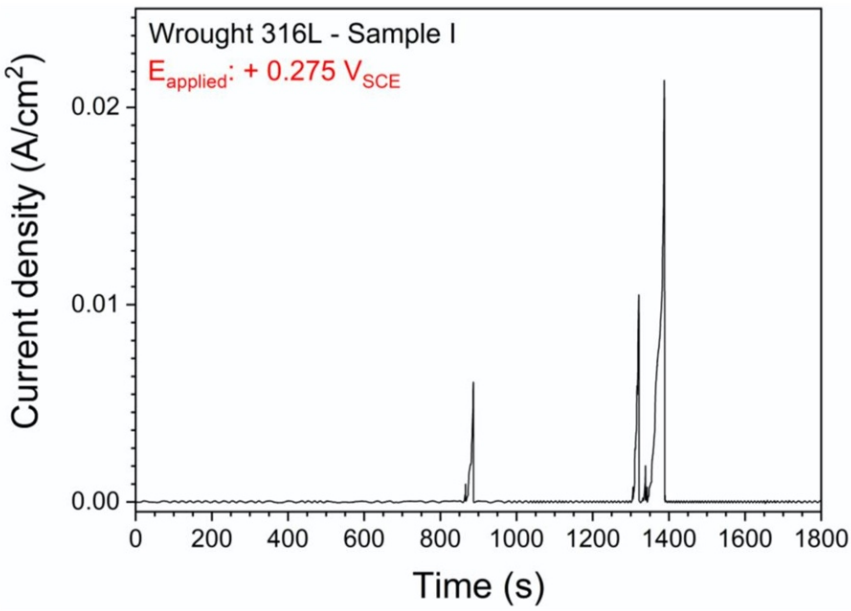

Figure 4: Chronoamperometry of the wrought 316L - Sample I in 0.1 M NaCl. The potential was fixed at + 0.275 V_{SCE}.

Current density transients were observed between 800 and 1400 seconds evidencing the occurrence of metastable pits [14]. The mpf for Sample I was calculated by utilising the MPA software presenting mpf of 15.5 $s^{-1}.cm^{-2}$. The charge passed on the surface, or total area under the current density transients was also measured by two different methods. The MPA software (in an automated manner) provided a charge of 0.408 C/cm^2 and curve integration utilising Origin® (which is a manual process conducted for sense-checking) also provided a charge of 0.408 C/cm^2. Mass loss (g) was calculated by Faraday's law as shown in **Equation 3**.

$$\text{mass loss} = \frac{\text{equivalent weight} \times \text{total charge}}{\text{Faraday's constant}}$$

(**Equation 3**)

Where the 'equivalent weight' corresponds to the atomic mass of the corrosion products

divided by their respective valences (g/mol) and Faraday's constant is 96,485 C/mol. For 316L stainless steel, congruent dissolution was considered to calculate the equivalent weight of pitting products. The chemical composition of 316L stainless was approximated to 18 wt. %, 14 wt. % and 3 wt. % for Cr, nickel and molybdenum respectively. The remaining wt. % was balanced with Fe (65 wt. %). The stoichiometric proportion of the '316L cation' product (Fe^{2+}, Cr^{3+}, Ni^{2+}, and Mo^{3+}; z = 2.2) specified by Srinivasan and Kelly [49] was employed for the mass loss calculations carried out herein.

The total mass loss after potentiostatic polarisation was calculated by Faraday's law utilising the total charge being 4.78 x 10^{-8} g for both MPA and Origin® measurements. The total charge values utilised for such mass loss measurements in this work was ***not*** normalised by area, as it was simply determined by the associated 'charge passed on the surface'. Consequently, these total charge values can be correlated intrinsically to the loss of mass caused by the observed metastable pits. This is an important not to make, as the local current density at metastable pit sites may be intense (but difficult to calculate as the local metastable pit site area is unknown (and even if it were, it would be a temporally evolving area). The initial surface of Sample I (prior to the potentiostatic polarisation) and after 30 minutes of polarisation at + 0.275 V_{SCE} is shown in **Figure 5**.

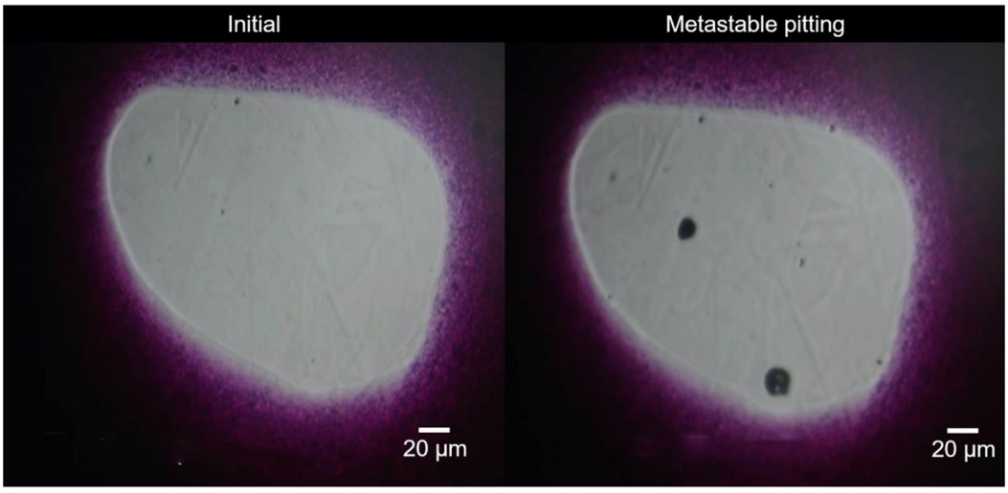

Figure 5: Snapshots of the surface of the Wrought 316L - Sample I - in the initial state (before potentiostatic polarisation) and the surface with metastable pits (after potentiostatic polarisation).

The comparison between the initial and final stages evidenced the presence of pits formed on the surface after potentiostatic polarisation. Sample II was polarised at + 0.35 V_{SCE} (0.05 V

above the average pitting potential to induce stable pit) for 16 minutes and the current density was measured as shown in **Figure 6**. The current density transients were observed between 400 and 800 seconds, characterising the presence of metastable pits. In addition, posteriorly to approximately 850 seconds the current density showed a constant increase with no repassivation which was associated with pitting followed by crevice corrosion. The peaks in **Figure 6** related to metastable pitting (highlighted) calculated by the MPA resulting in mpf of 78.31 $s^{-1}.cm^{-2}$. The charge passed on the surface of Sample II during potentiostatic polarisation testing was 0.193 C/cm^2 calculated by Origin® and 0.197 C/cm^2 by MPA software.

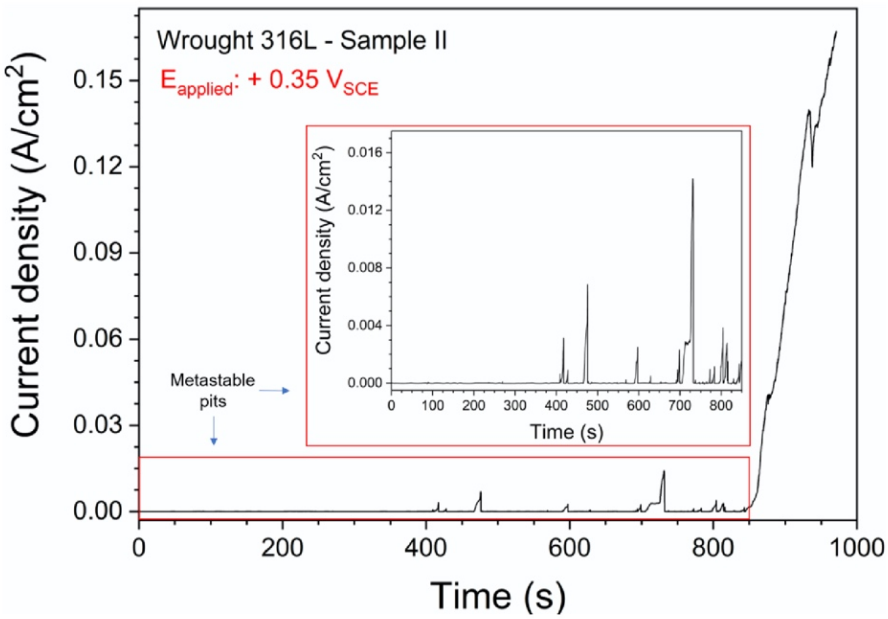

Figure 6: Chronoamperometry of the wrought 316L - Sample II in 0.1 M NaCl. The potential was fixed at + 0.35 V_{SCE}. The region with the occurrence of metastable pitting was highlighted and amplified. The stable pit was also indicated.

The region under the stable pitting region was not considered for the charge measurements of Sample II. Mass loss was calculated for the metastable pits in Sample II based on the total charge obtained from Origin® and MPA software being 3.68 x 10^{-8} g and 3.76 x 10^{-8} g respectively. The initial state, the metastable pits and stable pit formed on the surface of Sample II after 16 minutes of potentiostatic polarisation at + 0.35V_{SCE} are shown in **Figure 7**.

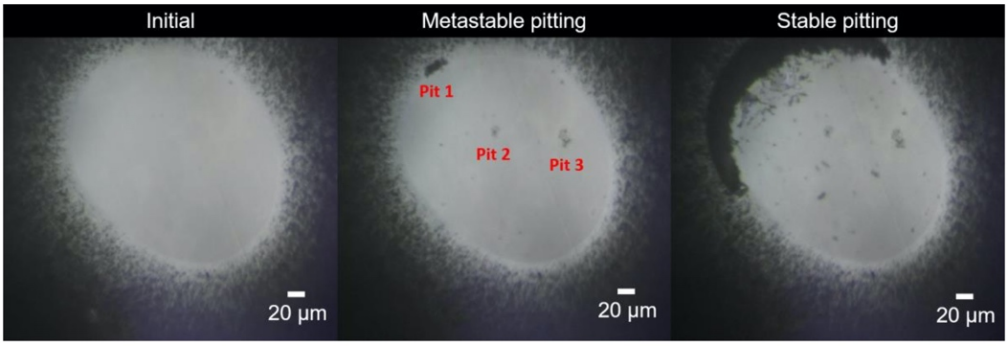

Figure 7: Snapshots of the surface of the Wrought 316L - Sample I - in the initial state (before potentiostatic polarisation), the surface with metastable and stable pits (after potentiostatic polarisation).

The metastable pit labelled '1' was the nucleation site for the pit growth and subsequent crevice corrosion, while the metastable pits '2' and '3 'did not appear to grow any further (**Figure 7**). Sample III was polarised at + 0.30 V_{SCE} for 4 minutes as shown in **Figure 8**. The potentiostatic polarisation of Sample III was stopped before stable pit growth in order to measure, by profilometry, the volume of the metastable pits nucleated after potentiostatic polarisation. The mpf of Sample III was 78.65 $s^{-1}.cm^{-2}$ by MPA calculation.

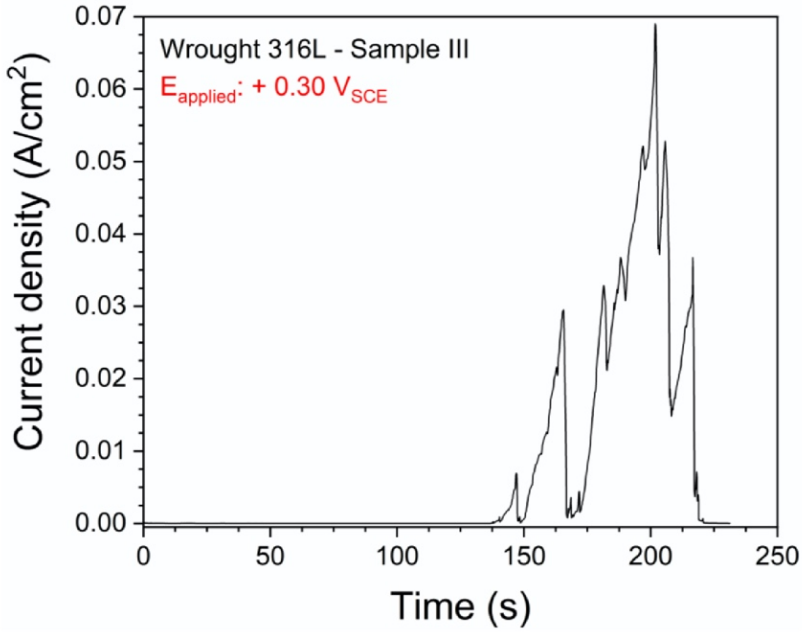

Figure 8: Chronoamperometry of the wrought 316L - Sample III in 0.1 M NaCl. The potential was fixed at + 0.30 V_{SCE}.

Both MPA and Origin® software calculated charge of 1.702 C/cm2 for Sample III. The theoretical mass loss owing to metastable pitting events was calculated based on both Origin® and MPA and total charge values of 5.44 x 10^{-7} g were obtained. **Figure 9** shows the surface of Sample III before potentiostatic polarisation (initial) and after 4 minutes of potentiostatic polarisation at + 0.30 V_{SCE} with the formation of two metastable pit clusters.

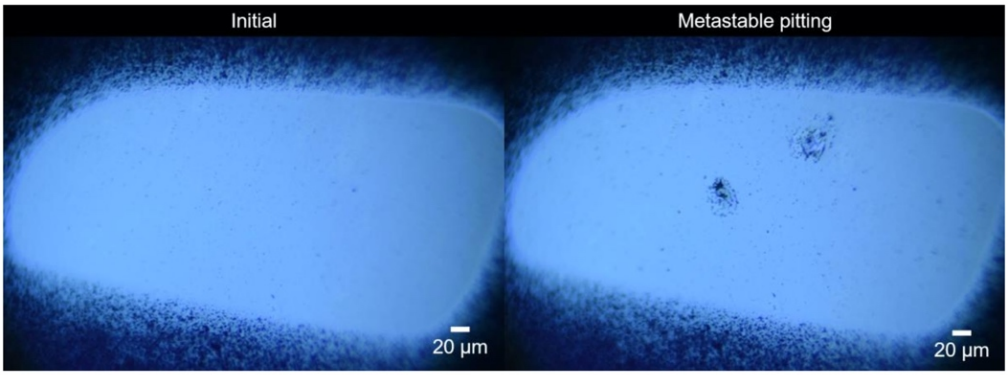

Figure 9: Snapshots of the surface of the Wrought 316L - Sample III - in the initial state (before potentiostatic polarisation) and the surface with metastable pits (after potentiostatic polarisation).

The results obtained from the potentiostatic polarisation testing of Samples I, II and III were summarised in

Table *3*. The mpf values calculated from each sample current density transients could not be

	Sample I			Sample II			Sample III		
Method	**mpf ($s^{-1}cm^{-2}$)**	**Charge (C/cm^2)**	**Mass loss (g)**	**mpf ($s^{-1}cm^{-2}$)**	**Charge (C/cm^2)**	**Mass loss (g)**	**mpf ($s^{-1}cm^{-2}$)**	**Charge (C/cm^2)**	**Mass loss (g)**
Origin®		0.408	4.78 x 10^{-8}	-	0.193	3.68 x 10^{-8}	-	1.702	5.44 x 10^{-7}
MPA	15.50	0.408	4.78 x 10^{-8}	78.31	0.197	3.76 x 10^{-8}	78.65	1.702	5.44 x 10^{-7}

used as a comparative variable since each experiment had different duration. In order to compare mpf values from different polarisation tests, the potential applied, the experimental time and the electrolyte should be kept the same.

Table 3: Summary of the results obtained by the potentiostatic polarisation of the wrought 316L (Sample I, II and III) measured by Origin® and by the metastable pitting analyser (MPA).

	Sample I			Sample II			Sample III		
Method	**mpf ($s^{-1}cm^{-2}$)**	**Charge (C/cm^2)**	**Mass loss (g)**	**mpf ($s^{-1}cm^{-2}$)**	**Charge (C/cm^2)**	**Mass loss (g)**	**mpf ($s^{-1}cm^{-2}$)**	**Charge (C/cm^2)**	**Mass loss (g)**
Origin®		0.408	4.78×10^{-8}	-	0.193	3.68×10^{-8}	-	1.702	5.44×10^{-7}
MPA	15.50	0.408	4.78×10^{-8}	78.31	0.197	3.76×10^{-8}	78.65	1.702	5.44×10^{-7}

Profilometry of 316L stainless steel – Sample III

The surface morphology of the wrought 316L – Sample III was observed using Vision software for profilometry after the potentiostatic polarisation test imaging as shown in **Figure 10**.

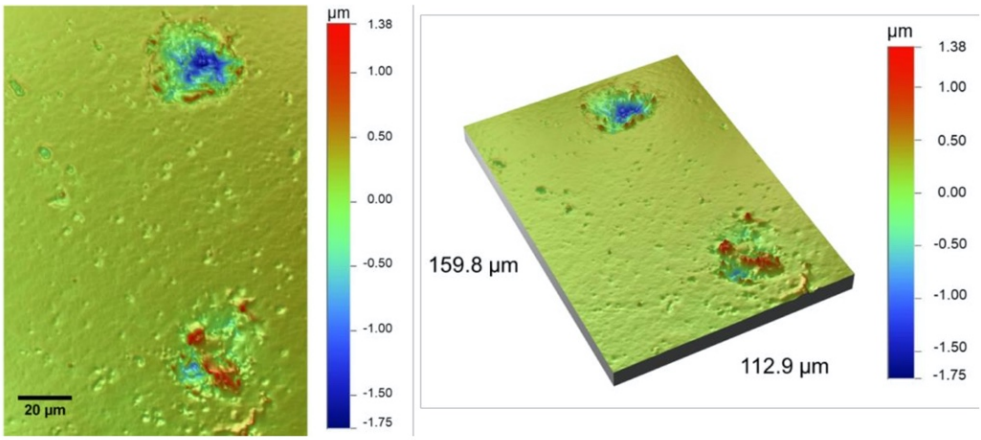

Figure 10: Surface profile as determined using vertical scanning interferometry of the 316L - Sample III after potentiostatic polarisation as depicted in **Figure 9**.

The analysis was carried out on the region shown where two metastable pits were visually recorded by the in-situ imaging. The three-dimensional (3D) images visually indicated that the metastable pit growth extended its depth to 1.75 µm from the metal surface. For the uppermost metastable pit, the total volume calculated by the software was 2.61×10^{-10} cm^3, whereas the other metastable pit total volume was 4.57×10^{-11} cm^3. Both pits combined had a total volume

of 3.06 x 10^{-10} cm^3. The mass loss was estimated considering that the majority of the material ejected from the bulk 316L stainless steel during the potentiostatic polarisation testing was composed of the '316L cation' described above. The density of 316L stainless steel (8.00 g/cm^3) was used to calculate a total mass loss of 2.45 x 10^{-9} g.

Discussion

In-situ imaging during potentiostatic polarisation of Sample I revealed that two metastable pits could nucleate at the same site as shown in **Video 1** [50]. This indicated that the passive layer formed inside (or in the immediate proximity of) the metastable pit after repassivation was also prone to breakdown. In the context of stable pit growth, previous studies conducted by several researchers described that pits can grow inside pits [19,51,52]. However, there is little evidence based on work to date, that the same could occur for metastable pits; in other words, metastable pits that grow within repassivated metastable pits. The corrosion of the repassivated metastable pit appeared to occur mainly on the edges of the nucleation pit as observed in **Video 1**. The first metastable pit nucleated at the first current density peak (between 800 and 1000 seconds) indicating that metastable pit (**Figure 5**) correlated to an individual current density transient (**Figure 4**). Between 1200 and 1400 seconds two major current density transients were measured (**Figure 4**) representing the nucleation of a new metastable pit and successive growth of a previously nucleated metastable pit (**Video 1**). The increase of the repassivated metastable pit diameter observed in **Video 1**, could also have represented the rupture of a pit cover that is commonly formed on pit mouths posteriorly to their nucleation [53]. However, such a cover was not visible on the surroundings of the described metastable pit (**Video 1**). This suggests that the observed increase in the pit radius (and respective current density transient) was more likely to be the consequence of a new metastable pit as opposed to the rupture of a pit cover. In addition, as noted by Frankel et. al [14] such lacy pit cover formed on the pit mouth is the result of a remnant thin oxide layer and their rupture is caused by osmotic pressure between the bulk electrolyte and pit bottom rather than by electrochemical reactions. Thus, no current transient would be detected simultaneously to the pit diameter increase which contrasted with the results observed here. Current density transients of lower intensity were detected close to the major peaks although no new visible pits were observed. This could either indicate that some metastable pitting events occurring on the surface were too small to be imaged with the apparatus utilised, or that current density transients of smaller intensity occurred ahead of major

metastable pits as suggested by Mattin and Burstein [54] in 304 stainless steels. The later could be correlated to micro passive layer breakdown occurring at different sites within the pit nucleation region. Therefore, metastable pit growth observed inside a repassivated metastable pit (**Video 1**) was either an invisible (within the capabilities of the utilised apparatus) pit cover that was ruptured or the nucleation of a new metastable pit. This is an important finding, as it contradicts the conclusions reported by Pistorius and Burstein [55] which stated that once metastable pitting is exhausted by repassivation of a site, the same metastable pit is no longer a site available for further pitting. The measurements of the charge passed on the surface of Sample I, performed by Origin® and MPA software showed same value which corroborated to validate the integration applied by the MPA.

Sample II developed significant pit growth from a repassivated metastable pit with further perpetuation of damage by crevice corrosion in the region adjacent to the lacquer enamel painting as shown in **Video 2** [50]. Potential above the pitting potential (+ 0.30 V_{SCE}) was applied on Sample II during potentiostatic polarisation (+ 0.35 V_{SCE}) in order to observe the transition between the metastable and the stable growth regime in 316L. Pit '1' growth (either by metastable or stable pit growth) triggered crevice corrosion as visualised in **Video 2** while the measured current density did not decrease to passive current values evidencing that no repassivation was prone to occur under the experimental conditions in place. Prior to pit growth and crevice corrosion, similarly to Sample I, metastable pits were detected inside pit '1' (**Figure 7**) without any visible pit cover (**Video 2**) which provides evidence that a repassivated metastable pit can serve as an initiation site for further metastable pitting. Pit covers with so-called lacelike appearance were observed for metastable pits '2' and '3' similarly to stable pits reported by Newman et. al [52] for 304 and 904L stainless steels. For those metastable pits there was no visual rupture of the cover while repassivation still occurred based on the absence of current density transients and successive pit growth. However, the current density transients could have been shadowed by the current density increase caused by the simultaneous growth of the crevice corrosion that initiated in pit '1' as observed in **Video 2**.

Metastable pits formed on the surface of Sample III during the in-situ imaging of the potentiostatic polarisation testing were observed in **Video 3** [50]. As observed for pits '2' and '3' on Sample II, the metastable pits observed on Sample III also presented lacelike pit cover. This cover was sustained until the repassivation of these pits and no major rupture was observed providing evidence that the metastable pits '2' and '3' on Sample II had already ceased their growth (i.e. repassivated) when pit '1' entered crevice corrosion regime.

The mass loss calculated based on the total charge passed on the surface of Sample III during the potentiostatic polarisation testing (5.44×10^{-7} g) was higher than the mass loss calculated by profilometry of the same metastable pits (2.45×10^{-9} g). This suggested that the number of electrons detected by the potentiostat did not tally directly to the ionisation / dissolution reaction. An explanation for this is that current transient measured may have a considerable associated capacitive effect related to the 'switching' of the surface condition owing to the local rupture of the surface film. For example, the capacitance associated with the switching of the surface condition can be phenomenologically considered by the surface being represented by a single resistor-capacitor (R-C) combination in the passive condition, and the activation of a second R-C combination when the surface has a pit. The so-called charging of the capacitance associated with the second time constant would be manifest in the moments immediately following passive film rupture. Assuming that the excess of electrons detected by the potentiostat charged the surface of the metal as a capacitor, the capacitance (C) can be calculated by:

$$C = \frac{Q}{V}$$

(**Equation 4**)

Where Q is the charge accumulated on the capacitor and V is the potential applied during the potentiostatic polarisation. The subtraction of the mass loss calculated from the profilometry from the mass loss calculated using the potentiostatic polarisation was utilised to calculate the charge difference and the hypothesised capacitance of Sample III (2.20 F/cm^2). The double layer influence or the deposit of other chemical species on the metal surface (such as salts) could also act as an electrical barrier between bulk metal and bulk electrolyte adding further basis to the capacitive effect hypothesised herein. The different mass loss obtained from both measurements indicated that the damage caused on the 316L stainless steel surface, during potentiostatic polarisation, could not be quantitatively correlated to the current density transients – the correlation between metastable pitting events (and perhaps even stable pitting events) as measured herein, and compared to physical damage accumulation, is an area of future work.

The MPA software proved to be an efficient tool for the calculation of charge or area under the current density transient curves and their respective mpf values. User feedback collection was implemented to further improve the software, via software launch ahead of this publication. The MPA software will remain open sourced to the public as a resource and tool for all.

Conclusion

Electrochemical testing and in-situ imaging were utilised to characterise key aspects related to the analysis of metastable pitting upon 316L stainless steel in 0.1 M NaCl. The work herein was able to reveal the following aspects that are of general utility in the utilisation of potentiostatic testing for quantification of metastable pitting. Findings include:

1. It was determined that multiple metastable pits can occur on the same site which implies that a repassivated metastable pit was still a potential pit nucleation site.
2. The physical metal dissolution caused by metastable pitting events was below the corresponding mass loss calculated by Faraday's law. That indicated that a parcel of the electrons detected by the potentiostat either (i) did not originate from the electrochemical reactions that led to metastable pitting, or (ii) there are significant capacitive effects imposed on the scenario of metastable pitting. Hence, the charge passed during a current density transient did not represent the total amount of metal lost by pitting, with electrochemical assessment over-estimating the physical damage observed.
3. It was shown that although one current transient could be correlated to an individual metastable pitting event, multiple current transients could also occur from one unique metastable pit site. This indicates that an individual metastable pitting event is not necessarily the result of a unique and singular current transient.

In addition, the development of a user friendly and freely available software tool (metastable pitting analyser, MPA) was presented and utilised within this study. This tool can be utilised for the analysis of potentiostatic test data (chronoamperometry) for any metal – electrolyte system.

CRediT authorship contribution statement

Guilherme Sander: Conceptualization, Writing – Original Draft, Methodology, Investigation. **Victor Cruz**: Methodology. **Ninad Baht**: Software. **Nick Birbilis**: Conceptualization, Writing – Review & Editing

Declaration of Competing Interest

The authors declare that they have no known competing financial interests or personal relationships that could have appeared to influence the work reported in this paper.

Acknowledgements

We acknowledge the support provided by Woodside Energy.

Data availability

The raw data required to reproduce these findings are available to download from [http://dx.doi.org/10.17632/z43xxs7hvv.1]. The source code for the metastable pitting analysis software developed is available from the authors.

References

[1] A.J. Sedriks, Corrosion of Stainless Steels, 2nd ed., 1996.

[2] G.S. Frankel, N. Sridhar, Understanding localized corrosion, Mater. Today. 11 (2008) 38–44. https://doi.org/10.1016/S1369-7021(08)70206-2.

[3] P.C. Pistorius, G.T. Burstein, Metastable Pitting Corrosion of Stainless Steel and the Transition to Stability, Philos. Trans. R. Soc. A Math. Phys. Eng. Sci. 341 (1992) 531–559. https://doi.org/10.1098/rsta.1992.0114.

[4] B.E. Wilde, E. Williams, The Relevance of Accelerated Electrochemical Pitting Tests to the Long-Term Pitting and Crevice Corrosion Behavior of Stainless Steels in Marine Environments, J. Electrochem. Soc. 118 (1971) 1057. https://doi.org/10.1149/1.2408246.

[5] G.O. Ilevbare, G.T. Burstein, The use of microelectrodes in the study of the effects of electrolyte composition, potential and metallurgical condition on nucleation and metastable pitting of stainless steel 316, in: Proc. - Electrochem. Soc., 2006: pp. 335–347.

[6] G.T. Burstein, C. Liu, R.M. Souto, S.P. Vines, Origins of pitting corrosion, Corros. Eng. Sci. Technol. 39 (2004) 25–30. https://doi.org/10.1179/147842204225016859.

[7] J. Soltis, Passivity breakdown, pit initiation and propagation of pits in metallic materials - Review, Corros. Sci. 90 (2015) 5–22. https://doi.org/10.1016/j.corsci.2014.10.006.

[8] R.C. Newman, 2001 W.R. Whitney award lecture: Understanding the corrosion of stainless steel, Corrosion. 57 (2001) 1030–1041. https://doi.org/10.5006/1.3281676.

[9] G.T. Burstein, Revealing corrosion pits, Nature. 350 (1991) 188–189. https://doi.org/10.1038/350188a0.

[10] G.S. Frankel, Errata: "Pitting Corrosion of Metals. A Review of the Critical Factors" [J. Electrochem. Soc., 145, 2186 (1998)], 1998. https://doi.org/10.1149/1.1838748.

[11] C.R. Rarey, A.H. Aronson, Pitting Corrosion of Sensitized Ferritic Stainless Steel., Corrosion. 28 (1972) 255–258. https://doi.org/10.5006/0010-9312-28.7.255.

[12] M.P. Ryan, D.E. Williams, R.J. Chater, B.M. Hutton, D.S. McPhail, Why stainless steel corrodes, Nature. 415 (2002) 770–774. https://doi.org/10.1038/415770a.

[13] D.E. Williams, Y.Y. Zhu, Explanation for Initiation of Pitting Corrosion of Stainless Steels at Sulfide Inclusions, J. Electrochem. Soc. 147 (2000) 1763. https://doi.org/10.1149/1.1393431.

[14] G.S. Frankel, L. Stockert, F. Hunkeler, H. Boehni, Metastable Pitting of Stainless Steel., Corrosion. 43 (1987) 429–436. https://doi.org/10.5006/1.3583880.

[15] J.R. Galvele, Transport Processes and the Mechanism of Pitting of Metals, J. Electrochem. Soc. 123 (1976) 464. https://doi.org/10.1149/1.2132857.

[16] J.R. Galvele, Transport processes in passivity breakdown-II. Full hydrolysis of the metal ions, Corros. Sci. 21 (1981) 551–579. https://doi.org/10.1016/0010-938X(81)90009-3.

[17] G. Frankel, G. Thornton, S. Street, T. Rayment, D. Williams, A. Cook, A. Davenport, S. Gibbon, D. Engelberg, C. Örnek, A. Mol, P. Marcus, D. Shoesmith, C. Wren, K. Yliniemi, G. Williams, S. Lyon, R. Lindsay, T. Hughes, J. Lützenkirchen, S.-T. Cheng, J. Scully, S.F. Lee, R. Newman, C. Taylor, R. Springell, J. Mauzeroll, S. Virtanen, S. Heurtault, J. Sullivan, Localised corrosion: general discussion, Faraday Discuss. 180 (2015) 381–414. https://doi.org/10.1039/C5FD90046H.

[18] H.H. Strehblow, Mechanisms of Pitting Corrosion, in: P. Marcus (Ed.), Corros. Mech. Theory Pract., 2nd ed., CRC Press, 2002: pp. 243–347.

[19] P. Ernst, R.C. Newman, Pit growth studies in stainless steel foils. II. Effect of temperature, chloride concentration and sulphate addition, Corros. Sci. 44 (2002) 943–954. https://doi.org/10.1016/S0010-938X(01)00134-2.

[20] G.T. Burstein, S.P. Mattin, Nucleation of corrosion pits on stainless steel, Philos. Mag. Lett. 66 (1992) 127–131. https://doi.org/10.1080/09500839208229274.

[21] Z. Szklarska-Smialowska, Measurement of the susceptibility to pitting, in: Pitting Corros. Met., National Association of Corrosion Engineers, 1986: pp. 39–67.

[22] Bernard Baroux, Further insights on the pitting corrosion of stainless steels, in: P. Marcus (Ed.), Corros. Mech. Theory Pract., 2nd ed., CRC Press, 2002: pp. 311–347.

[23] ASTM G48-11, Standard Test Methods for Pitting and Crevice Corrosion Resistance of Stainless, ASTM Internaltional. 11 (2011) 1–11. https://doi.org/10.1520/G0048-11R15.Copyright.

[24] D.E. Williams, C. Westcott, M. Fleischmann, Studies of the initiation of pitting corrosion on stainless steels, J. Electroanal. Chem. 180 (1984) 549–564. https://doi.org/10.1016/0368-1874(84)83606-0.

[25] R.K. Gupta, N.L. Sukiman, M.K. Cavanaugh, B.R.W. Hinton, C.R. Hutchinson, N. Birbilis, Metastable pitting characteristics of aluminium alloys measured using current transients during potentiostatic polarisation, Electrochim. Acta. 66 (2012) 245–254. https://doi.org/10.1016/j.electacta.2012.01.090.

[26] C.J. Semino, P. Pedeferri, G.T. Burstein, T.P. Hoar, The localized corrosion of resistant alloys in chloride solutions, Corros. Sci. 19 (1979) 1069–1078.

https://doi.org/10.1016/S0010-938X(79)80096-7.

[27] Y.F. Cheng, J.L. Luo, Statistical analysis of metastable pitting events on carbon steel, Br. Corros. J. 35 (2000) 125–130. https://doi.org/10.1179/000705900101501146.

[28] G. Sander, S. Thomas, V. Cruz, M. Jurg, N. Birbilis, X. Gao, M. Brameld, C.R. Hutchinson, On The Corrosion and Metastable Pitting Characteristics of 316L Stainless Steel Produced by Selective Laser Melting, J. Electrochem. Soc. 164 (2017) C250–C257. https://doi.org/10.1149/2.0551706jes.

[29] N.L. Sukiman, X. Zhou, N. Birbilis, A.E. Hughes, J.M.C. Mol, S.J. Garcia, G.E. Thompson, Aluminium Alloys - New Trends in Fabrication and Applications, in: Alum. Alloy. - New Trends Fabr. Appl., 2012: pp. 47–97. https://doi.org/10.5772/3354.

[30] M.K. Cavanaugh, N. Birbilis, R.G. Buchheit, A Quantitative Study on the Effects of Environment and Microstructure on Pit Initiation in Al-alloys, ECS Transitions. 16 (2009) 1–11. https://doi.org/10.1149/1.3229951.

[31] M. Gholami, M. Hoseinpoor, M.H. Moayed, A statistical study on the effect of annealing temperature on pitting corrosion resistance of 2205 duplex stainless steel, Corros. Sci. 94 (2015) 156–164. https://doi.org/10.1016/j.corsci.2015.01.054.

[32] M.K. Cavanaugh, N. Birbilis, R.G. Buchheit, Modeling pit initiation rate as a function of environment for Aluminum alloy 7075-T651, Electrochim. Acta. 59 (2012) 336–345. https://doi.org/10.1016/j.electacta.2011.10.069.

[33] M. Dornhege, C. Punckt, J.L. Hudson, H.H. Rotermund, Spreading of Corrosion on Stainless Steel, J. Electrochem. Soc. 154 (2007) C24. https://doi.org/10.1149/1.2387061.

[34] C.M. Liao, J.M. Olive, M. Gao, R.P. Wei, In-Situ Monitoring of Pitting Corrosion in Aluminum Alloy 2024, Corrosion. 54 (1998) 451–458. https://doi.org/10.5006/1.3284873.

[35] A. Chiba, I. Muto, Y. Sugawara, N. Hara, Development of a New Microelectrochemical Measurement System for, 41 (2012) 237–245. https://doi.org/10.1149/1.3697593.

[36] Y. Li, R. Hu, J. Wang, Y. Huang, C.J. Lin, Corrosion initiation of stainless steel in HCl solution studied using electrochemical noise and in-situ atomic force microscope, Electrochim. Acta. 54 (2009) 7134–7140. https://doi.org/10.1016/j.electacta.2009.07.042.

[37] Y. Wang, G. Cheng, Y. Li, Observation of the pitting corrosion and uniform corrosion for X80 steel in 3.5 wt.% NaCl solutions using in-situ and 3-D measuring microscope, Corros. Sci. 111 (2016) 508–517. https://doi.org/10.1016/j.corsci.2016.05.037.

[38] K. Wu, W.S. Jung, J.W. Byeon, In-situ monitoring of pitting corrosion on vertically positioned 304 stainless steel by analyzing acoustic-emission energy parameter, Corros. Sci. 105 (2016) 8–16. https://doi.org/10.1016/j.corsci.2015.12.010.

[39] P.E. Klages, M.K. Rotermund, H.H. Rotermund, Simultaneous holographic, ellipsometric, and optical imaging of pitting corrosion on SS 316LVM stainless steel, Corros. Sci. 65 (2012) 128–135. https://doi.org/10.1016/j.corsci.2012.08.023.

[40] O. Schneider, G.O. Ilevbare, R.G. Kelly, J.R. Scully, In Situ Confocal Laser Scanning Microscopy of AA2024-T3 Corrosion Metrology, J. Electrochem. Soc. 154 (2007) C397. https://doi.org/10.1149/1.2742804.

[41] N. Ida, I. Muto, Y. Sugawara, N. Hara, Local Electrochemistry and In Situ Microscopy of Pitting at Sensitized Grain Boundary of Type 304 Stainless Steel in NaCl Solution, J. Electrochem. Soc. 164 (2017) C779–C787. https://doi.org/10.1149/2.1011713jes.

[42] W. Tian, N. Du, S. Li, S. Chen, Q. Wu, Metastable pitting corrosion of 304 stainless steel in 3.5% NaCl solution, Corros. Sci. 85 (2014) 372–379. https://doi.org/10.1016/j.corsci.2014.04.033.

[43] M.H. Moayed, R.C. Newman, The Relationship Between Pit Chemistry and Pit Geometry Near the Critical Pitting Temperature, J. Electrochem. Soc. 153 (2006) B330. https://doi.org/10.1149/1.2210670.

[44] B.W. Davis, P.J. Moran, P.M. Natishan, Metastable pitting behavior of aluminum single crystals, Corros. Sci. 42 (2000) 2187–2192. https://doi.org/10.1016/S0010-938X(00)00032-9.

[45] R.K. Gupta, N.L. Sukiman, M.K. Cavanaugh, B.R.W. Hinton, C.R. Hutchinson, N. Birbilis, Metastable pitting characteristics of aluminium alloys measured using current transients during potentiostatic polarisation, Electrochim. Acta. 66 (2012) 245–254. https://doi.org/10.1016/j.electacta.2012.01.090.

[46] S.T. Pride, Metastable Pitting of Aluminum and Criteria for the Transition to Stable Pit Growth, J. Electrochem. Soc. 141 (1994) 3028. https://doi.org/10.1149/1.2059275.

[47] Y. González-García, G.T. Burstein, S. González, R.M. Souto, Imaging metastable pits on austenitic stainless steel in situ at the open-circuit corrosion potential, Electrochem. Commun. 6 (2004) 637–642. https://doi.org/10.1016/j.elecom.2004.04.018.

[48] N.J. Laycock, Metastable Pitting and the Critical Pitting Temperature, J. Electrochem. Soc. 145 (1998) 2622. https://doi.org/10.1149/1.1838691.

[49] J. Srinivasan, R.G. Kelly, Evaluating the Critical Chemistry for Repassivation at the Corroding Surface Using Mass Transport Model-Based Artificial Pit Experiments, J. Electrochem. Soc. 163 (2016) C768–C777. https://doi.org/10.1149/2.0661613jes.

[50] G. Sander, V. Cruz, N. Bhat, N. Birbilis, On the in-situ characterisation of metastable pitting using 316L stainless steel as a case study, Mendeley Data. (2020). https://doi.org/http://dx.doi.org/10.17632/z43xxs7hvv.2.

[51] M. Baumgärtner, H. Kaesche, Aluminum pitting in chloride solutions: morphology and pit growth kinetics, Corros. Sci. 31 (1990) 231–236. https://doi.org/10.1016/0010-938X(90)90112-I.

[52] P. Ernst, R.C. Newman, Pit growth studies in stainless steel foils. I. Introduction and

pit growth kinetics, Corros. Sci. 44 (2002) 927–941. https://doi.org/10.1016/S0010-938X(01)00133-0.

[53] N.J. Laycock, Perforated Covers for Propagating Pits, J. Electrochem. Soc. 145 (1998) 1101. https://doi.org/10.1149/1.1838423.

[54] S.P. Mattin, G.T. Burstein, Detailed resolution of microscopic depassivation events on stainless steel in chloride solution leading to pitting, Philos. Mag. Lett. 76 (1997) 341–347. https://doi.org/10.1080/095008397178940.

[55] P.C. Pistorius, G.T. Burstein, Aspects of the effects of electrolyte composition on the occurrence of metastable pitting on stainless steel, Corros. Sci. 36 (1994) 525–538. https://doi.org/10.1016/0010-938X(94)90041-8.

Chapter 6: Exploring the possibility of a stainless steel and glass composite produced by additive manufacturing

The unique layer-by-layer production process in selective laser melting (SLM) and the accompanying fast heating/cooling cycles (up to 10^8 K/s) illuminate a new pathway for the development of new alloys and metal-matrix composites. Materials that are usually immiscible in equilibrium could potentially may joined together to form material 'blends'. The exploration of the SLM (or more generally, additive manufacturing) of a previously unreported combination of materials could introduce a new range of engineering materials – which are also produced in net-shape.

Glass is a well-known material with extensive utilisation in a number of consumer applications. Consequently, the generation of glass waste (in a variety of shape and colours) becomes a public issue with significant environmental impact. In its powder form, glass waste has the potential to become feedstock material for the production of SLM components.

In this chapter, two groups of 316L/glass composite specimens were produced by SLM by blending glass powder with 316L powder 10 and 25 wt. % ratios. The SLM parameters were optimised to produce compact specimens able to undergo tensile and mechanical testing. Both groups of specimens were investigated by electron microscopy and x-ray diffraction for microstructure, chemical compositional and phase characterisation. In addition, corrosion was evaluated by electrochemical polarisation testing in 0.6 M NaCl solution. The response of the SLM 316L/glass composites to mechanical and corrosion testing was evaluated utilising a SLM 316L specimen as benchmark.

The present chapter was prepared as a journal article and it is under submission in ***Materials & Design***. The journal article appears here as resubmitted after peer review.

Exploring the possibility of a stainless steel and glass composite produced by additive manufacturing

G. Sander[1, *], D. Jiang[2], Y. Wu[1], N. Birbilis[3,*]

[1]Department of Materials Science and Engineering, Monash University, Clayton, Victoria, 3800, Australia
[2]Monash Centre for Additive Manufacturing, Monash University, Notting Hill, Victoria, 3168, Australia.
[3]College of Engineering and Computer Science, The Australian National University, Acton, A.C.T., 2601, Australia.

[*]guilherme.sandermalab@monash.edu; nick.birbilis@anu.edu.au

Keywords: selective laser melting, glass, stainless steel, 316L, composites, materials development

Abstract

The production of components using powder bed fusion presents unique possibilities for manufacturing. The process of selective laser melting (SLM) can permit fusion of powders, including powder blends and alloys comprised from elemental powders. In this context, exploring the possibility of making composites by blending stainless steel 316L and glass powder (the latter being a waste product) was explored. Such composites were investigated on the basis of (i) significant reduction in component cost, as glass powder waste is a common industrial by-product, (ii) upgrading recycled waste, (iii) the possibility of lowering component density (the density of glass is less than three times that of stainless steel), and (iv) the possibility of unique physical properties if glass remains amorphous. Herein, laser scan strategies were optimised in order to produce solid cubes and tensile test specimens. Microstructural and phase analysis were carried out by electron microscopy and x-ray techniques. Unique Cr-Si oxides were observed in the manufactured microstructure. The work herein presents an exploratory approach into the development of novel engineered composites utilising additive manufacturing.

Graphical abstract

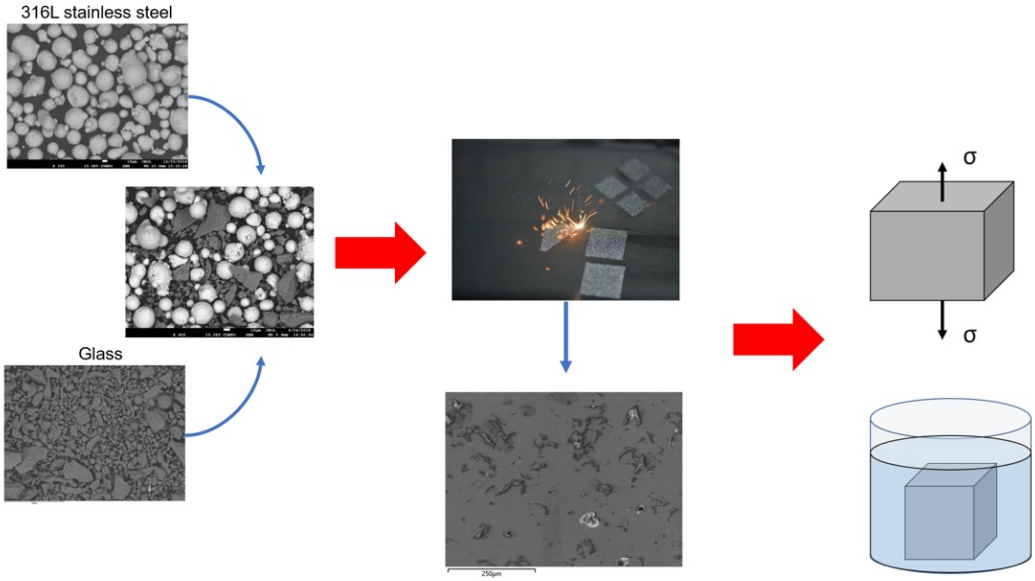

1 Introduction

Additive manufacturing (AM) for production of net shape components is disrupting the manufacturing industry for a diverse range of materials [1–5]. In the context of alloy development, production routes via AM can allow the production of novel materials and phases which were impossible or difficult to be achieved by conventional manufacturing methods [6–8]. For example, Soro et al. [9] developed a novel titanium-tantalum (Ti-25Ta) material through AM for improving orthodontic implants. Additionally, microstructures with unique features produced by AM have been broadly reported for a wide range of alloys [10–17]. Among other studies, Chao et al. [18] investigated fine dislocation cell structures within grains in additively manufactured stainless steels, and a previously unreported quasicrystal phase in additively manufactured aluminium alloy AA7075 was reported by Kairy et al. [19].

The AM method explored in the present study is a powder bed-based system, termed select laser melting (SLM). The SLM process consists of the application of a layer of powder over which a laser beam selectively scans the powder, in a pattern following a computer-aided design (CAD). The process follows a layer-by-layer procedure until the final component is completed [20,21]. During SLM, the interface of the laser and powder can reach temperatures up to ~ 4000 K (3727 ºC) [22]. In the same instance, cooling rates can range between ~ 10^4 and ~ 10^8 K/s [23,24] depending on the substrate material. The particular thermal behaviour obtained by SLM permits a route for the production of metastable and non-equilibrium phases in metallic materials.

Composites, a subset of which may be defined as hybrid materials, are defined as the combination of two or more materials that produce a final material with distinct properties [20,25,26]. The addition of individual materials of diverse mechanical, chemical and physical properties to one another will often result in properties that are retained from the original constituent materials [27,28]. To date, metal matrix composites have demonstrated the potential to increase mechanical resistance to shear/compression forces, whilst the specific weight of the final product is reduced [29,30]. Examples include, the addition of nanometre-sized ceramic particles or carbon fibre to a weaker matrix material [28,30].

Soda-lime-silica glass is one of the most common types of glass utilised in various applications and products (e.g. bottles, windowpanes, food containers, etc.) [31,32]. As the name suggests, such glass is principally composed of silicon (Si), calcium (Ca) and sodium (Na) oxides [33], and makes up close to 85% of all glass manufactured by the glass industry [34]. This type of glass possesses particular properties, such as high hardness and low (thermal and electrical) conductivity. Soda-lime-silica glass can be fabricated by cutting, and it can resist moderate temperature service, with a strain points up to ~600º C [35]. The broad utilisation of soda-lime-silica glass in a variety of consumer applications results in the ongoing generation of soda-lime-silica glass waste – with such waste in a variety of forms, colours and sizes [34]. Research regarding the use of glass waste for applications other than in glass reuse, is not as significant as the issue of glass waste would perhaps suggest, however some research has shown that glass waste may be used as an additive in concrete [36]. Potentially, glass waste in powder form (or ground glass) may be used as feedstock for powder-based

AM technologies such as SLM. In rationalising this, it is noted that in small dimensions (i.e. below 200 µm), glass can present significant flexibility in contrast to brittle macro-scale glass [37–39]. Therefore, if glass is added to a metallic matrix (and glass being present in sub 200 µm dimensions), if no or limited metallurgical occurs, the resultant mechanical properties of the composite may be enhanced (e.g. enhanced ductility, lower density and dramatically reduced alloy cost).

Stainless steels are a class of steels with particular resistance to corrosion in a variety of chemically aggressive environments [40]. This increased resistance to corrosion is observed in stainless steels is attributed to the presence of alloyed chromium (Cr) in quantities above 11 wt. % [41]. When in contact with oxygen, a thin self-healing chromium oxide film is rapidly formed on the surface of such steels [42].

At temperatures above 1500ºC, glass and stainless steels are immiscible liquids [43]. If these materials are simultaneously sustained at such a high temperate, the less dense phase (i.e. Ca-, Na-, Si-oxides) would separate from the denser (molten) stainless steel, prohibiting composite production owing to physicochemical incompatibility in equilibrium. However, the aforementioned localised rapid heating and high-cooling rate thermal cycles realised during SLM, may potentially allow the formation of composites comprised of a stainless steel matrix embedded with glass particles. Engineered steel-glass composites or hybrid components have been previously reported in construction research as a structural combination of these two materials at the component length scale [44–46], however, studies on the development of a bulk components composed of a micro-chemical composites of glass in a steel matrix have not been previously reported. One feasible advantage of blending glass and steel is the production of a composite with lower specific weight (lower density) than of stainless steels, which is beneficial if the physical properties of stainless steel are maintained. Glass also possesses a low thermal conductivity [35], which could – beneficially – reduce the thermal conductivity of stainless steels; whilst finally there are significant cost benefits to using recycled waste as a starting material.

In this study, glass powder was blended with 316L powder in different proportions to produce homogeneous SLM feedstock powder blends. The powder blends were utilised for the production of specimens via SLM optimising laser parameters until dense solid specimens were obtained. The resultant microstructures were characterised by a range of microscopy techniques and x-ray diffraction. Corrosion and mechanical performance were also explored and compared to the SLM 316L stainless steel specimen. This study also contributes to a window of future research for the advent of new engineered materials produced exclusively by AM technologies.

2 Experimental

2.1 *Materials and methods*

Gas atomised 316L stainless steel powder was sourced from Sandvik-Osprey^{LTD} (United Kingdom) with a powder size distribution of 10 – 53 µm. A soda-lime-silica type powder was sourced from the local industrial waste stream. The glass source and compositional uniformity is highly reproducible. Prior to the blending with stainless steel powder, the glass powder was dehydrated in an oven under atmospheric conditions at 100°C for 24 hours. Then both powders were sieved separately utilising individual sieves with a 63µm mesh size. The sieved glass powder was weighed and added to sieved 316L powder at two unique powder blend ratios: one containing 316L with 10 wt. % glass, and the other containing 25 wt. % glass. Each powder mixture was blended for 12 hours utilising a barrel mixer to homogenise the powder mixture.

The precise composition of both 316L and glass powders were measured by using inductively coupled plasma-atomic emission spectrometry (ICP-AES) and Leco® combustion analysis, and presented in **Table 1.**

Table 1: Chemical composition of 316L stainless steel and glass powders utilised to produce the specimens studied herein.

	Element wt. %																	
	Fe	**Mn**	**Si**	**P**	**Ni**	**Cr**	**Mo**	**Cu**	**V**	**Nb**	**Ti**	**Al**	**Ca**	**Na**	**Mg**	**S**	**O**	**Other**
316L powder	65.10	1.21	0.66	0.03	10.00	16.90	2.00	0.29	0.04	<0.01	<0.01	0.02	0.17	0.06	0.02	0.01	0.05	3.44
Glass powder	0.32	0.07	33.90	0.04	ND	0.01	<0.01	0.08	ND	ND	0.04	0.20	6.44	9.86	2.14	ND	46.58	0.32

ND – Not detected

The 316L, the 316L-10 wt. % glass, and 316L-25 wt. % glass powder mixtures were observed by scanning electron microscopy (SEM), via a JOEL JSM-7001F FEG-SEM instrument, and presented in **Figure 1.** These SEM images were also utilised for the analysis of powder morphology and validation of the powder size distribution of each powder mixture.

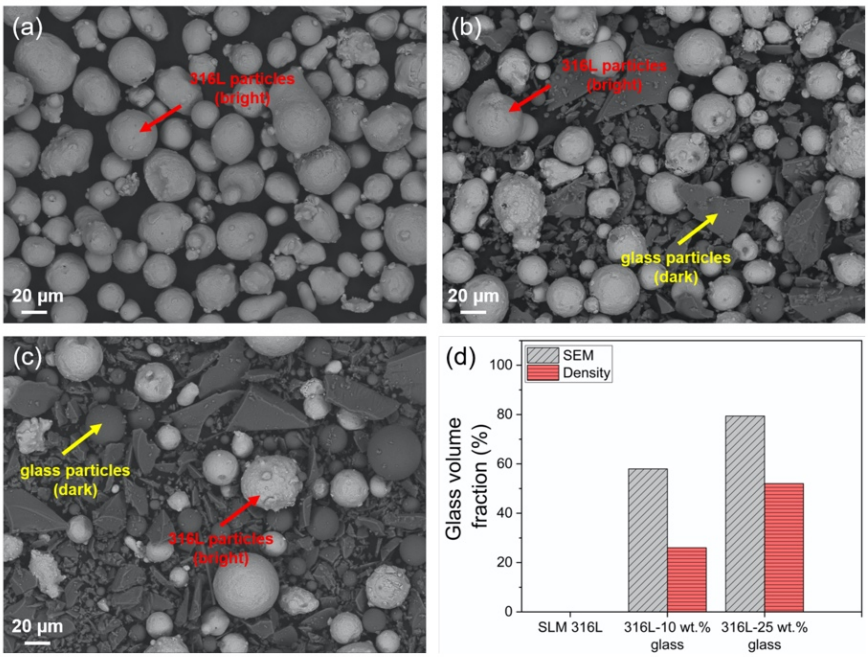

Figure 1: Backscattered electron micrographs of powders utilised in specimen production: (a) 316L stainless steel; b) 316L-10 wt. % glass; and (c) 316L-25 wt. % glass. (d) Theoretical glass volume fraction measured by utilising SEM images and calculated by utilising each 316L and glass respective powder densities.

The specimens studied in this work were produced utilising selective laser melting (SLM) via a Concept Laser® Mlab Cusing-R instrument, equipped with a 100 W fibre laser. The SLM process was carried out in a nitrogen-purged inert atmosphere (containing < 0.1 % oxygen). For each powder composition, cube specimens were manufactured through a series of laser scan strategies until compact solid cubes were obtained (with a density > 97% as determined from optical microscopy). The SLM laser spot size, layer thickness and hatch distance were not altered for specimen manufacture and were maintained at 100 µm, 0.025 mm and 0.08 mm respectively. The optimised SLM scan strategies determined herein, were then utilised to produce the solid cubes and tensile specimens that form the basis of the present study (the associated conditions for each powder blend type provided in **Table 2**).

Table 2: Laser scan strategy utilised to produce specimens studied herein.

	316L	**316L - 10 wt. % Glass**	**316L - 25 wt. % Glass**
Laser scan speed (mm/s)	1200	50	50
Laser Power (W)	90	80	90

2.2 *Microstructural characterisation*

Prior to microstructural characterisation, SLM 316L, 316L-10 wt. % glass and 316L-25 wt. % glass samples were metallographically prepared by successively grinding to a 4000 grit finish utilising silicon carbide (SiC) paper. Specimens were subsequently polished utilising 3 µm and 1 µm diamond suspensions. Between each surface grinding and polishing procedure, specimens were ultrasonically cleaned in ethanol for ~120 seconds. Optical microscopy (OM) was utilised to observe the microstructure of each polished sample, and these specimens were also analysed using SEM in the backscattered electron (BSE) mode. Additionally, energy-dispersive X-ray spectrometry (EDXS) was also carried out utilising an Oxford Instruments AZtec X-ray analysis system.

The microstructural features observed from SEM characterisation were also examined by transmission electron microscopy (TEM) utilising an FEI® Tecnai G2 T20 microscope. The composition of microstructural features observed by TEM was also investigated by EDXS utilising a Bruker® QUANTAX 30 mm^2 silicon drift detector.

The SLM prepared specimens were also analysed by X-ray diffraction (XRD). The XRD data were collected using a Bruker® D8 Advance diffractometer with Co K_α radiation and a Lynxeye® position sensitive detector. The crystalline phases were identified, and the crystalline phase fractions were quantified by whole-pattern Rietveld method as embodied in the software package TOPAS (Version 5, Bruker® AXS).

2.3 *Density measurements and mechanical testing*

Cube-shaped samples of SLM 316L, 316L-10 wt. % glass and 316L-25 wt. % glass specimens were metallographically prepared to a 1200 grit surface finish on all their surfaces for the empirical measurement of density by Archimedes' buoyant force method. The samples were weighed with a 0.0001 g precision scale in air and submerged in deionised water. The weight difference was utilised to calculate each cube's volume and consequently their respective density, which was compared to their wrought counterpart density. Each measurement was performed in triplicate for statistical validation.

Tensile testing was performed utilising an INSTRON 100 kN model 4505 instrument with a displacement rate of 0.02 mm/s using a 100 KN load cell and a 10 mm extensometer.

2.4 *Electrochemical testing*

Electrochemical testing to assess the corrosion performance of the specimens prepared herein was investigated by cyclic potentiodynamic polarisation (CPP) in 0.6 M NaCl solution. The electrochemical testing was performed utilising a three-electrode flat cell (PAR K-0235), which employed a platinum mesh counter electrode and a saturated calomel reference electrode. Prior to electrochemical testing, specimens were ground to a 2000 grit SiC finish and cleaned with ethanol in an ultrasonic bath. The CPP testing involved a 10 minute conditioning in the 0.6M NaCl solution at the open circuit potential (OCP), followed by polarisation with a

scan rate of 1 mV/s. Polarisation commenced from 0.20 V below the OCP until a current density of 0.1 mA/cm^2 reached, after which the scan was reversed to the starting potential of 0.20 V below OCP. Electrochemical testing was repeated in triplicate for each specimen.

3 Results

3.1 Powder analysis

The SEM images corresponding to each powder blend (**Figure 1**) reveal a significant decrease in the volumetric proportion of 316L powder particles when glass powder was added into the blended powder mixture. Theoretical glass powder volume fraction was calculated from the analysis of SEM images and based on the known values of 316L and glass powder densities. The volume fraction values of glass observed by SEM were higher for both powder blends in comparison to the theoretical values (**Figure 1d**).

3.2 Microstructure and physical characterisation

The corresponding chemical compositions for the SLM 316L, 316L-10 wt. % glass and 316L-25 wt. % glass are presented in **Table 3**.

Table 3: Chemical composition of the selective laser melted 316L, 316L-10 wt. % glass and 316L-25 wt. % glass specimens.

	Element wt. %																	
	Fe	**Mn**	**Si**	**P**	**Ni**	**Cr**	**Mo**	**Cu**	**V**	**Nb**	**Ti**	**Al**	**Ca**	**Na**	**Mg**	**S**	**C**	**O**
SLM 316L	67.35	1.26	0.66	0.04	11.1	16.8	2.28	0.24	0.08	0.02	< 0.01	0.04	ND	ND	ND	0.02	0.02	0.06
316L-10 wt. % glass	67.63	0.37	0.72	0.04	12.8	13.8	3.15	0.17	0.03	< 0.01	< 0.01	0.02	ND	ND	ND	0.03	0.02	1.22
316L-25 wt. % glass	74.06	0.15	0.55	0.04	13.6	6.48	3.52	0.14	0.01	< 0.01	< 0.01	0.06	ND	ND	ND	0.03	0.01	1.35

ND – Not detected

It can be noted that iron (Fe) wt. % was similar for both 316L-10 wt. % glass and SLM 316L specimens (~ 67 .3 wt. %). However, the 316L-25 wt. % glass presented approximately 7 wt. % more Fe in its chemical composition than the other two specimens. In comparison to SLM 316L, the final Cr concentration for the 316L-10 wt. % glass and 316L-25 wt. % glass is reduced by reduction of 3 and 10 wt. % respectively. A global decrease in the concentration of elements not present in the glass is anticipated for the composite blends. However, the most significant aspects of the final compositions (in **Table 3**) may be considered the lack of

integration of the original glass composition (albeit that glass is present in a higher volume fraction). What is meant by this, is that the concentration of Si is similar in all of the specimens, however Si is a principle component of the original glass powder. Furthermore, the concentration of oxygen (whilst above 1.2 wt. % for the 316L-glass blended samples) is indicative that the oxygen was not integrated into the final composite. The disparities in chemical composition led to atypical microstructures, mechanical and corrosion properties that are further discussed in the following sections below.

Metallographically prepared SLM 316L, 316L-10 wt. % glass and 316L-25 wt. % samples were analysed by OM and their respective collected images are shown in **Figure 2**. In spite of the aforementioned variations in expected final composition, the quality and density of the component integrity is considered to be excellent.

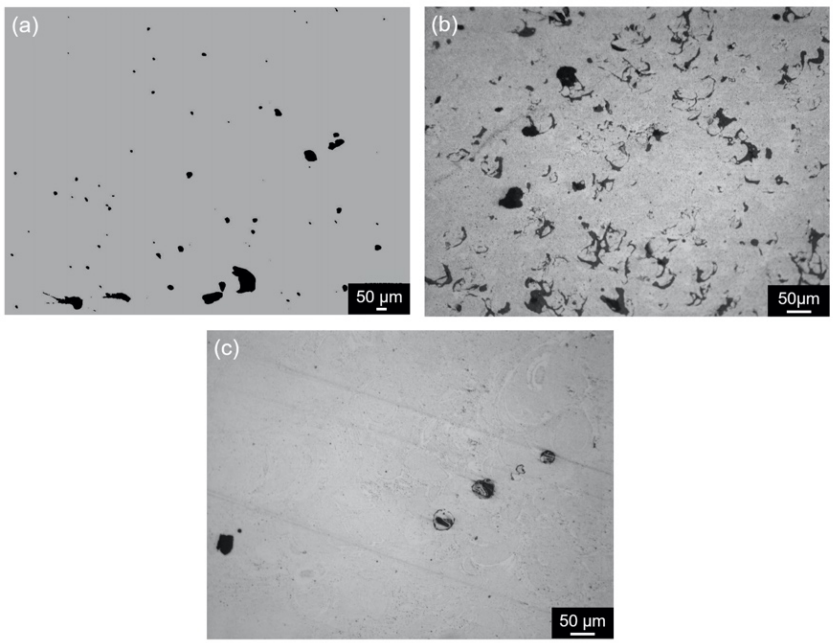

Figure 2: Optical micrographs of metallographically polished surfaces of: (a) 316L stainless steel; b) 316L-10 wt. % glass; and (c) 316L-25 wt. % glass.

The presence of porosity has been reported extensively in the literature as feature of well produced SLM stainless steels [47–49]. As therefore expected, the occurrence of porosity was evident for the SLM 316L specimen produced as seen in **Figure 2a**. Whilst in some cases, depending on alloy composition, pores may be associated were segregated particles [50,51], the corresponding EDXS mapping revealed that no microscale chemical segregation occurred for the SLM 316L (**Figure 3**).

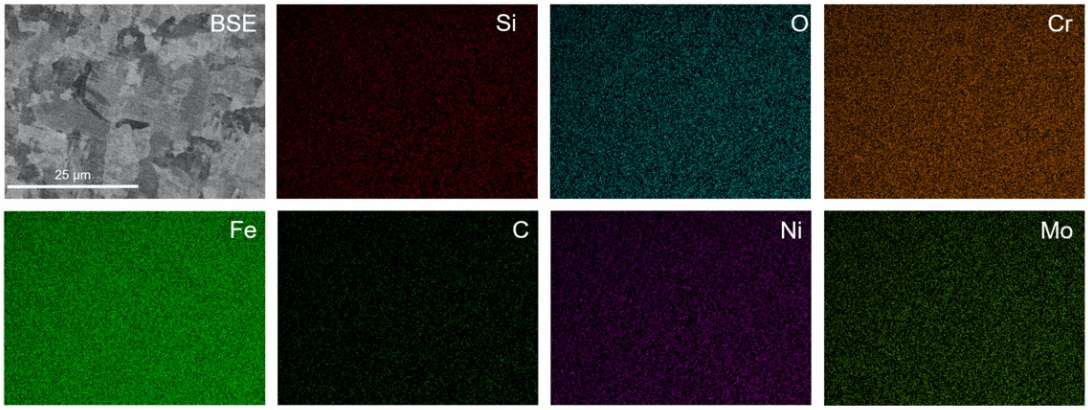

Figure 3: EDXS chemical composition maps of the SLM 316L specimen.

Heterogenous features were also observed on the surface of 316L-10 wt. % glass and 316L-25 wt. % glass as shown in **Figure 2b** and **Figure 2c** respectively. Initially, these features were also considered as pores remnant from the SLM process as noted for SLM 316L. However, composition maps obtained by EDXS revealed the qualitative element distribution for 316L-10 wt. % glass (**Figure 4**) and 316L-25 wt. % glass (**Figure 5**), indicating that such features observed optically, are not in fact pores.

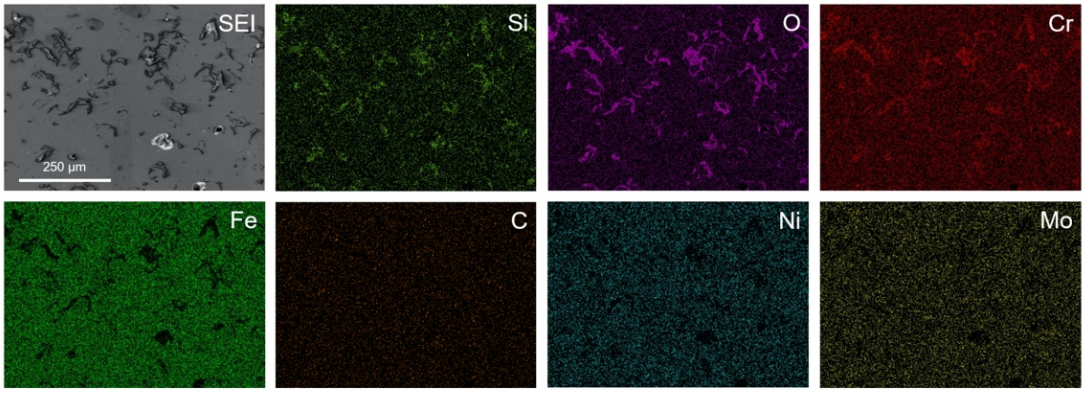

Figure 4: Chemical composition maps (EDXS mapping) of the 316-10 wt. % glass specimen.

The EDXS mapping of 316L – glass specimens reveals rather vividly, that the micro-features observed in **Figure 2** are not pores, and are regions of the microstructure associated with the segregation of Cr to the prior glass powder, forming Cr-Si oxides shown in **Figure 4** and **Figure 5**. It is noted that the shape of such Cr-Si oxides varied between the 316L-10 wt. % glass and 316L-25 wt. % glass. The former (316L-10 wt. % glass) presented large (~ 50 µm) irregular shaped segregates whilst the latter (316L-25 wt. % glass) presented smaller (~ 5 µm) circular ones.

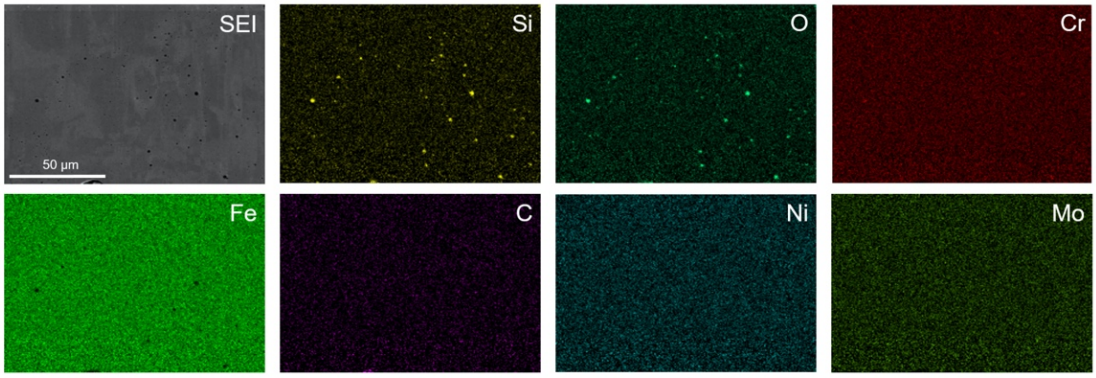

Figure 5: Chemical composition maps (EDXS mapping) of the 316-25 wt. % glass specimen.

The density, and concomitantly porosity, could not be accurately calculated by OM image analysis due to the presence of the Cr-Si oxides mentioned above. Alternatively, the Archimedes buoyant method was carried out to define the density for the SLM 316L, 316L-10 wt. % glass and 316L-25 wt. % glass as presented in **Table 4**. Wrought 316L density was added to **Table 4** for reference. The SLM 316L and 316L-25 wt. % glass specimens presented similar densities (~ 7.8 g/cm^3). Meanwhile, a lower density was measured for 316L-10 wt. % glass (~ 7.4 g/cm^3) which was most likely due to (and attributed to) the presence of the significantly larger Cr-Si oxides in the microstructure.

Table 4: Density of the selective laser melted specimens as measured by Archimedes buoyant method and the theoretically calculated density based on the respective feedstock composition.

	SLM 316L	**316L-10 wt. % glass**	**316L-25 wt. % glass**	**Wrought 316L**
Measured density (g/cm^3)	7.87 ± 0.03	7.41 ± 0.01	7.88 ± 0.03	8.00
Relative measured density to wrought (%)	98.45	92.63	98.52	100
Theoretical Density (g/cm^3)	8.00	7.45	6.62	-
Relative theoretical density to wrought (%)	100	93.12	82.75	-

The theoretical density, which is the density specimens would possess if no pores were present and all the wt. % glass (with density of 2.50 g/cm^3[52]) contained in the SLM feedstock material was incorporated into the SLM 316L bulk, was also presented in (**Table 4**). Both theoretical and measured densities were similar for the 316L-10 wt. % glass specimen (~ 7.4 g/cm^3). The theoretical density was however ~ 16 % lower than the measured density for the 316L-25 wt. % glass. The data provided in **Table 4** added to the EDXS maps presented above suggested that there was a threshold between 10 and 25 wt. % in which glass ceases to be effectively assimilated into the microstructure of 316L stainless steel.

Images from the Cr-Si oxide and bulk interface region were collected in bright field (BF) TEM mode for the 316L-10 wt. % and presented in **Figure 6a**.

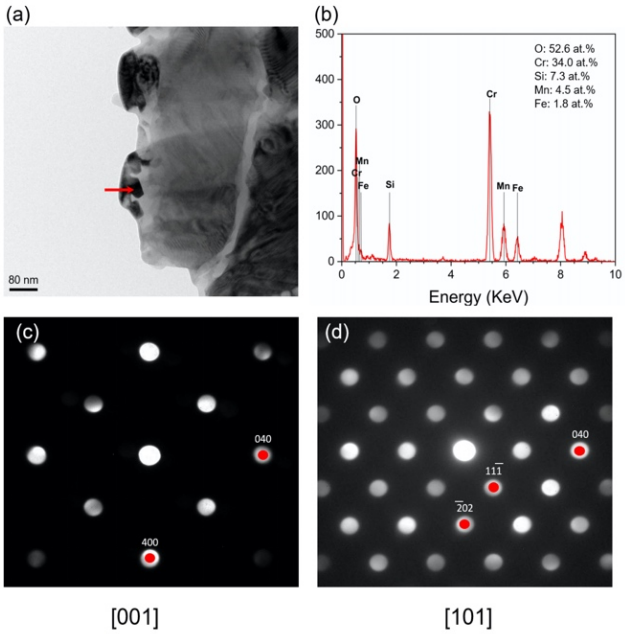

Figure 6: (a) BF-TEM image, (b) EDXS spectrum and (c) and (d) <001> and <101> zone axis micro-diffraction patterns, recorded from the particles observed in the 316L-10 wt. % sample.

For images collected using BF-TEM, the contrast variations distinguished local chemical composition, whereas the darkest regions (denoted by the arrow in **Figure 6a**) represent the Cr-Si oxides. Semi-quantitative chemical TEM-EDXS analysis (**Figure 6b**) was in agreement with the results obtained from SEM-EDXS assessment (**Figure 4**). Whilst noting the semi-quantitative nature of EDXS (and noting that the quantification of light elements including oxygen is approximate), an oxygen concentration of 52.6 at. % was determined for the particles, with a Cr and Si concentration of 34.0 at. % and 7.3 at. %, respectively. The remaining elements in the Cr-Si oxide particle were 4.5 at. % manganese (Mn) and 1.8 at. % of Fe. Selected area diffraction patterns were collected from a discrete Cr-Si oxide particle denoted by the point in **Figure 6a**, for both <001> and <101> directions, and shown in **Figure 6c and 6d**. A crystalline diamond cubic unit cell was indexed from the Cr-Si oxide diffraction pattern, without any evidence of an amorphous phase.

The XRD spectra (**Figure 7a**) determined for all specimen types revealed that SLM 316L was solely comprised of a face centred crystal (FCC) structure (austenite). Similarly, FCC was the principal and majority phase for 316L-10 wt. % glass and 316L-25 wt. % glass, however a body centred cubic (BCC) phase was also detected for the specimens containing the highest proportion of glass feedstock (**Figure 7a)**. The austenite lattice parameter (ALP) was also measured by XRD for each specimen and presented (**Figure 7b**). The 316L-10 wt. % glass revealed the lowest ALP of 3.5940 ± 9.8 x10^{-5} Å in comparison to 316L-25 wt. % and of SLM 316L with ALP of 3.5975 ± 1.24 x10^{-4} Å and 3.5980 ± 2.16 x10^{-4}Å respectively.

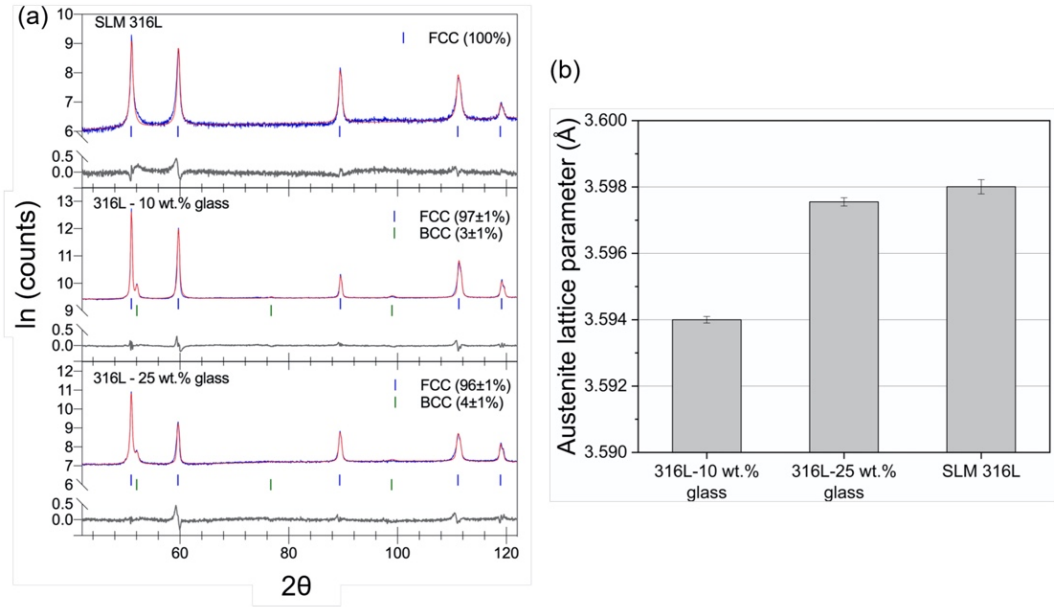

Figure 7: (a) XRD of SLM 316L, 316L-10 wt. % glass and 316L-25 wt. % glass noting the percentage of BCC and FCC phases forming their respective crystal structure. (b) Austenite lattice parameter measured by XRD for each specimen.

3.3 Mechanical performance

The results from uniaxial tensile testing are presented for SLM 316L, 316L-10 wt. % glass and 316L-25 wt. % glass specimens is shown in **Figure 8**.

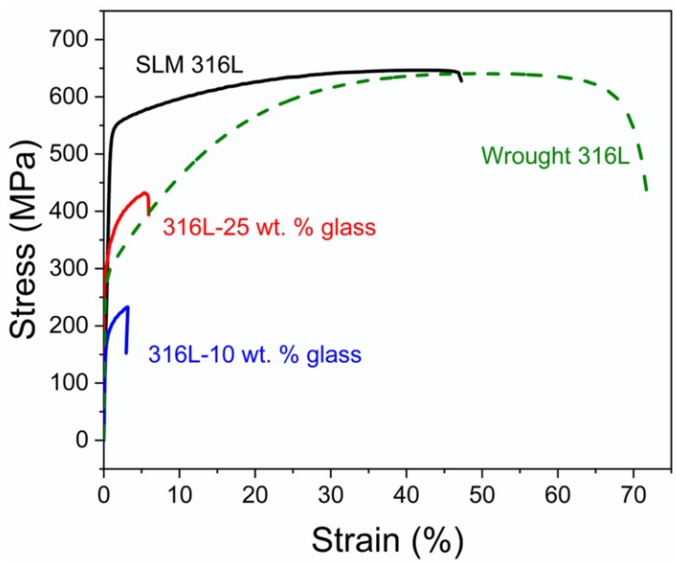

Figure 8: Representative stress-strain curves from uniaxial tensile testing for the SLM 316L, 316L-10 wt. % glass, 316L-25 wt. % glass and Wrought 316L.

The tensile response of wrought 316L was included in **Figure 8** as a benchmark for mechanical performance comparison. The 316L-10 wt. % glass specimen presented the lowest value of ultimate tensile strength (232 MPa) in comparison with the 316L-25 wt. % (431 MPa) and SLM 316L (650 MPa). Both 316L-glass specimens revealed elongation values lower than ~ 7 %, while the elongation of SLM 316L was 46.6 %.

Fracture surface imaging using SEM for a 316L-10 wt. % glass specimen following tensile fracture is presented in **Figure 9**. A ductile fracture pattern was observed although the specimens did not present significant elongation (relative to 100% 316L specimens) during tensile testing. Cavities with a diameter of ~ 100 µm as denoted in **Figure 9** presented some evidence of brittle fracture sites. Those sites may could also be associated with regions where the Cr-Si oxides are present, although it is note that given the Cr-Si oxide phase was only revealed in this work, its relative ductility (or brittleness) is not as yet determined. It is also noteworthy that evidence (albeit at low incidence) of unmelted powder was also visible, as highlighted by the dashed square in **Figure 9**, which has been noted as a common cause for porosity in SLM prepared alloys [53].

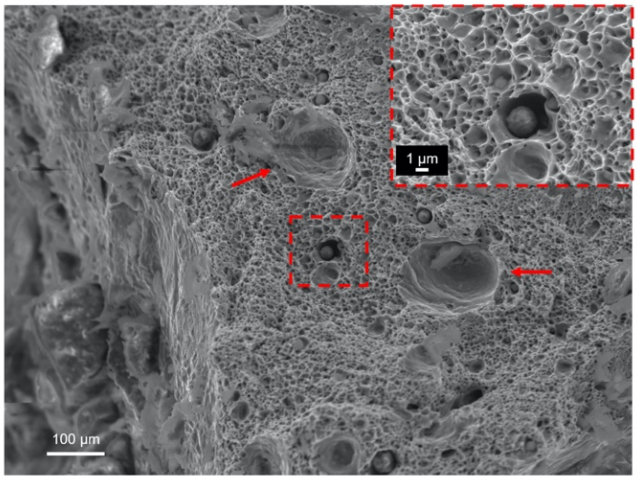

Figure 9: SEM image of the fracture surface of 316L-10 wt. % glass following tensile fracture . The dashed square highlights a cavity containing an un-melted powder particle.

3.4 Electrochemical performance

Representative cyclic potentiodynamic polarisation (CPP) curves for SLM 316L, 316L-10 wt. % glass and 316L-25 wt. % glass in 0.6 M NaCl are presented in **Figure 10a**.

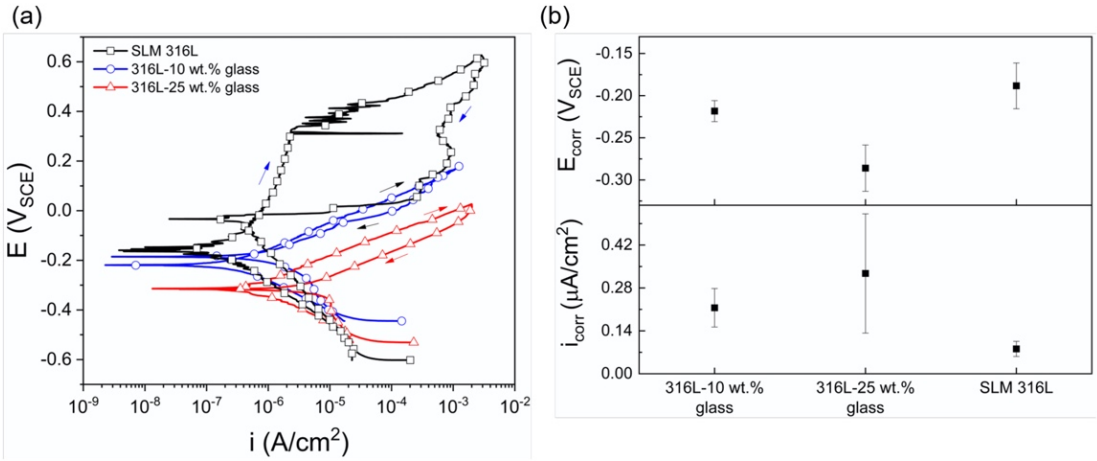

Figure 10: (a) Representative cyclic-potentiodynamic curves of the SLM 316L, 316L-10 wt. % glass and 316L-25 wt. % glass in 0.6 M NaCl solution and (b) their respective corrosion current density and corrosion potential.

The key observation derived from the CPP curves was that passive behaviour, defined as a low rate of current density (~ 10^{-6} A/cm^2) over a range of applied anodic potentials, was not observed during the polarisation of 316L-10 wt. % glass and 316L-25 wt. % glass. Consequently, the pitting potential (E_{pit}) (i.e. the potential at which current density increases abruptly during CPP as a consequence of passive regime breakdown) could not be measured for the 316L-glass specimens. The lack of passivity, hence lack of E_{pit} indicated that the addition of glass powder to the 316L powder hindered the passivation of the SLM 316L-glass specimens. In contrast, passive behaviour and passivity breakdown were observed for the SLM 316L with an average E_{pit} of +0.53 V_{SCE}. The corrosion potential (E_{corr}) and corrosion current density (i_{corr}) values were also extracted from the CPP curves for the SLM 316L, 316L-10 wt. % glass and 316L-25 wt. % glass specimens and compiled in **Table 5**.

As discernible from their respective CPP curves (**Figure 10a**), the SLM 316L presented higher E_{corr} and (-0.188 V_{SCE}) and lower i_{corr} (0.081 μA/cm^2) than both 316L-10 wt. % glass (-0.219 V_{SCE}; 0.195 μA/cm^2) and the 316L-25 wt. % glass (-0.290 V_{SCE}; 0.327 μA/cm^2) specimens.

Table 5: Summary of the electrochemically determined corrosion response of SLM 316L, 316L-10 wt. % glass and 316L-25 wt. % glass samples from cyclic potentiodynamic polarisation in 0.6 M NaCl.

	i_{corr} (μA/cm^2)	E_{corr} (V_{SCE})	E_{pit} (V_{SCE})
SLM 316L	0.081 ± 0.024	-0.188 ± 0.027	0.53 ± 0.12
316L-10 wt. % glass	0.195 ± 0.065	-0.219 ± 0.010	n/a
316L-25 wt. % glass	0.327 ± 0.194	-0.290 ± 0.024	n/a

4 Discussion

The results presented above demonstrate that it was possible to produce a dense, and net shape, composite of 316L stainless steel and glass. The results also reveal outcomes that were not anticipated ahead of the study (and discussed below), including novel outcomes that include the revelation of a new alloy phase that formed from the SLM production route employed.

In assessing the composites produced, it was noted that the blend of irregularly shaped glass particles with what was principally spherical 316L powder particles in the 316L-glass SLM feedstock (**Figure 1**) may have potentially hindered the flowability and compaction of the powder onto the substrate - during layer application (recoating) in the SLM process. A lower flowability and irregular distribution of particles can lead to the formation of "empty" spaces and unmelted powder regions and these regions becoming sites of porosity after solidification. Although pores were not observed clearly for the 316L-10 wt. % glass in OM images, there was evidence of porosity in the SEM images of the fracture surface specimen due to the presence of unmelted powder particles (**Figure 9**).

As anticipated for the SLM prepared 100% 316L [18], microscale heterogeneity in the microstructure was not observed, and a fully FCC structure (austenite) was formed (**Figure 3**). However, for the 316L-10 wt. % glass composite, the resultant microstructure revealed a considerable number of heterogeneous features (**Figure 4**). These features were determined to be a Cr-Si oxide phase, which has not been previously reported (in stainless steels, or in any domain). This phase formed as a result of co-segregation of Cr and Si, in response to the high temperatures realised in the SLM process. The phase also incorporates a significant concentration (>50 at. %) of oxygen, which is the only dominant remnant oxygen from the feedstock glass.

The chemical composition of glass and 316L powders along with their respective powder blends utilised to produce the specimens studied in this work (**Table 1**) revealed that most of the elements present in the glass (e.g. Si, Ca, Na, O) were partially or completely ejected from the melt pool region during SLM. This was verified by the lack of these elements in chemical composition measurements of the SLM 316L-glass specimens (**Table 3**). However, as noted, glass influenced the segregation of Cr, Si and oxygen into the 316L matrix during the 316L-glass powder blend melting.

For the SLM of 100% 316L stainless steel components, small to no variation of chemical composition is expected between the powder feedstock and final component. In the case of 316L- glass composites, the final compositions presented in |**Table 3** are also suggestive of selective loss of alloying elements and thus evidence of oxide development (viz. oxidation) during SLM, that creates reaction products that are 'lost' to SLM instrument chamber. This was not studied herein specifically, but the so-called loss of alloying elements may occur from a number of mechanisms. One mechanism is that lightweight oxides or oxidation products are physically displaced during the turbulence of the SLM build process (and also possibly displaced by the

recoater blade subsequently). Another mechanism is that splatter of liquid metal (in this case the melt pool) or ejection metal particles from the liquid phase can be aided by the presence of oxygen dissolving in the liquid phase – with the glass serving as a local oxygen source. The interaction between the laser and powder bed during SLM promotes extremely rapid cooling/heating cycles (up to ~ 10^8 K/s). This can generate unstable melt pools since two immiscible components (in their liquid phase) are concentrated in the melting region. Liquid glass (with lower density) and liquid stainless steel (with higher density) interaction at high temperatures could have promoted instantaneous glass ejection from the melt pool. The ejected liquid glass particles would solidify as they exited the melt pool region forming a high number of spatters (as in fact observed in this work) during the SLM of the 316L-glass.

Glass (as feedstock composition) was not retained in the 316L-glass blend after SLM since instead of an amorphous structure, a crystalline phase (or segregate) bonded to the austenitic 316L matrix. This phase is posited to have developed as a result of excess oxygen reacted with Cr and Si in the melt pool, forming the empirically observed Cr-Si oxides. As the melt pool cooled down (at extremely rapid rates), complete solidification would have commenced between ~ 1390 – 1440 ºC (melting temperature range for both 316L and glass) entrapping a parcel of such Si-Cr oxides in the metallic matrix. The newly observed crystalline phase was identified as a combination of Cr-Si oxides. Therefore, the results presented herein are evidence that a 316L-glass composite was not necessarily formed in this exploratory work. Nevertheless, the microstructure of 316L was altered by the presence of glass in their powder feedstock during SLM. Austenite was still the predominant phase (as for 316L stainless steels) for both 316L-10 wt.% glass and 316L-25 wt. % specimens, with low traces of a BCC phase in their microstructure. Interestingly, ferromagnetic behaviour was observed for the 316L-10 wt. % glass specimen as they reacted to the presence of a magnet which is a behaviour not commonly observed for austenitic stainless steels.

The 316L-25 wt. % glass specimen did not extensively form the Cr-Si oxides observed for the 316L-10 wt. % glass specimen. Instead, smaller oxide particles were formed as seen in **Figure 5**. The glass powder volumetric fraction in a 316L-glass blend containing 25 wt. % glass was somewhere between 50 and 80 %. This likely created conditions that allowed most of the glass to be ejected from the melt pool hindering the formation of the Cr-Si oxides. At the same time, XRD spectra for 316L-25 wt. % glass also showed a similar proportion of BCC phase as observed for 316L-10 wt. % glass. This indicated the existence of a saturation point for the formation BCC phase in the 316L-glass system that was independent of the presence of Cr-Si oxides. Additionally, blending glass to 316L stainless steel did not modify the bulk composition (after SLM) to the extent that can strongly change the FCC to BCC transformation sequence during solidification The aforementioned residual BCC may derive from the saturation of liquid Si present in the steel/glass melt pool that could have influenced BCC phase formation as Si has been reported to be a ferrite (BCC) stabilizer in steels [54].

Tensile testing revealed that both 316L-10 wt. % glass and 316L-25 wt. % glass specimens did not present mechanical properties similar to (and nor superior to(the SLM 316L specimen (**Figure 8**). In the case of 316L-10 wt. % glass, the Cr-Si oxide particles (possibly a brittle phase) could have markedly contributed to the low elongation observed. Additionally, the presence of unmelted powder led to the deduction that porosity caused by insufficient melting during SLM may also be present in the 316L-10 wt. % glass and 316L-25 wt. % glass microstructures (**Figure 10**). Nonetheless, whilst the properties of the 316L glass composites observed were not immediately encouraging, it does merit comment that the 316L-25 wt. % glass specimens could match (and exceed) the yield strength of wrought 316L, albeit with lower ductility. It also merits comment however, that the limited ductility observed herein, with the 316L-glass specimens, is not atypical of other engineering materials such as the ductility of high strength steels and high-strength aluminium alloys (i.e. ~7%) – which is suggestive that future work on the utilisation of waste materials for value added composites is a worthwhile research endeavour.

Finally, electrochemical tests revealed that the 316L-10 wt. % glass and 316L-25 wt. % glass specimens did not develop passive behaviour during their CPP in 0.6 M NaCl in contrast with what was observed for the SLM 316L. This is posited to be as a result of the disruption of the chromium oxide film which commonly passivates 316L, which may have not uniformly been able to develop upon 316L-glass composites that present a heterogenous microstructure (and hence, local solute enrichment and depletion of Cr). The local loss of passivity in stainless steels due to Cr depletion has been previously reported as a 'sensitisation' of such alloys [41]. In this phenomenon, solubilised Cr in the stainless steel matrix diffuses to carbon-rich regions (generally grain boundaries) forming Cr-carbides. The Cr depleted zones become anodic to their surroundings thus leading to localised corrosion. Analogously, the segregation of Cr to Si-O rich regions in the 316L-glass system could have caused the loss of passivity observed during the potentiodynamic polarisation of these specimens in 0.6 M NaCl. Although while it is noted that the corrosion current density (i_{corr}) values for the glass containing 316L stainless steel are higher than those of 100% 316L, they are still relatively low from an engineering perspective (i.e. they are $< \sim 1\ \mu A/cm^2$) which is still considered to be a low value of i_{corr} for engineering materials (and in a similar range to what is expected from pure aluminium). This therefore indicates that although the ductility and corrosion performance of 316L-glass composites are below the benchmark expectation of wrought 316L, there are adequate, and they indicate that future work in such AM specific composites is warranted.

5 Conclusions

The study herein sought to produce novel composites capable of being manufactured in net-shape by selective laser melting, by mixing waste glass powder with 316L stainless steel powder. Glass powder was added to 316L powder in 10 and 25 wt. % proportion, and such mixtures were capable of satisfactory net shape production with high densities achieved. This indicates that powder bed methods are indeed capable of producing unique composite blends, or bulk materials that are unable to be readily produced by other means. The microstructures, mechanical performance and electrochemical properties of produced specimens were also studied herein, and the findings in this work include:

- Glass powder, when integrated into solid specimens with 316L stainless steel, was not present as an amorphous phase. The glass was integrated into the stainless steel, resulting in 'alloying' in the metallurgical sense. The glass powder was intimately integrated into the alloy structure, and there was significant segregation of chromium to what was prior glass powder, which resulted in the empirical determination of previously unreported crystalline Cr-Si oxides particles, as detected by both SEM and TEM analysis.
- As anticipated, the specimens prepared from glass and 316L stainless steel blends resulted in specimens of lower density than the wrought 316L stainless steel.
- The stainless steel/glass samples were comparatively brittle in comparison with both wrought or SLM prepared 316L stainless steel. The maximum ultimate tensile stress obtained for a stainless steel-glass blend was up to 430 MPa, and the elongation realised for 25 wt. % glass was ~7. These properties are inferior to SLM prepared 316L – noting that SLM prepared 316L has improved properties compared to wrought 316L owing to a refined grain size. Nonetheless, the yield strength of the 25 wt. % glass specimen was not too dissimilar to that of wrought 316L, and in cases where lower elongation is tolerable, the mechanical performance of the stainless steel – glass 'alloys' presented herein are meaningful for an exploratory study – and warrant further future work.
- In terms of electrochemical performance – as corrosion resistance of stainless steels is a basic feature of their selection as metallic materials – it was observed that classical passive behaviour was not detected in the glass containing samples from polarisation testing in 0.6 M NaCl. This led to the conclusion that the observed Cr segregation hindered the formation of a Cr-rich oxide film on these specimens' surface in the manner formed for (100%) 316L.

6 Acknowledgements

We gratefully acknowledge the support of Woodside Energy, and also acknowledge the Monash Centre for Electron Microscopy (MCEM) where microscopy and microanalysis were performed. The technical assistance of Mr. Sam Gao is also acknowledged. The authors would also like to acknowledge the use of equipment within the Monash X-Ray Platform (MXP).

7 References

[1] W.E. Frazier, Metal additive manufacturing: A review, J. Mater. Eng. Perform. 23 (2014) 1917–1928. https://doi.org/10.1007/s11665-014-0958-z.

[2] T. DebRoy, H.L. Wei, J.S. Zuback, T. Mukherjee, J.W. Elmer, J.O. Milewski, A.M. Beese, A. Wilson-Heid, A. De, W. Zhang, Additive manufacturing of metallic components – Process, structure and properties, Prog. Mater. Sci. 92 (2018) 112–224. https://doi.org/10.1016/j.pmatsci.2017.10.001.

[3] T.D. Ngo, A. Kashani, G. Imbalzano, K.T.Q. Nguyen, D. Hui, Additive manufacturing (3D printing): A review of materials, methods, applications and challenges, Compos. Part B Eng. 143 (2018) 172–196. https://doi.org/10.1016/j.compositesb.2018.02.012.

[4] N. Travitzky, A. Bonet, B. Dermeik, T. Fey, I. Filbert-Demut, L. Schlier, T. Schlordt, P. Greil, Additive manufacturing of ceramic-based materials, Adv. Eng. Mater. 16 (2014) 729–754. https://doi.org/10.1002/adem.201400097.

[5] C. Körner, Additive manufacturing of metallic components by selective electron beam melting - A review, Int. Mater. Rev. 61 (2016) 361–377. https://doi.org/10.1080/09506608.2016.1176289.

[6] S.H. Huang, P. Liu, A. Mokasdar, L. Hou, Additive manufacturing and its societal impact: A literature review, Int. J. Adv. Manuf. Technol. 67 (2013) 1191–1203. https://doi.org/10.1007/s00170-012-4558-5.

[7] I. Gibson, D. Rosen, B. Stucker, Additive Manufacturing Technologies, Springer New York, New York, NY, 2015. https://doi.org/10.1007/978-1-4939-2113-3.

[8] C. Yan, L. Hao, A. Hussein, P. Young, D. Raymont, Advanced lightweight 316L stainless steel cellular lattice structures fabricated via selective laser melting, Mater. Des. 55 (2014) 533–541. https://doi.org/10.1016/j.matdes.2013.10.027.

[9] N. Soro, H. Attar, E. Brodie, M. Veidt, A. Molotnikov, M.S. Dargusch, Evaluation of the mechanical compatibility of additively manufactured porous Ti–25Ta alloy for load-bearing implant applications, J. Mech. Behav. Biomed. Mater. 97 (2019) 149–158. https://doi.org/10.1016/j.jmbbm.2019.05.019.

[10] O. Gharbi, D. Jiang, D.R. Feenstra, S.K. Kairy, Y. Wu, C.R. Hutchinson, N. Birbilis, On the corrosion of additively manufactured aluminium alloy AA2024 prepared by selective laser melting, Corros. Sci. (2018). https://doi.org/10.1016/j.corsci.2018.08.019.

[11] W. Li, S. Karnati, C. Kriewall, F. Liou, J. Newkirk, K.M. Brown Taminger, W.J. Seufzer, Fabrication and characterization of a functionally graded material from Ti-6Al-4V to SS316 by laser metal deposition, Addit. Manuf. 14 (2017) 95–104. https://doi.org/10.1016/j.addma.2016.12.006.

[12] L.Z. Zhao, M.J. Zhao, L.J. Song, J. Mazumder, Ultra-fine Al-Si hypereutectic alloy fabricated by direct metal deposition, Mater. Des. 56 (2014) 542–548. https://doi.org/10.1016/j.matdes.2013.11.059.

[13] M. Ma, Z. Wang, X. Zeng, Effect of energy input on microstructural evolution of direct laser fabricated IN718 alloy, Mater. Charact. 106 (2015) 420–427. https://doi.org/10.1016/j.matchar.2015.06.027.

[14] L.E. Murr, A Metallographic Review of 3D Printing/Additive Manufacturing of Metal and Alloy

Products and Components, Metallogr. Microstruct. Anal. 7 (2018) 103–132. https://doi.org/10.1007/s13632-018-0433-6.

[15] S. Gorsse, C. Hutchinson, M. Gouné, R. Banerjee, Additive manufacturing of metals: a brief review of the characteristic microstructures and properties of steels, Ti-6Al-4V and high-entropy alloys, Sci. Technol. Adv. Mater. 18 (2017) 584–610. https://doi.org/10.1080/14686996.2017.1361305.

[16] J.R. Croteau, S. Griffiths, M.D. Rossell, C. Leinenbach, C. Kenel, V. Jansen, D.N. Seidman, D.C. Dunand, N.Q. Vo, Microstructure and mechanical properties of Al-Mg-Zr alloys processed by selective laser melting, Acta Mater. 153 (2018) 35–44. https://doi.org/10.1016/j.actamat.2018.04.053.

[17] M. Awd, J. Tenkamp, M. Hirtler, S. Siddique, M. Bambach, F. Walther, Comparison of microstructure and mechanical properties of Scalmalloy® produced by selective laser melting and laser metal deposition, Materials (Basel). 11 (2017). https://doi.org/10.3390/ma11010017.

[18] Q. Chao, V. Cruz, S. Thomas, N. Birbilis, P. Collins, A. Taylor, P.D. Hodgson, D. Fabijanic, On the enhanced corrosion resistance of a selective laser melted austenitic stainless steel, Scr. Mater. 141 (2017) 94–98. https://doi.org/10.1016/j.scriptamat.2017.07.037.

[19] S.K. Kairy, O. Gharbi, J. Nicklaus, D. Jiang, C.R. Hutchinson, N. Birbilis, On the Characterization of a Hitherto Unreported Icosahedral Quasicrystal Phase in Additively Manufactured Aluminum Alloy AA7075, 2019. https://doi.org/10.1007/s11661-018-5025-1.

[20] C.Y. Yap, C.K. Chua, Z.L. Dong, Z.H. Liu, D.Q. Zhang, L.E. Loh, S.L. Sing, Review of selective laser melting: Materials and applications, Appl. Phys. Rev. 2 (2015). https://doi.org/10.1063/1.4935926.

[21] D.D. Gu, W. Meiners, K. Wissenbach, R. Poprawe, Laser additive manufacturing of metallic components: materials, processes and mechanisms, Int. Mater. Rev. 57 (2012) 133–164. https://doi.org/10.1179/1743280411Y.0000000014.

[22] P.A. Hooper, Melt pool temperature and cooling rates in laser powder bed fusion, Addit. Manuf. 22 (2018) 548–559. https://doi.org/10.1016/j.addma.2018.05.032.

[23] D. Gu, Laser Additive Manufacturing of High-Performance Materials, 1st ed., Springer Berlin Heidelberg, Berlin, Heidelberg, 2015. https://doi.org/10.1007/978-3-662-46089-4.

[24] U. Scipioni Bertoli, G. Guss, S. Wu, M.J. Matthews, J.M. Schoenung, In-situ characterization of laser-powder interaction and cooling rates through high-speed imaging of powder bed fusion additive manufacturing, Mater. Des. 135 (2017) 385–396. https://doi.org/10.1016/j.matdes.2017.09.044.

[25] H. Abramovich, Introduction to composite materials, 2017. https://doi.org/10.1016/B978-0-08-100410-4.00001-6.

[26] M.F. Ashby, Y.J.M. Bréchet, Designing hybrid materials, Acta Mater. 51 (2003) 5801–5821. https://doi.org/10.1016/S1359-6454(03)00441-5.

[27] K. Shirvanimoghaddam, S.U. Hamim, M. Karbalaei Akbari, S.M. Fakhrhoseini, H. Khayyam, A.H. Pakseresht, E. Ghasali, M. Zabet, K.S. Munir, S. Jia, J.P. Davim, M. Naebe, Carbon fiber reinforced metal matrix composites: Fabrication processes and properties, Compos. Part A Appl. Sci. Manuf. 92 (2017) 70–96. https://doi.org/10.1016/j.compositesa.2016.10.032.

[28] A. Mortensen, J. Llorca, Metal Matrix Composites, Annu. Rev. Mater. Res. 40 (2010) 243–270. https://doi.org/10.1146/annurev-matsci-070909-104511.

[29] K.K. Chawla, Composite Materials, Springer New York, New York, NY, 2012. https://doi.org/10.1007/978-0-387-74365-3.

[30] D.D.L. Chung, Metal-Matrix Composites, Elsevier, 1994. https://doi.org/10.1016/B978-0-08-050073-7.50011-7.

[31] J.E. Shelby, Introduction to Glass Science and Technology, in: R. Soc. Chem., 2005: pp. 249–261.

[32] R. V. Kumar, J. Buckett, Float glass, in: Encycl. Mater. Sci. Technol., Elsevier, 2002: pp. 1–8. https://linkinghub.elsevier.com/retrieve/pii/B0080431526018349.

[33] N. Marinoni, D. D'Alessio, V. Diella, A. Pavese, F. Francescon, Effects of soda-lime-silica waste glass on mullite formation kinetics and micro-structures development in vitreous ceramics, J. Environ. Manage. 124 (2013) 100–107. https://doi.org/10.1016/j.jenvman.2013.02.048.

[34] J.H. Butler, P.D. Hooper, Glass Waste, 2nd ed., Elsevier Inc., 2019. https://doi.org/10.1016/b978-0-12-815060-3.00015-3.

[35] N. El Khiati, N. Dideron, D. Ricoult, P. Laborde, United State Patent - Silica-Soda-Lime glass compositions and their applications, 6,063,718, 2000.

[36] A. Mohajerani, J. Vajna, T.H.H. Cheung, H. Kurmus, A. Arulrajah, S. Horpibulsuk, Practical recycling applications of crushed waste glass in construction materials: A review, Constr. Build. Mater. 156 (2017) 443–467. https://doi.org/10.1016/j.conbuildmat.2017.09.005.

[37] K. Dovidenko, J. Rullan, R. Moore, K. a Dunn, R.E. Geer, F. Heuchling, Ultra Thin Flexible Glass Substrates, in: MRS Proc., 2003: pp. 1–10.

[38] A. Plichta, A. Habeck, S. Knoche, A. Kruse, A. Weber, N. Hildebrand, Flexible Glass Substrates, Flex. Flat Panel Displays. 1 (2005) 35–55. https://doi.org/10.1002/0470870508.ch3.

[39] J. Wang, Z. Fang, H. Zhu, B. Gao, S. Garner, P. Cimo, Z. Barcikowski, A. Mignerey, L. Hu, Flexible, transparent, and conductive defrosting glass, Thin Solid Films. 556 (2014) 13–17. https://doi.org/10.1016/j.tsf.2013.12.060.

[40] R. Singh, Stainless Steels, Appl. Weld. Eng. (2012) 65–73. https://doi.org/10.1016/B978-0-12-391916-8.00008-X.

[41] A.J. Sedriks, Corrosion of Stainless Steels, 2nd ed., 1996.

[42] J.R. Davis, ASM Specialty Handbook - Stainless Steels, ASM International, 1994.

[43] C. Thomas, J. Rosales, J.A. Polanco, F. Agrela, Steel slags, Elsevier Ltd, 2018. https://doi.org/10.1016/B978-0-08-102480-5.00007-5.

[44] J. Cao, J.L. Grenestedt, Design and testing of joints for composite sandwich/steel hybrid ship hulls, Compos. Part A Appl. Sci. Manuf. 35 (2004) 1091–1105. https://doi.org/10.1016/j.compositesa.2004.02.010.

[45] J. Belis, D. Callewaert, D. Delincé, R. Van Impe, Experimental failure investigation of a hybrid glass/steel beam, Eng. Fail. Anal. 16 (2009) 1163–1173.

https://doi.org/10.1016/j.engfailanal.2008.07.011.

[46] D. Ungermann, E. Preckwinkel, Structural behaviour of hybrid steel-glass beams, Challenging Glas. 2 - Conf. Archit. Struct. Appl. Glas. CGC 2010. (2010) 485–495.

[47] G. Sander, S. Thomas, V. Cruz, M. Jurg, N. Birbilis, X. Gao, M. Brameld, C.R. Hutchinson, On The Corrosion and Metastable Pitting Characteristics of 316L Stainless Steel Produced by Selective Laser Melting, J. Electrochem. Soc. 164 (2017) C250–C257. https://doi.org/10.1149/2.0551706jes.

[48] Z. Sun, X. Tan, S.B.S.B. Tor, W.Y.W.Y. Yeong, Selective laser melting of stainless steel 316L with low porosity and high build rates, Mater. Des. 104 (2016) 197–204. https://doi.org/10.1016/j.matdes.2016.05.035.

[49] K. Geenen, A. Röttger, W. Theisen, Corrosion behavior of 316L austenitic steel processed by selective laser melting, hot-isostatic pressing, and casting, Mater. Corros. 68 (2017) 764–775. https://doi.org/10.1002/maco.201609210.

[50] M.P. Ryan, D.E. Williams, R.J. Chater, B.M. Hutton, D.S. McPhail, Why stainless steel corrodes, Nature. 415 (2002) 770–774. https://doi.org/10.1038/415770a.

[51] D.E. Williams, M.R. Kilburn, J. Cliff, G.I.N. Waterhouse, Composition changes around sulphide inclusions in stainless steels, and implications for the initiation of pitting corrosion, Corros. Sci. 52 (2010) 3702–3716. https://doi.org/10.1016/j.corsci.2010.07.021.

[52] N.P. Bansal, R.H. Doremus, Density, in: Handb. Glas. Prop., Elsevier, 1986.

[53] A. Sola, A. Nouri, Microstructural porosity in additive manufacturing: The formation and detection of pores in metal parts fabricated by powder bed fusion, J. Adv. Manuf. Process. 1 (2019). https://doi.org/10.1002/amp2.10021.

[54] W.T. Tsai, Y.N. Wen, J.T. Lee, H.Y. Liou, W.F. Wang, Effect of silicon addition on the microstructure and corrosion behavior of sintered stainless steel, Surf. Coatings Technol. 34 (1988) 209–217. https://doi.org/10.1016/0257-8972(88)90113-2.

The raw data from the work presented herein will be provided by the authors upon request.

Chapter 7: Summary and future work

Summary

The research reported in this thesis contributes to a more significant (and in many instances, a completely new) understanding on how the selective laser melting (SLM) process influences the corrosion of stainless steel 316L. In contrast to conventionally manufactured wrought 316L, the SLM 316L revealed a unique microstructure, density of build, and features unique to the SLM process (all of which were influenced by SLM process variables). The work embodied in the Chapters of this research thesis sought to investigated specific aspects – and these aspects were related to the SLM process parameters and the resultant microstructures as relevant.

The following aspects on the corrosion of 316L AM of stainless steel were discussed:

- In Chapter 3, the effect of altering process settings (namely laser power and laser scan speed) on the density (i.e. porosity) of SLM 316L was studied. Particular attention was paid to how porosity affected metastable and stable pitting mechanisms. It was concluded that although SLM 316L presented pores in their microstructure, pitting potentials values measured in 0.1 M NaCl solution were higher than the pitting potentials measured for their wrought counterpart under the same experimental conditions. To date, this chapter presents the most definitive presentation of the role of porosity in corrosion of SLM prepared alloys. This work was also the first to report the annihilation of MnS inclusions as a result of the SLM process.
- Chapter 4 focused on the investigation of the effect of build orientation and residual stress from the SLM process upon pitting of 316L in 0.6 M NaCl. Although microstructural changes (especially grain morphology) were detected by a combination of characterisation techniques, there was no significant effect observed on pitting susceptibility when specimens were built in different orientations. Residual stresses of compressive and tensile nature were measured for the SLM 316L, depending on specimen orientation. However, no significant trend regarding the effect of such residual stress on pitting could be defined. As revealed in Chapter 4, pitting potentials values were consistently higher than the values measured for wrought 316L even at 0.6 M NaCl.
- In Chapter 5, the principal focus was on developing an experimental setup for the in-situ observation of metastable pit nucleation, growth and repassivation. That was

achieved by coupling an optical recording system to an electrochemical potentiostat in a customised electrochemical cell. This system allowed visual observation of pits simultaneous to potentiostatic polarisation of 316L. Although this method was applied to wrought 316L, it is noted that the detailed electrochemical analysis in the work was able to illuminate the method of potentiostatic polarisation testing in a quantitative way. As such, the work validates the results in Chapter 3, in a meaningful manner – by qualifying the approach employed.

- An exploratory study that sought to combine 316L powder and glass powder at different mass ratios was pursued - in order to produce composites (i.e. a hybrid material) via SLM - as discussed in Chapter 6. The resultant material was investigated for corrosion and mechanical performance. Although the properties of these hybrid materials did not exceed those of SLM 316L, unusual and unique microstructures were detected for these new materials for the first time, including the revelation of a new phase. This discrete study revealed the potential to further optimise the composite studied, but also illuminated the possibilities for SLM of engineered novel composites. This study was the first to report such a composite of metal and glass, and is significant to the field.

In summary, this research thesis reported advantages and disadvantages (in a durability context) to produce stainless steel 316L using SLM. The findings discussed in the body of work contributes to the industrial implementation of this alloy in chloride-containing environments.

Future work

This project sought to identify the effect of the SLM production route on the pitting and corrosion of stainless steel 316L. A variety of experiments were conducted for a diverse group of specimens that were produced by a broad manufacturing test matrix. However, there are ample prospects for future work to advance the topic more broadly.

For example, the work contained herein focused on the interactions between NaCl containing electrolytes. The evaluation of the corrosion characteristics of pore containing stainless steels exposed to non-marine environments (e.g. sulphides, supercritical CO_2, pressurised and boiling water, etc.) must be carried out in future work.

The pitting characterisation and evaluation completed on for SLM 316L did not fully consider the effectiveness of this alloy to heal the protective Cr_2O_3 layer after pit initiation. The pit repassivation mechanisms are as important as the factors controlling pit nucleation and growth. Thus, a detailed examination of the effect of porosity on the transition from stable and metastable pitting states to passivation should be carefully examined.

The in-situ imaging of specimens under electrochemical polarisation has been proved to be an excellent tool to illustrate the stages of pitting occurring on a specimen surface. The same experimental system was employed herein to answer fundamental questions regarding the pitting characteristics of 316L. In future work, this in-situ characterisation can be utilised to examine pitting (and other corrosion mechanisms) in a diverse range of metals and alloys.

The exploratory approach used herein to manufacture 316L/glass composites by SLM demonstrated the capabilities of producing new materials utilising this AM technology. The optimisation of parameters utilised in this work was limited by the laser power capabilities of the SLM machine (95 W). Future work should consider the optimisation of parameters utilising SLM systems with higher laser power in order to obtain stable melt pools and enhance the blend of glass with 316L. Furthermore, the optimisation of SLM 316L/glass composite should include glass additions below 10 wt. %, preheated substrate, varied scan strategies and heat treatments.

The characterisation of 316L/glass composites did not include the thermal, electrical and magnetic properties of specimens. These properties could have been significantly altered by the blend of the base materials herein and should be investigated in future work.

References

[1] M. Schmidt, M. Merklein, D. Bourell, D. Dimitrov, T. Hausotte, K. Wegener, L. Overmeyer, F. Vollertsen, G.N. Levy, Laser based additive manufacturing in industry and academia, CIRP Ann. 66 (2017) 561–583. https://doi.org/10.1016/j.cirp.2017.05.011.

[2] I. Gibson, D. Rosen, B. Stucker, Additive Manufacturing Technologies, Springer New York, New York, NY, 2015. https://doi.org/10.1007/978-1-4939-2113-3.

[3] M. Attaran, The rise of 3-D printing: The advantages of additive manufacturing over traditional manufacturing, Bus. Horiz. 60 (2017) 677–688. https://doi.org/10.1016/j.bushor.2017.05.011.

[4] T.T. Wohlers, Wohlers report 2019 : 3D printing and additive manufacturing state of the industry, 2019.

[5] P. Moore, Technical Handbook of Stainless Steels, 2013.

[6] A.B. Kale, J. Singh, B.-K. Kim, D.-I. Kim, S.-H. Choi, Effect of initial microstructure on the deformation heterogeneities of 316L stainless steels fabricated by selective laser melting processing, J. Mater. Res. Technol. 9 (2020) 8867–8883. https://doi.org/10.1016/j.jmrt.2020.06.015.

[7] S. Yusuf, Y. Chen, R. Boardman, S. Yang, N. Gao, Investigation on Porosity and Microhardness of 316L Stainless Steel Fabricated by Selective Laser Melting, Metals (Basel). 7 (2017) 64. https://doi.org/10.3390/met7020064.

[8] S. Gorsse, C. Hutchinson, M. Gouné, R. Banerjee, Additive manufacturing of metals: a brief review of the characteristic microstructures and properties of steels, Ti-6Al-4V and high-entropy alloys, Sci. Technol. Adv. Mater. 18 (2017) 584–610. https://doi.org/10.1080/14686996.2017.1361305.

[9] Z. Szklarska-Smialowska, Review of Literature on Pitting Corrosion Published Since 1960, Corrosion. 27 (1971) 223–233. https://doi.org/10.5006/0010-9312-27.6.223.

[10] T.D. Ngo, A. Kashani, G. Imbalzano, K.T.Q. Nguyen, D. Hui, Additive manufacturing (3D printing): A review of materials, methods, applications and challenges, Compos. Part B Eng. 143 (2018) 172–196. https://doi.org/10.1016/j.compositesb.2018.02.012.

[11] L.E. Murr, A Metallographic Review of 3D Printing/Additive Manufacturing of Metal and Alloy Products and Components, Metallogr. Microstruct. Anal. 7 (2018) 103–132. https://doi.org/10.1007/s13632-018-0433-6.

[12] P.A. Hooper, Melt pool temperature and cooling rates in laser powder bed fusion, Addit. Manuf. 22 (2018) 548–559. https://doi.org/10.1016/j.addma.2018.05.032.

[13] N. Shamsaei, A. Yadollahi, L. Bian, S.M. Thompson, An overview of Direct Laser Deposition for additive manufacturing; Part II: Mechanical behavior, process parameter optimization and control, Addit. Manuf. 8 (2015) 12–35. https://doi.org/10.1016/j.addma.2015.07.002.

[14] S.W. Williams, F. Martina, A.C. Addison, J. Ding, G. Pardal, P. Colegrove, Wire + Arc Additive Manufacturing Wire þ Arc Additive Manufacturing, (2017) 1–35. https://doi.org/10.1179/1743284715Y.0000000073doi.org/10.1179/1743284715Y.0000000073.

[15] S.A.M. Tofail, E.P. Koumoulos, A. Bandyopadhyay, S. Bose, L. O'Donoghue, C. Charitidis, Additive manufacturing: Scientific and technological challenges, market uptake and opportunities, Mater. Today. 21 (2017) 22–37. https://doi.org/10.1016/j.mattod.2017.07.001.

[16] M.J. Galba, T. Reischle, Additive Manufacturing of Metals Using Powder-Based Technology, in: Addit. Manuf., 2015: pp. 97–142. https://doi.org/doi:10.1201/b18893-5.

[17] M.P. Ryan, D.E. Williams, R.J. Chater, B.M. Hutton, D.S. McPhail, Why stainless steel corrodes, Nature. 415 (2002) 770–774. https://doi.org/10.1038/415770a.

[18] G.S. Frankel, N. Sridhar, Understanding localized corrosion, Mater. Today. 11 (2008) 38–44. https://doi.org/10.1016/S1369-7021(08)70206-2.

[19] G.T. Burstein, C. Liu, R.M. Souto, S.P. Vines, Origins of pitting corrosion, Corros. Eng. Sci. Technol. 39 (2004) 25–30. https://doi.org/10.1179/147842204225016859.

[20] J. Soltis, Passivity breakdown, pit initiation and propagation of pits in metallic materials - Review, Corros. Sci. 90 (2015) 5–22. https://doi.org/10.1016/j.corsci.2014.10.006.

[21] G. Koch, Cost of corrosion, Elsevier Ltd, 2017. https://doi.org/10.1016/B978-0-08-101105-8.00001-2.

[22] P. Ernst, R.C. Newman, Explanation of the effect of high chloride concentration on the critical pitting temperature of stainless steel, Corros. Sci. 49 (2007) 3705–3715. https://doi.org/10.1016/j.corsci.2007.03.026.